

**Exploring and Exploiting  
Charge-Carrier Confinement in  
Semiconductor Nanostructures:**

**Heterodimensionality in Sub-Monolayer  
InAs in GaAs**

*and*

**Photoelectrolysis Using Type-II  
Heterojunctions**

Samuel Harrison

Master of Physics



This thesis is submitted in partial fulfilment of the requirements for  
the degree of Doctor of Philosophy.

November 2016

# Exploring and Exploiting Charge-Carrier Confinement in Semiconductor Nanostructures

Samuel Harrison

November 2016

## Abstract

In this thesis, semiconductor nanostructures are studied, both experimentally and theoretically, to help aid the development of two diverse and important technologies.

Firstly, charge-carrier confinement in stacked sub-monolayer (SML) InAs in GaAs: SML deposition results in the formation of In-rich agglomerations within a lateral InGaAs quantum well (QW) with lower In content. Low-temperature photoluminescence (PL) and magneto-PL reveals strong vertical and weak lateral confinement, indicative of a two-dimensional (2D) excitons. Paradoxically, high-temperature magneto-PL allows excited-state peaks to become resolved, which can be fitted by a Fock–Darwin spectrum, characteristic of a zero-dimensional (0D) system. To solve this contradiction, we postulate that stacked SML InAs in GaAs forms a *heterodimensional* system, in which electrons are 2D, and see only the lateral InGaAs QW, whilst the heavier holes are 0D, and are confined in the In-rich agglomerations. This description is fully supported by single-particle effective-mass and eight-band  $\mathbf{k} \cdot \mathbf{p}$  calculations, which show heterodimensional confinement is probable for a large variation in In content.

SML vertical-cavity surface-emitting lasers (VCSELs)—which prove to be one of the most promising candidates for datacoms applications—have been demonstrated at  $>20 \text{ Gbs}^{-1}$ , and we postulate that heterodimensionality is fundamental to this

high-speed operation. Efficient carrier injection is achieved by the lack of a wetting layer, along with the 2D electrons coupling to several In-rich agglomerations, making them quickly available to states that are lasing. Furthermore, the shallow confining potential of the In-rich agglomerations means that excess holes cannot build up in states that aren't lasing.

Secondly, semiconductor photoelectrolysis for the solar-powered generation of renewable hydrogen by water splitting is researched. The novel use of nanostructures at the semiconductor–electrolyte interface (SEI) in a photoelectrochemical cell (PEC) is proposed to help increase the maximum potential that can be photo-generated, thus increasing the likelihood of a given PEC being able to split water. By solving the Schrödinger, Poisson and drift–diffusion equations, we simulate the band alignment, confined carrier energy states and carrier densities for a variety of different material systems. ZnO quantum dots on  $\text{In}_x\text{Ga}_{1-x}\text{N}$  show the most promising band alignment, with electron-donating and -accepting states straddling the hydrogen- and oxygen-production potentials (respectively) for small  $x$  ( $x < 0.3$ ), indicating an ability to split water.

I hereby declare that, except where specific reference is made to the work of others, the contents of this thesis is my own work and has not been submitted in whole or in part for consideration for any other degree or qualification in this, or any other institute of learning.

Samuel Harrison

November 2016

# Acknowledgements

Firstly, I would like to express sincere gratitude to my supervisor, Dr. Manus Hayne, for his support, guidance and knowledge throughout my time at Lancaster University. His constant willingness to help, as well as an interest for and commitment to my work and a dedication to experimental work in the photoluminescence laboratory, has proved invaluable. My secondary supervisor, Dr. Robert Young, has also provided crucial support and advice when needed most.

I would like to thank Dr. Peter Hodgson for teaching me the operational principles of the photoluminescence laboratory, as well as demonstrating great commitment in its constant maintenance and upgrading. Dr. Lefteris Danos must also be commended for his enthusiasm in enabling time-resolved photoluminescence measurements. Thanks also to Matthew Young for helping with the collection of data in the preliminary studies of sub-monolayer samples.

Extending my gratitude further, I would like to thank members of the Quantum Nanotechnology group at Lancaster University for their help and friendship throughout my PhD, in particular fellow students who are or have been under Dr. Manus Hayne's supervision: Laura Hanks, Dr. Shaukat Khattak, Dr. Alex Robson, Dr. Kylie O'Shea and Ofogh Tizno.

The work on sub-monolayer heterostructures presented herein would not have been possible without samples, theoretical calculations, general support and kind words of encouragement from colleagues at Technische Universität Berlin, including Prof. Dieter Bimberg, Prof. Holger Eisele, Dr. Andrea Lenz, Prof. Udo W. Pohl, Dr. Andrei Schliwa and Dr. André Strittmatter.

All of my family, and especially my parents, have shown a great amount of support and patience over the past four years, and to them I am extremely grateful.

Finally, a special thanks goes to my wife, Lorna. Her constant encouragement, belief and understanding has made writing this thesis not just possible, but enjoyable as well.



# Contents

<b>Abstract</b>	<b>ii</b>
<b>Acknowledgements</b>	<b>v</b>
<b>1 Introduction</b>	<b>1</b>
1.1 Sub-Monolayer InAs in GaAs for High-Speed Datacoms . . . . .	1
1.2 Photoelectrolysis . . . . .	3
1.3 Synopsis . . . . .	5
<b>2 Theory &amp; Background Information</b>	<b>7</b>
2.1 Crystals . . . . .	7
2.1.1 Crystallographic Planes and Miller Indices . . . . .	9
2.2 Electronic Band Structure . . . . .	11
2.2.1 $E$ - $k$ Diagrams and Effective Masses . . . . .	13
2.2.2 Fermi Level, Electron Affinity and the Work Function . . . . .	15
2.2.3 Heterojunction Band Alignment . . . . .	16
2.2.4 Temperature Dependence of the Band Gap . . . . .	18
2.3 Low-Dimensional Nanostructures . . . . .	18
2.3.1 Quantum Wells . . . . .	19
2.3.2 Quantum Dots . . . . .	19
2.4 Carrier Distribution . . . . .	20
2.4.1 Density of States . . . . .	20
2.4.2 Fermi–Dirac Distribution . . . . .	22
2.5 Absorption, Recombination and Emission . . . . .	24
2.5.1 Direct and Indirect Band Gaps . . . . .	24
2.5.2 Absorption and Excitons . . . . .	25

2.5.3	Recombination . . . . .	28
2.5.4	Photoluminescence . . . . .	29
2.6	Doping . . . . .	31
2.6.1	Carrier Density . . . . .	31
2.6.2	P–N Junctions . . . . .	33
2.7	Lasers . . . . .	34
2.7.1	Gain . . . . .	36
2.7.2	Edge-Emitting Lasers . . . . .	37
2.7.3	Vertical-Cavity Surface-Emitting Lasers . . . . .	37
2.8	Excitons in a Magnetic Field . . . . .	38
2.8.1	Landau Levels . . . . .	39
2.8.2	Excitons . . . . .	40
2.8.3	Low-Dimensional Nanostructures . . . . .	40
2.8.4	Fock–Darwin Model . . . . .	41
2.8.5	Excitonic Model . . . . .	43
2.9	Electrochemistry Basics . . . . .	45
2.9.1	Electrodes and Electrolytes . . . . .	45
2.9.2	Half-Reactions, Reduction and Oxidation . . . . .	46
2.9.3	Conventions . . . . .	47
2.10	Semiconductor Photoelectrolysis . . . . .	48
2.10.1	Hydrogen and Oxygen Production . . . . .	49
2.10.2	Band Bending at the Semiconductor–Electrolyte Interface . . . . .	51
2.10.3	Illumination and the Flat-Band Potential . . . . .	53
2.10.4	Calculating the Schottky Barrier Height . . . . .	55
2.10.5	Semiconductor Electrode Material Requirements . . . . .	56
2.11	Epitaxial Growth . . . . .	58
2.11.1	Self-Assembled Growth . . . . .	58
<b>3</b>	<b>Experimental &amp; Theoretical Techniques</b>	<b>61</b>
3.1	Metal-Organic Chemical Vapour Deposition . . . . .	61
3.2	Cross-Sectional Scanning Tunnelling Microscopy . . . . .	63
3.3	Magneto-Photoluminescence . . . . .	65
3.3.1	The Cryostat and Magnet . . . . .	67

3.4	Time-Resolved Photoluminescence . . . . .	69
3.5	Theoretical Modelling . . . . .	72
3.5.1	A Very Brief Introduction to Quantum Mechanics . . . . .	72
3.5.2	Numerical Analysis . . . . .	73
3.5.3	COMSOL Multiphysics . . . . .	74
3.5.4	nextnano . . . . .	77
<b>4</b>	<b>Sub-Monolayer InAs in GaAs</b>	<b>87</b>
4.1	Literature Review . . . . .	87
4.1.1	Optics for Data Transmission . . . . .	87
4.1.2	VCSELS as Data Transmitters . . . . .	89
4.1.3	Quantum Dot Lasers . . . . .	90
4.1.4	Sub-Monolayer Growth . . . . .	94
4.2	Results . . . . .	102
4.2.1	Samples . . . . .	102
4.2.2	Evidence for a Two-Dimensional System . . . . .	104
4.2.3	Evidence for a Zero-Dimensional System . . . . .	113
4.2.4	Comparison with the Quantum Well . . . . .	114
4.2.5	Heterodimensionality . . . . .	119
4.2.6	Modelling . . . . .	121
4.2.7	Discussion . . . . .	126
<b>5</b>	<b>Photoelectrolysis</b>	<b>129</b>
5.1	Literature Review . . . . .	129
5.1.1	Historical Perspective . . . . .	129
5.1.2	Tandem (Multi-Junction) Cells . . . . .	131
5.1.3	Nanostructured Electrodes and Nanoparticles . . . . .	134
5.1.4	Electrode Stability . . . . .	136
5.2	Innovation Using Nanostructures . . . . .	137
5.3	Modelling Setup . . . . .	138
5.4	Results . . . . .	140
5.4.1	Bulk Semiconductor Electrodes . . . . .	140
5.4.2	Type-II Quantum Dot Materials . . . . .	144

5.4.3	BeSe, ZnO and ZnS . . . . .	146
5.4.4	Band Bending . . . . .	151
5.4.5	Discussion . . . . .	152
<b>6</b>	<b>Conclusions</b>	<b>157</b>
6.1	Sub-Monolayer InAs in GaAs . . . . .	157
6.1.1	Further Work . . . . .	159
6.2	Photoelectrolysis . . . . .	161
6.2.1	Further Work . . . . .	163
<b>A</b>	<b>Temperature Dependence</b>	<b>167</b>
	<b>References</b>	<b>171</b>

# List of Publications and Presentations

## Academic Papers

S. Harrison and M. Hayne. Photoelectrolysis using type-II semiconductor heterojunctions. *Submitted to Nature Energy*.

S. Harrison, M. P. Young, P. D. Hodgson, R. J. Young, M. Hayne, L. Danos, A. Schliwa, A. Strittmatter, A. Lenz, H. Eisle, U. W. Pohl and D. Bimberg. Heterodimensional charge-carrier confinement in stacked submonolayer InAs in GaAs. *Phys. Rev. B*, 93:085302, 2016. DOI: [10.1103/PhysRevB.93.085302](https://doi.org/10.1103/PhysRevB.93.085302).

Y.-C. Chang, A. Robson, S. Harrison, Q. Zhuang and M. Hayne. Phonon bottleneck in GaAs/Al<sub>x</sub>Ga<sub>1-x</sub>As quantum dots. *AIP Advances*, 5:067141, 2015. DOI: [10.1063/1.4922950](https://doi.org/10.1063/1.4922950).

## Conference Presentations

S. Harrison and M. Hayne. Photoelectrolysis. *RAMS Conference*, Lancaster, 22-23 September 2016 (oral presentation).

S. Harrison and M. Hayne. Photoelectrolysis. *Lancaster University Faculty and Science and Technology Christmas Conference*, Lancaster, 15 December 2015 (oral presentation).

S. Harrison, M. P. Young, P. D. Hodgson, R. J. Young, M. Hayne, L. Danos, A. Schliwa, A. Strittmatter, A. Lenz, H. Eisle, U. W. Pohl and D. Bimberg. Heterodimensional charge-carrier confinement in stacked submonolayer InAs in GaAs. *UK Semiconductors Conference*, Sheffield, 1-2 July 2015 (poster presentation).

S. Harrison, M. P. Young, P. D. Hodgson, R. J. Young, M. Hayne, L. Danos, A. Schliwa, A. Strittmatter, A. Lenz, H. Eisle, U. W. Pohl and D. Bimberg. Heterodimensional charge-carrier confinement in stacked submonolayer InAs in GaAs. *COMSOL Conference*, Cambridge, 17-19 September 2014 (oral presentation).

S. Harrison, M. P. Young, P. D. Hodgson, R. J. Young, M. Hayne, L. Danos, A. Schliwa, A. Strittmatter, A. Lenz, H. Eisle, U. W. Pohl and D. Bimberg. Heterodimensional charge-carrier confinement in stacked submonolayer InAs in GaAs. *UK Semiconductors Conference*, Sheffield, 9-10 July 2014 (oral presentation).

S. Harrison, M. P. Young, P. D. Hodgson, R. J. Young, M. Hayne, L. Danos, A. Schliwa, A. Strittmatter, A. Lenz, H. Eisle, U. W. Pohl and D. Bimberg. Heterodimensional charge-carrier confinement in stacked submonolayer InAs in GaAs. *International Conference on Quantum Dots*, Pisa, Italy, 11-16 May 2014 (poster presentation).

S. Harrison, A. Robson, R. Wilbraham, C. Boxall and M. Hayne. Photoelectrolysis: Solar-powered production of hydrogen. *Lancaster University Faculty and Science and Technology Christmas Conference*, Lancaster, 17 December 2013 (poster presentation).

S. Harrison, M. P. Young, P. D. Hodgson, R. J. Young, M. Hayne, L. Danos, A. Schliwa, A. Strittmatter, A. Lenz, H. Eisle, U. W. Pohl and D. Bimberg. Heterodimensional charge-carrier confinement in stacked submonolayer InAs in GaAs. *UK Semiconductors Conference*, Sheffield, 3-4 July 2013 (oral presentation).

# List of Figures

1.1	Simplified scheme of communication length scales. Arrows points in the direction of smaller interconnect distances. Optics are already used for global area network (GAN), metropolitan area network (MAN) and local area network (LAN) applications, whilst copper wiring still dominates for box, board and chip levels. . . . .	2
1.2	Primary energy consumption by source in 2014, for <b>(a)</b> the UK and <b>(b)</b> the world [1]. . . . .	3
1.3	Energy densities per unit volume ( $\text{MJ L}^{-1}$ ) and per unit weight ( $\text{MJ kg}^{-1}$ ) for selected materials. Adapted from Reference 2. . . . .	4
2.1	Czochralski growth process. <b>(a)</b> Poly-crystalline semiconductor material is melted. <b>(b)</b> A seed is introduced. <b>(c)</b> Crystal growth begins around the seed. <b>(d)</b> Seed is pulled out to achieve a cylindrical single-crystalline boule. <b>(e)</b> Formed crystal with residue of melted poly-crystal. Adapted from Reference 3. . . . .	8
2.2	Two of the most common semiconductor Bravais lattices, face-centred cubic and hexagonal close-packed. . . . .	9
2.3	<b>(a)</b> Zinc-blende and <b>(b)</b> wurtzite crystal structures. Unit cells are shown by black dashed lines and for wurtzite, the remainder of the “hexagonal” structure is shown faded for a demonstration of how wurtzite relates to the hexagonal close-packed lattice. . . . .	10
2.4	Various crystallographic planes and their Miller indices, $(hkl)$ . . . . .	10

2.5	Miller–Bravais indexing of crystal planes for hexagonal structures, introducing a third axis, $i$ . The three coloured planes are crystallographically equivalent, which is easier to tell from their Miller–Bravais indices $(1\bar{1}00)$ , $(10\bar{1}0)$ and $(01\bar{1}0)$ , as opposed to their Miller indices $(1\bar{1}0)$ , $(100)$ and $(010)$ . . . . .	11
2.6	Formation of energy bands in diamond as atoms are brought close together. As a single atom, the highest-energy atomic orbitals are 2s and 2p, which are shown. When the lattice constant is that of diamond, $a_0$ , a conduction and valence band can be clearly seen, with band edges $E_c$ and $E_v$ , respectively [4, 5]. . . . .	12
2.7	Energy band diagrams for: <b>(a)</b> a metal with partially filled valence band; <b>(b)</b> a metal with overlapping valence and conduction bands; <b>(c)</b> a semiconductor, and; <b>(d)</b> an insulator with band gap $E_g$ . Shaded grey area represents electron occupation. . . . .	13
2.8	A simplified representation of the conduction and valence band edges as a function of wave number $k$ . . . . .	14
2.9	Band structure of GaAs, showing the presence of $X$ -valley, $\Gamma$ -valley and $L$ -valley band gaps [6]. . . . .	15
2.10	Heterojunction band alignment for <b>(a)</b> type-I, <b>(b)</b> type-II and <b>(c)</b> type-II broken-gap systems. . . . .	16
2.11	Low-dimensional nanostructures (coloured regions): <b>(a)</b> Quantum well (QW); <b>(b)</b> quantum wire and; <b>(c)</b> quantum dots (QDs), all embedded in another semiconductor material (transparent box). . . .	19
2.12	Conduction band density of states (DOS) $g(E)$ as a function of energy $E$ for a bulk semiconductor (green solid line), QW (blue dashed line) and QD (orange dotted line). . . . .	21
2.13	Fermi–Dirac distribution, represented by the solid red line, for: <b>(a)</b> absolute zero; <b>(b)</b> some finite temperature above absolute zero, and; <b>(c)</b> an temperate higher than in <b>(b)</b> . In <b>(c)</b> the temperature is high enough that it is probable that conduction band states will be occupied. There are no states available to be occupied in the band gap. . . . .	22

2.14	Charge carrier distribution for electrons in the conduction band (green) and holes in the valence band (blue) at an elevated temperature, which is a product of the DOS (blue dashed lines) and the Fermi-Dirac distribution (red dotted lines). The remaining available states in the valence band will be occupied by electrons, but this is omitted from the diagram for simplicity. . . . .	23
2.15	Recombination of electrons (solid circles) from the valence band into holes (hollow circles) in the conduction band for <b>(a)</b> direct and <b>(b)</b> indirect semiconductors. Direct recombination results in the emission of a photon with energy $h\nu = E_g$ , whilst indirect recombination is a two-step process also necessitating the emission of a phonon with energy $E_p$ , such that the energy of the emitted photon is $h\nu = E_g - E_p$ .	24
2.16	Absorption of a photon with an energy <b>(a)</b> less than the band gap, <b>(b)</b> equal to the band gap and <b>(c)</b> greater than the band gap. . . . .	26
2.17	Solar irradiance spectrum above the atmosphere and at the surface of the Earth. Adapted from Reference 7. . . . .	26
2.18	The generation of an exciton from a photon with energy less than the band gap by a factor of the exciton binding energy $E_b$ , for a direct band gap semiconductor. . . . .	27
2.19	Non-radiative recombination mechanisms. <b>(a)</b> Shockley-Read-Hall recombination via mid-gap trap states. <b>(b)</b> Auger recombination, resulting in the excitation of a third charge carrier. . . . .	28
2.20	The most common radiative recombination processes: <b>(a)</b> Band-to-band; <b>(b)</b> conduction band to acceptor state; <b>(c)</b> donor state to valence band; <b>(d)</b> donor state to acceptor state, and; <b>(e)</b> excitonic radiative recombination. . . . .	29
2.21	Representation of the photoluminescence (PL) process for a heterostructure. An incident photon from excitation light is absorbed, for example, in the bulk semiconductor, before relaxing down into the nanostructure or QW and recombining to give a photon with energy equal to the difference between electron and hole states. . . . .	30

2.22	Fermi–Dirac distribution $f(E)$ (dotted lines), conduction and valence band density of states $g_{c,v}(E)$ (dashed lines) and carrier population (solid shapes) for <b>(a)</b> n-type and <b>(b)</b> p-type semiconductors. Donor and acceptor energy levels, $E_d$ and $E_a$ , are shown as lying close to the conduction and valence band edges, respectively. The Fermi level is pushed up towards the conduction band in n-type materials, and pulled down to the valence band in p-type materials. . . . .	32
2.23	Band diagram of a p–n junction in equilibrium, where band bending results in an built-in potential $V_0$ . . . . .	34
2.24	P–n junction under <b>(a)</b> forward bias, enabling radiative recombination, and <b>(b)</b> reverse bias, preventing the recombination of charge carriers. . . . .	34
2.25	The principle of light amplification through the stimulated emission of a photon, prompted by the collision of a photon with an excited electron in the conduction band. . . . .	35
2.26	Band diagram for an GaAs/AlGaAs QW laser. <b>(a)</b> In equilibrium, when the large band bending between the n-AlGaAs and GaAs QW prevents carriers recombining. <b>(b)</b> Under forward bias $V_{app}$ , so that electrons and holes can be injected into the QW active region and radiatively recombine. . . . .	36
2.27	Simplified representation of <b>(a)</b> an edge-emitting laser, and <b>(b)</b> a vertical-cavity surface-emitting laser (VCSEL). Red regions demonstrate where light emission is from. Adapted from Reference 8. . . . .	38
2.28	Fock–Darwin (FD) spectrum from Equation 2.35 for $\hbar\omega_0 = 3\text{ meV}$ , $m_e^* = 0.067m_0$ and $E_0 = 0$ , for $0 \geq n \geq 3$ and $-5 \geq l \geq 5$ . $n = 0$ states represented by blue solid lines, $n = 1$ by green, $n = 2$ by red and $n = 3$ by black. The formation of Landau levels at higher magnetic fields can clearly be seen, and the Landau levels themselves, from Equation 2.31, are shown by the thicker yellow lines for comparison. . . . .	42
2.29	A simplified schematic of a photoelectrochemical cell (PEC), consisting of a semiconductor electrode and a counter electrode immersed in an aqueous electrolyte. . . . .	49

2.30	<p>Energy band diagrams for the semiconductor–electrolyte interface (SEI). <b>(a)</b> Not in equilibrium. In the semiconductor, the conduction and valence band edges, <math>E_c</math> and <math>E_v</math>, semiconductor Fermi level <math>E_{F,s}</math> and vacuum level <math>E_{vac}</math> are shown, with the distance from <math>E_c</math> to <math>E_{vac}</math> represented by the electron affinity <math>\chi</math>, and the gap between <math>E_c</math> and <math>E_{F,s}</math> defined as <math>\alpha</math>. In the electrolyte, the two distribution functions shown are the density of ionic energy states available for oxidation and reduction, which arise due to fluctuations in individual ionic states [9], with peaks at the oxidation and reduction potentials, <math>E_{ox}</math> and <math>E_{red}</math>, and an overlap at the redox Fermi potential, <math>E_{F,redox}</math>. <b>(b)</b> N-type semiconductor in equilibrium, showing the upwards bending of the bands so that the semiconductor and electrolyte Fermi levels meet at <math>E_F</math>. <math>V_{fb}</math> is the flatband potential and <math>\phi_B = E_{c,SEI} - E_F</math> is the Schottky barrier, where <math>E_{c,SEI}</math> is the conduction band edge at the SEI. <b>(c)</b> Equivalent to (b) but for p-type semiconductor in equilibrium. . . . .</p>	52
2.31	<p>Energy band diagram for a PEC with n-type semiconductor electrode <b>(a)</b> in the dark and <b>(b)</b> illuminated. Incident sunlight generates a photovoltage <math>V_{ph}</math> that raises the semiconductor and hence counter-electrode Fermi level, so that it and the valence band edge at the SEI straddle the oxygen- and hydrogen-production potentials, which are shown in the electrolyte. Holes and electrons can then transfer to the solution to drive the water-splitting half-reactions, shown in <b>(b)</b>. . . . .</p>	54
2.32	<p>Mechanisms of epitaxial growth: <b>(a)</b> Frank–van der Merwe (layer-by-layer); <b>(b)</b> Volmer–Weber (island) and; <b>(c)</b> Stranski–Krastanow (layer-by-layer plus island) . . . . .</p>	58
3.1	<p>Schematic representation of the key metal-organic chemical vapour deposition (MOCVD) processes. Precursor molecules undergo gas-phase reactions as they are transported to the surface, where they are adsorbed and diffuse to energetically favourable sites, before the desorption of reaction products. . . . .</p>	62

3.2	Simplified MOCVD system. Precursors are carried to the reaction chamber by an inert carrier gas, via an injection control system. Reaction products are transported away by an effluent control system. . . . .	63
3.3	Schematic representation of tunnelling in scanning tunnelling microscopy (STM) devices, showing the Fermi level $E_F$ , vacuum energy level $E_{vac}$ and the difference between them (the work function) $\Phi = E_{vac} - E_F$ . <b>(a)</b> With zero bias, the Fermi level of the sample and tip are the same. <b>(b)</b> With a bias applied, the sample's Fermi level is raised with respect to the tip's. Empty states now exist in the tip and the tunnelling of electrons through the potential barrier (represented in the diagram by the electron wave function) results in a tunnelling current. . . . .	64
3.4	A simplified illustration of the magneto-PL laboratory setup. Laser light is sent down an optic fibre to the sample, and the subsequent PL emission sent via another fibre to a spectrometer, detector and finally a control computer for data analysis. The sample is mounted on the end of a tube that can be inserted into a cryostat with superconducting magnet (Section 3.3.1). . . . .	65
3.5	Brass sample holder for <b>(a)</b> Faraday geometry and <b>(b)</b> Voigt geometry measurements. The holder is screwed into the end of the sample tube through which the optical fibres pass. . . . .	66
3.6	Simplified illustration of the cryostat used for magneto-PL measurements. Not shown is an outlet to a pump from the lambda coils so that they too can be pumped on. . . . .	67

3.7	Simplification of the time-correlated single-photon counting (TCSPC) method used to take time-resolved PL (TRPL) measurements. Light from a laser diode is split so part of it hits the sample and part travels to a time-to-amplitude converter (TAC) via a constant-fraction discriminator (CFD). The PL emission from the sample passes through a monochromator, photomultiplier tube (PMT) and a CFD before reaching the TAC. The timing signal from the TAC then passes through an analogue-to-digital converter (ADC) before finally reaching a control computer for analysis. . . . .	70
3.8	(a) Threshold triggering. A timing signal is triggered at time $t$ , when the peak reaches a certain voltage threshold, resulting in a dependence of the timing signal on the peak amplitude. (b) Constant-fraction discrimination. Here, the timing signal is triggered at a constant fraction $k$ of the peak's amplitude $A$ . . . . .	71
3.9	The process by which the TAC operates. The first signal initiates linear charging of a capacitor and the second signal stops this charging at a voltage proportional to the time difference between these signals. When applied to TCSPC systems, the first signal is the synchronisation signal from the laser, the second is from the detector after PL emission has occurred, and the time difference between these is the decay time of the particular photon detected. . . . .	71
3.10	Schematic representation of the real part of a Bloch wave in 1D, $\psi_{n,k} = e^{ikx}u_{n,k}(x)$ (black solid line), for an arbitrary Bloch function $u_{n,k}(x) = \frac{1}{3} \cos(4\pi x)$ (green solid line) and plane wave $e^{ikx}$ (blue dashed line). Adapted from Reference 10. . . . .	80
3.11	Flow chart of the self-consistent solving of the Schrödinger, Poisson and drift-diffusion equations, sometimes referred to as a <i>quantum drift-diffusion</i> solver. In <code>nextnano</code> , a trial potential $V_0$ and carrier density $n_0$ is obtained from solving the Schrödinger and Poisson equations self-consistently in equilibrium (without any applied field), to determine the built-in field. . . . .	84

4.1	Representative band alignment for an InAs/GaAs QD laser. InAs Stranski–Krastanow (SK) QDs are grown in a GaAs matrix, which is surrounded by cladding to prevent the escape of carriers (for example, made of AlGaAs). QD electron and hole states are shown, as well as the wetting layer states. As holes have a higher effective mass, their energy levels are packed more closely than for the electron. . . . .	91
4.2	Publication and citation data from Reference 11 using the following italicised search terms: <b>(a)</b> Annual number of publications with <i>quantum dot laser</i> (green) or <i>quantum dot laser AND (submonolayer OR sub-monolayer)</i> (blue) in the title. <b>(b)</b> Annual number of citations for publications with <i>(submonolayer OR sub-monolayer) AND ((InAs GaAs) OR (quantum dot))</i> (orange) in the title. . . . .	94
4.3	The nominal growth of a sub-monolayer (SML) system, in which the <1-ML deposition of InAs (green) results in the formation of ~1-ML-high, vertically-aligned, InAs islands in a GaAs matrix (grey). Self-assembled island formation is due to different surface stresses, $\tau_i$ and $\tau_j$ (black arrows), resulting in an elastic relaxation force $F$ (white arrows). . . . .	96
4.4	Cross-sectional scanning tunnelling microscopy (XSTM) image, taken at $V = \pm 2.9$ volt, $I = 80$ pA, of a SML sample with 2.3 ML GaAs spacer-layer thickness. In <b>(b)</b> , yellow dashed lines are a guide for the eye to highlight the In-rich agglomerations. . . . .	98
4.5	<b>(a)</b> The nominal growth of a SML system, in which the <1-ML deposition of InAs (green) results in the formation of ~1-ML-high, vertically-aligned, InAs islands in a GaAs matrix (grey). <b>(b)</b> A XSTM image, taken at $V = \pm 2.9$ V, $I = 80$ pA, of a SML sample with 2.3 ML GaAs spacer-layer thickness. The yellow dashed lines are a guide for the eye to highlight the In-rich agglomerations. <b>(c)</b> Representative band structure that the SML system in <b>(b)</b> is likely to result in, with the In-rich agglomerations (QDs) offering a confining potential within the SML stack (QW). . . . .	103

4.6	2-K zero-field normalised PL from the three SML samples and the QW sample. The inset shows the linewidth dependence on the stack height of the three SML samples (or the QW thickness, indicated by the circle). . . . .	104
4.7	Room-temperature zero-field normalised PL from the three SML samples and the QW sample, showing both homogeneous and inhomogeneous broadening compared to the low-temperature PL. . . . .	106
4.8	2-K magneto-PL in Faraday geometry for the three SML samples and the QW, showing the PL peak energy shift dependence on magnetic field $B$ . Shapes represent the data, whilst solid lines show the excitonic model fit. The crossover from low- to high-field regime is indicated by the arrow for each sample. The inset shows the individual PL spectra for the four samples at 15 T. Parameters interpreted from excitonic fitting are summarised in Table 4.2. . . . .	107
4.9	2-K magneto-PL in Voigt geometry for the three SML samples. The inset shows the diamagnetic energy shift coefficient $\Gamma$ dependence on the square of the stack height. . . . .	108
4.10	Voigt-geometry PL linewidth dependence on the magnetic field. Strong vertical confinement means the magnetic field has marginal effect in squeezing exciton wave functions. . . . .	110
4.11	Faraday-geometry PL linewidth dependence on the magnetic field. Two disorder length scales result in the initial reduction in linewidth with field, followed by the subsequent monotonic increase. . . . .	112
4.12	A schematic representation of the two disorder length scales, $\chi_1$ and $\chi_2$ , present in the SML samples. Ellipses illustrate exciton sizes at $B = 0$ (solid line) and $B \gg 0$ (dashed line). Applying a magnetic field squeezes the exciton so it only sees the smaller $\chi_1$ , which is most likely due to monolayer fluctuations in the QW thickness. . . . .	112

4.13	(a) 400-K magneto-PL for sample C in Faraday geometry. The solid lines are fits to a FD spectrum with Landau-level index $n$ and orbital angular momentum $l$ . The (red) dotted lines show the best attempt at a Landau-level fit. (b) 400-K 17-T spectrum corresponding to the 17-T data points in (a). The data are represented by the thick black line, the individual Lorentzian fitting peaks by the thin red lines, and the sum of the fitting peaks by the blue line. . . . .	114
4.14	15-T 300-K PL spectra of the QW sample in Faraday geometry with excitation laser powers of 400, 40 and 0.4 mW. . . . .	115
4.15	Room-temperature TRPL measured at the main PL peak wavelength of 1029 nm for sample A (black), and 986 nm for the QW (green). The intensity-weighted average carrier lifetimes $\tau$ are indicated by the arrows. The inset shows the same data as the main graph for sample A, but enlarged so its convexity is clearer. . . . .	116
4.16	2-K field-dependence of the main and excited-state PL peaks for the QW, in Faraday geometry. Solid (black) lines show a Landau-level fit, whilst the dotted (red) lines are the best attempt at a FD fit. . .	117
4.17	Temperature dependence of the PL peak energy for all four samples at high power (700 mW). Grey shaded area represents the expected range for $\text{In}_x\text{Ga}_{1-x}\text{As}$ . . . . .	118
4.18	Temperature dependence of the PL peak energies for the QW and sample A, focussed on 0 to 50 K to show an S-shaped dependence at lower powers. . . . .	119
4.19	Example band structure of (a) a heterodimensional system, and (b) a type-II system. . . . .	120
4.20	Schematic representation of the extent of electron (white) and hole (grey) wave functions in a heterodimensional system. Electrons see only the lateral InGaAs QW and extend over several In-rich QDs, whilst the heavier holes are confined within the QDs. . . . .	121
4.21	Same data as Figure 4.13, but this time fitted with a modified FD (see Section 2.8.4), giving effective masses of $m_e^* = 0.052m_0$ and $m_h^* = 0.49m_0$ . . . . .	122

4.22	Schematic representation of the QW–QD heterostructure modelled, consisting of a 5-nm-diameter $\text{In}_x\text{Ga}_{1-x}\text{As}$ QD in a 13-nm-high $\text{In}_y\text{Ga}_{1-y}\text{As}$ QW. . . . .	123
4.23	Calculated ground-state energy levels for an electron and hole in the system shown in Figure 4.22, with an In content of $x = 0.5$ for the QD and $y = 0.15$ for the QW. The resulting confinement is heterodimensional. . . . .	123
4.24	Phase diagram of electron e and hole h confinement for the system shown in Figure 4.22, with varying In content. The shaded regions are defined by the calculation, whilst the solid lines are guides to the eye indicating the approximate positions of the phase boundaries, corresponding to $x = 2.2y + 0.33$ and $x = 1.1y + 0.06$ . . . . .	124
4.25	Colour contour plots of the electron and hole wave functions in a 14-nm $\text{In}_{0.25}\text{Ga}_{0.75}\text{As}$ QW with (a) no QDs, (b) an array of QDs with In content $x \leq 0.5$ and (c) an array of QDs with $x \leq 0.75$ . The QD In content is defined by a $\cos^2$ function for each dot, superposed by a Gaussian distribution spanning the entire array and centred on the middle dot. The left-hand panel shows this morphology, and the right two panels show the electron and hole wave functions. . . . .	125
5.1	A simplified p–n tandem PEC, in which an n-type anode and p-type cathode are jointly responsible for providing the photovoltage to split water. The n-type valence band edge $E_{v,n}$ and p-type conduction band edge $E_{c,p}$ must straddle the oxygen- and hydrogen-production potentials, respectively. . . . .	132

5.2	Simplified representation of a multi-junction n/p-GaInP/GaAs tandem PEC. <b>(a)</b> shows the layered structure, which can be thought of as a multi-junction photovoltaic solar cell ohmically connected to an anode and cathode such that the photovoltage drives the water-splitting reaction. <b>(b)</b> Band structure of the same cell architecture. Sunlight shines on the larger-band-gap GaInP; photons with an energy greater than the band gap of GaInP, $E_{\gamma,1} > E_{g,\text{GaInP}}$ , are absorbed in the GaInP layers, whilst those with less energy than the band gap of GaInP pass through and (if their energy is greater than the band gap of GaAs) are absorbed in the GaAs layers. The p-n junctions in the two materials split up carriers and a photo-generated current ensues, leading to a separate photovoltage for each material, $V_{\text{ph},1}$ and $V_{\text{ph},2}$ . . . . .	133
5.3	A simplified schematic band diagram of a small nanoparticle, from which photo-generated carriers transfer to the electrolyte via catalysts. Nanometre-sized particles, such as in this diagram, are too small to support a space-charge region, and transport is via diffusion (or simply because the carrier wave functions already occupy the entire particle). Micron-sized particles may encompass a space-charge region and charge transport is instead via drift. Adapted from Reference 12. . . . .	136
5.4	Ideal band structure of a PEC utilising nanostructures (e.g., QDs) at the SEI to limit the flattening of the bands due to photo-generated current. . . . .	138
5.5	A simple two-dimensional (2D) semiconductor electrode model with a QD included at the SEI. . . . .	139

5.6 Simulated band structure of a wurtzite n-GaN semiconductor electrode in water (pH = 7) with a dopant (Si) concentration of  $1 \times 10^{18} \text{ cm}^{-2}$ . For  $\phi_B = -0.1 \pm 0.5 \text{ eV}$  (deduced from  $\chi = 3.4 \pm 0.5 \text{ eV}$  and  $V_{fb} = 3.5 \pm 0.2 \text{ V}$  vs. vacuum), the conduction band edge is shown as a green solid line, the (heavy hole) valence band edge as a blue solid line and the Fermi energy as a dashed black line. The uncertainties in the band edge values are shaded in grey. For  $\phi_B = 0.5 \pm 0.3 \text{ eV}$  (obtained from literature), an electron affinity of  $\chi = 4.0 \pm 0.2 \text{ eV}$  is obtained and the subsequent conduction and valence band edges are shown as dotted lines (uncertainties are omitted for clarity). Other parameters were taken from Reference 13 or the nextnano database [14]. Band edges are positioned relative to the vacuum by the electron affinity, and it is this that gives rise to the  $\pm 0.5 \text{ eV}$  uncertainty in the energy axis. The hydrogen- and oxygen-production potentials are positioned using Equations 2.50 and 2.52, such that  $E_{red} = 4.0 \pm 0.2 \text{ V}$  vs. vacuum and  $E_{ox} = -5.2 \pm 0.2 \text{ V}$  vs. vacuum. The error arises from their conversion to values relative to the vacuum from values relative to the standard hydrogen electrode (SHE). . . . . 142

5.7 Conduction and (heavy hole) valence band edges at the SEI,  $E_{c,SEI}$  and  $E_{v,SEI}$ , for varying In content. Values for  $V_{fb}$  were taken from Reference 15 and  $\phi_B$  was calculated using these and a non-linear interpolation of  $\chi$  from  $3.4 \pm 0.5 \text{ eV}$  for GaN, to  $5.5 \pm 0.3 \text{ eV}$  for InN, with a bowing parameter of  $1.4 \text{ eV}$  [13]. . . . . 143

5.8 Eight-band  $\mathbf{k} \cdot \mathbf{p}$  calculations with strain, for a QD fabricated from different materials, grown on n-GaN. Italics indicate that the ZnO/n-GaN system is wurtzite (growth along the  $l$  axis), whilst the others are zinc-blende. The data are from a one-dimensional (1D) slice through the centre of the dot, along the growth direction. **(a)**  $E_F - \varepsilon_{h,0}$  for each of the different materials, of which three clearly meet the water-splitting requirement that  $E_F - \varepsilon_{h,0} > 1.8$  eV. Two of the materials (shown by hollow bars) result in a type-I system, whilst the rest are type-II (with broken-gap alignment highlighted by a negative  $E_F - \varepsilon_{h,0}$ ). **(b)** Band alignment of the three systems that meet the water-splitting requirement, showing the conduction band edge  $E_c$  and the (heavy hole) valence band edge  $E_v$  (solid lines), along with the first of the confined hole states  $\varepsilon_{h,0}$  (dashed lines). . . . . 145

5.9 Top: Conduction and (heavy hole) valence band alignment for **(a)** BeSe, **(b)** ZnO and **(c)** ZnS QDs on  $\text{In}_x\text{Ga}_{1-x}\text{N}$ , for  $x = 0$  (thick solid lines, lighter colour) and  $x = 0.3$  (thick dashed lines, darker colour). The band edge data represent a 1D slice through the centre of the dot.  $E_F$  and  $\varepsilon_{h,0}$  are also shown (thin dotted lines), with  $E_F$  lying close to the bulk conduction band edge, and  $\varepsilon_{h,0}$  being completely confined in the QD. The thin (black) dashed lines represent the hydrogen- and oxygen-production potentials,  $E_{\text{red}}$  and  $E_{\text{ox}}$ . Uncertainties are omitted for clarity. Bottom: Contour plot of the corresponding wave function probability amplitudes for the heavy hole ground state  $|\psi_{h,0}|^2$ , overlaid on the model structure. Black represents the highest probability, through blue, green, yellow, then red, to white (transparent), which represents the lowest probability. Thus, the hole is shown to be localised in the QD for all three material systems. . . . 147

5.10 Dependence of  $E_F - \varepsilon_{h,0}$  on  $x$  for ZnO, BeSe and ZnS QDs on  $\text{In}_x\text{Ga}_{1-x}\text{N}$ . The solid lines represent linear fits to the data, corresponding to  $E_F - \varepsilon_{h,0} = -3.1x + 2.7$  for ZnO,  $E_F - \varepsilon_{h,0} = -2.8x + 2.4$  for BeSe and  $E_F - \varepsilon_{h,0} = -2.8x + 2.0$  for ZnS. The dashed line is the water-splitting criterion that  $E_F - \varepsilon_{h,0} > 1.8$  eV. . . . . 148

5.11	Fermi level $E_F$ and first confined hole state $\varepsilon_{h,0}$ for a BeSe QD on $\text{In}_x\text{Ga}_{1-x}\text{N}$ with varying $x$ . Hydrogen- and oxygen-production potentials, $E_{\text{red}}$ and $E_{\text{ox}}$ , are shown as dashed lines, with their associated uncertainty represented by the shaded grey areas. . . . .	149
5.12	As Figure 5.11, but for a ZnO QD. . . . .	149
5.13	As Figure 5.11, but for a ZnS QD. . . . .	150
5.14	An illustration of the desired band structure and electron density, calculated by choosing the optimal parameter values within the uncertainties previously discussed. . . . .	153
5.15	Conduction and valence band edges (solid lines) for <b>(a)</b> a buried ZnO QD with a 5-nm-thick capping layer between it and the SEI, and <b>(b)</b> a 5-nm ZnO film at the SEI. The thin dashed lines represent the Fermi level (near the conduction band) and the heavy hole ground state (in the nanostructure). . . . .	155
6.1	A water-tight polytetrafluoroethylene (PTFE) sample holder design to be use in a PEC, enabling light to be shone on a semiconductor electrode, which is electrically connected to an external circuit. . . . .	164
6.2	A simplified Randles Cell, with a resistor $R_s$ representing the solution's resistance, another resistor $R_{\text{ct}}$ representing the charge transfer resistance and a capacitor $C$ representing the double-layer capacitance at the SEI. . . . .	165
A.1	Evolution of the PL spectra for Sample C with varying temperature. . . . .	168
A.2	PL linewidth of Sample C for varying temperature. . . . .	169



# List of Tables

2.1	Electric potentials of the standard hydrogen electrode (SHE) and saturated calomel electrode (SCE) relative to each other [16] and the vacuum level [17]. . . . .	46
3.1	Summary of the input data and subsequent calculation output data for next <b>n</b> ano. . . . .	78
4.1	Summary of the three SML and one QW samples studied. . . . .	104
4.2	Parameters extracted from the excitonic-model-fitting of Faraday- and Voigt-geometry magneto-PL data. No data was taken for the QW in Voigt geometry. . . . .	109
4.3	Varshni parameters obtained from the fitting of data in Figure 4.17. .	118



# Chapter 1

## Introduction

The demands posed by an ever-increasing world population, along with the industrialisation of developing countries, leads to the significant need for research in both the technologies we rely on, and the technologies we wish to develop to cope with these demands. Semiconductor nanotechnology has a huge role to play in meeting these needs, and this thesis highlights research to aid the development of two such diverse technologies.

### 1.1 Sub-Monolayer InAs in GaAs for High-Speed Datacoms

The efficient communication of knowledge and information is fundamental to modern society, and the invention of computers and the internet have revolutionised the way that this knowledge and information is transmitted. Today, a myriad of different transmission methods are used to transfer data on a multitude of different length scales. Copper wires, optical fibres and radio waves communicate information on global, national and local length scales, as well as between components inside computers.

Figure 1.1 distinguishes between different communication length scales. Global area networks (GANs), wide area networks (WANs) and metropolitan area networks (MANs) are examples of what is commonly referred to as *telecommunication* or *telecom*, whilst transmission on shorter length scales, such as in local area networks (LANs), data centres and between different components within computers, is

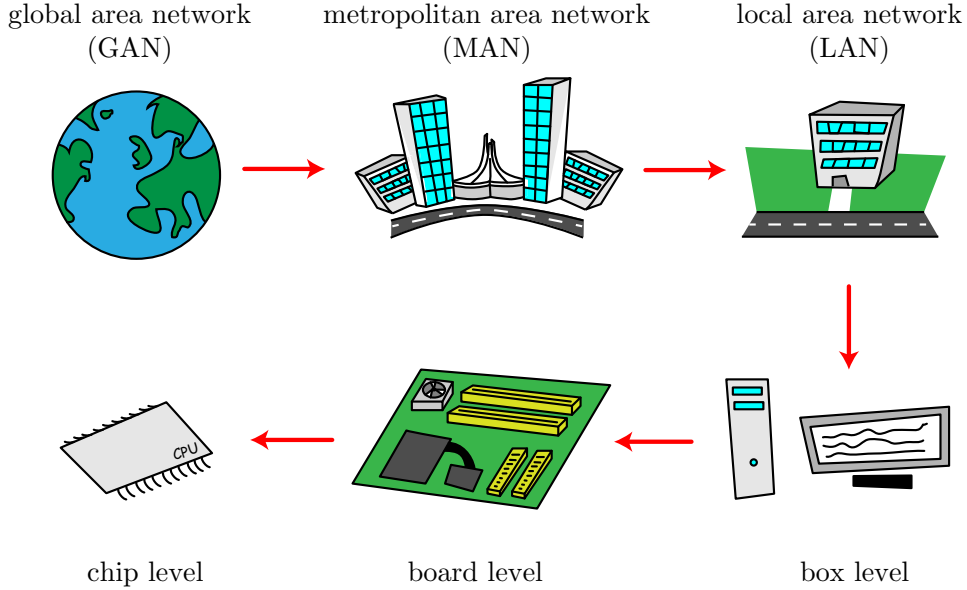


**Figure 1.1:** Simplified scheme of communication length scales. Arrows points in the direction of smaller interconnect distances. Optics are already used for global area network (GAN), metropolitan area network (MAN) and local area network (LAN) applications, whilst copper wiring still dominates for box, board and chip levels.

commonly called *data communication* or *datacom*.

A desire for the transition to optics for datacoms is borne out of the limitations that are inherent in copper circuitry. For example, attenuation losses at higher frequencies limit modulation bandwidths, and the high density of copper wiring results in undesirable crosstalk and a high power consumption [18].

Vertical-cavity surface-emitting lasers (VCSELs) are currently seen as one of the most promising methods of transmitting light down optic fibres in datacoms networks, due to their small footprint, low beam divergence (making for easy coupling to optic fibres) and on-wafer testing [18]. VCSELs based on the sub-monolayer (SML) deposition of InAs on GaAs have demonstrated fast bit rates of  $>20 \text{ Gb s}^{-1}$ , but until now, charge-carrier confinement in SML systems was not well understood.

Structurally, SML depositions form a quantum-dot–quantum-well (QD–QW) heterostructure, consisting of a lateral InGaAs QW with low In content, in which are embedded highly–non-uniform In-rich agglomerations [19, 20]. In this work, the technique of photoluminescence (PL) in a magnetic field is employed to probe the extent of charge-carrier wave functions and determine whether the QD–QW heterostructure is zero- or two-dimensional. This experimental work is backed up by Schrödinger equation modelling of the confined carrier energy states.

## 1.2 Photoelectrolysis

Energy is indispensable for the existence of life on Earth, be it in the food we eat or the fuels we burn to drive our cars, heat our homes and power the vast array of electronic devices that we use. The aforementioned problems of an increasing world population, coupled with the industrialisation of developing countries, has led to vast increases in global demand for energy [21]. Currently, fossil fuels are used by industrialised nations to meet the majority of energy demands (Figure 1.2) [1], but our over-reliance on these fuels is fundamentally flawed for the simple reasons that their combustion releases atmospheric carbon dioxide, causing global climate change, and there is only a finite amount of them available for extraction. For us to successfully adhere to the mantra of sustainable development—to meet the needs of the present without compromising the ability of future generations to meet their own needs—we clearly need to transition to a renewable and low-greenhouse-gas energy infrastructure.

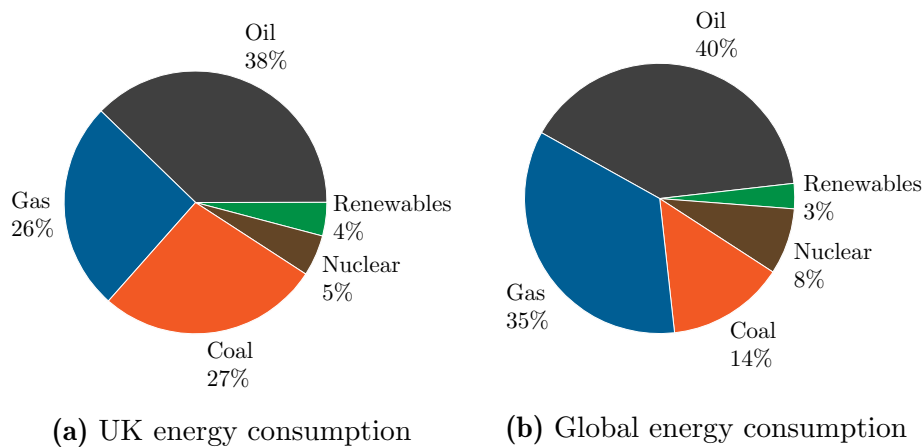


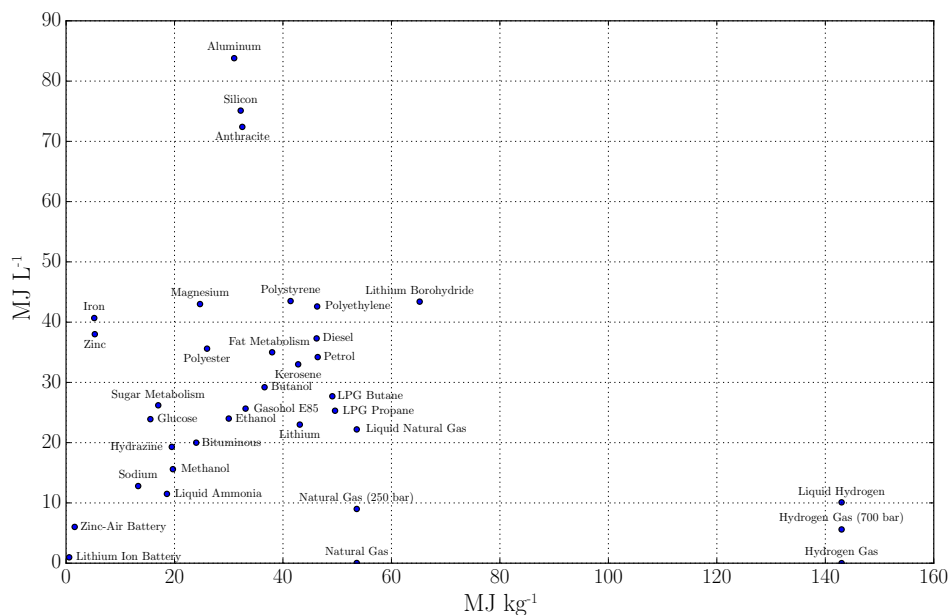
**Figure 1.2:** Primary energy consumption by source in 2014, for (a) the UK and (b) the world [1].

Solar power should play a large part of the solution to this problem; the Sun delivers enough energy to the Earth in one hour to meet our global energy demand for an entire year. Currently, solar energy is directly converted to more flexible energy forms predominantly through the use of solar cells<sup>1</sup>, which convert sunlight into electrical energy, providing approximately 1% of the UK's electricity supply in

<sup>1</sup>Excluding more complex routes from sunlight to energy, such as biomass.

2014, and over 5 % of Germany’s the same year [1]. However, generating electricity directly from sunlight doesn’t address other energy demands, such as those related to transport. In the UK, transport accounts for around 40 % of fossil fuel demand [22]. A high energy density is the major attraction of liquid fuels over batteries, and thus a method of storing solar energy as a high–energy-density fuel is desirable.

One such fuel is hydrogen, which can be converted to electricity in a fuel cell, the only by-product from which is water. Hydrogen as a fuel has already more than proved itself, having powered rockets and instruments on space craft since the 1970s [23]. Per unit weight, its energy density of  $\sim 142 \text{ MJ kg}^{-1}$  far outstrips that of any other fuel source, though per unit volume, even in liquid form ( $\sim 10 \text{ MJ L}^{-1}$ ), it is considerably worse than, for example, diesel ( $\sim 38 \text{ MJ L}^{-1}$ ) and petrol ( $\sim 34 \text{ MJ L}^{-1}$ ), as illustrated in Figure 1.3. Furthermore, it can be converted to electricity at higher efficiencies (40 to 60 % in hydrogen fuel cells) [24] than the combustion of fuels in a combustion engine (25 to 30 %) [25].



simply burned as a fuel for heating or cooking) as and when needed, in a localised stand-alone energy system. Of course, there are limitations with solar hydrogen, the most obvious being that storing hydrogen and then converting it to electricity is not as efficient as using solar energy directly to generate electricity (i.e., in photovoltaic solar cells). Therefore, solar hydrogen should form just one part of a mix of clean and sustainable energy sources, each used according to their own merit.

Photoelectrolysis research has been harboured thus far by difficulties in developing semiconductor electrode materials with suitably positioned energy bands, as well as issues with the resistance of electrodes to unwanted oxidation and reduction reactions. A particular limiting factor is the flat-band potential, which is the maximum potential that can be photo-generated under illumination, corresponding to when band bending at the semiconductor electrode surface (i.e., the interface with the water/electrolyte) is completely flattened. In this thesis, we theoretically explore the possibility of using hole-confining type-II QDs on the surface of the semiconductor electrode in order to preserve this band bending and thus maximise the flat-band potential. We do so through the use of a self-consistent quantum drift–diffusion model, which solves the Schrödinger, Poisson and drift–diffusion equations simultaneously.

### 1.3 Synopsis

This thesis begins in earnest in [Chapter 2](#) with an overview of relevant theoretical concepts. Basic semiconductor theory such as crystal and electronic structure ([Sections 2.1](#) and [2.2](#)) are first introduced, before a more specific discussion of low-dimensional nanostructures ([Section 2.3](#)), carrier distribution ([Section 2.4](#)), absorption, recombination, emission ([Section 2.5](#)) and doping ([Section 2.6](#)). A brief introduction of the theory behind the operation of lasers is presented in [Section 2.7](#), before we delve into the concepts relevant to PL in a magnetic field in [Section 2.8](#). [Sections 2.9](#) and [2.10](#) highlight the theory relevant to photoelectrolysis research, and finally the epitaxial growth of semiconductors is discussed in [Section 2.11](#).

[Chapter 3](#) is devoted to the experimental and theoretical techniques employed in this thesis, such as those used to grow ([Section 3.1](#)), image ([Section 3.2](#)) and optically

study (Sections 3.3 and 3.4) samples, as well as an overview of the mathematics used to model them (Section 3.5).

The next two chapters are devoted to the specific areas of research undertaken, firstly of SML InAs in GaAs (Chapter 4) and then semiconductor photoelectrolysis (Chapter 5). Both encompass a literature review (Sections 4.1 and 5.1) and experimental and theoretical results (Sections 4.2 and 5.4).

Finally, in Chapter 6, we conclude and discuss ideas for further work.

# Chapter 2

## Theory & Background Information

Semiconductors, as the name suggests, lie part way between insulators and conductors. In their natural state, they have a resistance much higher than a typical conductor, but given some external stimulus—for example, an applied voltage or irradiation from a light source—they become conductive. This makes them useful for all kinds of optical and electronic devices where current control is important, such as diodes, transistors and lasers.

This chapter introduces theoretical concepts and background information relevant to the experimental and modelling work carried out in this thesis. A basic outline of crystals and semiconductor band structure is presented in [Sections 2.1](#) and [2.2](#), before low-dimensional nanostructures are introduced in [Section 2.3](#). The specifics of charge-carrier distribution and recombination is discussed in [Sections 2.4](#) and [2.5](#), as well the effect of doping in [Section 2.6](#). We then move on to the theory behind the experimental technique of magneto-PL in [Section 2.8](#), before concluding with an introduction to electrochemistry ([Section 2.9](#)), its application to photoelectrolysis ([Section 2.10](#)), and finally a brief overview of epitaxial semiconductor growth ([Section 2.11](#)).

### 2.1 Crystals

The semiconductors that we study in solid-state physics are crystalline in nature, meaning that atoms are arranged in a highly-ordered structure, as opposed to being

placed at random (as in amorphous materials). Perfect crystals, with complete periodicity of atoms or groups of atoms, are called single-crystalline. Poly-crystalline structures, consisting of many single-crystalline grains and having no long-range order, occur naturally as a material cools down from a liquid to a solid. Semiconductor wafers are usually grown to be single-crystalline (but not always, e.g., Si solar cells are mostly polycrystalline), typically by a technique known as Czochralski growth [26]: Poly-crystalline grains are melted and a “seed” introduced to the melt. The seed is slowly pulled upwards (out of the melt) and in doing so a single-crystalline cylindrical “boule” is formed (Figure 2.1).

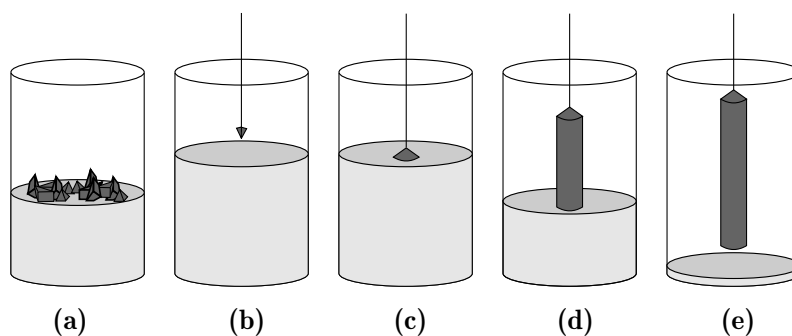


**Figure 2.1:** Czochralski growth process. (a) Poly-crystalline semiconductor material is melted. (b) A seed is introduced. (c) Crystal growth begins around the seed. (d) Seed is pulled out to achieve a cylindrical single-crystalline boule. (e) Formed crystal with residue of melted polycrystal. Adapted from Reference 3.

A brief summary of the crystallographic concepts most relevant to this thesis will now be presented. For further information, the reader is referred to the many other texts introducing the field of crystallography in a solid-state physics context, such as References 27–29.

A crystal structure can be described by a basis attached to a lattice. The lattice is a geometrical arrangement of points in space, each point having identical surroundings, whilst a basis represents atoms and their spacing. In the simplest crystals, such as copper and gold, this basis is simply a single atom, but for most semiconductor lattices, it is instead a group of atoms. The spacing between individual lattice points is known as the lattice constant, and as such, for a crystal structure, the lattice constant represents the spacing between (the centres of) atoms. There are fourteen so-called *Bravais lattices* that represent all possible lattice arrangements, and the most relevant to this work are the *face-centred cubic* and *hexagonal close-packed*

lattices, both illustrated in [Figure 2.2](#).

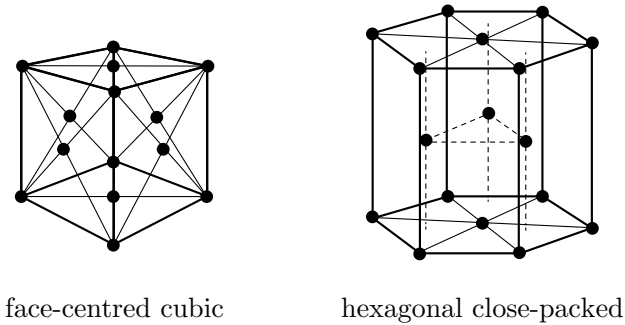


**Figure 2.2:** Two of the most common semiconductor Bravais lattices, face-centred cubic and hexagonal close-packed.

The crystal structure a material forms is the one that is energetically favourable and therefore the one that has the closest packed atoms [4]. Accordingly, most bulk III-V<sup>1</sup> semiconductor materials, including GaAs and InAs, usually have a *zinc-blende* crystal structure, a modified face-centred cubic lattice formed from two interpenetrating face-centred cubic lattices, as shown in [Figure 2.3\(a\)](#). III-nitride semiconductors are slightly different in that they may also form a modified hexagonal close-packed structure, known as *wurtzite* and shown in [Figure 2.3\(b\)](#). This structure, which is more closely packed than zinc-blende, is achievable by III-V nitrides due to the nitrogen atom being considerably smaller than the atoms of other group V elements. Under certain circumstances, non-nitrogenous III-V materials can also form wurtzite structures, for example, GaAs nanowires can switch between wurtzite and zinc-blende structures along their length [30]. Zinc-blende materials, being cubic in structure, have just the one lattice constant,  $a$ , whilst wurtzite materials have a second,  $c$  or  $a_3$ , such that in an ideal hexagonal close-packed structure  $c = 1.633a$  [27]. It is of note that the optical and electronic properties of the same material in wurtzite and zinc-blende form may be different due to the different arrangement of atoms.

### 2.1.1 Crystallographic Planes and Miller Indices

It is also of note that structural, and hence many optical and electronic, properties of semiconductors are anisotropic, meaning that they are dependent on the direction

---

<sup>1</sup>III-V refers to the semiconductor material consisting of one element from group III and another from group V of the periodic table.

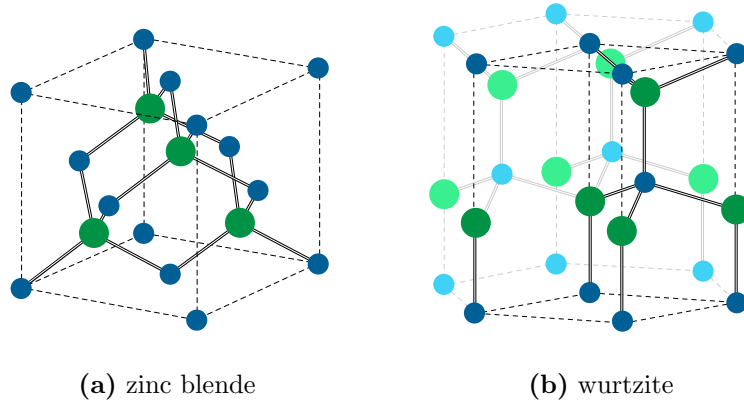


**Figure 2.3:** (a) Zinc-blende and (b) wurtzite crystal structures. Unit cells are shown by black dashed lines and for wurtzite, the remainder of the “hexagonal” structure is shown faded for a demonstration of how wurtzite relates to the hexagonal close-packed lattice.

through a crystal for which they are measured. It is therefore important to know the relevant directions or planes to consider when undertaking experiments. To account for this, one can use *Miller indices*.  $(hkl)$  is the Miller index of a plane, where  $h$ ,  $k$  and  $l$  are integers that can be found by: Finding the intercepts on the three-dimensional lattice axes in terms of the lattice constants, taking the reciprocal of these numbers, and reducing to three integers having the same ratio. For example, if a plane runs parallel to the  $k$  and  $l$  axes and intercepts the  $h$ -axis a distance of one lattice constant away from the origin (i.e., the plane  $h = 1$ ), then the Miller index of the plane is  $(100)$ . Figure 2.4 gives examples for several different planes. A bar above one of the numbers indicates the intercept is negative. In a similar fashion, one can also use square brackets,  $[hkl]$ , to denote directions through a crystal. For example,  $[100]$  is the direction perpendicular to the  $(100)$  plane.

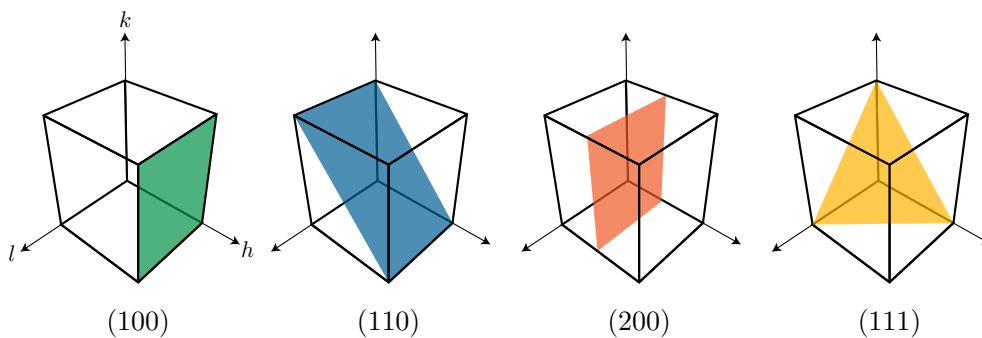


**Figure 2.4:** Various crystallographic planes and their Miller indices,  $(hkl)$ .

Using Miller indices for the hexagonal close-packed (and hence wurtzite) struc-

ture results in crystallographically-equivalent planes having different indices. To make this more apparent, it is useful to introduce a fourth axis and an accompanying four-index system  $(hkil)$ , such that  $h + k + i = 0$  [28]. This is known as the Miller–Bravais indices and is shown in Figure 2.5. For example, take the crystallographically-equivalent planes with Miller indices  $(1\bar{1}0)$ ,  $(100)$  and  $(010)$ . Using Miller–Bravais indices, these can be written  $(1\bar{1}00)$ ,  $(10\bar{1}0)$  and  $(01\bar{1}0)$ , respectively, making it easier to spot their equivalence.

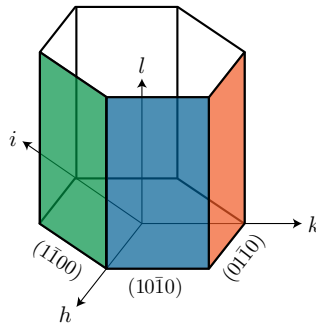


**Figure 2.5:** Miller–Bravais indexing of crystal planes for hexagonal structures, introducing a third axis,  $i$ . The three coloured planes are crystallographically equivalent, which is easier to tell from their Miller–Bravais indices  $(1\bar{1}00)$ ,  $(10\bar{1}0)$  and  $(01\bar{1}0)$ , as opposed to their Miller indices  $(1\bar{1}0)$ ,  $(100)$  and  $(010)$ .

## 2.2 Electronic Band Structure

Electrons orbiting individual atoms do so at discrete energy levels. When these atoms are brought close together, electrons interact with each other and due to the Pauli exclusion principle—that states no two electrons can occupy the same energy level<sup>2</sup>—their energy levels split. For large numbers of atoms, these energy levels become so closely spaced that they can be described as energy bands instead. This series of bands and their accompanying band gaps (forbidden energies) is termed the *band structure*. Figure 2.6 shows how the formation of these bands occurs as atoms are brought from very far apart to typical-crystal atomic spacing.

The electron-filling of these bands is fundamental to a crystal’s conductance. Bands that are partially full have higher energy levels available and hence electrons

<sup>2</sup>More rigorously, the Pauli exclusion principle states that no two fermions (an elementary particle with spin-half, of which an electron is an example) can have the same quantum numbers, and thus two electrons can occupy the same atomic orbital but only if their spin is different [27].

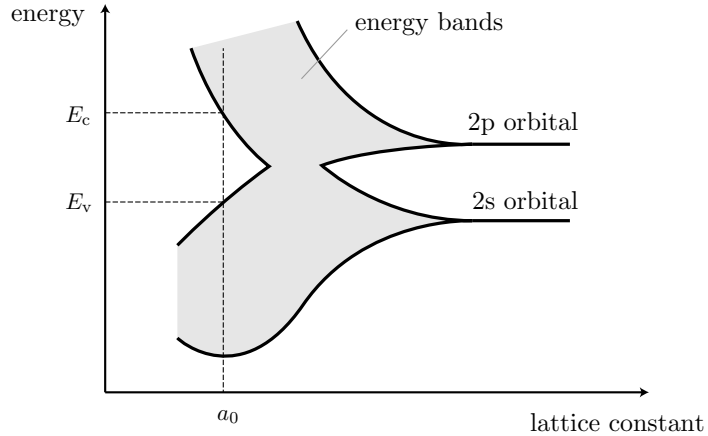


**Figure 2.6:** Formation of energy bands in diamond as atoms are brought close together. As a single atom, the highest-energy atomic orbitals are 2s and 2p, which are shown. When the lattice constant is that of diamond,  $a_0$ , a conduction and valence band can be clearly seen, with band edges  $E_c$  and  $E_v$ , respectively [4, 5].

can gain energy and move in an applied electric field (i.e., they can conduct). Bands that are completely full have no higher energy levels available and therefore don't contribute to the conductance. Bands that are empty do have available energy levels, but no electrons to fill them and hence they also do not contribute to the conductance [4].

The most important bands are the *valence* and *conduction* bands. The valence band is made up of the energy levels of valence electrons in the outermost atomic energy shells, the conduction band is the band that lies above this (at a higher energy) and the gap between them is the so-called *band gap*. In metals, these bands either overlap, or in the case of metals with only one valence electron per atom (e.g., copper), the valence band is only partially filled. In both cases, electrons can move freely and hence metals have a high conductance. In insulators, the band gap is large and so a prohibitively large amount of energy is needed to move electrons from the valence to the conduction band. Semiconductors are an intermediate case; they have a band gap, but it is small enough that given some external energy (e.g., heating to room temperature), electrons can be promoted to the conduction band and they can conduct electricity [4]. The differences in energy bands between metals, semiconductors and insulators is shown in Figure 2.7. The band gap value at which a semiconductor becomes an insulator is not strictly defined, but  $\sim 3$  eV seems to be a widely accepted figure [31].

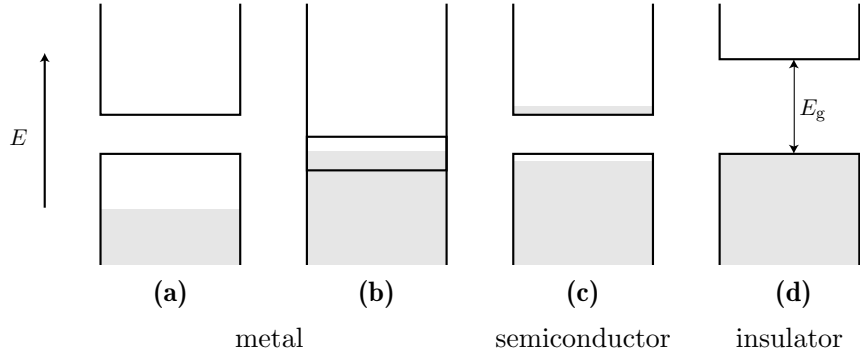


**Figure 2.7:** Energy band diagrams for: (a) a metal with partially filled valence band; (b) a metal with overlapping valence and conduction bands; (c) a semiconductor, and; (d) an insulator with band gap  $E_g$ . Shaded grey area represents electron occupation.

The seemingly-contradictory terms *valence band energy* and *conduction band energy* are often used to describe discrete energy values. These values in fact correspond to the uppermost edge of the valence band and the lowermost edge of the conduction band and are labelled  $E_v$  and  $E_c$ , respectively, so that the band gap energy is given by  $E_g = E_c - E_v$ .

Convention has it that band diagrams, depicting the conduction and valence bands, have increasing energy in the upwards direction (as in Figure 2.7), and this convention will be employed herein when no explicit direction is labelled on a diagram, for simplicity.

### 2.2.1 $E-k$ Diagrams and Effective Masses

It is common to depict the band structure of a material using an energy–wave vector diagram. The wave vector  $\mathbf{k}$  is related to a charge carrier’s momentum by de Broglie’s relation,  $\mathbf{p} = \hbar\mathbf{k}$ , and as such, these  $E-k$  diagrams demonstrate how energy states are distributed in momentum space [5]. Figure 2.8 shows a simplified  $E-k$  diagram (for one-dimensional momentum space with wave number  $k$ ), in which one can see the presence of a minimum in the conduction and a maximum in the valence band at  $k = 0$ . Around these extrema, the bands appear approximately parabolic, similarly to the behaviour of free electrons, for which

$$E = \frac{\hbar^2 k^2}{2m_0}, \quad (2.1)$$

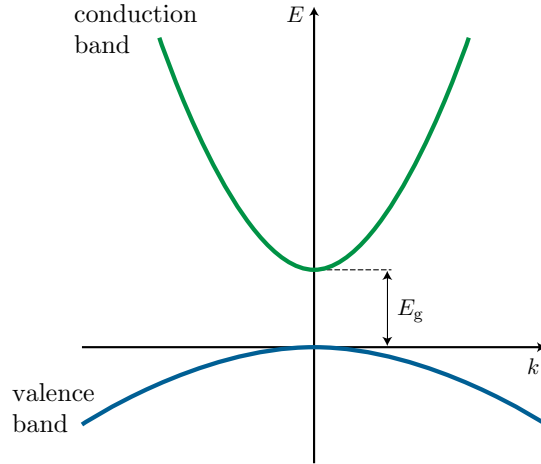


**Figure 2.8:** A simplified representation of the conduction and valence band edges as a function of wave number  $k$ .

where  $m_0 = 9.11 \times 10^{-31}$  kg is the (free) electron mass [27]. Here, the curvature of the bands is dependent on the reciprocal electron mass  $1/m_0$ . For electrons in semiconductors, the curvature of the bands near to the minima can be far higher than the free electron case, and therefore it *seems* as though the semiconductor electron mass is much smaller than the free electron mass. This mass the semiconductor electrons appear to have is called the *effective mass* and we can use it to re-write Equation 2.1 for the conduction and valence bands in Figure 2.8:

$$E_c = E_g + \frac{2\hbar k^2}{2m_e^*} \quad \text{and} \quad (2.2)$$

$$E_v = -\frac{2\hbar k^2}{2m_h^*}. \quad (2.3)$$

Here,  $m_e^*$  and  $m_h^*$  are the electron and hole<sup>3</sup> effective masses, respectively. Note that these energies are relative to  $E = 0$  being at the valence band maximum, and unless otherwise stated, this convention shall be used throughout this thesis.

In reality, band structures are much more complex than the simplified representation shown in Figure 2.8. For instance, it is common for there to be multiple

---

<sup>3</sup>A “hole” is the space left behind by an electron when it is promoted from the valence to the conduction band. It is useful to think of it as a positively-charged counterpart to the electron, that flows in the valence band. Indeed, the shape of the valence band in Figure 2.8 implies a negative effective mass, a confusion that can be resolved by introducing the concept of a positively-charged hole with positive effective mass.

valence bands, two of which are degenerate at  $k = 0$ : the heavy hole (hh) and light hole (lh) bands. These come with their own separate effective masses ( $m_{\text{hh}}^*$  and  $m_{\text{lh}}^*$ ) and therefore Equation 2.3 can be replaced with:

$$E_{\text{hh,lh}} = -\frac{2\hbar k^2}{2m_{\text{hh,lh}}^*}. \quad (2.4)$$

Figure 2.9 shows the band structure of GaAs, demonstrating this complex nature and reminding us that the above parabolic  $E$ - $k$  relations are only approximations around the extrema of the energy bands. The band gap of a material is always the difference between the lowest minimum in the conduction band and the highest maximum in the valence band. The relevance of the  $k$ -positions of these extrema in relation to each other will be discussed in Section 2.5.1.

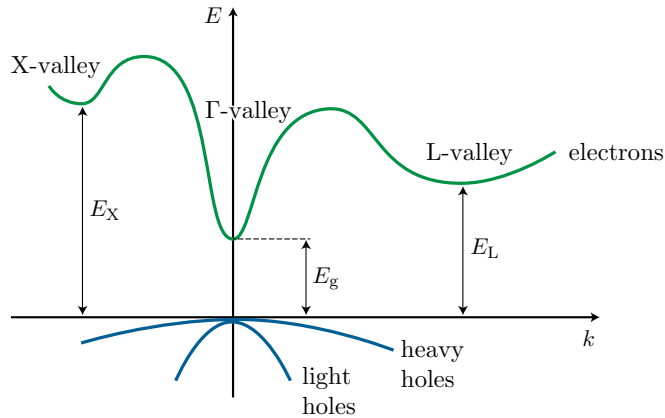


**Figure 2.9:** Band structure of GaAs, showing the presence of  $X$ -valley,  $\Gamma$ -valley and  $L$ -valley band gaps [6].

## 2.2.2 Fermi Level, Electron Affinity and the Work Function

The *Fermi level*  $E_F$  is defined as the energy of a state which has a 50% probability of being occupied, and as thermal excitation by higher temperatures means it is more likely that a higher energy state will be occupied, it is dependent on temperature. In semiconductors (and insulators), the Fermi level lies within the band gap and is hence a hypothetical energy level that no electron can actually occupy. In metals, it sits within the conduction band, availing free electrons that contribute towards a high conductance. The *Fermi energy* is discreetly different in definition; it is the highest occupied state at absolute zero and is therefore temperature-independent.

A quantity that is often used to compare different materials, and one that is largely a material constant, is the *electron affinity*  $\chi$ , which in solid-state physics is defined as the energy required to move an electron from the conduction band edge to the vacuum level  $E_{\text{vac}}$ :

$$\chi = E_{\text{vac}} - E_c. \quad (2.5)$$

The *work function*  $\Phi$  is related to the electron affinity, but is the energy required to move an electron to the vacuum from the Fermi level, as opposed to from the conduction band edge:

$$\Phi = E_{\text{vac}} - E_F. \quad (2.6)$$

### 2.2.3 Heterojunction Band Alignment

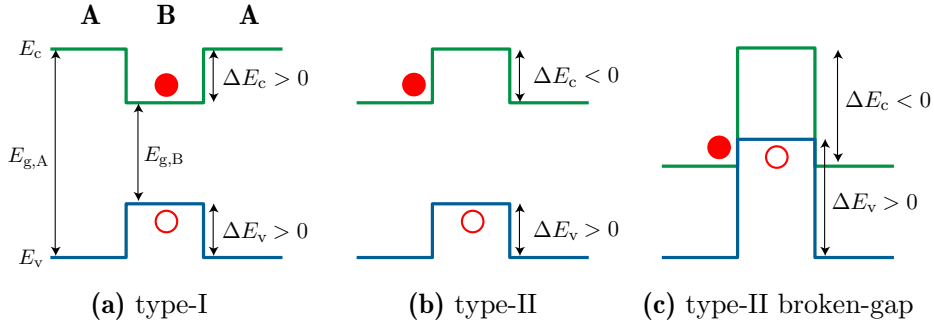


**Figure 2.10:** Heterojunction band alignment for (a) type-I, (b) type-II and (c) type-II broken-gap systems.

A heterostructure is formed when layers of two or more different semiconductor materials are grown on top of each other so that they have one common crystal structure. The band alignments of the valence and conduction bands in these materials will be different, and hence discontinuities in the overall band structure can occur. These alignments can be classified into three types [27].

If one assumes the vacuum level is the same for both materials, the band alignment of heterojunctions can be calculated by using the electron affinity  $\chi$  to position the conduction band, and the sum of the electron affinity and band gap  $E_g$  to position the valence band:

$$\Delta E_c = \chi_A - \chi_B \quad \text{and} \quad (2.7)$$

$$\Delta E_v = (\chi_A + E_{g,A}) - (\chi_B + E_{g,B}). \quad (2.8)$$

### Type-I Alignment

Let us consider a layer of material B sandwiched within another material A. Type-I alignment occurs when material B has a smaller band gap than A and is it aligned such that it lies within the band gap of material A. That is,  $\Delta E_c > 0$  and  $\Delta E_v > 0$ , as shown in [Figure 2.10\(a\)](#). The consequence of this, if the layer of material B is thin enough, is that charge carriers may become trapped in this layer.

Examples of material combinations that result in type-I band alignment include InAs/GaAs and GaAs/AlGaAs (where material B is listed first, e.g., InAs). The former is of particular relevance to this thesis.

### Type-II Alignment

Type-II alignment occurs when the conduction and the valence band edges of material B are at higher energies than those of material A, such that  $\Delta E_c$  and  $\Delta E_v$  have opposite signs. [Figure 2.10\(b\)](#) shows this for the case when  $\Delta E_c < 0$  and  $\Delta E_v > 0$ . Only one of the charge carriers may be confined for this alignment (in the case of [Figure 2.10\(b\)](#), the hole). GaSb/GaAs is an example of a system that can exhibit type-II alignment where the hole is confined to the GaSb.

### Type-II Broken-Gap Alignment

An extreme example of type-II alignment is when the valence and conduction band edges of material B are higher (or lower) than those of material A, resulting in a “broken” alignment, as illustrated in [Figure 2.10\(c\)](#). This alignment is referred to as either type-II broken-gap or type-III band alignment. InAs/GaSb is an example of such a system.

## 2.2.4 Temperature Dependence of the Band Gap

The band gap of a semiconductor reduces with increasing temperature and the rate at which it does so differs between materials. As the temperature increases, atomic bonds weaken and atoms move farther apart. Less energy is therefore needed to promote an electron from the valence to the conduction band; the band gap is reduced. This dependence of the band gap on the lattice constant is shown graphically in [Figure 2.6](#).

There exists numerous empirical and semi-empirical descriptions of this behaviour [\[32\]](#) and by far the most widely used is the empirical equation deduced by Varshni in 1967, the so-called *Varshni equation* [\[33\]](#):

$$E_g(T) = E_g(0) - \frac{\alpha T^2}{\beta + T}, \quad (2.9)$$

where  $\alpha$  and  $\beta$  are material constants, whose units are  $\text{meV K}^{-1}$  and  $\text{K}$ , respectively.

## 2.3 Low-Dimensional Nanostructures

In bulk semiconductors, the size of the material doesn't affect its optical or electronic properties. However, when we scale down this size to nanometre length-scales—to the order of the electron's de Broglie wavelength  $\lambda_e = h/p_e$ , where  $p_e$  is the electron's momentum—the laws of quantum mechanics take hold and *quantum confinement* has an effect [\[34\]](#).

The most obvious consequence is that charge carriers can become trapped in local potential variations caused due to the band alignment of nanostructures embedded in bulk materials, as discussed in [Section 2.2.3](#). This squeezing of the charge carrier wave functions results in the formation of discrete energy levels (or sub-bands) and an enlarging of the band gap.

The individual classification of different types of nanostructures is enormous; from nanoflowers [\[35, 36\]](#) to nanofoams [\[37\]](#) and from QDs [\[38\]](#) to quantum posts [\[39\]](#). This work focusses primarily on the semiconductor heterostructures of QWs and QDs.

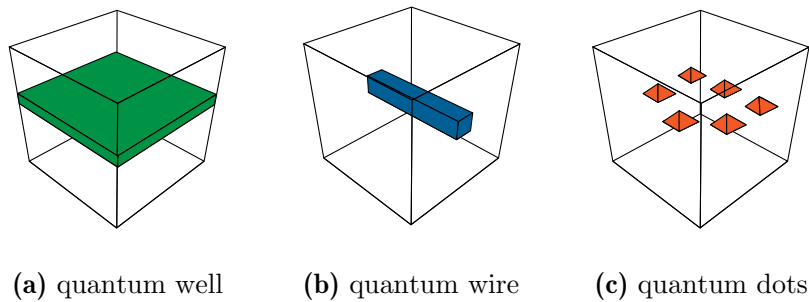


**Figure 2.11:** Low-dimensional nanostructures (coloured regions): (a) Quantum well (QW); (b) quantum wire and; (c) quantum dots (QDs), all embedded in another semiconductor material (transparent box).

### 2.3.1 Quantum Wells

Semiconductor QWs are typically formed from the embedding of a thin plane-like area of a narrower-band-gap material, such as GaAs, within a larger-band-gap material, such as AlGaAs (Figure 2.11(a)). If this results in type-I band alignment, then electrons and holes become localised in the QW in their attempt to lie in the most energetically-favourable location (i.e., with the lowest available energy). Charge carriers are free (unconfined) in two dimensions and they are therefore said to be two-dimensional (2D).

### 2.3.2 Quantum Dots

A QD is formed when a semiconductor is downsized to the nanoscale in all three spatial dimensions (Figure 2.11(c)), so that charge carriers are completely localised in space; they are zero-dimensional (0D). Type-I band alignment means both electrons and holes can be tightly confined within the dot, whilst type-II alignment can result in one carrier being confined, with the other being free to roam in the surrounding material (though Coulomb attraction between the two may partially localise the free carrier) [40].

QDs come in many varieties, including so-called “colloidal” QDs that are fabricated suspended in a solution. This thesis focusses solely upon semiconductor heterostructure QDs, formed by self-assembly, as will be introduced in Section 2.11.1.

The intermediate case, between QWs and QDs, are quantum wires, which are not

studied explicitly in this work. As the name suggests, these confine carriers to a one-dimensional (1D) wire-shaped region, as in [Figure 2.11\(b\)](#).

## 2.4 Carrier Distribution

To interpret data from optical and electronic experiments that will be carried out, it is important to understand how charge carriers are distributed, which is dependent on the density of energy states available at a given energy, as well as the probability of an electron occupying a particular state [[5](#), [27](#), [41](#)].

### 2.4.1 Density of States

Even though we describe energies in the bands that form our band structure, they are still comprised of a finite number of closely-packed states, and as such it is useful to introduce a density of states (DOS) to tell us where charge carriers can sit within these bands. This DOS is defined as the number of energy states available per unit energy, and is usually denoted by  $g(E)$ ,  $D(E)$  or  $\rho(E)$ ; the former shall be used herein. In bulk semiconductors, the DOS is proportional to the square root of the energy at which it is calculated, and specifically for electrons in the conduction band, it is given by

$$g(E)_{3D} = \frac{V}{2\pi^2} \left( \frac{2m_e^*}{\hbar^2} \right)^{3/2} \sqrt{E - E_g}, \quad (2.10)$$

remembering that  $E = 0$  is taken to be at the valence band edge. Though not always,  $g(E)$  is often given per unit volume, in which case  $V = 1$  in the above equation. [Figure 2.12](#) shows an illustration of the DOS for energies above the conduction band edge. The implication of this, which is immediately striking, is that the number of states available to electrons is at its lowest at the conduction band edge and increases with increasing energy.

The DOS for 2D QWs and 0D QDs is markedly different. The former takes the form of a step function, whilst the later is completely discretised, as one would expect for an atom. For a QW:

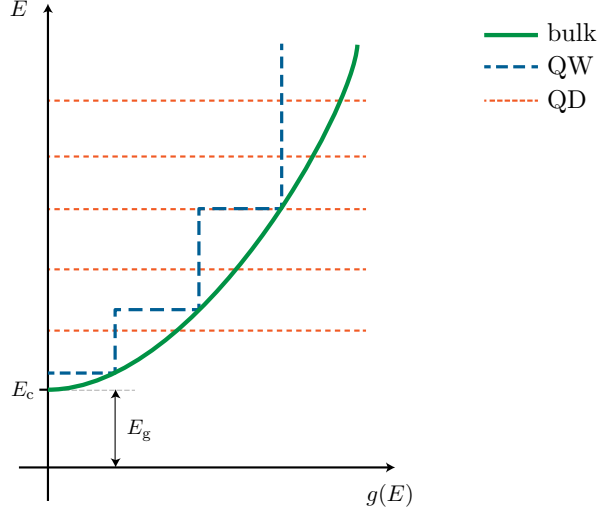


**Figure 2.12:** Conduction band density of states (DOS)  $g(E)$  as a function of energy  $E$  for a bulk semiconductor (green solid line), QW (blue dashed line) and QD (orange dotted line).

$$g(E)_{2D} = \frac{m_e^*}{\pi \hbar^2} \sum_n H(E - E_n), \quad (2.11)$$

We already saw in [Section 2.3.2](#) that the increased confinement in a QW leads to quantised energy levels and here,  $E_n$  is the energy of the  $n$ th level in the QW.  $H$  is the Heaviside step function,

$$H(E - E_n) = \begin{cases} 0, & \text{for } E < E_n \\ 1, & \text{for } E \geq E_n. \end{cases} \quad (2.12)$$

and [Equation 2.11](#) is formulated such that the steps in this function occur at the energy of each quantised energy level.

Additional confinement in different spatial dimensions leads to the further quantisation of energy levels and hence a degeneracy of QD levels compared with QW levels. We account for these sub-levels by introducing the sub-indices  $l$  and  $m$  for confinement to 1D and 0D, respectively, and accordingly the DOS is calculated by summing over them:

$$g(E)_{0D} = 2 \sum_{n,l,m} \delta(E - E_{n,l,m}), \quad (2.13)$$

where  $\delta$  is the Dirac delta function, which is zero everywhere except for when its argument equals zero ( $E - E_{n,l,m} = 0$ , in this case), in which case it equals infinity.

Of course, applied to a QD, this simply means that one and only one available state exists at each energy level  $E_{n,l,m}$ ; the DOS is not infinite. Figure 2.12 illustrates this quantisation and degeneracy by comparing bulk, QW and QD DOS side-by-side.

## 2.4.2 Fermi–Dirac Distribution

The *Fermi–Dirac distribution*  $f(E)$  gives the probability of finding a fermion in a given energy state  $E_i$  at a given temperature  $T$ :

$$f(E_i) = \frac{1}{e^{(E_i - E_F)/k_B T} + 1}, \quad (2.14)$$

Figure 2.13 shows  $f(E)$  for a semiconductor with an arbitrary band gap at differing temperatures. At absolute zero, all energy states up to the valence band edge are occupied, whilst at higher temperatures, electrons can be thermally excited into the conduction band and there is a small but finite probability of them reaching such energy levels and therefore contributing to the conductance. Remember that even though the Fermi–Dirac distribution has a non-zero value in the band gap, no electrons can be present as there are no states available to be occupied. As a hole is simply the absence of an electron, the probability of finding a hole occupying a particular energy level is given by  $1 - f(E)$ .

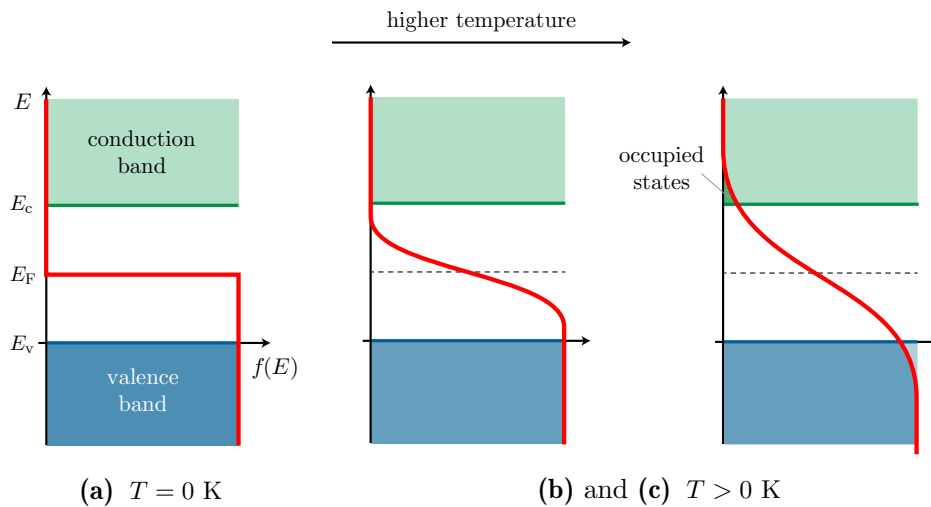


**Figure 2.13:** Fermi–Dirac distribution, represented by the solid red line, for: (a) absolute zero; (b) some finite temperature above absolute zero, and; (c) an temperature higher than in (b). In (c) the temperature is high enough that it is probable that conduction band states will be occupied. There are no states available to be occupied in the band gap.

The actual carrier distribution is given by the product of the DOS and the Fermi–Dirac distribution, such that the electron density in the conduction band is:

$$n = \int_{E_c}^{\infty} g_c(E) f(E) dE. \quad (2.15)$$

The upper limit of the integral should strictly equal the energy at the top of the conduction band, but in reality for most semiconductors at realistic temperatures, there will be no states populated above the conduction band and  $\infty$  can be used instead. Note that we have introduced a conduction band density of states  $g_c(E)$ , which is simply the density of states available for electrons in the conduction band. Similarly, for the density of holes in the valence band  $p$ , we can use the valence band density of states  $g_v(E)$ :

$$p = \int_{-\infty}^{E_v} g_v(E) (1 - f(E)) dE. \quad (2.16)$$

Figure 2.14 shows the distribution of electrons in the valence and conduction bands in a bulk semiconductor at a finite temperature that is high enough that thermally-excited electrons have enough energy to populate conduction band states. Equations 2.15 and 2.16 result in the largest number of carriers being concentrated at  $\pm k_B T/2$  from the band edges.

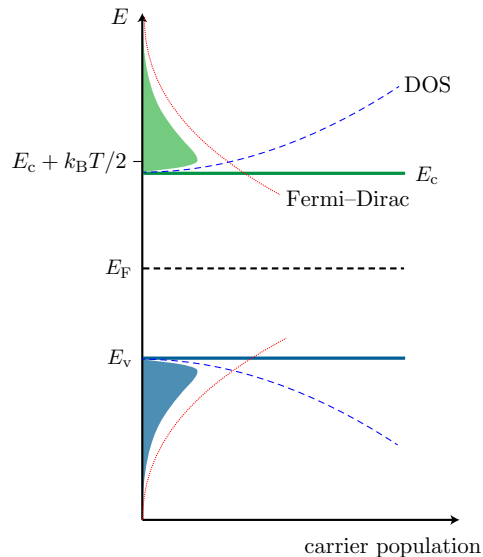


**Figure 2.14:** Charge carrier distribution for electrons in the conduction band (green) and holes in the valence band (blue) at an elevated temperature, which is a product of the DOS (blue dashed lines) and the Fermi–Dirac distribution (red dotted lines). The remaining available states in the valence band will be occupied by electrons, but this is omitted from the diagram for simplicity.

## 2.5 Absorption, Recombination and Emission

The principles of absorption, recombination and emission are fundamental to the operation of most optoelectronic devices. In brief: Electrons can be promoted from an energy level in the valence band to an energy level in the conduction band by the absorption of a photon. This leaves behind a hole in the valence band and some time later, the electron will recombine with the hole, emitting a photon with a wavelength equal to the energy difference between the electron and hole energy levels.

### 2.5.1 Direct and Indirect Band Gaps

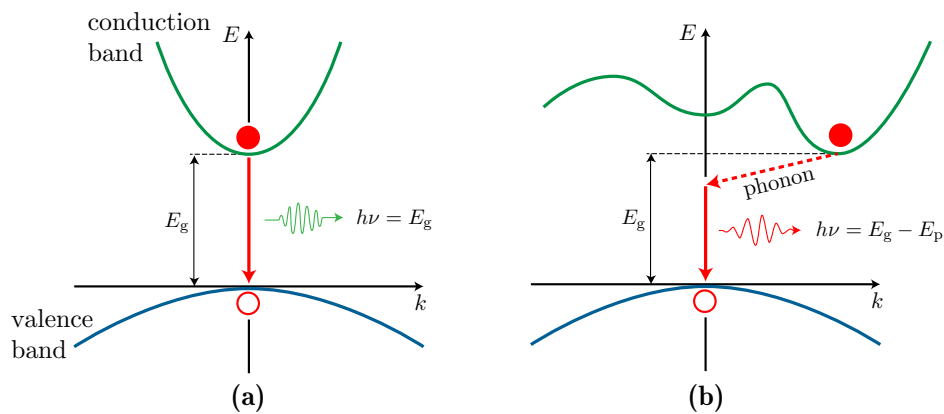


**Figure 2.15:** Recombination of electrons (solid circles) from the valence band into holes (hollow circles) in the conduction band for (a) direct and (b) indirect semiconductors. Direct recombination results in the emission of a photon with energy  $h\nu = E_g$ , whilst indirect recombination is a two-step process also necessitating the emission of a phonon with energy  $E_p$ , such that the energy of the emitted photon is  $h\nu = E_g - E_p$ .

Observing where the global minimum in the conduction band lies with respect to the global maximum in the valence band tells us whether the material has a *direct* or an *indirect* band gap. In direct band gap semiconductors, these extrema lie at the same  $k$  value and hence transitions between the two conserve momentum (Figure 2.15(a)). In contrast, the extrema are positioned at different  $k$  values for indirect band gap semiconductors and hence a transition requires a change in both energy and momentum. For momentum to be conserved, any transition must be a two-step process in which a phonon (quantised lattice vibration) is emitted or absorbed (Figure 2.15(b)). For this reason, recombination in indirect semiconductors

occurs at a much slower rate and they make poor optical emitters (though this is less of an issue for absorption, demonstrated by popularity of Si as a material for detectors) [4].

## 2.5.2 Absorption and Excitons

Photons incident on the surface of a semiconductor, be them from sunlight or another excitation source, will either be reflected, transmitted through the material, or absorbed. Whether they are absorbed or transmitted through is dependent on the photon's wavelength in relation to the band gap. For photons of wavelength  $\lambda$  with energy  $E_\gamma = \frac{hc}{\lambda}$ , where  $c \approx 3 \times 10^8 \text{ m s}^{-1}$  is the speed of light (photons) in a vacuum:

$E_\gamma < E_g$  Photons with energy less than the band gap only interact weakly with the semiconductor and most will pass straight through (Figure 2.16(a)).

$E_\gamma > E_g$  Photons with energy greater than the band gap can be absorbed (depending on the thickness of the semiconductor), but any energy above the band gap is wasted as conduction electrons quickly thermalise to the band edge (Figure 2.16(c)).

$E_\gamma = E_g$  The ideal case is photons having the same energy as the band gap, in which case they are absorbed without the loss of any excess energy (Figure 2.16(b)).

Absorption considerations are particularly relevant for applications involving the harnessing of solar energy. The solar spectrum, shown in Figure 2.17, is broad and it is hence a fine balance selecting a band gap that maximises the amount of the spectrum that is absorbed (by having a smaller band gap) but at the same time ensuring thermal losses are not too large (by having a larger band gap) [42].

When an electron is excited to the conduction band, a hole is left behind in the valence band. These oppositely-charged particles experience Coulomb attraction and can form a bound state in which both particles orbit each other. This bound

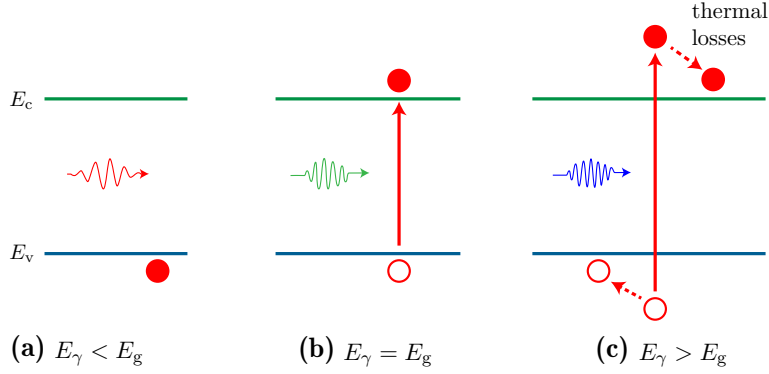


**Figure 2.16:** Absorption of a photon with an energy (a) less than the band gap, (b) equal to the band gap and (c) greater than the band gap.

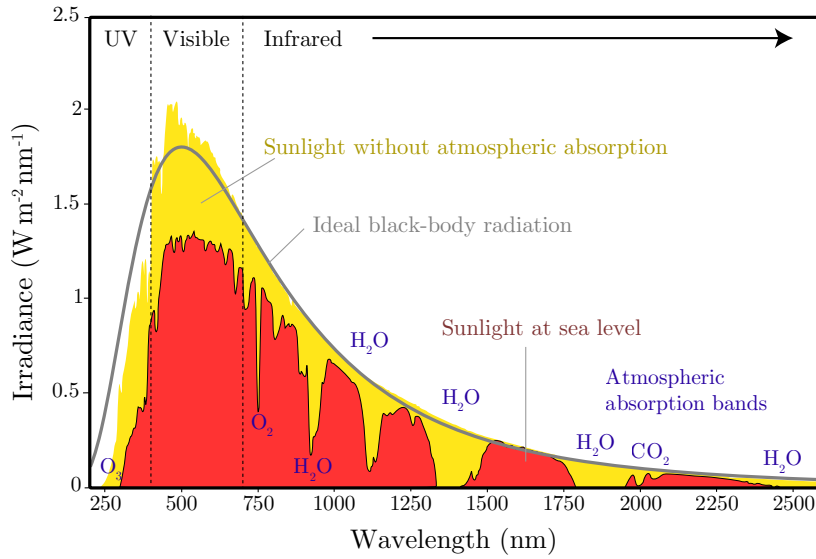


**Figure 2.17:** Solar irradiance spectrum above the atmosphere and at the surface of the Earth. Adapted from Reference 7.

state is known as an *exciton* and this exciton can move through the crystal as if it were a single particle [43]. The electron, being the lighter of the two particles, has the largest orbital radius and thus the analogy between excitons and the hydrogen atom is often made (indeed, the exciton wave function is often assumed to be hydrogenic). We can introduce an exciton reduced (effective) mass  $\mu$  as the reciprocal of the summation of the reciprocals of the electron and hole effective masses,

$$\frac{1}{\mu} = \frac{1}{m_e^*} + \frac{1}{m_h^*}, \quad (2.17)$$

and an exciton Bohr radius  $a_B$  as the exciton's radius (in a similar fashion to the hydrogenic Bohr radius  $a_B^H$  being the radius of the electron's orbit in a hydrogen

atom):

$$a_B = \frac{a_B^H \varepsilon m_0}{\mu}, \quad (2.18)$$

where  $\varepsilon$  is the semiconductor's dielectric constant.

The energy of the exciton is less than the energy of a free electron and hole by a factor of the exciton binding energy [44]:

$$E_b = \frac{\mu R_y}{\varepsilon^2 m_0} \cdot \frac{1}{n^2}, \quad (2.19)$$

which for most bulk III-V semiconductors is in the order of a few meV [27]. Here,  $n$  is the quantum number associated with the excitonic energy level. A consequence of this is that an exciton may be created from an incident photon with an energy less than the band gap.

Local electric fields inside the semiconductor, for example at a Schottky junction (see Section 2.10.2), exert forces acting in opposite directions on the electron and hole. When the strength of this field exceeds that of the Coulomb attraction within the exciton, the electron and hole are torn apart and travel as free particles, a process known as dissociation [5]. Similarly, thermal dissociation can break up the carriers at high temperatures and for this reason, excitons are generally seen in bulk semiconductors only at low temperatures [45].

QWs and QDs have dimensions that are in the order of  $a_B$  and when the well width or dot diameter becomes less than  $a_B$ , then the binding energy of the exciton becomes considerably enhanced [46]. Hence, excitonic effects can be seen in QWs and QDs at higher temperature, for example, room temperature [47].

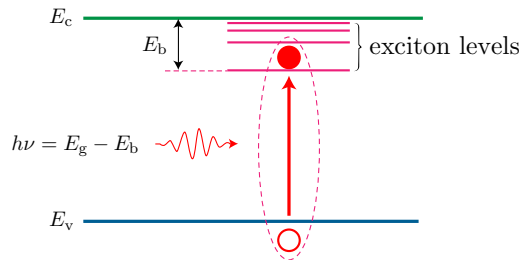


**Figure 2.18:** The generation of an exciton from a photon with energy less than the band gap by a factor of the exciton binding energy  $E_b$ , for a direct band gap semiconductor.

### 2.5.3 Recombination

The process of an electron relaxing back into an empty hole state, in doing so giving off the energy it has lost, is known as recombination. The three main processes by which recombination occurs are: radiative, Shockley-Read-Hall and Auger recombination [4, 48].

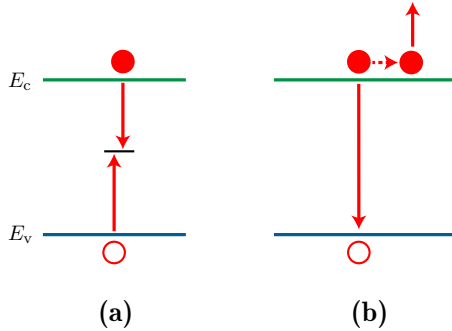


**Figure 2.19:** Non-radiative recombination mechanisms. (a) Shockley-Read-Hall recombination via mid-gap trap states. (b) Auger recombination, resulting in the excitation of a third charge carrier.

Shockley-Read-Hall recombination, shown in Figure 2.19(a), occurs via mid-gap energy states, called traps. These traps are usually present due to crystal defects or impurities (the presence of foreign atoms). An electron can become trapped by these mid-gap states and a hole moves up from the valence band to recombine with the electron.

Auger recombination, shown in Figure 2.19(b), is the recombination of an electron in the conduction band into a hole in the valence band (or, the recombination of an exciton) with the subsequent transfer of the energy lost to a third charge carrier, promoting that to a higher energy level. For example, the third carrier may be an electron which is promoted to a higher-energy conduction band state, or it may be a hole with some non-zero  $k$ -value that is promoted from the heavy hole to the light hole band.

Radiative recombination involves the emission of a photon and is hence the most relevant to this work. An electron and hole recombine across the band gap, in doing so releasing the energy lost to a photon. This energy is typically equal to or greater than the band gap of the material, however excitonic recombination or recombination from and to impurity states (e.g., donor and acceptor states, discussed

in Section 2.6) can result in energies less than the band gap. These different radiative recombination processes are illustrated in Figure 2.20.

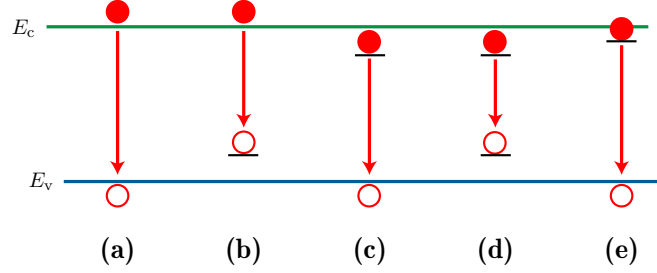


**Figure 2.20:** The most common radiative recombination processes: (a) Band-to-band; (b) conduction band to acceptor state; (c) donor state to valence band; (d) donor state to acceptor state, and; (e) excitonic radiative recombination.

Band-to-band recombination results in the emission of a photon with the most probabilistic energy of

$$E_\gamma = h\nu = E_g(T) + k_B T, \quad (2.20)$$

where  $h\nu$  is the photon energy,  $k_B$  is the Boltzmann constant and  $T$  is the temperature. The factor  $k_B T$  is due to the thermal excitation of carriers, as discussed further in Section 2.4.2. Note the dependence of the band gap  $E_g$  on temperature, a dependence which is detailed in Section 2.2.4.

Both Shockley-Read-Hall and Auger recombination are non-radiative and hence are detrimental to the performance of most semiconductor devices.

## 2.5.4 Photoluminescence

The emission of light subsequent to the radiative recombination of charge carriers, and that which is specifically not as a result of heating, is called *luminescence*. If the excitation source is itself light, for example from a laser, then this process is known as *photoluminescence* (PL) [49], which is illustrated for a heterostructure in Figure 2.21. Other types of luminescence include electroluminescence, when the excitation source is an electrical current, and cathodoluminescence, when the excitation source is a beam of electrons.

Used as an experimental method, PL spectroscopy (commonly referred to simply as PL) is an incredibly useful tool from which one can obtain PL spectra with

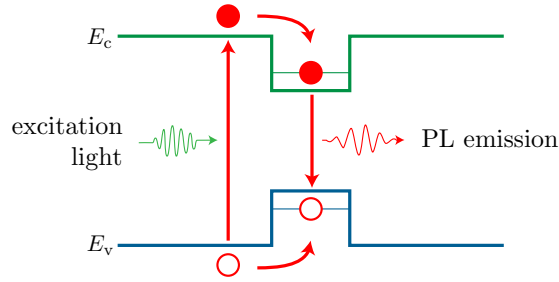


**Figure 2.21:** Representation of the photoluminescence (PL) process for a heterostructure. An incident photon from excitation light is absorbed, for example, in the bulk semiconductor, before relaxing down into the nanostructure or QW and recombining to give a photon with energy equal to the difference between electron and hole states.

accompanying PL peak energies that give an indication of the emission energy of photons emitted by radiative recombination. The influence of a magnetic field on PL energies, and what this can tell us about charge carriers within semiconductors, will be introduced in [Section 2.8](#). The experimental methodology behind PL experiments is discussed in [Section 3.3](#).

Photo-excited carriers with energies above the band gap quickly thermalise to or near the band edges and in bulk semiconductors; their distribution is determined by the product of the DOS and the Fermi–Dirac distribution ([Section 2.4](#)) [5]. Hence, the low-energy side of PL spectra is the DOS, whilst the high-energy side is the Fermi–Dirac distribution, similar to the carrier distributions illustrated in [Figure 2.14](#). Indeed, fitting a PL spectrum with the Fermi–Dirac distribution is often used to obtain the carrier temperature [50].

However, many other factors have an impact on PL spectra, such as compositional variations or impurities. More importantly in the scope of this work, the presence of low-dimensional nanostructures can mean a considerably different interpretation of the line shape is needed. Most notably, Gaussian broadening due to statistical QW–width, QD–size or compositional fluctuations over the area covered by excitation light can have a large influence [51]. One must also remember that the DOS in 2D and 0D is far from that of the bulk three-dimensional (3D) case.

## 2.6 Doping

So far we have limited our discussion to *intrinsic* semiconductors, where the density of electrons in the conduction band equals the density of holes in the valence band. For the condition of charge neutrality to be obeyed, the Fermi level must sit at a mid-gap position, equi-distance from each band (Figure 2.14). Most (but not all) semiconductors are naturally intrinsic. In Section 2.4, we saw the effect that thermal excitation can have on carrier population, and that the  $k_{\text{B}}T \approx 25 \text{ meV}$  thermal energy that is provided at room temperature is normally not significant enough (compared to typical band gaps in the order of 1 eV) for a notable concentration of electrons to be thermally excited to the conduction band.

However, it is often desirable to have a higher electron/hole concentration in the conduction/valence band so as to obtain a higher conductance, and we can achieve this by the introduction of impurity atoms into the crystal lattice with extra/fewer valence electrons (compared to the semiconductor material), a technique known as *doping*. N-type doping (the “n” standing for “negative”) is the addition of impurity atoms with an extra valence electron, which has the effect of pushing up the Fermi level towards the conduction band. The impurity—known as a *donor* due to its donation of an electron to the conduction band—creates its own donor energy band close to the conduction band and within the band gap, as illustrated in Figure 2.22(a). On the contrary, p-type doping (the “p” standing for—you guessed it—“positive”), is the addition of impurity atoms with one less valence electron, having the effect of dragging down the Fermi level towards the valence band and creating an *acceptor* energy band close to the valence band in the band gap, as illustrated in Figure 2.22(b). The presence of energy levels within the band gap is of relevance when considering absorption, recombination and emission, as in Section 2.5.

### 2.6.1 Carrier Density

Making the assumption that our semiconductor is *non-degenerate*, meaning that the Fermi level is at least  $3k_{\text{B}}T$  away from either band edge, allows us to simplify the Fermi–Dirac distribution to a simple exponential function,  $f(E) \approx e^{(E-E_{\text{F}})/k_{\text{B}}T}$ , thus enabling us to solve Equation 2.15 analytically to obtain a value for the bulk-

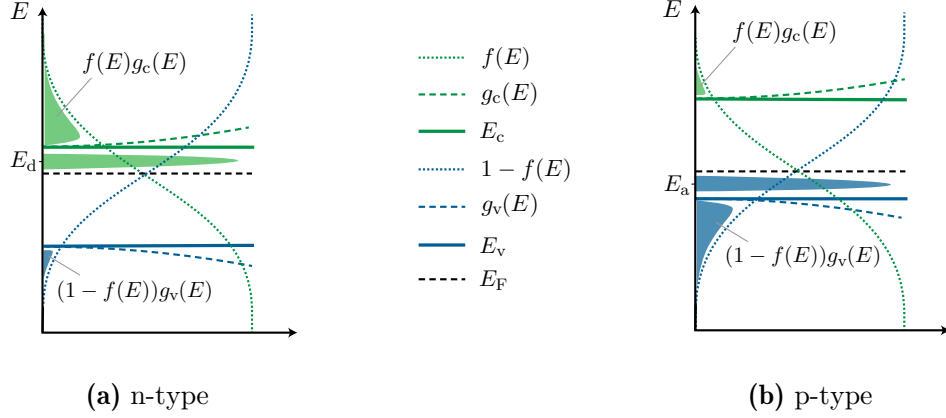


**Figure 2.22:** Fermi–Dirac distribution  $f(E)$  (dotted lines), conduction and valence band density of states  $g_{c,v}(E)$  (dashed lines) and carrier population (solid shapes) for **(a)** n-type and **(b)** p-type semiconductors. Donor and acceptor energy levels,  $E_d$  and  $E_a$ , are shown as lying close to the conduction and valence band edges, respectively. The Fermi level is pushed up towards the conduction band in n-type materials, and pulled down to the valence band in p-type materials.

semiconductor electron density [4]:

$$n \approx N_c e^{\frac{E_F - E_c}{k_B T}}, \quad (2.21)$$

where  $N_c$  is the *effective DOS* of the conduction band and is given by:

$$N_c = 2 \left( \frac{2\pi m_e^* k_B T}{h^2} \right)^{\frac{3}{2}}. \quad (2.22)$$

Rearranging [Equation 2.21](#) and taking logarithms of both sides results in an expression for the Fermi level:

$$E_F \approx E_c + k_B T \ln \frac{n}{N_c}. \quad (2.23)$$

Similarly, for p-type semiconductors,

$$E_F \approx E_v + k_B T \ln \frac{p}{N_v}, \quad (2.24)$$

where  $N_v$  is the effective DOS of the valence band:

$$N_v = 2 \left( \frac{2\pi m_h^* k_B T}{h^2} \right)^{\frac{3}{2}}. \quad (2.25)$$

In the above, we can make the assumption that the dopant density is much greater than the intrinsic carrier density (the undoped carrier density)— $N_d \gg n_i$  for n-

type and  $N_a \gg n_i$  for p-type—in doing so enabling us to approximate the electron and hole densities as the dopant densities:  $n \approx N_d$  and  $p \approx N_a$  [21].

If the Fermi level is closer than approximately  $3k_B T$  to either band edge, then the semiconductor is said to be *degenerate* and we can no longer simplify the Fermi–Dirac function to a simple exponential function. Instead, a useful approximation which can be used is the so-called *Joyce–Dixon* approximation, which, to second order for an n-type semiconductor, is given by [4]:

$$E_F - E_c = k_B T \ln \left( \frac{n}{N_c} \right) + \frac{1}{\sqrt{8}} \frac{n}{N_c} - \left( \frac{3}{16} - \frac{\sqrt{3}}{9} \right) \left( \frac{n}{N_c} \right)^2, \quad (2.26)$$

and for a p-type semiconductor, is:

$$E_F - E_c = k_B T \ln \left( \frac{p}{N_v} \right) + \frac{1}{\sqrt{8}} \frac{p}{N_v} - \left( \frac{3}{16} - \frac{\sqrt{3}}{9} \right) \left( \frac{p}{N_v} \right)^2. \quad (2.27)$$

## 2.6.2 P–N Junctions

The bringing together of a p-type region and an n-type region creates a discontinuity in Fermi levels between the two, and to achieve equilibrium, charge carriers diffuse across the junction; holes from the p-type to the n-type, and electrons vice-versa. This leaves behind ionised donors in the n-type region and acceptors in the p-type region, creating an area around the junction free of carriers, the *depletion region*, resulting in an electric field across the junction. This field in turn causes a drift of carriers in the opposite direction to the diffusion, and when the drift current matches the diffusion current, equilibrium has been achieved [4, 41]. This junction is known as a *p–n junction* and an in-equilibrium band diagram is shown in [Figure 2.23](#). This equilibrating process brings about a built-in potential  $V_0$  and thus the creation of a diode; a system in which carriers can flow in one direction but not the other.

We can apply an external voltage, or *bias*, to either enhance or shrink the depletion region. Applying a forward bias reduces the voltage drop across the junction ([Figure 2.24\(a\)](#)), whilst applying a reverse bias increases the voltage drop ([Figure 2.24\(b\)](#)). The former has the effect of pushing carriers into the depletion region, where they can radiatively recombine to give out light. This process is the principal behind the operation of light emitting diodes (LEDs).

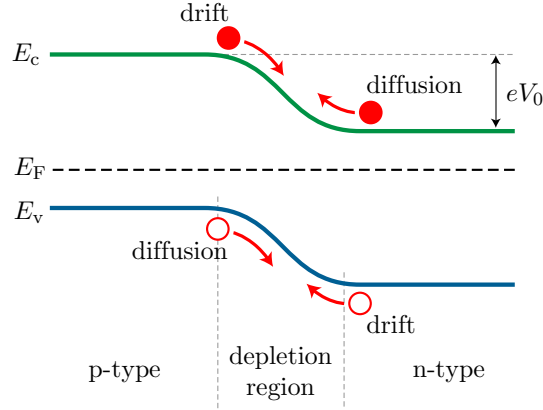


**Figure 2.23:** Band diagram of a p–n junction in equilibrium, where band bending results in an built-in potential  $V_0$ .

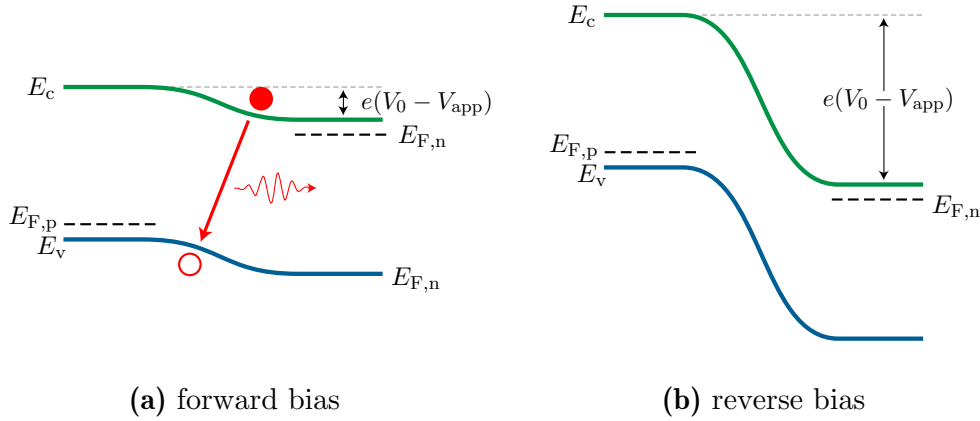


**Figure 2.24:** P–n junction under (a) forward bias, enabling radiative recombination, and (b) reverse bias, preventing the recombination of charge carriers.

## 2.7 Lasers

The inner workings of semiconductor lasers is a vast and complex subject, but the simplified principle of their operation is surprisingly straightforward, albeit if such a description is rather hand-waving in nature. As this thesis only encompasses lasers as a potential application of the SML samples studied, such a simplified description is justified. There are numerous excellent texts devoted entirely to the subject of semiconductor lasers, such as [References 52](#) and [53](#).

A laser is an optical device that produces coherent light by the stimulated emission of photons. In spontaneous emission, electrons in the conduction band recombine with holes in the valence band in a somewhat random manner and they therefore emit incoherent light. If an electron in the conduction band is hit by

a photon with the same energy, it can be stimulated to recombine and thus emit another photon with the same energy, as shown in [Figure 2.25](#). This is known as stimulated emission and results in coherent light with the same wavelength, phase and polarisation. For stimulated emission to occur, there must be more electrons in the conduction band than in the valence band, known as a *population inversion*.

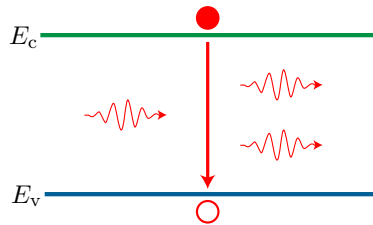


**Figure 2.25:** The principle of light amplification through the stimulated emission of a photon, prompted by the collision of a photon with an excited electron in the conduction band.

The fundamental scheme of laser operation is thus: Spontaneous emission is prompted by the excitation of electrons to the conduction band, by optical or electrical pumping. Mirrors are used to reflect some of these photons back and forth, and they are confined within the structure in a resonator cavity, such that a standing wave is set up along the cavity (along the so-called optical axis). If pumping is sufficient to achieve a population inversion, these photons trigger the stimulated emission of further photons, thus increasing the total number of photons and amplifying the light. The threshold for lasing to occur is when the round-trip optical gain created by this stimulated emission is equal to the losses (due to absorption and loss of photons through the mirrors and in the material), and above this threshold an increase in the pumping serves to increase the light intensity rather than increasing the population inversion.

A p–n junction under forward bias can form a basic laser, with the bias offering the initial pumping to encourage electrons to recombine with holes across the junction (as in LED operation), turning the depletion layer into the so-called *active region*. However, a huge current is needed for lasing to occur as there is no defined region for radiative recombination, and electron and holes can drift through the junction without recombining. Instead, it is common to use a double heterostructure or a QW, in which the band alignment serves the role of confining carriers and creating the active region. A common example, as illustrated in [Figure 2.26](#), is a

p-GaAs QW embedded in n- and p-type AlGaAs cladding. In equilibrium (with no bias), the Fermi level sits well below the GaAs QW conduction band and thus the QW is depleted of electrons. Under sufficient forward bias (Figure 2.26(b)), the electrons have enough energy to flow from the n-AlGaAs into the QW, where they can recombine radiatively with the holes.

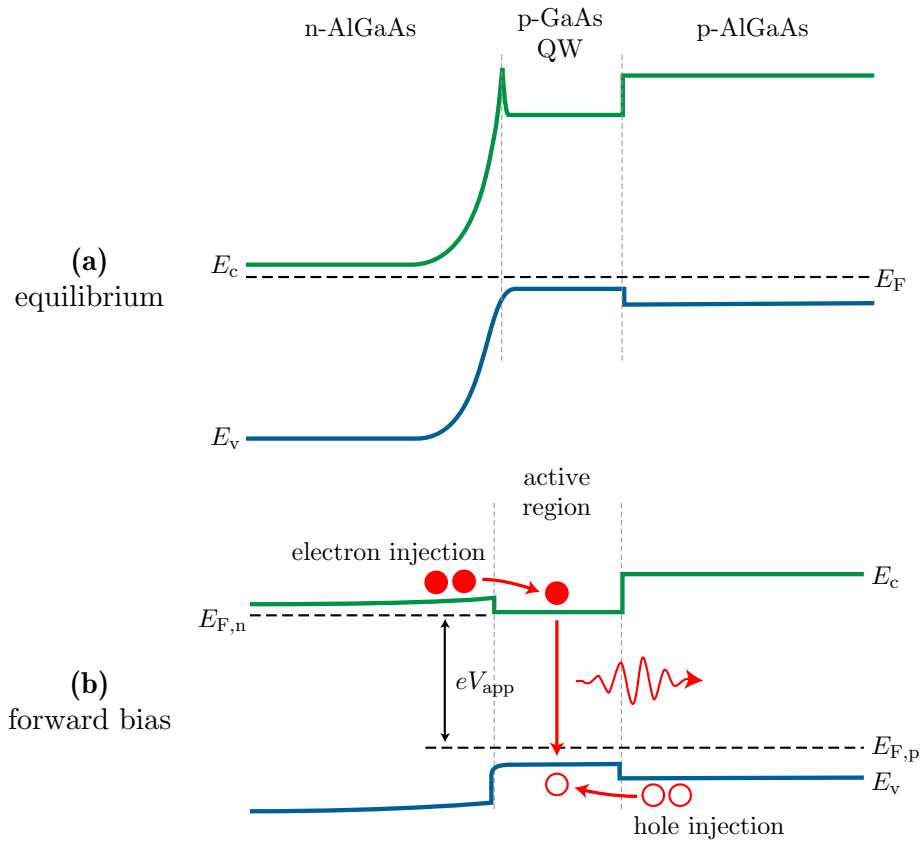


**Figure 2.26:** Band diagram for an GaAs/AlGaAs QW laser. **(a)** In equilibrium, when the large band bending between the n-AlGaAs and GaAs QW prevents carriers recombining. **(b)** Under forward bias  $V_{app}$ , so that electrons and holes can be injected into the QW active region and radiatively recombine.

### 2.7.1 Gain

A full mathematical description of gain in semiconductor lasers is not necessary in the scope of this work, but nonetheless, a qualitative distinction between terminologies used in literature is useful [4]:

**Gain** Sometimes referred to as material gain, or optical gain, this quantity refers to the optical amplification that an active medium provides per unit length of the optical axis, and can be thought of as the amount by which the number

of photons is multiplied per unit length. It therefore represents the difference between the absorption and stimulated emission, meaning gain is negative if no pumping is applied. The gain  $g$  required for lasing to commence (the threshold gain) can be given in terms of the cavity length  $L$  and the reflectivities of the mirrors,  $R_1$  and  $R_2$ :

$$g = \frac{1}{2L} \ln \frac{1}{R_1 R_2}. \quad (2.28)$$

**Modal gain** The gain of an optical mode is given by the modal gain, and it is useful to distinguish between this and the material gain as there is often a poor overlap between the optical mode and the gain medium, especially in confined structures. Thus, we can introduce a confinement factor  $\Gamma$  to distinguish between modal gain and material gain  $g(N)$ , where  $N$  is the carrier density:

$$\text{modal gain} = g(N)\Gamma. \quad (2.29)$$

**Differential gain** The differential gain is the rate at which gain increases as more carriers are injected:

$$\text{differential gain} = \frac{dg(N)}{dN}. \quad (2.30)$$

### 2.7.2 Edge-Emitting Lasers

Edge-emitting semiconductor lasers are amongst the most common semiconductor lasers in use today. As their name implies, light emission occurs from the edge of the structure (perpendicularly to the growth direction), as illustrated in [Figure 2.27\(a\)](#). The double heterostructure described in the last paragraph is typically used to construct an edge laser.

### 2.7.3 Vertical-Cavity Surface-Emitting Lasers

Vertical-cavity surface-emitting lasers (VCSELs), on the other hand, emit light from the surface, as shown in [Figure 2.27\(b\)](#). The cavity length along the optical axis is much shorter than for edge-emitting lasers, typically only a few wavelengths in size, and as such the probability of a photon triggering stimulated emission in one round trip is much lower. To counteract this, high reflectivities of typically above 99%

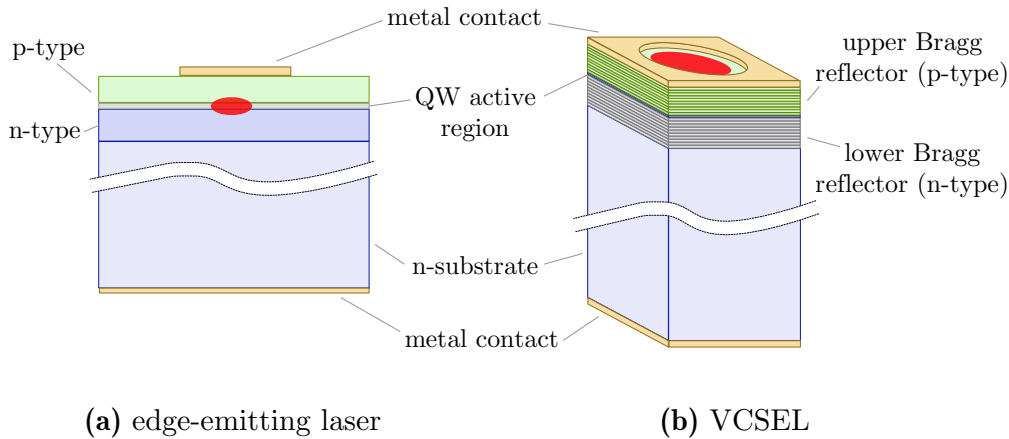


**Figure 2.27:** Simplified representation of (a) an edge-emitting laser, and (b) a vertical-cavity surface-emitting laser (VCSEL). Red regions demonstrate where light emission is from. Adapted from Reference 8.

are needed, as opposed to  $\sim 30\%$  for the mirrors used in edge lasers. Such a high reflectivity is usually achieved by the use of distributed Bragg reflectors, formed of layers with alternating high and low refractive indices. The advantages of VCSELs over edge-emitting and other lasers is discussed in Section 4.1.2.

## 2.8 Excitons in a Magnetic Field

High magnetic fields have a considerable effect on the charge carriers within semiconductors, and this manifests itself in emission spectra in noticeable and analytically-useful ways. Before we continue, it is vital to introduce two quantum-mechanical material properties related to magnetism:

**Diamagnetism** All materials are to some extent diamagnetic, meaning that they create an induced magnetic field that opposes an applied field.

**Paramagnetism** Paramagnetic materials exhibit a magnetisation that is directly proportional to the applied field. A particular atomic manifestation of paramagnetism that is of interest is that the magnetic moment due to an electron's spin tends to align with an applied field (without an applied field these magnetic moments align randomly and cancel). This causes a so-called *Zeeman splitting* of atomic energy levels, a phenomenon first observed by Pieter Zeeman in 1896 [54] when he discovered that the emission spectrum of a sodium lamp, when placed between the poles of an electromagnet, showed splitting of

its spectral lines into several components [55]. Semiconductor nanostructures such as QDs have been frequently shown to demonstrate Zeeman splitting [56–58].

This section focusses solely upon diamagnetic effects, as Zeeman splitting is often much less than the inhomogeneous broadening of typical III-V semiconductor nanostructure emission spectra.

### 2.8.1 Landau Levels

The cyclotron orbits of charged particles in a magnetic field with magnitude  $B$ , which are due to the magnetically-induced Lorentz forces acting upon them, are quantised. As such, charged particles can only occupy discrete energy levels; so-called *Landau levels*. One can deduce this purely quantum-mechanical effect by solving the Schrödinger equation  $\hat{H}\psi = E_n\psi$  with a Hamiltonian  $\hat{H}$  that encompasses the vector potential of the magnetic field, in doing so obtaining values for these discrete energy levels [59]:

$$E_n(B) = E_0(0) + \left(n + \frac{1}{2}\right) \hbar\omega_c, \quad (2.31)$$

where  $n$  is the Landau-level index,  $E_0(0)$  is the ground state energy level in the absence of an applied field,  $\omega_c = |eB|/m^*$  is the classical cyclotron frequency,  $m^*$  is the particle’s effective mass and we have neglected Zeeman splitting of states due to electron spin (see the preamble to this section). The derivation of Equation 2.31 can be found in most quantum mechanics textbooks. If we limit ourselves to the parabolic region around the conduction band minimum, then we can use the electron dispersion relation from Equation 2.2 to express the energy spectrum due to Landau quantisation as:

$$E = \frac{\hbar^2 k^2}{2m_e^*} + \left(n + \frac{1}{2}\right) \hbar\omega_c. \quad (2.32)$$

Here,  $k$  is the component of the wave vector  $\mathbf{k}$  that is parallel to the applied magnetic field. This cyclotron motion acts to confine the electrons and holes in the directions perpendicular to the applied field. The classical orbit size of these carriers in the lowest Landau level ( $n = 0$ ) is given by the magnetic length:

$$l_B = \sqrt{\frac{\hbar}{eB}}. \quad (2.33)$$

### 2.8.2 Excitons

So far, we have only considered free electrons, but at least at low temperatures, electrons and holes can form bound excitonic states with hydrogenic wave functions (Section 2.5.2). It is well established that second-order perturbation theory accurately describes the energy shift of low-lying atomic energy states under the influence of an applied field, as the field is only a small perturbation to the ground state. If we again ignore paramagnetic effects, the energy shift is quadratic in  $B$  [60, 61]:

$$\Delta E = \frac{e^2 a_B^2}{8\mu} B^2. \quad (2.34)$$

For semiconductors, exciton Bohr radii are considerably larger than the hydrogen Bohr radius and exciton binding energies are considerably smaller than the hydrogen binding energy (Rydberg energy). As such, perturbation theory is no longer valid as a complete description for fields achievable in a laboratory setup. For example,  $a_B = 10.2$  nm and  $E_b = 4.8$  meV for GaAs (from Equations 2.18 and 2.19, respectively, and parameters from Reference 62), meaning that above a few Tesla, we see a return to the Landau-level linear dependence described above.

### 2.8.3 Low-Dimensional Nanostructures

In QWs, QDs and other such nanostructures, the confinement due to an applied field competes against the confinement offered by the nanostructure due to composition-induced potential variations, and we can exploit this by observing the field dependence of energy states (e.g., by observing PL emission peak energies) to see whether composition or magnetic confinement is dominant:

$l_B \gg a_B$  When the magnetic length  $l_B$  is much greater than the Bohr radius  $a_B$  of the confined exciton, then the field offers only a small perturbation and a quadratic field dependence prevails, as in Equation 2.34.

$l_B \ll a_B$  When the applied field has a greater confining effect than the nanos-

structure(s), the field dependence is instead linear and follows the Landau-level dependence of [Equation 2.31](#).

In the case of QWs, a field applied perpendicularly to the plane of the well has the effect of confining excitons laterally (along the plane) and as such can be treated similarly to the bulk case. A field that is in parallel with the plane of the well confines excitons vertically, and whether it is the field or the well that confines the exciton can tell us about the composition and structure of the sample (or indeed, whether exciton wave functions from adjacent wells are coupled, increasing the wave function extent).

Mathematical solutions to the problem of nanostructures in a magnetic field are much more difficult to obtain, as compared to bulk materials, due to the presence of the three competing confinement energies, due to composition, Coulomb interaction and the magnetic field. Accordingly, one needs to know detailed information about the morphology and composition of the system, information which is often impractical or impossible to gather. As such, analytic models are an invaluable tool to gather fundamental physical information about the system based on justified assumptions and simplifications. The two analytical models used herein are the *Fock–Darwin* and the *excitonic* models, the former making the simplification of neglecting the excitonic binding energy and the latter the confinement energy [\[61\]](#).

#### 2.8.4 Fock–Darwin Model

The Fock–Darwin (FD) model was independently derived by Fock [\[63\]](#) and Darwin [\[64\]](#) in the late 1920s and early 1930s to solve the problem of an electron confined by a 2D harmonic potential in a perpendicularly applied magnetic field. This problem accurately describes not just an atomic system, but also excitons in a QD, due to the dot’s atom-like energy states and the fact that these states can often be described by a 2D harmonic oscillator [\[61, 65\]](#). For a 2D potential of energy  $\hbar\omega_0$ , the  $(n, l)$ th energy level is given by:

$$E_{n,l} = E_0 + (2n + |l| + 1)\hbar\sqrt{\omega_0^2 + \frac{\omega_c^2}{4}} - \frac{1}{2}l\hbar\omega_c, \quad (2.35)$$

where  $E_0$  is the confinement energy in the direction of the field, and  $n$  and  $l$  are quantum numbers relating to the atomic energy shells:  $n = 0, 1, 2, \dots$  is the radial quantum number (Landau level index) and  $l = 0, \pm 1, \pm 2, \dots$  is the orbital angular momentum quantum number. As before, Zeeman splitting is ignored and as such the ground state  $(0, 0)$  is two-fold spin degenerate. An example FD spectrum for an electron in GaAs is presented in [Figure 2.28](#), using a typical confining potential of  $\hbar\omega_0 = 3 \text{ meV}$  [66] and an electron effective mass of  $m_e^* = 0.067m_0$  [62]. Note that for large fields, the FD states become asymptotic towards Landau levels and therefore for very large fields, all states become degenerate Landau levels. The explanation for this is intuitively obvious; in very strong fields, charges are no longer being confined by the 2D harmonic potential (i.e., the QD), but by the magnetic field instead. Landau levels are shown on [Figure 2.28](#) (yellow lines) for comparison.

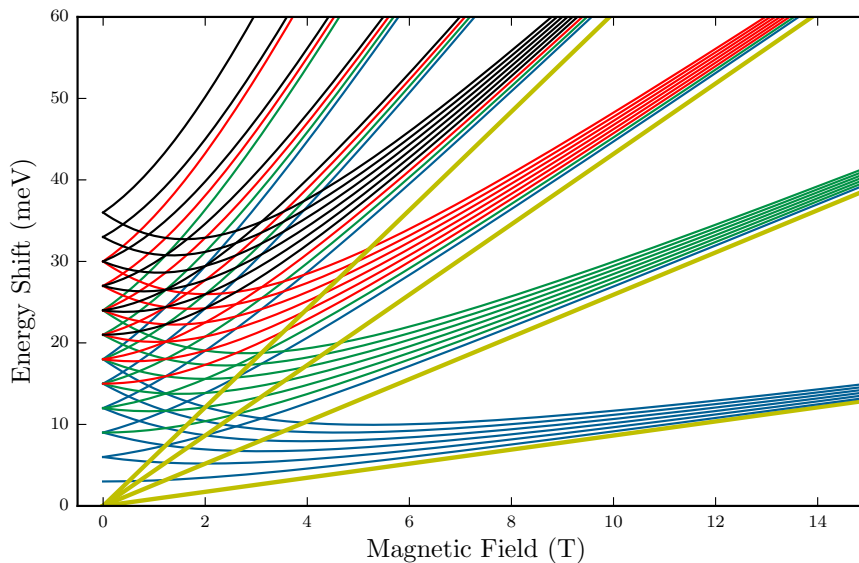


**Figure 2.28:** Fock–Darwin (FD) spectrum from Equation 2.35 for  $\hbar\omega_0 = 3 \text{ meV}$ ,  $m_e^* = 0.067m_0$  and  $E_0 = 0$ , for  $0 \geq n \geq 3$  and  $-5 \geq l \geq 5$ .  $n = 0$  states represented by blue solid lines,  $n = 1$  by green,  $n = 2$  by red and  $n = 3$  by black. The formation of Landau levels at higher magnetic fields can clearly be seen, and the Landau levels themselves, from Equation 2.31, are shown by the thicker yellow lines for comparison.

As the FD model is for a single particle, its application to excitons treats them as single particles and hence neglects their binding energy. This isn't as rash an assumption as one would initially think, however, as the confinement energy due to the QD is inextricably linked to the exciton binding energy: confinement of excitons in nanostructures increases their binding energy by squeezing the carriers into a smaller

volume [61]. One approach which has been employed in literature before [65] is to treat the electron and hole wave functions as identical on equivalent atomic shells, such that  $m_e^* \omega_0^e = m_h^* \omega_0^h$ , in which case the harmonic confining energy  $\hbar\omega_0$  becomes the sum of the electron and hole confining energies,  $\hbar\omega_0 = \hbar(\omega_0^e + \omega_0^h)$  and we can use the reduced exciton mass  $\mu$  as opposed to single-particle effective masses in the cyclotron frequency  $\omega_c = |eB|/\mu$ :

$$E_{n,l} = E_0 + (2n + |l| + 1)\hbar\sqrt{(\omega_0^e + \omega_0^h)^2 + \frac{\omega_c^2}{4}} - \frac{1}{2}l\hbar\omega_c. \quad (2.36)$$

$E_0$  now encompasses the exciton binding energy as well as the band gap. Whether this approach is justified or not is dependent on the exact problem studied and one must bear in mind that the assumption that electron and hole wave functions are identical is often not true. For example, in type-II systems (Section 2.2.3) one carrier is localised and its wave function may be squeezed into its confining potential (e.g., a QD), whilst the other carrier is free and its wave function extends to its intrinsic, unconfined size.

### 2.8.5 Excitonic Model

The so-called excitonic model [61] differs from the FD model in that there is no extended intermediate field regime, but instead it passes straight from the low-field to the high-field regime, without discontinuity, at a critical field  $B_c$ . Furthermore, the excitonic model differs in that it takes into account the exciton binding energy and chooses to neglect the confinement energy, though as previously detailed, the two are inter-dependent.

The low-field regime is quadratic and given by Equation 2.34, whilst the high-field regime is linear and given by the ground state Landau level dependence shown in Equation 2.31:

$$E = E_0 + \frac{e^2 a_B^2}{8\mu} B^2 \quad \text{for } B \leq B_c \quad (2.37)$$

and

$$E = E_0 + E_1 + \frac{1}{2}\hbar\omega_c \quad (2.38)$$

$$= E_0 + E_1 + \frac{\hbar e B}{2\mu} \quad \text{for } B \geq B_c, \quad (2.39)$$

where  $E_1$  is a constant required for continuity. Applying this condition for continuity results in a critical field of

$$B_c = \frac{2\hbar}{a_B^2 e}, \quad (2.40)$$

which corresponds to a critical magnetic length of  $l_c = a_B/\sqrt{2}$ , such that the crossover between the two regimes is when the magnetic length is  $1/\sqrt{2}$  times the zero-field Bohr radius. It follows after algebraic manipulation that  $E_1$  equates to the exciton binding energy,  $E_1 = -\frac{\hbar^2}{2\mu a_B^2}$ . It is important to note that this is the unconfined binding energy, whilst in reality the squeezing together of electrons and holes has the effect of increasing the binding energy, as previously discussed.

We can amalgamate these results to form final expressions for the excitonic model:

$$E = \begin{cases} E_0 + \frac{e^2 a_B^2 B^2}{8\mu} & \text{for } B \leq \frac{2\hbar}{ea_B^2} \\ E_0 - \frac{\hbar^2}{2\mu a_B^2} + \frac{\hbar e B}{2\mu} & \text{for } B \geq \frac{2\hbar}{ea_B^2}. \end{cases} \quad (2.41)$$

Finally, introducing the fitting parameter  $\Gamma = e^2 a_B^2 / 8\mu$ , we can write:

$$E = \begin{cases} E_0 + \Gamma B^2 & \text{for } B \leq B_c \\ E_0 - \Gamma B_c^2 + 2\Gamma B_c B & \text{for } B \geq B_c. \end{cases} \quad (2.42)$$

$\Gamma$  is the *diamagnetic shift coefficient* and is a useful quantity in itself, representing the rate at which the magnetic field shifts energy levels, usually expressed with units of  $\text{meV T}^{-1}$ . Simple algebraic rearrangement yields values for the Bohr radius and effective mass of

$$a_B = \sqrt{\frac{2\hbar}{eB_c}} \quad (2.43)$$

and

$$\mu = \frac{e\hbar}{4\Gamma B_c}. \quad (2.44)$$

## 2.9 Electrochemistry Basics

Electrochemical cells are ubiquitous in modern society in the form of the batteries that power our vast array of portable electronic devices. They typically consist of two electrically-connected conducting or semiconducting electrodes placed in an electrolyte solution. *Voltaic* cells are those that generate an electric current, and therefore batteries are a form of (or more strictly, a series of) voltaic cells, whilst *electrolytic* cells use an electric current to drive a chemical reaction that would not occur spontaneously [41]. “Photo” refers to the use of sunlight to drive a process and so, for example, *photovoltaic* refers to the use of sunlight to produce electrical currents, usually in reference to a semiconductor solar cell. By definition, it then stands that *photoelectrolysis* is the use of sunlight to drive a chemical reaction, though by convention the term is commonly used to refer solely to the splitting of water into hydrogen and oxygen (as opposed to other electrolytic processes, such as splitting bauxite to obtain aluminium). Similarly, a *photoelectrochemical* or *photoelectrolytic* cell (PEC) is used to refer to an electrochemical cell used to split water. Before we delve into the specific case of PECs, it is important to introduce some basic electrochemical definitions and concepts [67].

### 2.9.1 Electrodes and Electrolytes

An electrode is a (semi)conductor in which electrons or holes carry charge, whilst an electrolyte is an ionic conductor in which ions (charged atoms) carry charge. Liquid-phase electrolytes containing an ionic species (for example,  $\text{H}^+$ ,  $\text{Na}^+$  or  $\text{Cl}^-$ ) are typically used to aid the transport of charge across the electrolyte. For photoelectrolysis, this electrolyte must be an aqueous solution.

In addition to the two electrodes that facilitate the overall electrochemical process, a third electrode with a fixed potential, named the *reference electrode*, is often used to standardise the measurement of potentials. The potentials of common reference electrodes, such as the standard hydrogen electrode (SHE) and saturated

**Table 2.1:** Electric potentials of the standard hydrogen electrode (SHE) and saturated calomel electrode (SCE) relative to each other [16] and the vacuum level [17].

	SHE (V)	SCE (V)	Vacuum (V)
vs. SHE	0	+0.244	$\sim -4.4^a$
vs. SCE	-0.244	0	$\sim -4.6^b$
vs. vacuum	$\sim +4.4^a$	$\sim +4.6^b$	0

<sup>a</sup> Literature values for the SHE relative to the vacuum vary from as low as 4.2 V [68] to 4.6 V [69] but tend to average at approximately 4.4 V; the reader is invited to pick their own uncertainty!

<sup>b</sup> Values for the SCE relative to the vacuum (and vice versa) are calculated from the SHE relative to vacuum [17] and the SCE relative to the SHE [17], rounded to 2 s.f.

calomel electrode (SCE), are well defined in reference to each other but with a degree of uncertainty relative to the vacuum, as shown in Table 2.1. Values for potentials are often written “vs.” the reference electrode, for example “vs. SHE” for potentials measured with the SHE as a reference electrode.

## 2.9.2 Half-Reactions, Reduction and Oxidation

The overall chemical reaction in a cell is usually made up of two independent half-reactions occurring at the two separate electrodes, each of which can be written separately but which will only occur in a complete electrochemical cell. In the case where it is only one of these half-reactions that we are interested in, the electrode at which this occurs is labelled the *working electrode*, and the other electrode, the *counter electrode*.

We observe or control (depending on whether our cell is voltaic or electrolytic) the potential of the working electrode with respect to the reference electrode, which amounts to controlling the energy of electrons in the electrode. If we drive the electrode to more negative potentials, the energy of electrons is raised and they can reach a high enough level to transfer into vacant electrolyte states, that is, empty spaces in the molecular orbits of ionic species in the electrolyte. If this flow of electrons from the electrode to the electrolyte proceeds at a constant rate, it is known as a *reduction current*. In contrast, driving the electrode to more positive potentials lowers the energy of the electrons (increases the energy of the holes) and

electrons in the electrolyte will find more favourable states to transfer to on the electrode (or equivalently, holes will reach a low enough energy level to transfer into vacant hole states in the electrolyte). This flow of electrons from the electrolyte to the electrode (and therefore the flow of holes from the electrode to the electrolyte) is known as an *oxidation current*.

The reduction and oxidation half-reactions occur in parallel at the separate electrodes. Each half-reaction has a potential associated with it and under “standard conditions” (25 °C, 1 atmosphere and 1 mol L<sup>-1</sup>) these are called the standard reduction potential  $E_{\text{red}}^{\ominus}$  and the standard oxidation potential  $E_{\text{ox}}^{\ominus}$ . The overall *redox* potential  $E_{\text{redox}}$  lies midway between  $E_{\text{red}}$  and  $E_{\text{ox}}$  and is analogous to the semiconductor Fermi level. Under standard conditions it is named the standard redox potential  $E_{\text{redox}}^{\ominus}$  [9]. Rather confusingly, some texts refer to  $E_{\text{redox}}$  as the reduction potential. Convention has it that the symbol  $E$  is used to refer to these potentials, despite them being potentials and not energies (see [Section 2.9.3](#)).

## Overpotential

The reduction and oxidation potentials give us the theoretical, thermodynamically-determined potential that a chemical reaction should take place at. The difference between this and the experimentally-observed potential that the reaction takes place at is called the *overpotential*, which is due to a number of difficult-to-determine energy losses in the electrochemical cell, such as charge-carrier depletion near to electrode surfaces and resistance losses across the electrolyte [67].

### 2.9.3 Conventions

The development of electrochemistry and solid-state physics as separate research fields has led to many contradictory conventions and overlapping definitions. The most notable of these is the parallel use of the terms Fermi level, in reference to the electrode, and redox potential, in reference to the electrolyte. In reality, the difference between these two terms is purely conceptual; they both refer to the chemical potential of the electron. Reiss [70] argued that there is no reason to not use the term Fermi level in relation to electrolytes, and to avoid confusion, this convention of referring to all chemical potentials as Fermi levels will be employed

herein, with the Fermi level in the electrolyte referred to as the redox Fermi level  $E_{F,\text{redox}}$  and the Fermi level in the semiconductor referred to as the semiconductor Fermi level  $E_{F,s}$ .

The most probable reason that the co-existence of these two equivalent terms has persisted is that they are often given, sometimes without qualification, with reference to different absolute levels. The Fermi level in solids is often given relative to the vacuum, whilst the redox potential (Fermi level in electrolytes) is normally given relative to the SHE. Converting between the two is of course trivial (see [Table 2.1](#)) and the author will endeavour to make absolutely clear what any quantities presented are relative to.

The final nuance to note is that energies and potentials are often used interchangeably. For example, experimentally-measurable quantities will be expressed as a potential, whilst energy levels (e.g., the semiconductor band edges) will be given as an energy. As we are dealing with electrons whose charge  $q = -e$  is well established, expressing an energy  $E$  as a voltage  $V$  (or vice-versa) is simple:  $E = qV = -eV$ . Indeed, using units of electronvolts so that  $E[\text{eV}] = -V[\text{V}]$  makes things even easier. It is important to note the negative sign, which arises because conventional current flows in the opposite direction to electron current.

## 2.10 Semiconductor Photoelectrolysis

Semiconductor photoelectrolysis utilises physics from photovoltaic solar cells in an electrochemical environment to split water by the use of a semiconductor electrode. This multidisciplinary research topic requires theoretical concepts from the fields of solid-state physics, electrochemistry and materials science, to name but a few. Work in this thesis focusses mainly upon band alignment in the semiconductor and at the semiconductor–electrolyte interface (SEI).

A typical semiconductor PEC is shown in [Figure 2.29](#). Before delving into the physics behind its operation, a simplified overview of the photoelectrolysis process is useful so the reader can get their bearings: A semiconductor electrode is ohmically contacted to a counter electrode and the two electrodes immersed in an aqueous solution. The conduction and valence bands in the semiconductor are bent upwards

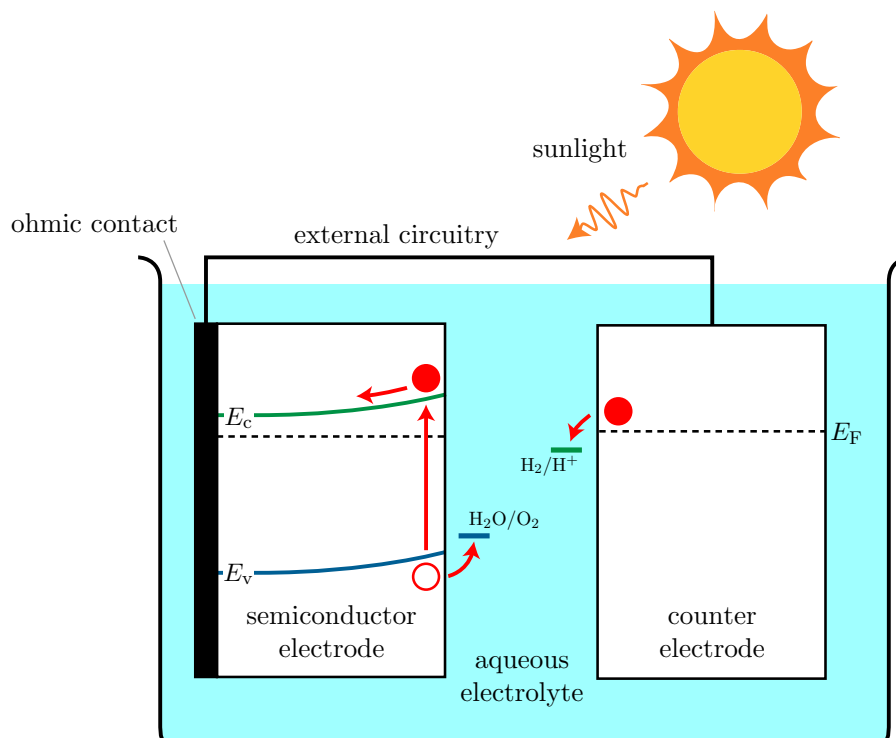


**Figure 2.29:** A simplified schematic of a photoelectrochemical cell (PEC), consisting of a semiconductor electrode and a counter electrode immersed in an aqueous electrolyte.

(for an n-type semiconductor) or downwards (for a p-type semiconductor) at the SEI and this creates an internal electric field in the semiconductor. Upon illumination, excitons are created near the SEI and subsequently split up by this internal field. Depending on the direction of the band bending, either electrons or holes flow towards the counter electrode, whilst the oppositely-charged carriers travel to the SEI. Given that the energy levels are positioned correctly, these charges transfer to the electrolyte and drive chemical reactions to split up the water.

### 2.10.1 Hydrogen and Oxygen Production

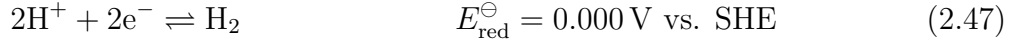
The overall water-splitting reaction that occurs in a PEC can be described by hydrogen and oxygen half-reactions, each occurring in parallel but at separate electrodes. For n-type (p-type) semiconductors, oxygen (hydrogen) evolution typically occurs at the semiconductor electrode, with hydrogen (oxygen) evolution occurring at the counter electrode. The energy of electrons and holes relative to the hydrogen-production potential  $E_{\text{red}}$  (the reduction potential for water) and the oxygen-production potential  $E_{\text{ox}}$  (the oxidation potential for water) tells us whether

or not water splitting can occur, as is discussed further in [Section 2.10.3](#).

The two half-reactions are written differently depending on whether they are in an alkaline or an acidic electrolyte [9, 15]. For an alkaline electrolyte with a pH of 14:



For an acidic electrolyte with a pH of 0:



The so-called *Nernst equation* can be used to give a value for the hydrogen- and oxygen-production potentials as a function of the pH. The derivation of the Nernst equation for the particular case of water electrolysis can be found in standard electrochemistry textbooks [71]. For hydrogen production,

$$E_{\text{red}} = E_{\text{red}}^\ominus + \left( \log(10) \frac{k_{\text{B}}T}{e} \right) \times \text{pH} \quad (2.49)$$

$$= -0.059 \times \text{pH} \quad \text{vs. SHE at } 25^\circ\text{C}, \quad (2.50)$$

where  $E_{\text{red}}$  is the hydrogen-production potential at a particular pH and  $E_{\text{red}}^\ominus$  is the standard hydrogen potential at pH = 0, given vs. SHE in [Equation 2.47](#) above. It goes without saying that relative to the SHE,  $E_{\text{red}}^\ominus = 0 \text{ V}$ , as this is after all how the SHE is defined. This physical meaning of [Equation 2.50](#) is that the hydrogen production potential decreases by 59 mV per pH unit at 25 °C.

Similarly, for oxygen production,

$$E_{\text{ox}} = E_{\text{ox}}^{\ominus} + \left( \log(10) \frac{k_{\text{B}}T}{e} \right) \times \text{pH} \quad (2.51)$$

$$= 1.229 - 0.059 \times \text{pH} \quad \text{vs. SHE at } 25 \text{ }^{\circ}\text{C}, \quad (2.52)$$

where  $E_{\text{ox}}$  is the oxygen-production potential at a particular pH and  $E_{\text{ox}}^{\ominus}$  is the standard oxygen potential at pH = 0, given vs. SHE in Equation 2.48 above.

## 2.10.2 Band Bending at the Semiconductor–Electrolyte Interface

Fundamental to the photoelectrolytic process is the bending of the valence and conduction bands at the SEI. The theory behind this band bending was originally developed by Nevill Mott and Walter Schottky in the context of a metal–semiconductor contact, and as such its presence at an interface is referred to as a *Schottky barrier* [72].

The process by which band bending occurs is similar to the creation of a p–n junction, as detailed in Section 2.7: When two materials join—for example, when a metallic contact is deposited on a semiconductor, or in the case of photoelectrolysis, when a semiconductor is immersed in an electrolyte—their individual Fermi levels are discontinuous, as shown in Figure 2.30(a). Equilibration of this interface necessitates the flow of charges across the interface so that these Fermi levels equate, causing band bending. In the case of the SEI, the exact form of this charge transfer is complex and has seen much discussion in literature [9, 73, 74]. Direct transfer from the band edges, transfer via surface states<sup>4</sup> and transfer via adsorbed surface molecule states, all play a role. Nonetheless, it is common to make the simplification of comparing the bulk semiconductor Fermi level  $E_{\text{F},\text{s}}$  relative to the redox Fermi level  $E_{\text{F},\text{redox}}$  to gain a qualitative picture of band bending [17, 74, 75]:

$E_{\text{F},\text{s}} > E_{\text{F},\text{redox}}$  If the semiconductor Fermi level is higher than the redox Fermi level, as is usually the case for **n-type semiconductors**, then

---

<sup>4</sup>The termination of crystal periodicity at a semiconductor’s surface leads to “dangling” bonds of surface atoms. These bonds can interact with each other to form a narrow energy band in the band gap with its own surface Fermi level [9, 74].

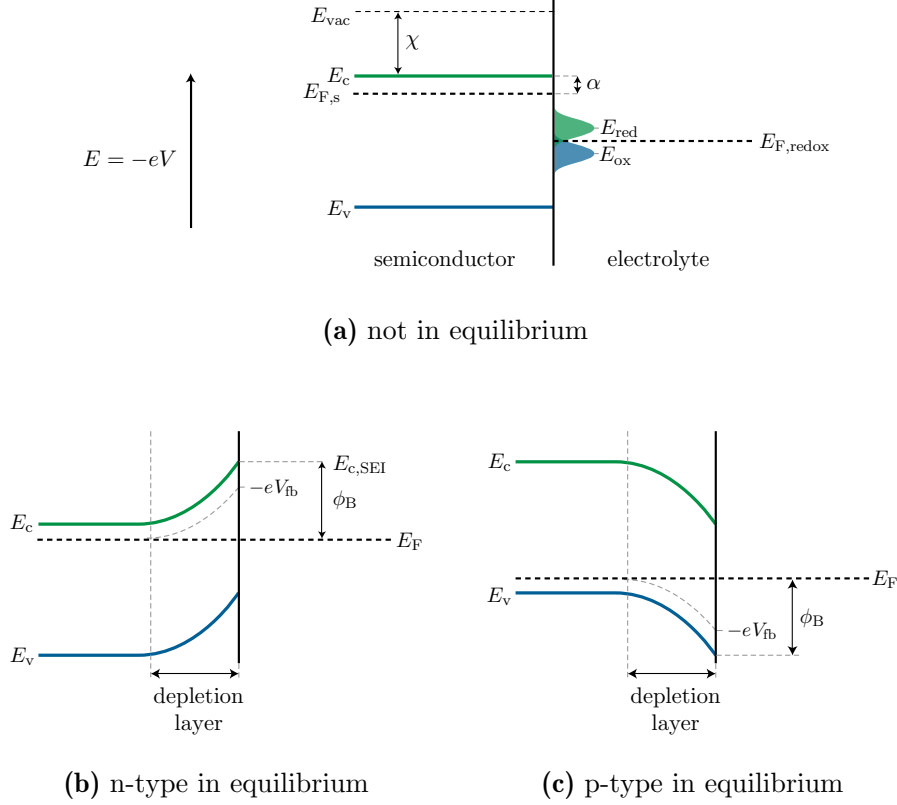


**Figure 2.30:** Energy band diagrams for the semiconductor–electrolyte interface (SEI). **(a)** Not in equilibrium. In the semiconductor, the conduction and valence band edges,  $E_c$  and  $E_v$ , semiconductor Fermi level  $E_{F,s}$  and vacuum level  $E_{vac}$  are shown, with the distance from  $E_c$  to  $E_{vac}$  represented by the electron affinity  $\chi$ , and the gap between  $E_c$  and  $E_{F,s}$  defined as  $\alpha$ . In the electrolyte, the two distribution functions shown are the density of ionic energy states available for oxidation and reduction, which arise due to fluctuations in individual ionic states [9], with peaks at the oxidation and reduction potentials,  $E_{ox}$  and  $E_{red}$ , and an overlap at the redox Fermi potential,  $E_{F,redox}$ . **(b)** N-type semiconductor in equilibrium, showing the upwards bending of the bands so that the semiconductor and electrolyte Fermi levels meet at  $E_F$ .  $V_{fb}$  is the flatband potential and  $\phi_B = E_{c,SEI} - E_F$  is the Schottky barrier, where  $E_{c,SEI}$  is the conduction band edge at the SEI. **(c)** Equivalent to (b) but for p-type semiconductor in equilibrium.

electrons will flow from the semiconductor to the electrolyte and thus the semiconductor Fermi level moves down until it aligns with the redox Fermi level such that  $E_{F,s} = E_{F,redox}$ , as shown in Figure 2.30(b). This transfer of electrons bends the bands upwards and creates a layer near the semiconductor surface that is depleted of electrons; the aptly named *depletion layer*.

$E_{F,s} < E_{F,redox}$  On the other hand, if the semiconductor Fermi level is lower than the redox Fermi level, as is typical for **p-type semiconductors**, then it is the holes that flow from the semiconduc-

tor to the electrolyte, thereby raising the semiconductor Fermi level until it equals the redox Fermi level, as shown in [Figure 2.30\(c\)](#). Similarly, a depletion layer that is depleted of holes is formed.

The term “equilibrium Fermi level”, labelled  $E_F$ , will be used to refer to the energy of  $E_{F,s}$  and  $E_{F,\text{redox}}$  when they equal each other (are in equilibrium). The extent of the band bending is quantified by the Schottky barrier height  $\phi_B$ , which is defined as the energy difference between the conduction band edge at the SEI and the equilibrium Fermi level, as shown in [Figure 2.30 \[76\]](#). If  $E_{c,\text{SEI}}$  is the energy of the conduction band edge at the SEI, then

$$\phi_B = E_{c,\text{SEI}} - E_F. \quad (2.53)$$

The depletion layer encompasses an in-built electric field, which has the effect of splitting up photo-generated excitons, preventing them from recombining. Other band-bending regimes exist, for example, when  $E_{F,s} < E_{F,\text{redox}}$  in an n-type semiconductor, electrons transfer from the electrolyte to the semiconductor and hence downward band bending ensues and an accumulation layer of excess electrons forms, instead of a depletion layer. The common name for a depletion layer, accumulation layer or inversion layer (which is the extreme case of a depletion layer when the minority carriers outnumber the majority carriers near the surface) is a *space charge layer*.

The semiconductor electrode is contacted to the counter electrode via an ohmic contact, which is essentially a Schottky junction but with negligible band bending such that current–voltage curves are linear (and thus follow Ohm’s law). As such, the Fermi level in the counter electrode equals the semiconductor Fermi level. An ohmic contact can be created by the careful selection of metallic contact materials, though a perfect ohmic contact is notoriously difficult to achieve.

### 2.10.3 Illumination and the Flat-Band Potential

From now on, we shall limit ourselves to discussing n-type semiconductors. Incident photons on the surface of the semiconductor excite electrons in or near the depletion

region and these photo-generated carriers are soon split up by the in-built field. The electrons now flow towards the counter electrode, whilst the holes move towards the SEI. This photocurrent is responsible for a photovoltage  $V_{\text{ph}}$ , which has the effect of raising the semiconductor and counter-electrode Fermi levels (which are equal) and thereby reducing the band bending. If they are raised sufficiently so that they are above the hydrogen-production potential (Equation 2.50), then electrons transfer from the counter electrode to the electrolyte to drive hydrogen production. Similarly, if the valence band edge at the SEI is lower than the oxygen-production potential (Equation 2.52), then holes transfer to the electrolyte to drive the oxygen production. This is shown schematically in Figure 2.31.

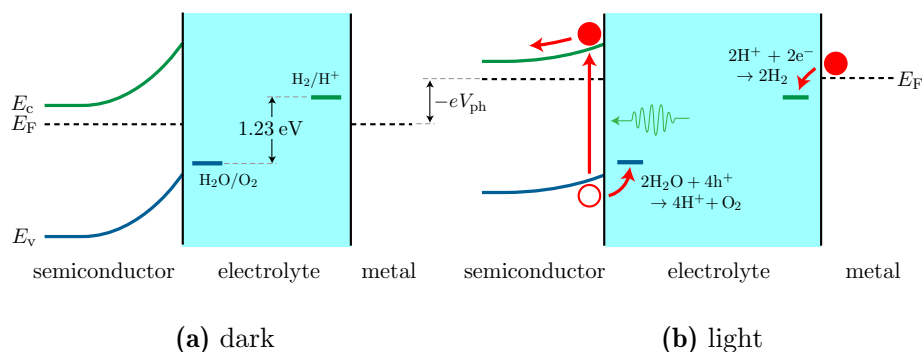


**Figure 2.31:** Energy band diagram for a PEC with n-type semiconductor electrode **(a)** in the dark and **(b)** illuminated. Incident sunlight generates a photovoltage  $V_{\text{ph}}$  that raises the semiconductor and hence counter-electrode Fermi level, so that it and the valence band edge at the SEI straddle the oxygen- and hydrogen-production potentials, which are shown in the electrolyte. Holes and electrons can then transfer to the solution to drive the water-splitting half-reactions, shown in **(b)**.

Given sufficient illumination, the bands will fully flatten and the potential of the semiconductor Fermi level at which this occurs is called the *flat-band potential*,  $V_{\text{fb}}$  [9]. This is labelled on Figure 2.30 (in the dark) and Figure 2.31 (when illuminated). It is an absolute value (i.e., not a potential difference) and in the dark, it sits below the conduction band edge at the SEI by the difference between the bulk conduction band edge  $E_c$  and the equilibrium Fermi level:

$$-eV_{\text{fb}} = E_{c,\text{SEI}} - |E_c - E_F|. \quad (2.54)$$

It is an easily measurable property and is as such reported frequently in literature, usually relative to a reference electrode.

Without band bending, no photocurrent can be generated from the splitting up

of excitons, and thus no photovoltage to further raise Fermi levels. Therefore, the importance of the flat-band potential is that it represents the highest possible energy that the semiconductor Fermi level and therefore the counter-electrode Fermi level can reach under illumination, hence dictating whether or not a particular n-type semiconductor has the ability to reduce water to hydrogen.

#### 2.10.4 Calculating the Schottky Barrier Height

Of particular relevance to this work is that the Schottky barrier height can be calculated from the flat-band potential along with a few other well established material properties. Rearranging [Equation 2.54](#) and substituting it into [Equation 2.53](#), we obtain:

$$\phi_B = -eV_{fb} - E_F + E_c - E_F. \quad (2.55)$$

As long as all of the values in this expression are taken with reference to the same level (for example, the same reference electrode), then this equation holds true.

Suppose that we take our values relative to the vacuum level. In doing so, we are able to introduce the electron affinity  $\chi$  from [Equation 2.5](#), which implies that the conduction band edge relative to the vacuum sits at the negative of the electron affinity:  $E_c = E_{vac} - \chi$ , which written relative to the vacuum level becomes  $E_c|_{E_{vac}=0} = -\chi$ . For simplicity, let us also define  $\alpha = E_c - E_F$ . We can now rewrite the equilibrium Fermi level relative to the vacuum as  $E_F|_{E_{vac}=0} = -(\chi + \alpha)$ . If we convert whatever literature value we have for  $V_{fb}$  so that it is also relative to the vacuum, we can use  $E_F|_{E_{vac}=0}$  in [Equation 2.55](#) to give us a final expression for the Schottky barrier height:

$$\phi_B = -eV_{fb}|_{E_{vac}=0} + \chi + 2\alpha. \quad (2.56)$$

$\alpha$  can be found by the simple rearrangement of [Equation 2.23](#),

$$\alpha = E_c - E_F = k_B T \ln \left( \frac{N_c}{n} \right), \quad (2.57)$$

and we can use [Equation 2.22](#) to calculate  $N_c$ , the effective density of states of the conduction band. We now have a value for the Schottky barrier height that

depends on the material properties  $V_{\text{fb}}$ ,  $\chi$ ,  $m_e^*$  and  $n$ , which for most semiconductor materials are easily found in literature, or in the case of  $n$ , depends on the doping during the growth of the sample and we can assume  $n \approx N_{\text{d}}$  for sufficiently large doping densities.

### 2.10.5 Semiconductor Electrode Material Requirements

The theory presented in this section has already given the first of the requirements for our chosen semiconductor to make a successful electrode in a PEC; that its electron-donating and electron-accepting states must straddle the hydrogen- and oxygen-production potentials, which are given by [Equations 2.50](#) and [2.52](#). For an n-type semiconductor, the electron-accepting state is the valence band edge at the SEI. If we make the assumption that this remains fixed under illumination (as is commonly done [[9](#), [21](#)]), then it can be determined by the subtraction of the band gap  $E_{\text{g}}$  from the conduction band edge at the SEI  $E_{\text{c,SEI}}$ :

$$\begin{aligned}
 E_{\text{v,SEI}} &= E_{\text{c,SEI}} - E_{\text{g}} \\
 &= -eV_{\text{fb}} + (E_{\text{c}} - E_{\text{F}}) - E_{\text{g}} \\
 &= -eV_{\text{fb}} + \alpha - E_{\text{g}},
 \end{aligned}
 \tag{2.58}$$

where  $\alpha = E_{\text{c}} - E_{\text{F}}$  can be calculated from [Equation 2.57](#). If  $E_{\text{v,SEI}}$  is more negative than the energy of the oxygen-production potential, then oxygen production can occur at the SEI.

The electron-donating state for a PEC with an n-type semiconductor electrode is the counter-electrode Fermi level, and is therefore equal to the semiconductor Fermi level  $E_{\text{F,s}}$ . The highest level that  $E_{\text{F,s}}$  can reach under illumination is the flat-band potential  $V_{\text{fb}}$ , achieved when the bands are completely flat, and thus if  $-eV_{\text{fb}}$  is more positive than the energy of the hydrogen-production potential (that is,  $V_{\text{fb}}$  is more negative than the hydrogen-production potential), then hydrogen production can occur at the counter electrode.

Whilst theory dictates the above to be true, in reality, overpotentials for both the hydrogen and oxygen half-reactions are needed and it is well established in

literature that the oxygen half-reaction requires an overpotential of 0.275 V, whilst the hydrogen half-reaction requires an overpotential of 0.050 V [77, 78]. Furthermore, photo-excitation of electrons is to the conduction band and there is therefore an energy loss of  $\alpha$  when electrons move down to the Fermi level in the counter electrode, which is typically 0.05-0.2 V, depending on the material and doping [15]. With these factors taken into account, the 1.229 eV gap between the oxygen- and hydrogen-production potentials results in the need for a band gap of approximately 1.8 eV. The optimal band gap is, of course, a trade off between maximising solar absorption whilst meeting the aforementioned criteria. The solar irradiance spectrum, given in Figure 2.17, shows that below about 400 nm there is a large drop in the intensity of solar radiation. This equates to an energy of  $\sim 3.1$  eV and thus our semiconductor band gap should be considerably smaller than this.

The final crucial requirement of a semiconductor electrode is that it is chemically stable in a water-splitting environment, in particular, that it doesn't participate in unwanted semiconductor oxidation or reduction reactions and therefore corrode. At the SEI in p-type materials, electrons transfer to the electrolyte and as such, semiconductor reduction reactions are possible. Conversely, at the SEI in n-type materials, holes accept an electron from the electrolyte and semiconductor oxidation reactions can take place. This presence of an oxide layer can prevent the further transfer of electrons from the electrolyte to the electrode.

To summarise, an n-type semiconductor electrode must meet the criteria of having:

- A band gap of over 1.8 eV, but low enough so that it captures enough of the solar spectrum.
- A valence band edge at the SEI that is lower in energy than the oxygen-production potential, with an overpotential of 0.275 V or greater.
- A flat-band potential that is higher than the hydrogen-production potential, with an overpotential of 0.050 V or greater.
- Sufficient chemical stability so that it doesn't undergo unwanted oxidation reactions.

## 2.11 Epitaxial Growth

The word epitaxy is derived from the Greek words *epi*, meaning “upon” or “above”, and *taxis*, meaning “order” or “arrangement”, and when applied to semiconductor growth, it indicates ordered atomic layer-by-layer deposition, during which the crystallographic position of deposited atoms is maintained. This section will introduce the fundamental growth mechanisms relative to nanostructures in this work, whilst the technique used to fabricate the semiconductor heterostructures studied in this thesis will be discussed in [Section 3.1](#).

### 2.11.1 Self-Assembled Growth

QD growth by self-assembly is a process by which epitaxially-deposited layers assemble themselves into QDs because a mismatch between lattice constants at heterojunctions causes a strain energy. Given the right conditions, the most energetically-favourable way for this strain to relax is by the formation of 3D islands, that is, QDs.

Three standard regimes characterise epitaxial growth: Frank–van der Merwe (FM), Volmer–Weber (VW) and Stranski–Krastanow (SK) growth, as illustrated in [Figure 2.32](#). They are distinguished by the ratio of the sum of the epilayer (new epitaxial layer) surface and interface energies to the substrate surface energy [40].

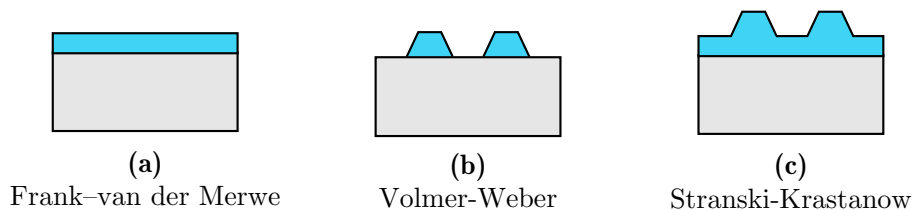


**Figure 2.32:** Mechanisms of epitaxial growth: (a) Frank–van der Merwe (layer-by-layer); (b) Volmer–Weber (island) and; (c) Stranski–Krastanow (layer-by-layer plus island)

**FM** If the substrate surface energy is greater than the sum of the epilayer surface and interface energies, then adatoms are predominantly attracted to the substrate surface and not each other, resulting in FM growth ([Figure 2.32\(a\)](#)). This tends to occur when the lattice mismatch is small. FM growth is commonly used to fabricate QWs.

**VW** In contrast, if the substrate surface energy is smaller than the sum of the epilayer surface and interface energies, then adatoms are attracted more to each other and island growth is instantly energetically favourable, resulting in VW growth ([Figure 2.32\(b\)](#)). Larger lattice mismatches tend to produce VW growth.

**SK** The intermediate case is when the substrate surface energy is roughly equal to the sum of the epilayer surface and interface energies, in which case a *wetting layer* grows to a certain critical thickness before island formation becomes energetically favourable as thicker layers have a larger strain energy. This process is known as SK growth and is amongst the most common methods for growing self-assembled QDs.

It is notable that strain energy within the crystal can have an impact on the band structure and therefore on material parameters such as the effective mass. Indeed, strain-induced band gap engineering is frequently used to tune band gaps without altering the materials themselves [79].

The thicker a layer of lattice-mismatched material becomes as it is deposited on another material, the more strained it becomes, until a point where crystal defects are formed to release this strain. Details of different forms of defects aren't discussed here, but it is nevertheless important to remember that a large number of defects can have a detrimental impact on device performance.

Analysis of nanostructures grown by SML deposition forms a large part of this thesis, and concepts regarding SML growth will be introduced in the literature review of this area of research, presented in [Section 4.1](#).



# Chapter 3

## Experimental & Theoretical Techniques

This chapter gives an overview of the various techniques used to grow and analyse samples studied in this work, as well as those used to mathematically model them. Samples were grown by metal-organic chemical vapour deposition (MOCVD) (Section 3.1), before being analysed by the imaging technique of cross-sectional scanning tunnelling microscopy (XSTM) (Section 3.2). Steady-state magneto-PL and time-resolved PL (TRPL) were used to probe their optoelectronic properties (Sections 3.3 and 3.4), and one-band effective-mass and eight-band  $\mathbf{k} \cdot \mathbf{p}$  calculations were performed to gain further insight into carrier confinement (Section 3.5). MOCVD and XSTM were carried out at Technische Universität Berlin, whilst all other work was undertaken at Lancaster University.

### 3.1 Metal-Organic Chemical Vapour Deposition

MOCVD is a method of thin-film semiconductor growth by the chemical reaction of metal-organic vapour-phase precursors. The first historical examples of CVD growth are from the late nineteenth century, when a number of patents were filed for processes to produce lamp filaments. However, it wasn't until the 1960s that interest in the use of metal-organic precursors developed, specifically for the production of III-V semiconductor materials [80].

The chemical processes by which CVD occurs can be simplified into a number

of key steps, as illustrated in Figure 3.1:

1. Precursor molecules are evaporated and transported into the reaction chamber.
2. Gas-phase reactions of precursors in the reaction chamber.
3. Transport of reactants to the substrate surface.
4. Adsorption of reactants to the substrate surface.
5. Diffusion along the surface to energetically favourable (e.g. nucleation) sites, leading to thin-film growth.
6. Desorption of gaseous reaction products and their removal, along with non-reacted precursor molecules.

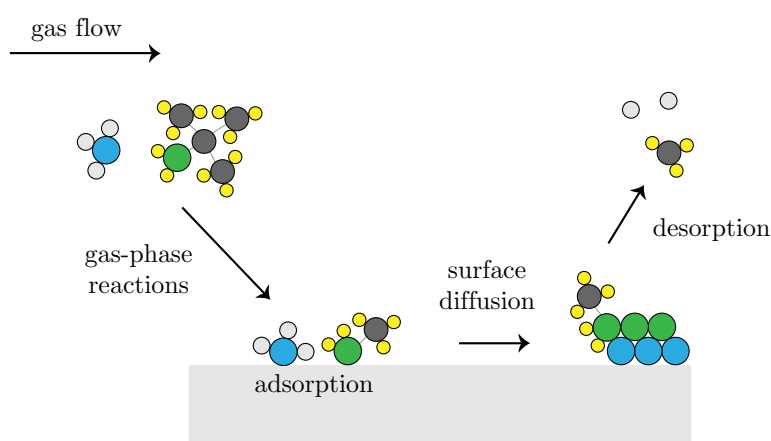


**Figure 3.1:** Schematic representation of the key metal-organic chemical vapour deposition (MOCVD) processes. Precursor molecules undergo gas-phase reactions as they are transported to the surface, where they are adsorbed and diffuse to energetically favourable sites, before the desorption of reaction products.

The rate at which thin-film growth proceeds is dependent on the temperature of the substrate, the pressure of the reaction chamber and the chemistry of the gas phase. This complex set of parameters means growth by MOCVD is more difficult to control than, for example, molecular beam epitaxy. The samples studied in this work were grown at Technische Universität Berlin by metal-organic vapour phase epitaxy (MOVPE), an MOCVD process that produces single-crystal (epitaxial) layers. The precursors of tertiarybutylarsine ( $C_4H_{11}As$ , for As), trimethylgallium ( $Ga(CH_3)_3$ , for Ga) and trimethylindium ( $In(CH_3)_3$ , for In) were used to grow GaAs and InAs.

A major consideration in MOCVD processes is that these precursors and the subsequent exhaust gases are often highly toxic.

Figure 3.2 shows a simplified MOCVD setup, consisting of precursor sources, a gas handling system to control the input of precursors, a reaction chamber and an exhaust system to remove waste products. The precursors are contained in stainless steel temperature-controlled “bubblers” and transport into the reaction chamber is controlled by passing an inert carrier gas (such as  $H_2$ , Ar or  $N_2$ ) through the bubblers. The substrate sits on a susceptor to control the substrate temperature. The reaction zone is held at the desired pressure, which, along with the temperature, is chosen according to what is being grown. The exhaust removes toxic gases for further processing into liquid or solid wastes for safe disposal.

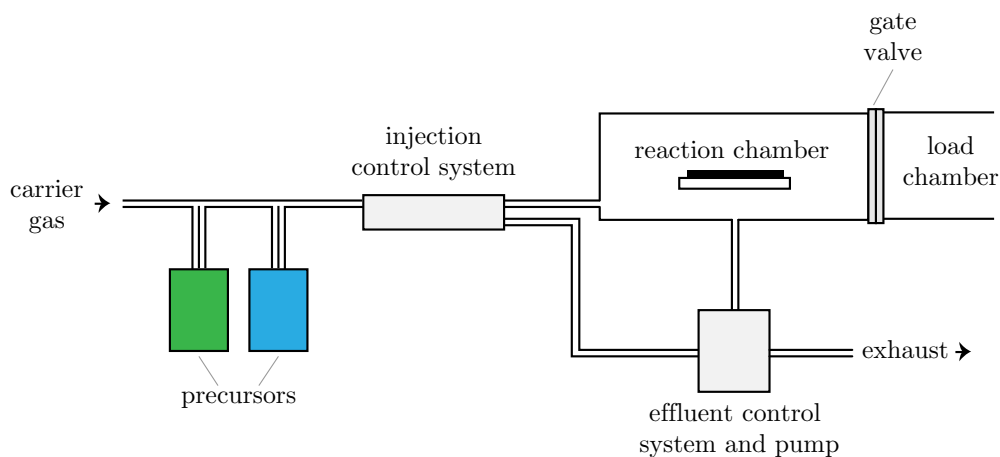


**Figure 3.2:** Simplified MOCVD system. Precursors are carried to the reaction chamber by an inert carrier gas, via an injection control system. Reaction products are transported away by an effluent control system.

## 3.2 Cross-Sectional Scanning Tunnelling Microscopy

STM is an incredibly powerful tool for imaging surfaces with atom-level resolution. It was invented by Gerd Binnig and Heinrich Rohrer (IBM) in 1981 and they were subsequently awarded the 1986 Nobel Prize in Physics for their achievement [81]. Resolutions down to hundredths of a nanometre are common, though such accuracy comes at the cost of additional challenges in ensuring clean samples, sharp tips and minimising external vibrations.

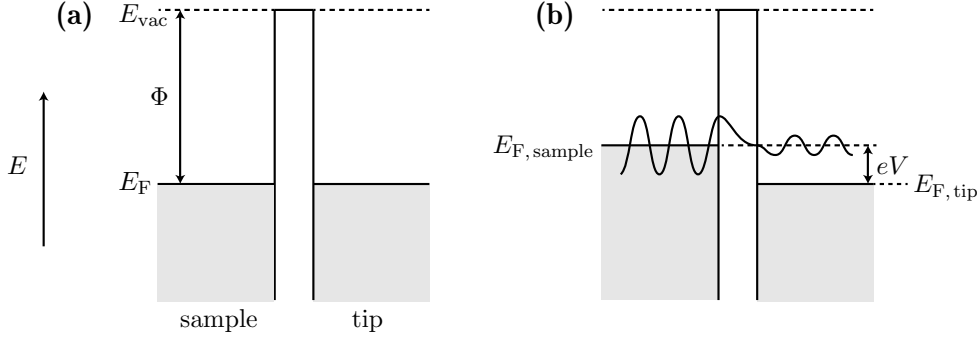


**Figure 3.3:** Schematic representation of tunnelling in scanning tunnelling microscopy (STM) devices, showing the Fermi level  $E_F$ , vacuum energy level  $E_{vac}$  and the difference between them (the work function)  $\Phi = E_{vac} - E_F$ . **(a)** With zero bias, the Fermi level of the sample and tip are the same. **(b)** With a bias applied, the sample's Fermi level is raised with respect to the tip's. Empty states now exist in the tip and the tunnelling of electrons through the potential barrier (represented in the diagram by the electron wave function) results in a tunnelling current.

The technique relies on the quantum phenomenon of tunnelling, whereby a particle *tunnels* through a potential barrier that would classically be forbidden (Figure 3.3). In STM, electrons tunnel between a conducting tip and the sample, the gap between the two being the potential barrier. The tip is brought to within fractions of a nanometre (0.4 to 0.7 nm) of the sample using piezoelectric transducers<sup>1</sup>, so that electron wave functions in the tip and sample overlap. A bias potential is applied to the tip, resulting in a tunnelling current as electrons tunnel across the gap, with the direction they tunnel determined by the direction of the bias.

As the tip is moved across the surface, changes in the tip–sample distance and the local density of states causes changes to the tunnelling current. This dependence of tunnelling current on distance is strong enough that single-atom imaging is easily achievable. If the current is held constant by adjusting the height of the tip (via a feedback loop), the tip follows a contour of constant local density of states, and hence for the atoms of the same type, a topographical map can be obtained. Conversely, for a flat sample, any change in tip height is due to changes in the local density of states and hence in the atomic composition (different atoms have different electron densities).

As the name implies, XSTM involves the same technique as described above, but applied to the cross-section of a sample, enabling one to observe buried nanostruc-

<sup>1</sup>The application of a voltage to a piezoelectric material can make it expand or contract. Piezoelectric transducers exploit this for precision control over cantilever position by the use of three transducers perpendicular to each other.

tures such as QWs and QDs. III-V semiconductors such as GaAs are particularly suited to XSTM, for two main reasons: Cleaving to expose the (110) plane usually leaves an atomically flat surface, and; surface states in the (110) plane are usually outside of the band gap and hence STM probes bulk features and defects rather than those specific to the cleaved surface [82]. As the surfaces scanned are atomically flat, XSTM images of III-V materials provide information about atomic composition, that is, contrast in the rendered images (e.g., Figure 4.4) is an indication of composition.

The XSTM imaging in this thesis was carried out at Technische Universität Berlin.

### 3.3 Magneto-Photoluminescence

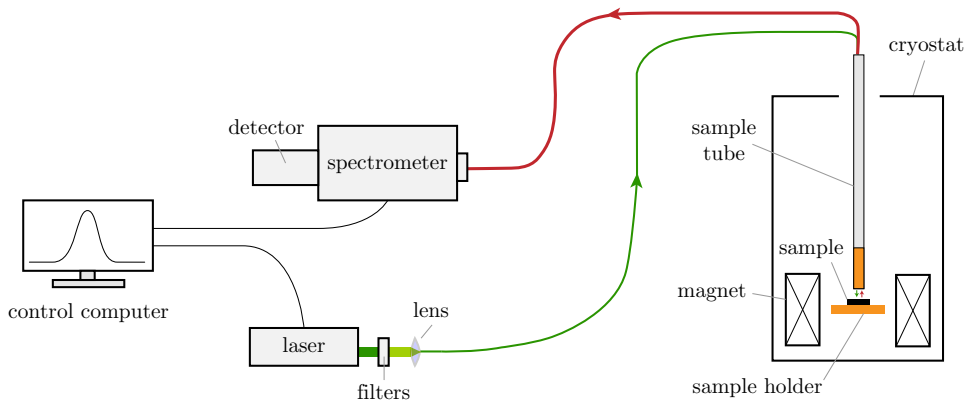


**Figure 3.4:** A simplified illustration of the magneto-PL laboratory setup. Laser light is sent down an optic fibre to the sample, and the subsequent PL emission sent via another fibre to a spectrometer, detector and finally a control computer for data analysis. The sample is mounted on the end of a tube that can be inserted into a cryostat with superconducting magnet (Section 3.3.1).

Magneto-PL measurements were obtained using the setup presented in Figure 3.4. A frequency-doubled neodymium-doped yttrium aluminium garnet solid-state laser, emitting at 1064 nm, sends excitation light down a 200- $\mu\text{m}$ -core multi-mode silica optical fibre via one or none of four neutral-density filters and a focussing lens. Each filter reduces the laser power by approximately an order of magnitude, enabling one to achieve stable powers from  $\sim 0.04$  to 700 mW. With a laser spot size on the sample of  $\sim 2$  mm in diameter, this corresponds to excitation power densities from  $2 \text{ mW cm}^{-2}$  to  $35 \text{ W cm}^{-2}$ . A beam splitter redirects a small amount of the

light to a power meter so that the power can be monitored, and a shutter is in place to block the light completely.

A second multi-mode optical fibre, with a core width of 550  $\mu\text{m}$ , transports the subsequent luminescence to a 0.3-m-focal-length Princeton Instruments diffraction grating spectrometer fitted with an Andor Technology InGaAs diode linear array, thermoelectrically cooled to  $-60^\circ\text{C}$  to reduce noise. The spectrometer uses three diffraction gratings (150, 300 and 600 lines/mm) to achieve different resolutions as it splits the continuous luminescence light into discrete wavelengths for measurement by the InGaAs array. A long pass filter is used to block out any light reflected from the laser at 532 nm.

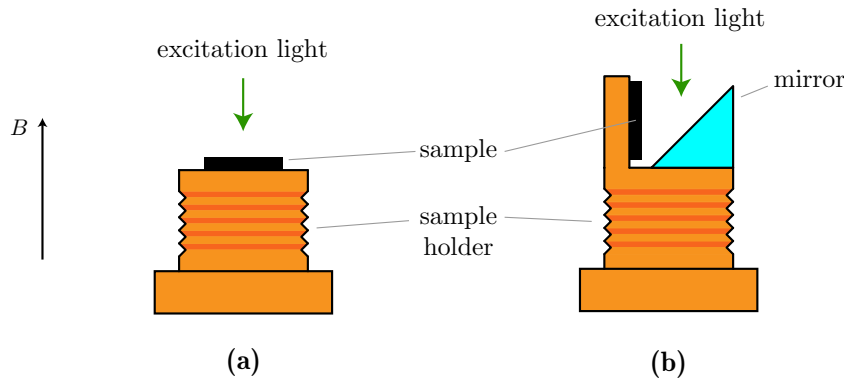


**Figure 3.5:** Brass sample holder for (a) Faraday geometry and (b) Voigt geometry measurements. The holder is screwed into the end of the sample tube through which the optical fibres pass.

Samples are glued, using electrodag, onto a small brass sample holder, which can be screwed into the end of a steel sample tube through which the optical fibres pass. Two variations of sample holder were used in this work, so that the sample could be held either parallel or perpendicular to the applied magnetic field when inserted into the cryostat (Section 3.3.1). Figure 3.5(a) shows the sample holder for Faraday geometry measurements, with the sample placed perpendicular to the field, whilst Figure 3.5(b) shows the use of a mirror to first reflect light by  $90^\circ$ , so that it strikes the sample when it is placed parallel to the field (Voigt geometry). It is important to note that, because of the use of a mirror to reflect the laser light, zero-field PL measurements in Faraday and Voigt geometry are not entirely equivalent. The mirror may have the effect of dispersing the light and in this case, the laser spot size will be large; that is, more of the sample is measured, which is particularly relevant in linewidth studies (Section 4.2.2).

The end of the sample tube is brass, to maintain thermal equilibrium between it and the sample holder, and a thermometer located close to the sample provides temperature measurements. This setup allows optical access to the sample whilst the tube is either inserted into a helium dewar, the cryostat, or simply at room temperature in the lab.

### 3.3.1 The Cryostat and Magnet

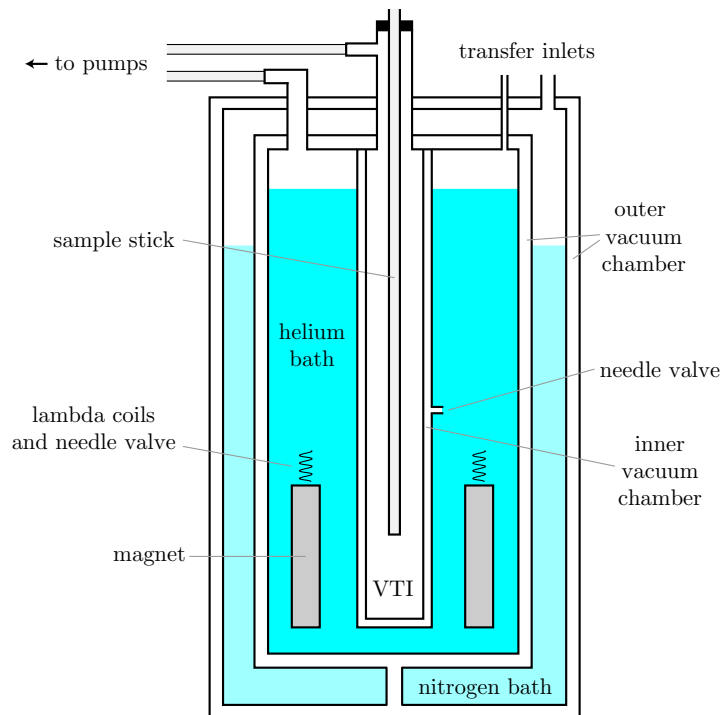


**Figure 3.6:** Simplified illustration of the cryostat used for magneto-PL measurements. Not shown is an outlet to a pump from the lambda coils so that they too can be pumped on.

Figure 3.6 shows a simplified diagram of the Oxford Instruments cryostat used for magneto-PL experiments. An outer vacuum chamber provides insulation between the lab and the helium-4 bath, aided by a liquid nitrogen jacket, which sits between two compartments of the outer vacuum chamber. When inserted using the sample tube, the sample sits in the bore of a superconducting magnet within a variable-temperature insert (VTI), which is isolated from the helium bath by an inner vacuum chamber. The vacuum chambers can be independently pumped on using a turbo pump, to pressures of  $10^{-4}$  to  $10^{-6}$  mbar.

The VTI is capable of achieving temperatures from 1.4 to 400 K, whilst at the same time, just centimetres away, the magnet is kept at a constant 4.2 K or lower.

A needle valve connects the VTI to the helium bath via a heat exchanger with integrated heater and temperature sensor, and the VTI can be pumped on through the use of a rotary vane vacuum pump. Low temperatures can be achieved by opening the needle valve to draw in helium from the helium bath whilst simultaneously pumping on the VTI. High temperatures are attained by the use of the heater. An integrated temperature controller (ITC) uses a feedback loop between the heat exchanger, the heater and the temperature sensor, controlling the heater accordingly based on the desired temperature. The needle valve and VTI pump are both controlled manually to aid the ITC in reaching this temperature. An optimal VTI pressure of around 6 to 10 mbar is a good trade-off between quick cooling and boiling off too much (expensive) helium, and this is achieved by opening the valve to the pump fully and partially opening the needle valve to let a small flow of helium into the VTI.

The magnet, a Nb<sub>3</sub>Sn solenoid manufactured by Oxford Instruments, can provide fields from 0 to  $\pm 15$  T when at 4.2 K, and up  $\pm 17$  T to when cooled below 2.2 K, the lambda point of helium-4<sup>2</sup>. These lower temperatures are achieved through the use of a lambda point refrigerator, negating the need to cool the entire helium bath to below the lambda point. A series of lambda point refrigerator coils sit above the magnet, through which liquid helium is pumped by the use of a further rotary vane pump and needle valve (in a similar fashion to the VTI). These cool down the surrounding helium in the helium bath, setting up convection currents. The colder, denser liquid convects downwards, towards the bottom of the magnet, displacing warmer liquid from around the magnet. The temperature of the magnet is monitored by two resistance thermometers, one at the top and one at the bottom of the magnet, and when the temperature is stable at 2.2 K, the magnet can be used above 15 T.

The risk of a quench is ever-present when using the magnet. A quench can occur when part of the superconducting coil ceases to be superconducting (and therefore becomes resistive), usually due to excessively high fields or changing the field strength too fast. This subjects that particular part of the magnet to rapid resistive heating, which in turn raises the temperature of the surrounding regions,

---

<sup>2</sup>The lambda point of helium is the temperature below which normal fluid helium I transitions to superfluid helium II.

causing a chain reaction which soon sees the entire magnet entering the normal state. A potentially dangerous consequence of this is the rapid boil-off of the surrounding liquid helium, filling the lab with gaseous helium, asphyxiating any users not quick enough to realise what is going on. As such (as the author well knows to his own detriment!), care must be taken to set suitably slow sweep rates, especially when using the magnet above 15 T. An oxygen alarm and extraction system is present in the lab for this reason.

A number of specially designed LabView interfaces are implemented on a control computer for operation of the entire laboratory setup, making instrument control and data acquisition a seamless operation.

### 3.4 Time-Resolved Photoluminescence

TRPL measurements were taken at room temperature, using a PicoQuant FluoTime 300 optical setup. This automated and modular system contains the integrated optics and electronics for recording time-resolved or steady-state PL, and can be used in conjunction with a variety of excitation lasers and optical detectors. For our measurements, excitation light was provided by a 640-nm PicoQuant Picosecond pulsed diode laser head operating at a 40 MHz repetition rate and capable of pulse widths of less than 90 ps (full-width half-maximum). The resultant PL light was then measured using a Hamamatsu near-infrared photomultiplier tube in the spectral range of 950 to 1400 nm. Samples were mounted, using electrodag, onto glass slides for ease of insertion into and removal from the TRPL system.

TRPL measurements were performed via time-correlated single-photon counting (TCSPC), a common technique for measuring carrier lifetimes on sub-nanosecond time scales. A complete description of the complex TCSPC system employed by PicoQuant in their optical setup is beyond the scope of this thesis, and instead the author prefers to present a description of a simplified TCSPC system, which is more than sufficient in the context of this work. A full description of PicoQuant's TCSPC system can be found in [Reference 83](#).

The basic processes involved in TCSPC are illustrated in [Figure 3.7](#). The pulse of excitation light from the laser diode is split so that part of it hits the sample and

part of it, a synchronisation signal, bypasses the sample and goes straight to a time-to-amplitude (TAC) converter. PL emission from the sample passes firstly through a monochromator (to select the desired wavelength), followed by the photomultiplier tube (PMT) to detect and amplify the signal. These electronic pulses from the PMT often have different amplitudes but the same rise times, meaning conventional threshold triggering, whereby a timing signal is triggered at a certain voltage threshold, would result in a dependence of the timing signal on the original pulse's amplitude (Figure 3.8(a)). This is obviously undesirable for systems reliant on precise timing information, and so instead, a constant-fraction discriminator (CFD) is used, triggering the timing signal at a constant fraction of the pulse width, which for pulses from the PMT will yield a timing signal independent of pulse amplitudes (Figure 3.8(b)). As such, this also allows the CFD to be used to set a lower amplitude limit to suppress background noise. A CFD is typically implemented by the comparison of the original detector signal with an amplified, inverted and delayed version of itself, such that the signal derived from this comparison changes its polarity at a constant fraction of the detector pulse height.

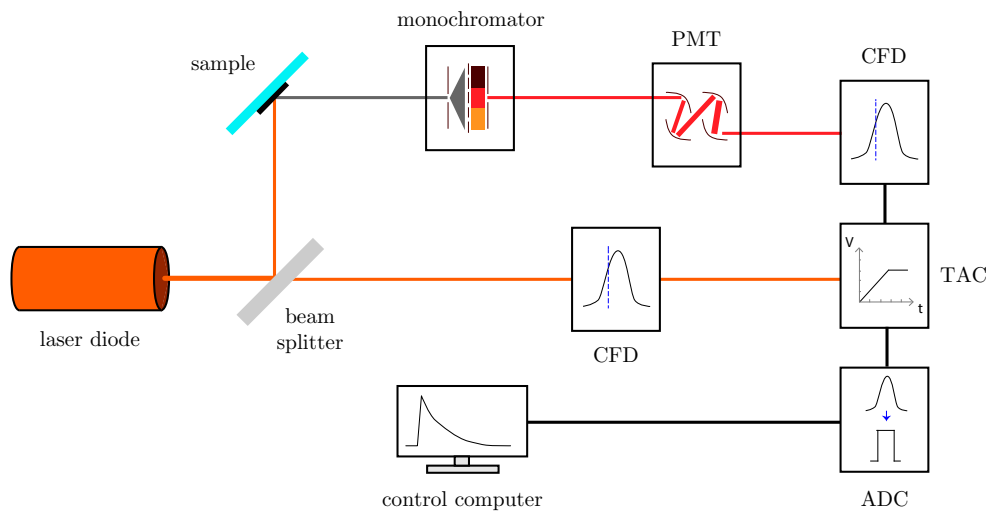


**Figure 3.7:** Simplification of the time-correlated single-photon counting (TCSPC) method used to take time-resolved PL (TRPL) measurements. Light from a laser diode is split so part of it hits the sample and part travels to a time-to-amplitude converter (TAC) via a constant-fraction discriminator (CFD). The PL emission from the sample passes through a monochromator, photomultiplier tube (PMT) and a CFD before reaching the TAC. The timing signal from the TAC then passes through an analogue-to-digital converter (ADC) before finally reaching a control computer for analysis.

The signal from the CFD then arrives at the same TAC as the synchronisation

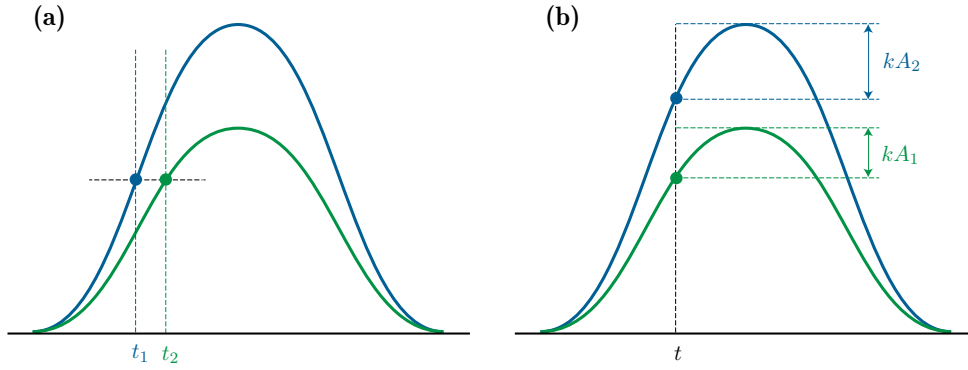


**Figure 3.8:** (a) Threshold triggering. A timing signal is triggered at time  $t$ , when the peak reaches a certain voltage threshold, resulting in a dependence of the timing signal on the peak amplitude. (b) Constant-fraction discrimination. Here, the timing signal is triggered at a constant fraction  $k$  of the peak's amplitude  $A$ .

signal. The TAC is essentially a capacitor that is linearly charged when one signal reaches it, and held at whatever voltage it has been charged to whenever a second signal reaches it (Figure 3.9). To this effect, the initial synchronisation signal starts the linear charging, and the PL signal stops it at a voltage proportional to the time difference between the two signals. Thus, the longer the excited electron takes to decay from its excited state to the ground state, the higher the voltage. This voltage is then fed into an analogue-to-digital converter, which gives the time value to be passed, via a histogrammer, to a control computer. This process is repeated numerous times until a delay curve representing the full range of individual delays between excitation laser pulse and PL emission is obtained, from which one can obtain a value for the average decay rate.

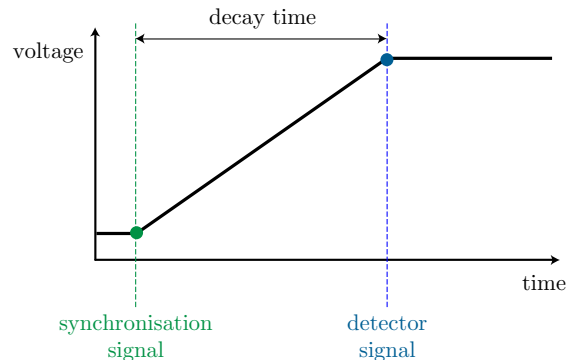


**Figure 3.9:** The process by which the TAC operates. The first signal initiates linear charging of a capacitor and the second signal stops this charging at a voltage proportional to the time difference between these signals. When applied to TCSPC systems, the first signal is the synchronisation signal from the laser, the second is from the detector after PL emission has occurred, and the time difference between these is the decay time of the particular photon detected.

PicoQuant distribute their own *EasyTau* software for complete user-friendly control of and data collection from the TRPL system.

## 3.5 Theoretical Modelling

The experimental work in this thesis is complemented by mathematical modelling of band alignments, quantised energy levels and charge-carrier flow. Two software packages are utilised: COMSOL Multiphysics [84] and nextnano [14]. In the former, the one-band Schrödinger equation in the effective-mass approximation is solved by the use of a coefficient-form partial-differential-equation (PDE) solver, whilst in the later, a multi-band  $\mathbf{k} \cdot \mathbf{p}$  Schrödinger solver is employed self-consistently with the Poisson and drift–diffusion equations for modelling of the electronic structure (under bias) and current density close to equilibrium. Further eight-band  $\mathbf{k} \cdot \mathbf{p}$  calculations in conjunction with a self-consistent Hartree approach were carried out at Technische Universität Berlin, taking into account strain, piezoelectricity and the Coulomb interaction.

Here will be presented a brief overview of the theory behind these models and the practicalities of their implementation in the software packages used, whilst a full mathematical description is left to the many texts available on the subject, for example, [References 85](#) and [86](#).

### 3.5.1 A Very Brief Introduction to Quantum Mechanics

The wave function  $\Psi$  encompasses all possible information about a given quantum system, such as a particle, atom or molecule. For example, the probability amplitude of a single-particle wave function in position-space gives the probability density  $\rho(\mathbf{r}, t)$  of finding that particle at a given position  $\mathbf{r}$ , at time  $t$  [87]:

$$\rho(\mathbf{r}, t) = |\Psi(\mathbf{r}, t)|^2. \quad (3.1)$$

The Schrödinger equation is a PDE that describes how the wave function of a physical system evolves over time, and as such can be used to compute the energy states within a quantum structure. In its time-dependent form, it is given by [87]:

$$i\hbar \frac{\partial}{\partial t} \Psi(\mathbf{r}, t) = \hat{\mathbf{H}} \Psi(\mathbf{r}, t), \quad (3.2)$$

where  $\hat{\mathbf{H}}$  is the Hamiltonian operator, which characterises the total energy of any given system; that is, it is the sum of a system's kinetic energy  $\hat{\mathbf{K}}$  and potential energy  $\hat{\mathbf{V}}$ :  $\hat{\mathbf{H}} \equiv \hat{\mathbf{K}} + \hat{\mathbf{V}}$ . Of particular relevance for charged particles in a semiconductor is the single–non-relativistic–particle Hamiltonian:

$$\hat{\mathbf{H}} = -\frac{\hbar^2}{2\mu} \nabla^2 + V(\mathbf{r}, t), \quad (3.3)$$

where  $\mu$  is the particle's reduced mass.

### 3.5.2 Numerical Analysis

Obtaining an exact solution for a PDE is not always possible and instead a solution has to be approximated by a numerical method. These work on the basis of splitting the domain of the function we want to solve for into a discrete set of function values that approximate the initial function at a given point. This partition of the domain into subdomains is called a *mesh* or *grid*. The finite difference method (FDM) and finite element method (FEM) are two such numerical methods that work in discretely different ways (no pun intended!) [88]:

**FDM** The derivative of a function  $f(x)$  is defined by:

$$\frac{\partial f(x)}{\partial x} = \lim_{h \rightarrow 0} \frac{f(x+h) - f(x)}{h}. \quad (3.4)$$

Thus, for small  $h$ :  $\partial f/\partial x \approx (f(x+h) - f(x))/h$ . If the lines on our mesh are separated by  $h$ , we can use this approximation to solve the PDE at each point on the mesh. Making the mesh finer increases the accuracy by decreasing  $h$ .

**FEM** Whilst FDM uses the differential form of the equation(s) we are solving, FEM uses the integral form, making it more suitable to discontinuities. A trial function is fitted to the PDE and weighted according to its error. This can then be minimised (integrated and set equal to zero), eliminating any spatial derivatives from the PDE and

thus approximating it locally as either a set of algebraic equations (steady state problems) or ordinary differential equations (transient problems). This can then be solved using appropriate numeric methods and a global system of equations is obtained through coordinate transformation.

FDM has the advantage over FEM that it is generally easier to implement and computationally quicker. FEM is much better at handling complex geometries (that are not easily split into a rectilinear grid), but can be computationally heavy for non-linear PDEs. COMSOL Multiphysics solves PDEs using FEM, whilst `nextnano` uses FDM.

### 3.5.3 COMSOL Multiphysics

COMSOL Multiphysics includes a coefficient-form PDE solver that solves the PDE given in [Equation 3.5](#), given the input of the coefficients  $c$ ,  $\alpha$ ,  $\gamma$ ,  $a$ ,  $\beta$  and  $d_a$  [89, 90]:

$$\nabla \cdot (-c\nabla u - \alpha u + \gamma) + au + \beta \cdot \nabla u = d_a \lambda u \quad (3.5)$$

where  $u$  is an eigenfunction and  $\lambda$  is the corresponding eigenvalue.

We can rearrange the one-band Schrödinger equation in the effective-mass approximation to this form to be solved by COMSOL, enabling us to obtain a value for the energy states of an electron in the conduction band (or a hole in the valence band). In doing so, we are making the assumption that there is no interaction between electrons and holes. As we are interested in the *stationary* states of an electron, we can use the time-independent Schrödinger equation,  $E\psi = \hat{\mathbf{H}}\psi$ —note the use of lowercase  $\psi$  to denote its time-independence—with the Hamiltonian given in [Equation 3.3](#):

$$E\psi(\mathbf{r}) = \left( -\frac{\hbar^2}{2m_e^*} \nabla^2 + V(\mathbf{r}) \right) \psi(\mathbf{r}), \quad (3.6)$$

where  $E$  is the energy eigenvalue and  $m_e^*$  is the electron effective mass. The hole effective mass  $m_h^*$  could of course be used instead if we were interested in the valence band. We have also removed the time-dependence of  $V$ .

Let's take the example of an InAs QD in GaAs: QDs usually have relatively cylindrical bases, so choosing a cylindrical coordinate system makes sense. We can rewrite the wave function in cylindrical coordinates:  $\psi(\mathbf{r}) = \chi(z, r)\Theta(\varphi)$ , where  $z$  is the height (i.e., the growth direction),  $r$  the radius, and  $\varphi$  the azimuthal angle. Expressing the Schrödinger equation in cylindrical coordinates:

$$E\chi\Theta = -\frac{\hbar^2}{2} \left[ \frac{\partial}{\partial z} \left( \frac{1}{m_e^*} \frac{\partial \chi}{\partial z} \right) + \frac{1}{r} \frac{\partial}{\partial r} \left( \frac{r}{m_e^*} \frac{\partial \chi}{\partial r} \right) \right] \Theta - \frac{\hbar^2}{2} \frac{\chi}{m_e^* r^2} \frac{d^2 \Theta}{d\varphi^2} + V\chi\Theta. \quad (3.7)$$

We can separate this into two independent equations by introducing the variable  $n$ , one dependent only on  $\varphi$ , and the other on  $z$  and  $r$ . Dividing [Equation 3.7](#) by  $(\chi(z, r)/m_e^* r^2)\Theta(\varphi)$  and rearranging, we obtain

$$\frac{1}{\Theta} \frac{d^2 \Theta}{d\varphi^2} = -n^2 \quad (3.8)$$

and

$$-m_e^* r^2 \frac{\hbar^2}{2\chi} \left[ \frac{\partial}{\partial z} \left( \frac{1}{m_e^*} \frac{\partial \chi}{\partial z} \right) + \frac{1}{r} \frac{\partial}{\partial r} \left( \frac{r}{m_e^*} \frac{\partial \chi}{\partial r} \right) \right] + m_e^* r^2 (V - E) = -\frac{\hbar^2 n^2}{2}, \quad (3.9)$$

[Equation 3.8](#) has solutions of the form  $\Theta = \exp(in\varphi)$ , implying that  $n$  must be an integer (as  $\Theta(\varphi + 2\pi) = \Theta(\varphi)$ ), and it transpires that it is the principal quantum number. Finally, we can rewrite [Equation 3.9](#) in the coefficient form:

$$-\frac{\hbar^2}{2} \left[ \frac{\partial}{\partial z} \left( \frac{1}{m_e^*} \frac{\partial \chi_n}{\partial z} \right) + \frac{1}{r} \frac{\partial}{\partial r} \left( \frac{r}{m_e^*} \frac{\partial \chi_n}{\partial r} \right) \right] + \left( \frac{\hbar^2 n^2}{2m_e^* r^2} + V \right) \chi_n = E_n \chi_n \quad n \in \mathbb{Z}, \quad (3.10)$$

Thus, the coefficients in [Equation 3.5](#) are:

$$c = \frac{\hbar^2}{2m_e^*} \quad (3.11)$$

$$a = \frac{\hbar^2 n^2}{2m_e^* r^2} + V \quad (3.12)$$

$$\beta_r = -\frac{\hbar^2}{2m_e^* r} \quad (3.13)$$

$$d_a = 1 \quad (3.14)$$

$$\alpha = \beta_z = \gamma = 0 \quad (3.15)$$

and  $\lambda = E_n$ .

COMSOL's interface allows us to create different domains and input these coefficients for each domain separately. In our case, these domains are the different semiconductor materials, which have different effective masses and band alignments.  $V$  represents the potential of the band edge and we are free to arbitrarily choose where  $V = 0$  is set. The energy eigenvalue obtained as the solution will also be relative to that level, and therefore when simulating QDs, it is useful to set  $V = 0$  as the band edge in the QD. Similarly, how many dimensions we solve the problem in is also our choice. A 1D simulation is too limited if we want to give the QD some shape (for example, a pyramid), whilst 3D is unnecessary if we approximate the QD as having a symmetrical base, so choosing 2D makes sense.

Finally, we must specify any boundary conditions. COMSOL gives us a choice of boundary condition types and that most suitable to our application is the *Dirichlet boundary condition*, which enables us to specify a value that the *solution* needs to take at the given boundary. If we assume that electrons can't travel outside of our simulation region, their wave functions must vanish at the boundary and thus our Dirichlet boundary condition is that the solution vanishes.

COMSOL discretises our simulation region for us (though we can choose to do so ourselves, if we wish), and so all we are left to do is choose how many eigenvalues to calculate, and then run the simulation.

### 3.5.4 nextnano

Whereas COMSOL provides a user-friendly interface for all manner of physics simulations, but doesn't contain an in-house Schrödinger solver—and thus we had to manipulate the Schrödinger equation into coefficient-form to be solved by the program—next**nano** is designed specifically for simulating semiconductor nanostructures and as such, most of the underlying mathematics is hidden away. Nonetheless, it is important to at least understand the principle of how any problem is being solved, and so here will be presented a summary of the models employed and the scheme in which next**nano** solves them. The information regarding the computational schemes of the program is accurate to the author's best knowledge, based on documentation on next**nano**'s website [14] and [Reference 91](#)<sup>3</sup>. Two versions of the program exist that are discreetly different in their capabilities; next**nano**<sup>3</sup> and next**nano**++, the former written in Fortran and the latter in C++. It is the latter that is used herein, mainly because it was found to be computationally quicker. Both of these are console applications that run via the command line, using a text-based input file, but a convenient graphical user interface next**nanomat** is provided for generating input files and visualising results. Both versions of the program include an extensive material database with referenced material parameters, though the user is of course free to specify their own parameters. [Table 3.1](#) summarises the input data required by next**nano**, and the data output after the program has been run.

#### Computational Scheme

Before we go on to discuss the models next**nano** uses, it is useful to give an overview of the computational scheme the program follows:

- Input file is processed, material parameters obtained from the database and the structure that is specified is mapped to the mesh.
- Strain is calculated and band edges positioned accordingly.

---

<sup>3</sup>It should be pointed out that the online documentation and [Reference 91](#) aren't completely compatible, as they describe different versions of the code. Indeed, it is likely that they both describe a different version of the code than used for simulations in this thesis as they are both a number of years old. Therefore, it is probably best to treat this section as an illustrative example rather than a definitive description.

**Table 3.1:** Summary of the input data and subsequent calculation output data for nextnano.

Input	Output
Simulation dimension (1D, 2D or 3D)	Band Structure
Structure, materials and doping	Strain
Mesh structure	Piezoelectric and pyroelectric charge
Strain model to be used	Electron/hole densities
Contacts and applied bias	Electrostatic potential
Regions to be solved quantum-mechanically	Wave functions
Output that is desired	Current

- Eight-band  $\mathbf{k} \cdot \mathbf{p}$  Schrödinger equation, Poisson equation and drift–diffusion equations are solved self-consistently:
  - Built-in potential calculated for zero applied bias by solving Schrödinger and Poisson equations self-consistently.
  - Potentials (Fermi level and potential at contacts) shifted according to applied bias.
  - Quasi–Fermi levels calculated from drift–diffusion and current continuity equations, keeping the wave functions and potential fixed.
  - Carrier densities and potentials are calculated self-consistently from the Schrödinger and Poisson equations, whilst the quasi–Fermi levels are fixed.

## Strain

Strain within a semiconductor heterostructure can have a large impact on its electronic structure, including the creation of a piezoelectric fields, shifting of the band edges and altering the  $\mathbf{k} \cdot \mathbf{p}$  Hamiltonian. nextnano calculates strain prior to and independently of the Schrödinger, Poisson and drift–diffusion equations. Whilst this approach is suitable for most structures, certain wurtzite crystals (e.g., nitrides) have strong pyroelectric fields and thus self-consistent solving of the strain and Poisson equations may be required. The strain tensor  $\epsilon$  is calculated numerically by minimising the elastic energy, details of which can be found in [Reference 91](#). Alternatively,

the user can choose for strain to be calculated analytically for either 1D structures or 2D/3D structures with uniform layers along the growth direction. This is possible due to the fact that the strain-tensor components parallel to the substrate plane for cubic crystals are given by the lattice mismatch [91]:

$$\epsilon_{\parallel} = \frac{a_{\text{substrate}} - a_{\text{layer}}}{a_{\text{layer}}}, \quad (3.16)$$

where  $a_{\text{substrate}}$  and  $a_{\text{layer}}$  are the lattice constants of the substrate and layer materials, respectively. It is also possible for the user to input their own strain tensor. In this work, the approach of calculating strain numerically by minimising the elastic energy was employed.

### Eight-band $\mathbf{k} \cdot \mathbf{p}$ Modelling

The multi-band  $\mathbf{k} \cdot \mathbf{p}$  model is one of many electronic structure models, popular due to its balance between accuracy and computational time. Eight-band  $\mathbf{k} \cdot \mathbf{p}$  models employ  $\mathbf{k} \cdot \mathbf{p}$  calculations to solve for the conduction, light hole, heavy hole and spin-orbit bands, each one of which is two-fold spin degenerate (hence, eight bands). Many different  $\mathbf{k} \cdot \mathbf{p}$  models exist, differing mainly in the number of bands considered and their treatment of strain and the spin-orbit interaction. `nextnano` utilises an eight-band model similar to [Reference 92](#).

Multi-band  $\mathbf{k} \cdot \mathbf{p}$  modelling uses the fact that, in a crystal, atom nuclei form a periodic potential with the same period as the crystal lattice, and thus electron wave functions must also be periodic. We can use *Bloch's theorem* to approximate the wave function as a product of a the function  $u_{\mathbf{k}}(\mathbf{r})$ , which describes the periodic potential from the atoms, and  $e^{i\mathbf{k}\cdot\mathbf{r}}$ , which represents the electron plane waves:

$$\psi_{n,\mathbf{k}} = e^{i\mathbf{k}\cdot\mathbf{r}} u_{n,\mathbf{k}}(\mathbf{r}) \quad (3.17)$$

This is demonstrated schematically in [Figure 3.10](#). We can substitute the Bloch wave functions into the one-band Schrödinger equation given in [Equation 3.6](#) and use the momentum operator  $\hat{\mathbf{p}} = -i\hbar\nabla$  as so:

$$\left( \frac{\hat{\mathbf{p}}^2}{2m} + V(\mathbf{r}) \right) e^{i\mathbf{k}\cdot\mathbf{r}} u_{n,\mathbf{k}}(\mathbf{r}) = E_n(\mathbf{k}) e^{i\mathbf{k}\cdot\mathbf{r}} u_{n,\mathbf{k}}(\mathbf{r}). \quad (3.18)$$

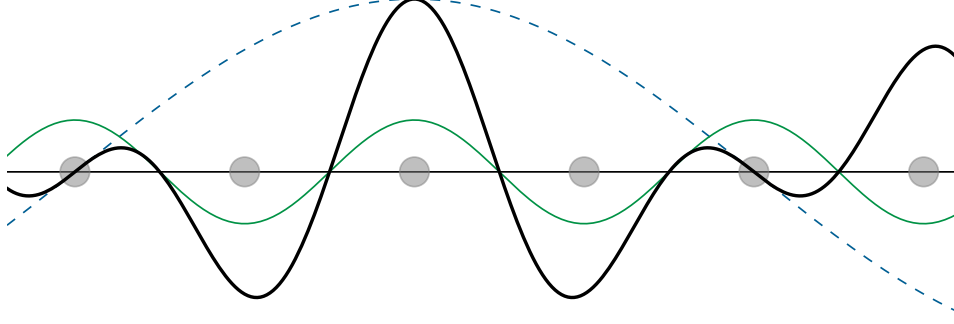


**Figure 3.10:** Schematic representation of the real part of a Bloch wave in 1D,  $\psi_{n,k} = e^{ikx}u_{n,k}(x)$  (black solid line), for an arbitrary Bloch function  $u_{n,k}(x) = \frac{1}{3} \cos(4\pi x)$  (green solid line) and plane wave  $e^{ikx}$  (blue dashed line). Adapted from [Reference 10](#).

Note that the mass  $m$  is now not specifically the electron effective mass. Using the chain rule and subsequently cancelling out the plane-wave term  $e^{i\mathbf{k}\cdot\mathbf{r}}$ , we obtain a modified Schrödinger-like equation:

$$\left( \frac{\hat{\mathbf{p}}^2}{2m} + V(\mathbf{r}) + \frac{\hbar^2 k^2}{2m} + \frac{\hbar}{m} \mathbf{k} \cdot \hat{\mathbf{p}} \right) u_{n,\mathbf{k}}(\mathbf{r}) = E_n(\mathbf{k})u_{n,\mathbf{k}}(\mathbf{r}). \quad (3.19)$$

The  $\mathbf{k} \cdot \hat{\mathbf{p}}$  term is where the name  $\mathbf{k} \cdot \mathbf{p}$  theory originates from. Our Hamiltonian now includes two extra terms. If  $\hat{\mathbf{H}}_0$  was the original Hamiltonian and  $\hat{\mathbf{H}}'_\mathbf{k}$  represents the extra two terms, then the Schrödinger-like [Equation 3.19](#) reads:

$$(\hat{\mathbf{H}}_0 + \hat{\mathbf{H}}'_\mathbf{k})u_{n,\mathbf{k}} = E_n(\mathbf{k})u_{n,\mathbf{k}}(\mathbf{r}). \quad (3.20)$$

We can add a final term  $\hat{\mathbf{H}}_{\text{so}}$  to account for the spin-orbit interaction,

$$\hat{\mathbf{H}}_{\text{so}} = \frac{\hbar^2}{4m^2c^2} (\nabla V \times \hat{\mathbf{p}}) \cdot \vec{\sigma}, \quad (3.21)$$

where  $\vec{\sigma}$  is a vector of the Pauli matrices,  $\sigma = (\sigma_1, \sigma_2, \sigma_3)^T$ , and

$$\sigma_1 = \begin{pmatrix} 0 & 1 \\ 1 & 0 \end{pmatrix}, \quad \sigma_2 = \begin{pmatrix} 0 & -i \\ i & 0 \end{pmatrix} \quad \text{and} \quad \sigma_3 = \begin{pmatrix} 1 & 0 \\ 0 & -1 \end{pmatrix}. \quad (3.22)$$

Therefore, our final  $\mathbf{k} \cdot \mathbf{p}$  equation is:

$$(\hat{\mathbf{H}}_0 + \hat{\mathbf{H}}'_\mathbf{k} + \hat{\mathbf{H}}_{\text{so}})u_{n,\mathbf{k}} = E_n(\mathbf{k})u_{n,\mathbf{k}}(\mathbf{r}). \quad (3.23)$$

The general procedure is now to solve this problem at  $\mathbf{k} = 0$ , for as many bands

(denoted by  $n$ ) as desired, to obtain energy eigenvalues  $E_n(0)$  at that point, then use perturbation theory to obtain energies  $E_n(\mathbf{k})$  away from that point. Details of such a procedure can be found in many quantum mechanics textbooks and specifically with regards to  $\mathbf{k} \cdot \mathbf{p}$  theory, in, for example, [References 91](#) and [93](#). It is important to note that, unlike `nextnano`, we haven't incorporated strain into our  $\mathbf{k} \cdot \mathbf{p}$  Hamiltonian in this description.

The carrier density  $n(\mathbf{r})$  can be calculated from the wave function as follows [\[94\]](#):

$$n(\mathbf{r}) = \sum_k n_k |\Psi_n(\mathbf{r})|^2, \quad (3.24)$$

where we have introduced a new band index  $k$  to avoid confusion with the carrier density  $n$ , and  $n_k$  is the carrier density for the  $k$ th band. This is particularly relevant for solving the Schrödinger equation self-consistently with the Poisson equation, as discussed later.

## Poisson Equation

The Poisson equation is a classical (rather than quantum-mechanical) electrostatics equation that is used to describe a potential field caused by a given charge distribution:

$$\nabla \cdot (\varepsilon_0 \varepsilon_r \nabla \phi) = -\rho, \quad (3.25)$$

where  $\varepsilon_0$  is the vacuum permittivity,  $\varepsilon_r$  is the dielectric constant,  $\phi$  is the electrostatic potential and  $\rho$  is the charge density distribution, which can in turn be given by:

$$\rho = e(-n + p + N_d^+ - N_a^- + \rho_{\text{fixed}}), \quad (3.26)$$

where  $n$  and  $p$  are the electron and hole densities, respectively,  $N_d^+$  and  $N_a^-$  are the *ionised* donor and acceptor dopant concentrations and  $\rho_{\text{fixed}}$  is the charge density due to any fixed charges, for example, piezoelectric or pyroelectric charges (which can be input by the user). Note that it is the ionised donor and acceptor concentrations that are used, which require the input of an *ionisation energy*, defined as the distance from the band edge to the dopant energy level:

$$E_d^{\text{ion}} = E_d - E_c \quad \text{for donors,} \quad (3.27)$$

$$E_a^{\text{ion}} = E_a - E_v \quad \text{for acceptors.} \quad (3.28)$$

We can assume that all dopant atoms are ionised, which may be the case at room temperature, by setting the ionisation to a “cheat” parameter of, for example,  $-1000$  eV. The ionised dopant concentrations can be calculated by summing over all donors/acceptors  $i$  (which can for simplicity be assumed to have the same energy):

$$N_d^+ = \sum_i \frac{N_{d,i}}{1 + g_{d,i} \exp \frac{E_{F,n} - E_{d,i}}{k_B T}} \quad \text{and} \quad (3.29)$$

$$N_a^- = \sum_i \frac{N_{a,i}}{1 + g_{a,i} \exp \frac{E_{a,i} - E_{F,p}}{k_B T}}, \quad (3.30)$$

where  $E_{F,n}$  and  $E_{F,p}$  are the electron and hole quasi-Fermi levels.  $g_{d,i}$  and  $g_{a,i}$  are dopant degeneracy levels, which are dependent on the occupation of outer orbitals (e.g., an outer  $s$  orbital that is occupied by one electron is two-fold degenerate, when accounting for spin). These can be set by the user, or by default are  $g_{d,i} = 2$  and  $g_{a,i} = 4$ .

In **nextnano**, the Poisson equation is solved numerically by Newton’s method, details of which can be found in most mathematics textbooks. The choice of boundary conditions is handled by the program and depends on whether a bias is applied or not (i.e., we are in equilibrium or non-equilibrium). For non-equilibrium situations, such as in the presence of a Schottky junction, the equilibrium (built-in) potential is first calculated using Neumann boundary conditions (that state the electric field vanishes at the boundaries,  $\partial\phi/\partial x = 0$ ), before Dirichlet boundary conditions are used to fix the field at the boundaries, taking into account the built-in potential.

Though it is omitted in the above equations, for brevity, there is an  $\mathbf{r}$ -dependence in the dielectric constant, electrostatic potential, charge densities, dopant densities and energy levels. This also applies to the following discussion on drift–diffusion and current continuity, where the charge mobilities and current densities also have an  $\mathbf{r}$ -dependence.

## Drift–Diffusion and Current Continuity

The link between the quasi-Fermi levels,  $E_{F,n}$  and  $E_{F,p}$ , and the carrier densities,  $n$  and  $p$ , is provided by the drift–diffusion equation, which describes how carriers move in an electric field [94]:

$$\mathbf{J}_n = en\mu_n\nabla\phi + \mu_n k_B T \nabla n = e\mu_n n \nabla E_{F,n} \quad \text{and} \quad (3.31)$$

$$\mathbf{J}_p = ep\mu_p\nabla\phi - \mu_p k_B T \nabla p = e\mu_p p \nabla E_{F,p}, \quad (3.32)$$

where  $\mathbf{J}$  is the current density and  $\mu$  is the carrier mobility. The  $\nabla\phi$  term represents the drift of carriers (in an electric field) and the  $\nabla n$  term represents the diffusion of carriers. The current continuity equation states that:

$$\nabla \cdot \mathbf{J}_n = q \left( \frac{\partial n}{\partial t} - R \right) \quad \text{and} \quad (3.33)$$

$$\nabla \cdot \mathbf{J}_p = q \left( R - \frac{\partial p}{\partial t} \right). \quad (3.34)$$

Here,  $R$  is the recombination rate, which is positive for the generation and negative for the recombination of carriers. If we assume that no generation or recombination is occurring ( $R = 0$ ) and we are in a stationary state ( $\partial n/\partial t = \partial p/\partial t = 0$ ), then the current continuity simplifies to:

$$\nabla \cdot \mathbf{J} = 0. \quad (3.35)$$

We can use this to solve [Equations 3.31](#) and [3.32](#) to obtain an expression for the quasi-Fermi levels, which can then be injected into the Poisson equation, to be solved self-consistently with the Schrödinger equation.

## Self-Consistency

So far, we have talked a lot about the “self-consistent” solving of equations, without really discussing what this means. The Schrödinger and Poisson equations both have inter-dependent terms (the potential  $V(\mathbf{r})$  and the carrier density  $n(\mathbf{r})$ ) and

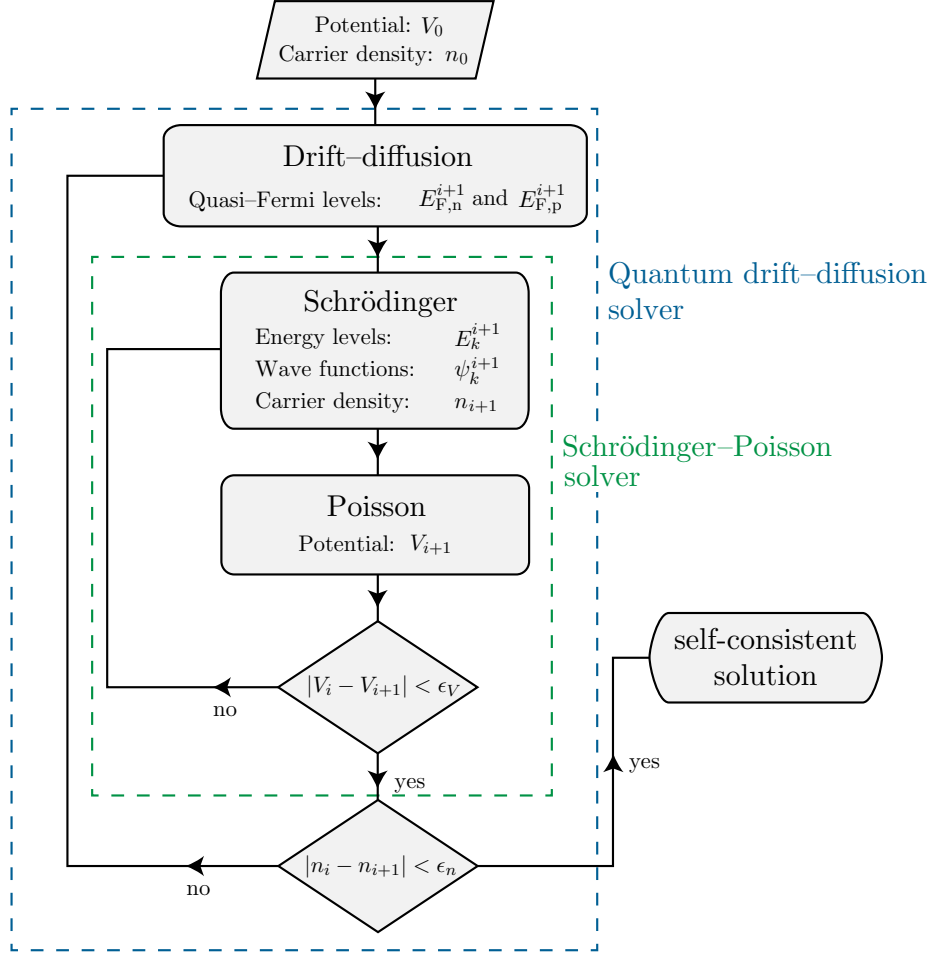


**Figure 3.11:** Flow chart of the self-consistent solving of the Schrödinger, Poisson and drift-diffusion equations, sometimes referred to as a *quantum drift-diffusion* solver. In *nextnano*, a trial potential  $V_0$  and carrier density  $n_0$  is obtained from solving the Schrödinger and Poisson equations self-consistently in equilibrium (without any applied field), to determine the built-in field.

their self-consistent solving entails using the output from one as the input to the other, iteratively, until the difference between the current and previous solutions falls below a certain limit.

More specifically, a trial potential  $V_0(\mathbf{r})$  is used to solve the Schrödinger equation,  $n(\mathbf{r})$  is then calculated (using [Equation 3.24](#)) and used in the Poisson equation to obtain a new value for the potential,  $V_1(\mathbf{r})$ , which is in turn fed back into the Schrödinger equation. This proceeds until  $|V_i(\mathbf{r}) - V_{i+1}(\mathbf{r})| < \epsilon$ , where  $\epsilon$  is some predefined limit.

Before this self-consistency loop begins, the quasi-Fermi levels are calculated from the drift-diffusion and carrier-continuity equations and fed into the Schrödinger-Poisson solver. The quasi-Fermi levels can then be recalculated by the drift-diffusion

and carrier-continuity equations, using the carrier density from the Schrödinger–Poisson solver, in turn forming another self-consistency loop. This is much easier to understand by observing the flow chart presented in [Figure 3.11](#).

This solving of the Schrödinger, Poisson and drift–diffusion equations is commonly referred to as the *quantum drift–diffusion* method in literature.



# Chapter 4

## Sub-Monolayer InAs in GaAs

This chapter concentrates on the optoelectronic study of SML depositions of InAs in GaAs. Such a growth technique has been shown to produce a QD–QW heterostructure, encompassing a lateral InGaAs QW with low In content, in which are embedded In-rich QD-like agglomerations with a wide variety of shapes and sizes.

As will be seen in [Section 4.1.4](#), lasers fabricated from SML systems have demonstrated high-speed operation and show great promise as optical interconnects for data communication applications. Our work is therefore motivated by a desire to better understand charge-carrier confinement in such complicated systems, to further aid the development and optimisation of SML optical devices.

### 4.1 Literature Review

In the following, we will discuss the use of optical devices for data communications ([Section 4.1.1](#)), the potential that VCSELs offer to this application ([Section 4.1.2](#)), the development of QD lasers ([Section 4.1.3](#)), and finally, SML systems, their atomic structure, optoelectronic characteristics and use in high-speed VCSELs ([Section 4.1.4](#)).

#### 4.1.1 Optics for Data Transmission

The use of optical fibres for telecoms has been commonplace since the end of the 20th century. Modern networks, such as the submarine data cables that carry our communications from continent to continent, enjoy transmission rates upwards of

100 Gb s<sup>-1</sup> per channel [95, 96]. Single-core single-mode fibre optic cables, which currently form the backbone of the world’s telecoms [97], have been pushed to error-free transmission rates in excess of 1 Tb s<sup>-1</sup> [98], whilst single-mode multi-core fibres have been used to transfer data at a staggering rate of 2.15 Pb s<sup>-1</sup> [99], and multi-mode multi-core fibres are set to push this up to 10 Pb s<sup>-1</sup> [100].

It is only natural that we endeavour to introduce optical interconnects on smaller and smaller length scales, replacing the copper wiring that is commonly used now. Optics are already ubiquitous in data centres [101], bringing data to the computer, and so we turn our attention to data transfer within computers; at board-to-board, chip-to-chip and on-chip levels. This transition from electrical to optical transmission is borne out of the limitations inherent in copper wiring and the fact that copper-based interconnects are ever-increasingly becoming the bottleneck to the advancement of processor development [102].

With regards to telecoms, optical fibres boast exceptionally low attenuation (losses) over long distances, allowing for >100 km stretches of optical cabling without the need for optical amplifiers (the counterpart to electronic repeaters) to boost the signal, compared with only a few kilometres for copper cabling [103, 104]. The “skin effect” in copper wire has a large effect in attenuating signals [105, 106]: Alternating current tends to become distributed mainly near the surface of a conductor and increasing the frequency amplifies this effect, such that the effective channel through which current flows is decreased at higher frequencies, thereby increasing the resistance and attenuation losses.

This frequency dependence is of relevance in the context of datacoms as the data transmission rate is directly determined by the frequency at which data is sent through the cable, and as a result copper wiring is typically limited to  $\sim 10$  Gb s<sup>-1</sup> for distances in the order of one metre [107–109]. At the shorter distances encountered within computers, the high density of interconnects and their proximity to each other causes other issues for copper wiring, such as crosstalk (whereby signals leak from one line to another, due to capacitive coupling) and high power consumption [18, 110]. The negligible frequency-dependence of attenuation and crosstalk in optical systems is due to the high frequency of light ( $\sim 10^{14}$  Hz) relative to the frequency used to send data (in the order GHz or less); increasing the data-transmission frequency

sent down optical fibres has little or no impact on the overall propagation of the light [105, 106]. Other advantages of optical interconnects include their immunity to electromagnetic interference from nearby devices, the difficulty to “tap” into optical circuits without disrupting the signal [103] and the fact that an optical system carries no electrical information about the sending and receiving circuits. The latter of these advantages provides perfect voltage isolation between the two circuits, such that high voltages or sudden power surges from one can’t damage the other, negating the need for so-called “opto-isolators” that are currently used in electronic circuitry to achieve the same effect [105, 106]. The fact that optical fibre setups are lighter weight and lower in volume is also of note.

### 4.1.2 VCSELs as Data Transmitters

A key component of any optical transmission setup is, of course, the light source that sends the signal down the optical fibre. Edge-emitting semiconductor lasers are currently the standard for telecoms applications, emitting at around 1.55  $\mu\text{m}$ , a wavelength chosen because silica, which is used to make optical fibres, has a minimum in its absorption spectrum at that point [18]. At shorter distances, losses due to absorption and dispersion aren’t such an issue, and therefore the wavelength of 850 nm has emerged as the standard for LAN and storage area network (SAN). GaAs-based lasers and photodetectors have proven to be cost effective and reliable in the past few decades, and the choice of 850 nm has been largely to match the best working wavelengths (i.e., band gap) of these devices [18, 111].

VCSELs are by far and away ruling the roost in their market share of datacoms transmitters, with GaAs-based VCSELs currently being used in 95 % of all optical networking applications below 1 km [112]. The inherent advantages to using VCSELs as opposed to edge-emitting lasers is numerous [18, 102, 112–115]: The large output aperture results in a beam with a low divergence angle and a circular profile, making for easier coupling to fibre optic cables. Because they emit from the surface, samples can be tested on-wafer, as they are fabricated, as opposed to edge-emitters that must be cleaved before testing. This, as well as their small footprint, also means that it is possible to fabricate tens of thousands of devices on a single wafer, making them not just cost-effective, but particularly useful in microprocessors, where scaling down

the size of components is crucial. Furthermore, 2D arrays of VCSELs can easily be fabricated side-by-side and driven in parallel to obtain higher output powers. The active region in VCSELs is only a fraction of the size of that in edge-emitters, meaning low threshold currents (above which lasing commences) and therefore lower power consumption. This is a key factor in circuit design, where power consumption is a large consideration. On-board and on-chip operating temperatures often reach 85 °C or higher and so it is significant that VCSELs have been shown to be reliably temperature-stable, demonstrating high speeds with low bit error rates over and above 85 °C [116, 117]. Also of note is that their emission wavelength shifts only a small amount under varying temperatures.

There is currently no standardised wavelength for transmission on length scales smaller than LAN and SAN, and 850, 980 and 1100 nm have developed as the most commonly researched. Longer wavelengths bring the advantage of deeper confining barriers and therefore less chance of non-equilibrium carrier escape, improving the temperature stability. A smaller band gap also means lower photon energies and thus lower operating voltages. 1100 nm provides the best of these advantages, but has the disadvantage of higher free-carrier losses in the AlGaAs surrounding the active region (as the absorption coefficient increases with wavelength) [18, 117]. Room-temperature transmission rates at all three wavelengths have passed the 40 Gb s<sup>-1</sup> mark, with current benchmarks of 85-°C operation being the 40 Gb s<sup>-1</sup> achieved with an 850-nm VCSEL by Westbergh et al. [118] at the Chalmers University of Technology in 2013, and more recently, the 46 Gb s<sup>-1</sup> operation of a 980-nm VCSEL by Moser et al. [119] at Technische Universität Berlin in 2015.

### 4.1.3 Quantum Dot Lasers

The advantages that VCSELs offer due to their small active regions also apply to QWs. Indeed, nowadays most VCSELs employ one or more QW as their active region. Lower threshold current, lower power consumption and better temperature stability are all brought about by the tighter confinement of electrons and holes. In addition, QWs offer a degree of wavelength-tuning capability, as their band gap is, to a degree, dependent on the well width. Notably, Chin et al. [120] and Holonyak et al. [121] found, in 1980, that moving from a conventional double-heterostructure

VCSEL to a QW VCSEL improved the temperature stability of the threshold current, attributed to the step-like nature of the QW DOS (Equation 2.11).

It stands to reason that these advantages can be enhanced by further reducing the dimensionality of the system, that is, using QDs in the active region and exploiting their  $\delta$ -like DOS (Equation 2.13) and superior wavelength-tuning capabilities. It was predicted in 1982 by Arakawa and Sakaki [122], in what has become one of the defining papers of semiconductor physics, that there would be a marked increase in temperature stability upon confining carriers in all three spatial dimensions. This was later expanded upon by Asada et al. [123] in 1986, to include a prediction of enhanced gain and lower threshold current density. These predictions were validated with numerous reports of high gain and impressive temperature stability from experimental measurements during the following decade, based almost entirely on SK QDs grown by self-assembly [124–127]. Material gain figures that showed an order-of-magnitude increase (to  $1.5 \times 10^{-5} \text{ cm}^{-1}$ ) from that seen in QW lasers, and differential gain that was three times larger ( $10^{-12} \text{ cm}^2$ ), was reported by Kirstaedter et al. [125] in 1996. This increase was attributed to size quantisation in the QDs decreasing the number of states that need to be filled to achieve a given gain [128]. A schematic representation of the band alignment and energy levels for an InAs/GaAs QD laser is shown in Figure 4.1.

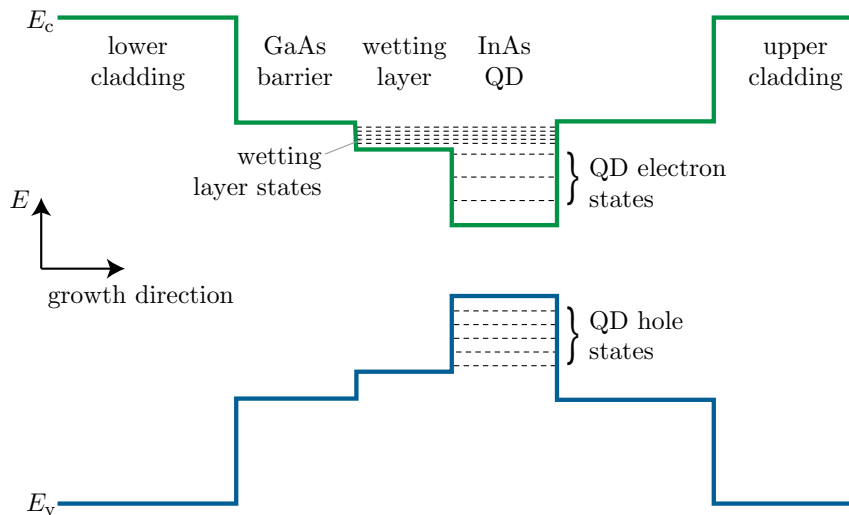


**Figure 4.1:** Representative band alignment for an InAs/GaAs QD laser. InAs Stranski–Krastanow (SK) QDs are grown in a GaAs matrix, which is surrounded by cladding to prevent the escape of carriers (for example, made of AlGaAs). QD electron and hole states are shown, as well as the wetting layer states. As holes have a higher effective mass, their energy levels are packed more closely than for the electron.

Significant as these achievements were, it was clear that the full potential of a truly  $\delta$ -like DOS and discrete energy spectra could not be exploited, as fabricating samples of completely uniform QDs was not possible. The non-uniform nature of QD ensembles results in inhomogeneous broadening of PL spectra, leading to a spreading of the gain over a wider spectral range, reducing the peak gain. Furthermore, whilst it is true that the trapping of carriers in QD states has the effect of suppressing the escape of non-equilibrium carriers from the active region, as well as preventing non-radiative recombination at defect sites, this doesn't necessarily hold true at higher temperatures, when the thermal energy  $k_B T$  has the effect of pushing carriers out of the dots that have insufficient confinement potential. Ledentsov et al. [128] concluded this was having a significant effect in lowering the gain for a given current density.

Other than producing QDs with a greater size homogeneity, another approach to improve the gain is to increase the dot density in an attempt to speed up carrier relaxation into the QDs, and therefore shorten radiative recombination times. This was achieved by Ledentsov et al. [129] in 1996 by the growth of vertically-coupled QDs, experimentally demonstrating a larger optical gain and ground-state lasing up to room temperature. Non-radiative recombination was still seen as a significant problem, however, with a low differential efficiency attributed to it.

The thermal ejection of carriers from QDs into wetting layer and matrix material states was addressed by the use of AlGaAs as a matrix material, instead of GaAs, thereby increasing the energy gap between QD states and those of the wetting layer and matrix. This eventually led to the realisation of a QD laser capable of continuous-wave room-temperature operation with an output power of 1 W, demonstrated by Shernyakov et al. [130] in 1997.

Nowadays, QD lasers have more than proved themselves capable of achieving low threshold currents, compared to QW lasers [131]. However, efficient carrier injection remains one of the most stubborn problems, with high-frequency modulation bandwidths still proving difficult to achieve as a result [132]. The reason for this is well-established as being due to the trapping of carriers in wetting layer states, of which, for conventional SK QDs, there is a high density (compared to QD states, see Figure 4.1). Urayama et al. [133] showed, experimentally and by Monte Carlo simu-

lations<sup>1</sup>, that carriers tend to stay in wetting layer or barrier states at temperatures above 100 K, and relaxation to lasing QD states is very slow. In 2005-06, Cornet et al. [134, 135] used the approach of lateral QD-coupling in an attempt to solve this problem: Working with an InAs/InP system, they used the relative proximity of wetting layer states to the QD ground state to demonstrate, theoretically and experimentally, lateral coupling between high-density arrays of QDs. They showed that there exists an advantageous intermediate coupling regime which doesn't degrade the atom-like properties of the QD ground state, whilst still enhancing charge-carrier redistribution efficiency through the coupling of excited states. Furthermore, they argued that faster relaxation times in coupled QDs, compared to uncoupled QDs, may lead to better high-frequency modulation bandwidths. Another approach was taken by Fathpour et al. [132], who used a “tunnel injection” layer (effectively a QW) close to the QDs, so that carriers could be injected straight into QD states, in doing so raising the modulation bandwidth of near-infrared QD lasers from  $\sim 7$  GHz to  $\sim 22$  GHz.

The transmission rate is of particular interest in the context of datacoms, and so the difficulties in realising fast-response lasers is a worrying one. To the author's best knowledge, the record SK-QD bit rate demonstrated at room temperature is  $25 \text{ Gb s}^{-1}$ , achieved by Tanaka et al. [136] in 2010 for a  $1.3\text{-}\mu\text{m}$  InAs/GaAs QD laser with a high areal density of  $5.9 \times 10^{10} \text{ cm}^{-2}$ . In the same paper,  $10 \text{ Gb s}^{-1}$  operation was seen up to  $100^\circ\text{C}$ .

As is clear from the previous paragraphs, the relative merits of QW and QD lasers are difficult to compare and contrast. Chow et al. [137] make an attempt at doing so by utilising rigorous first-principles theory without any free parameters. Their conclusion is, rather unsurprisingly, that QD lasers offer far superior lasing threshold values, but size inhomogeneities are still the lead constraint on desired gains and speeds. The answer to the question they pose in the title of their paper, “will quantum dots replace quantum wells as the active medium of choice in future semiconductor lasers?”, is a rather ambiguous “it depends”, and it will ultimately be determined by future experimental and theoretical progress. One thing is for sure;

---

<sup>1</sup>Monte Carlo simulations repeatedly simulate possible outcomes based on input variables obtained at random from a distribution function. They are particularly useful to solve problems with a large number of input variables that would otherwise be almost impossible to solve.

QW lasers currently enjoy ubiquity in the modern world, and will take some shifting from their top spot.

For further reading, the reader is referred [Reference 138](#) for a very thorough review of long-wavelength self-assembled QD lasers, and to [Reference 139](#) for a briefer but more recent review, again of long-wavelength lasers.

#### 4.1.4 Sub-Monolayer Growth

SML superlattice growth involves the deposition of  $<1 \text{ ML}^2$  of, for example, InAs on GaAs, capping it with a few MLs of GaAs and repeating several times to form a SML stack. The resulting system can range from a simple InGaAs QW, to SML islands (QDs) embedded in a QW, as discussed below.

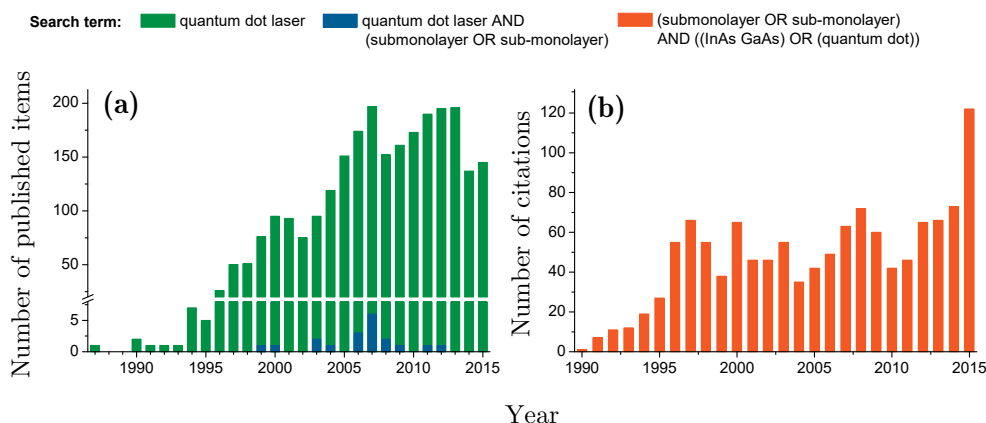


**Figure 4.2:** Publication and citation data from [Reference 11](#) using the following italicised search terms: **(a)** Annual number of publications with *quantum dot laser* (green) or *quantum dot laser AND (submonolayer OR sub-monolayer)* (blue) in the title. **(b)** Annual number of citations for publications with *(submonolayer OR sub-monolayer) AND ((InAs GaAs) OR (quantum dot))* (orange) in the title.

SML growth has seen relatively little attention, especially compared to the field of QD lasers as a whole. As shown in [Figure 4.2](#), searching Web of Science [11] for articles with “quantum dot laser” in the title returns 2583 results, with 24 of these being review articles. Stipulating the presence of “sub(-)monolayer” in the title as well reduces the total to 19, of which only one is a review article<sup>3</sup>. In fact, the number

<sup>2</sup>Depositing  $<1 \text{ ML}$  simply means depositing a quantity of material that is too small to constitute a complete atomic layer; it doesn’t mean we chop atoms in half!

<sup>3</sup>Searching only for “sub(-)monolayer laser” increases this to 31 results, though most of the extra papers are unrelated, e.g., “Quantification of metal trace contaminants on Si wafer surfaces by Laser-SNMS and TOF-SIMS using sputter deposited submonolayer standards”.

of articles with “sub(-)monolayer InAs GaAs” or “sub(-)monolayer quantum dot” in the title only amasses to 110. This demonstrates a broad scope for expansion of research in this exciting area of semiconductor physics, and it is encouraging that the trend of citations per year (Figure 4.2(b)) is slowly on the rise.

### Structural Characteristics, Pre-2000

The first few papers that detailed something which at least in part resembles what we now call SML growth were published around the start of the 1990s. These early studies involved the deposition of fractional monolayers of InAs on *vicinal* GaAs surfaces, as an alternative to SK QD growth [140–142]. Vicinal (or terraced) crystal surfaces are those cut at a relatively low angle (typically, a few degrees) to the main crystallographic planes, such as (100), and thus in an ideal case form a series of “terraces” with monatomic steps. Brandt et al. [140, 141] hypothesised that In adatoms would nucleate on the step edges, thereby forming a uniform heterostructure in which surface morphology dictates the arrangement of epitaxial layers, rather than a precise control of deposition rates, as is needed for high-quality SK-QD growth. However, in 1994, Bressler-Hill et al. [142] showed that InAs nucleates not just on step edges, but also on terraces and in terrace defects; in other words, the use of vicinal surfaces to produce uniform growth was somewhat futile. The first optical characterisation of submonolayer InAs in GaAs was also presented in 1994, by Wang et al. [143], showing “extremely high optical quality” and greatly improved luminescence efficiency, when compared with ML-or-greater deposition and bulk InGaAs. Interestingly, their paper was the first to refer to this growth as “submonolayer epitaxy”.

At a similar time, Egorov et al. [144] proposed that SML deposition, this time not on a vicinal surface, could be used for the growth of InGaAs QWs. They reported a significant increase in the PL intensity from these “wells”, as compared to growth with an InGaAs solution. Another attempt at growth on vicinal surfaces, as well as non-vicinal surfaces, was made by Guryanov et al. [145] in 1996. On the non-vicinal surfaces, they saw wire-like formations for 1-ML InAs deposition, and “parquet”-like structures with a characteristic period of 50-60 nm for 1.5-ML deposition. The wire-like formations were seen on vicinal surfaces for both 1 and 1.5 ML depositions.

In 1998, Shchukin et al. [146] published a detailed paper on the energetics of stacked 2D-island deposition, demonstrating theoretically that SML deposition resulted in vertically-correlated ML-high islands, explained by the strain due to buried islands reducing the mismatch between the surface and the island, creating energetically-favourable nucleation sites directly above them. This was in part following on from previous experimental and theoretical work on the vertical correlation of InAs/GaAs QDs [147–149]. The theory and observation of the self-assembly of 2D islands was not a new topic and the reader is referred to Reference 150 for a comprehensive review. In a nutshell; if two phases with different values of intrinsic surface stress,  $\tau_i$  and  $\tau_j$ , coexist on a crystal surface, formation of boundaries will result in an elastic energy relaxation of the more stressed phase along the boundaries between the domains.

This focus on the structural characteristics brought about by SML deposition led to the nominal picture of SML systems that persisted for over two decades; of vertically-correlated ML-high InAs islands, separated by spacer layers consisting of pure GaAs, illustrated in Figure 4.3.

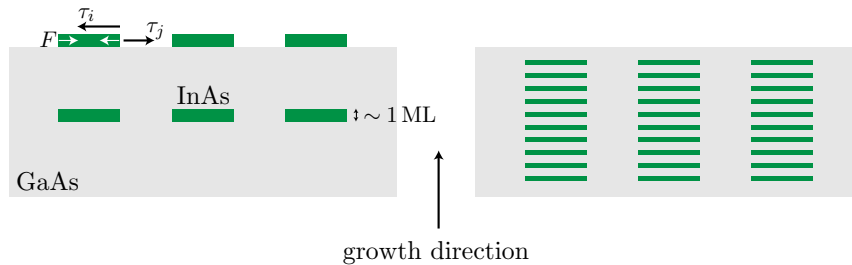


**Figure 4.3:** The nominal growth of a sub-monolayer (SML) system, in which the  $<1$ -ML deposition of InAs (green) results in the formation of  $\sim 1$ -ML-high, vertically-aligned, InAs islands in a GaAs matrix (grey). Self-assembled island formation is due to different surface stresses,  $\tau_i$  and  $\tau_j$  (black arrows), resulting in an elastic relaxation force  $F$  (white arrows).

## Quantum-Dot–Quantum-Well Heterostructure

In the years 2003 to 2006, Xu et al. [151, 152, 153] took a more detailed look at the optoelectronic properties of SML systems, performing PL, micro-PL<sup>4</sup> and TRPL on SML samples comprising 10 cycles of InAs (0.5 ML) and GaAs (2.5 ML).

<sup>4</sup>Micro-PL is an experimental technique analogous to conventional PL, except a smaller excitation laser spot size is used so only a small area of the sample is studied. This is particularly useful for observing the emission from individual QDs.

Low-temperature and low-power micro-PL demonstrated the presence of discrete QD emission lines, whilst exciting the system at different energies, some below the band gap of GaAs, showed little change in the PL line shape. They postulated that this highlights the existence of QW states, because such states are needed to transfer carriers to the QDs if the excitation energy is below the GaAs band gap. In conclusion, they proposed that SML deposition leads to the formation of a QD–QW heterostructure, pointing out that such a structure could be beneficial to optoelectronic device applications where efficient carrier injection into QD states could be provided by the extended QW states. Indeed, the TRPL measurements they performed demonstrated fast recombination times.

### **Atomic Structure and Optical Properties, Lenz et al. [19, 20]**

Xu et al. [151] hinted that there may be more to the picture than the nominal structure presented in Figure 4.3, but it wasn't until 2010 that the consensus was challenged by further structural characterisation. In that year and the following, Lenz et al. [19, 20] published two papers in which they performed an in-depth and thorough analysis of the atomic structure of SML InAs in GaAs by the use of XSTM. They studied 10-fold 0.5-ML InAs depositions separated by 16, 4, 2.8 and 1.5 ML of GaAs. The sample with the largest spacer-layer thickness of 16 ML showed InAs-rich agglomerations laterally along each SML deposition that were not concentrated within a single ML, but typically distributed over several rows. Along the growth direction, InAs concentration increases abruptly, followed by a decay toward zero, indicating that the vertical segregation of In happens during the GaAs capping process. A vertical In segregation length of  $\sim 1$  nm is calculated from the experimental data. The lateral size of the islands is found to be very roughly 5 nm, with each island separated by about 2 nm, leading to a very high lateral density of  $\sim 10^{12}$  cm $^{-2}$ , much higher than the  $10^{10}$  to  $10^{11}$  cm $^{-2}$  that is typical for SK QDs. A slight vertical correlation along the growth direction is also seen, as predicted by Shchukin et al. [146].

Decreasing the spacer-layer thickness to values more typical for device applications ( $\leq 4$  ML) means that the segregation length is in the order of the spacer-layer thickness and thus individual SMLs can hardly be distinguished. Instead, In-rich

agglomerations with a range of shapes and sizes are present, often extending across the entire SML stack and having lateral and vertical sizes of very roughly 5 nm. This In segregation has led to the formation of a low-In-content InGaAs QW spanning the entire stack height, in which are embedded the In-rich agglomerations that have a lateral density of  $10^{12} \text{ cm}^{-2}$ . A XSTM image for a sample with 2.3-ML spacer-layer thickness is shown in [Figure 4.4](#), and though this image isn't present in the publications referenced, it is from the same research group. Yellow dashed lines are shown as a guide for the eye to highlight the presence of In-rich agglomerations. These results were supported by high-resolution transmission electron microscopy performed by Niermann et al. [[154](#)] in 2012.

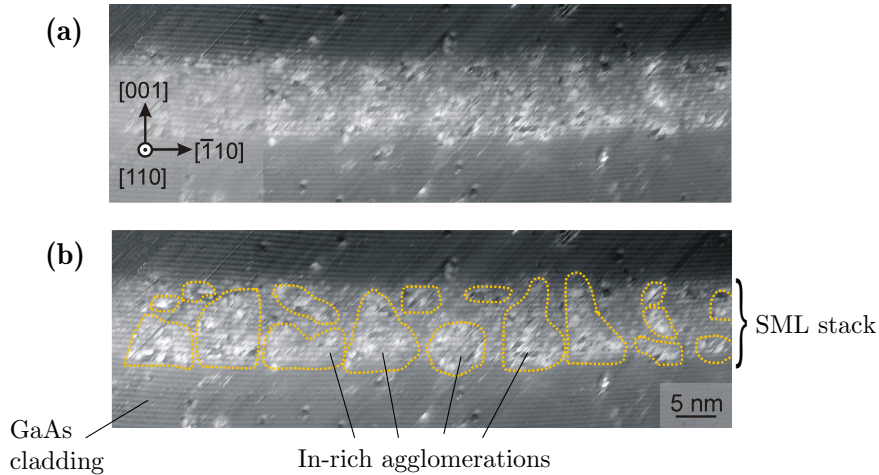


**Figure 4.4:** Cross-sectional scanning tunnelling microscopy (XSTM) image, taken at  $V = \pm 2.9$  volt,  $I = 80$  pA, of a SML sample with 2.3 ML GaAs spacer-layer thickness. In (b), yellow dashed lines are a guide for the eye to highlight the In-rich agglomerations.

This picture fits well with the QD-QW heterostructure described in [Reference 151](#), where the In-rich agglomerations act as InGaAs QDs with a high In content, embedded laterally in an InGaAs QW with a low In content. Lenz et al. [[20](#)] postulate that the absence of a wetting layer and the high lateral density and small spacing between QDs could favour high-speed optoelectronic devices, such as VCSELs. The findings of their optical study supports this interpretation: PL data are incredibly narrow and bright; similar but redshifted compared to a QW with the same thickness and In content, the redshift attributed to 0D localisation in the In-rich QDs. PL peak energies also redshift with decreasing spacer-layer thickness, due to an increasing vertical coupling of excitons across the spacers. Lateral coupling across the agglomerations leads to a mixture of 0D and 2D states, which manifests

itself in the emission spectra, as verified by a PL line-shape analysis.

## Sub-Monolayer Lasers

At the turn of the millennium, a number of articles detailing the use of SML systems as the active medium in a laser were published. In 1999, Zhukov et al. [155] demonstrated a 947-nm edge-emitting laser that could achieve a continuous-wave output power of 3.9 W at 10 °C, based on the deposition of 0.4 ML InAs, followed by 2.5 ML GaAs, cycled 10 times. A year later, Mikhrin et al. [156] compared a similar SML laser to a SK QD laser, finding the SML laser had much lower internal losses and double the material gain of the SK QD laser, attributing it to better uniformity of SML QDs than SK QDs. In 2003, again using a similar laser, Kovsh et al. [157] increased this high-power operation to 6 W at 20 °C. A high modal gain of  $44 \text{ cm}^{-1}$  for a 964-nm edge-emitting laser was seen by Xu et al. [152] in 2004, attributed to the high density and uniformity of QDs.

In the mid-to-late-2000s, there was a flurry of research into using SML systems as the active medium in VCSELs, in part contributing to the spike in the number of publications seen in Figure 4.2(a) (blue). Blokhin et al. [158] fabricated the first SML VCSEL in 2006, achieving a continuous-wave output power of 4 W at 980 nm, with internal optical losses of less than 0.1 %. Also in that year, Hopfer et al. [159] highlighted the potential of SML VCSELs for high-speed applications (e.g., datacoms), demonstrating a modulation bandwidth of 10.5 GHz and low threshold current of 170  $\mu\text{A}$  from a triple stack of 10-fold 0.5-ML InAs / 2.3-ML GaAs depositions with 13-nm-thick GaAs spacers between each SML stack. The following year, the same group from Technische Universität Berlin produced a 980-nm SML VCSEL capable of error-free 24-Gb s<sup>-1</sup> operation at room temperature, and 20-Gb s<sup>-1</sup> operation at 85 °C, without current adjustment [160]. To the author’s best knowledge, this remains the highest-speed SML VCSEL demonstrated to-date. It is also faster than the highest-speed SK QD laser at high temperatures, which achieved 25 Gb s<sup>-1</sup> at room temperature and 10 Gb s<sup>-1</sup> at 100 °C [136]. Furthermore, the 980-nm operating wavelength of the SML laser is potentially more suited to datacoms than the 1.3- $\mu\text{m}$  SK QD laser. The same research group published a review on “Submonolayer Quantum Dots for High Speed Surface Emitting Lasers” in 2007 [107], postulating

that  $>40\text{-Gbs}^{-1}$  transmission might be possible if the device resistance is further reduced and an optimised heat-dissipating design used, as in [Reference 161](#). Finally, in 2009,  $20\text{-Gbs}^{-1}$  error-free transmission was realised for an 850-nm SML VCSEL at room temperature [[162](#)].

## Other Applications

Whilst SML VCSELs prove to be the most promising application to emerge from SML research, a number of other potential uses have been documented. Infrared photodetectors were investigated by Ting et al. [[163](#)] in 2009, motivated by the prediction that QD infrared photodetectors could have a significantly better detectivity than QW infrared photodetectors if high-density arrays of small QDs could be fabricated. Their results were somewhat encouraging, showing clear infrared images up to 80 K.

Lam et al. [[164](#)], in 2014, reported on their investigations on SML InGaAs/GaAs QD solar cells. Nanostructures are desirable in solar cells due to their ability to absorb photons below the band gap of the bulk material (sub-band gap), and SML systems more so because of the high lateral density of QDs and unique strain relaxation compared to QWs (lattice mismatch between an InGaAs QW and a GaAs matrix limits the number of QWs that can be incorporated into a device). They demonstrated that, in comparison to an InGaAs QW solar cell with the same In content, the SML solar cells showed an enhanced open-circuit voltage and an increased short-circuit current.

## Recent Work and Extensions to the SML System

One interesting extension to the conventional SML system was investigated by Switański et al. [[165](#)] in 2013, whereby a SK QD layer was coupled to a SML stack, the two separated by a GaAs spacer of varying thickness. An increase in coupling was seen for decreasing SK–SML spacer thickness and carrier transfer from the SML stack into the SK QDs was verified. This coupling led to a spacer-thickness-dependent acceleration in the carrier dynamics inside the SML stack, caused by the capture of carriers from the SML stack into the QDs, and thus a fast gain recovery for the QDs, tunable by differing the SK–SML spacer thickness as well as the growth

of the SK QDs and SML stack.

Another technique that offered tunability—this time of wavelength and confinement—was presented by Quandt et al. [166] in 2015, by the introduction of an Sb flush during the growth process, leading to the incorporation of Sb into the In-rich agglomerations. They discovered that the addition of Sb leads to strong electronic confinement that is dependent on the amount of Sb added. Different degrees of localisation can be achieved for the same target wavelength by simultaneously adjusting the SML stack height and the Sb supply.

Finally, later that year, Herzog et al. [167] published a detailed analysis of the gain and phase recovery of semiconductor optical amplifiers based on SML deposition, discovering recovery dynamics were as fast as those for other QD-in-a-well structures and a fast recovery time constant of a few picoseconds was attributed to the InGaAs QW acting as an efficient carrier reservoir. Eight-band  $\mathbf{k} \cdot \mathbf{p}$  calculations for an SML system showed a high degree of localisation for the hole, whilst the electron extended to neighbouring SML islands and the embedding QW. Thus, carriers localised in the active region are likely to respond fast to changes in the potential caused by the creation (or annihilation) of an exciton. The high amplitude of this fast recovery component is promising for high-speed optoelectronic devices, and offers further explanation to the impressive performance of SML VCSELs already demonstrated.

Two main conclusions can be drawn from the literature presented here: The first is that SML systems with a sufficiently small ( $<4$  ML) GaAs spacer-layer thickness consist of a lateral InGaAs QW with low In content, in which are embedded In-rich QD-like agglomerations. Referring to these systems as “SML QDs” is therefore misleading and the phrase QD–QW heterostructure is more descriptive. Herein, the complete structure will be referred to as a SML “system”, “deposition” or similar, whilst the use of the term “QDs” will be reserved for the In-rich agglomerations. Secondly, SML systems have demonstrated impressively-fast VCSELs and other devices, attributable to fast carrier relaxation dynamics, due to the presence of 2D and 0D states. However, up until now, the true nature of confinement has not been fully explored or explained, motivating our work to qualify the exact form that

the mix of 2D and 0D states take, and their subsequent influence on charge-carrier confinement.

## 4.2 Results

In the previous section, we saw that SML systems form a QD–QW heterostructure, with  $\sim 5$ -nm In-rich QD-like regions embedded in a lateral In-poor InGaAs QW that is the height of the SML stack, far from the nominal structure of  $\sim 1$ -ML-high InAs islands in a GaAs matrix. [Figures 4.3](#) and [4.4](#) are amalgamated in [Figure 4.5](#), along with a representation of the likely band structure, to reiterate these findings. Such a structure as the XSTM image in [Figure 4.5\(b\)](#) immediately raises questions about the nature of charge-carrier confinement, motivating the work presented in this section to experimentally and theoretically explore whether SML systems are 2D or 0D.

### 4.2.1 Samples

Three InAs/GaAs SML samples and one InGaAs QW sample are studied in this work, as summarised in [Table 4.1](#), all of which were grown at Technische Universität Berlin by MOCVD. The three SML samples were grown at  $500^\circ\text{C}$  on a (001) GaAs substrate using tertiarybutylarsine, trimethylgallium and trimethylindium precursors, the growth only differing in the GaAs spacer-layer thickness. 0.5 ML of InAs was deposited with a V/III ratio of 9 and a growth rate of 0.25 ML/s, followed by a 1-s growth interruption to allow for surface smoothing and InAs diffusion. 1.5, 2.0 or 2.5 ML of GaAs (for samples A, B and C, respectively) was then deposited with a V/III ratio of 5 and a growth rate of 0.5 ML/s, followed by a further 1-s interruption. The procedure was repeated another nine times, until 10-fold SMLs of InAs had been deposited. These SML structures are surrounded by a 300-nm-thick GaAs matrix, which is sandwiched between 50 nm of  $\text{Al}_{0.6}\text{Ga}_{0.40}\text{As}$  below the SML stack and 20 nm of  $\text{Al}_{0.4}\text{Ga}_{0.60}\text{As}$  above, to prevent the escape of photogenerated carriers. Finally, a 10 nm GaAs cap layer was grown on top to achieve significant separation from the cleavage edge and reduce surface oxidation.

The choice of GaAs spacer-layer thicknesses corresponds to typical thicknesses

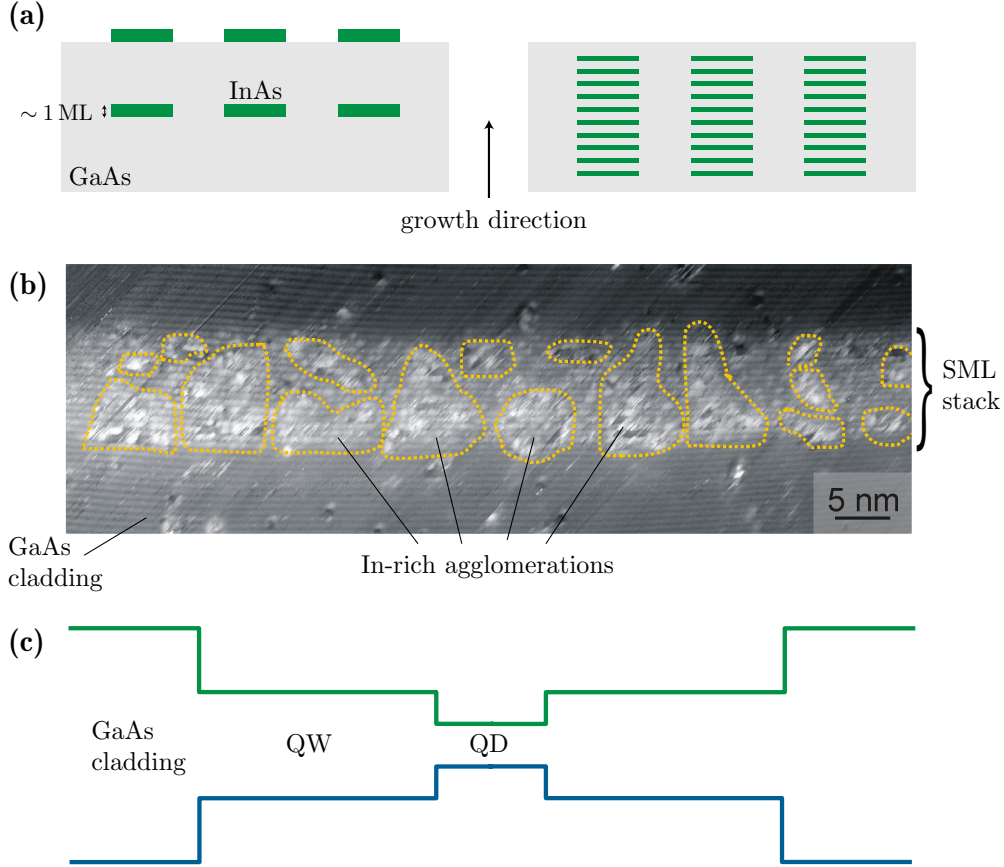


**Figure 4.5:** (a) The nominal growth of a SML system, in which the  $<1$ -ML deposition of InAs (green) results in the formation of  $\sim 1$ -ML-high, vertically-aligned, InAs islands in a GaAs matrix (grey). (b) A XSTM image, taken at  $V = \pm 2.9$  V,  $I = 80$  pA, of a SML sample with 2.3 ML GaAs spacer-layer thickness. The yellow dashed lines are a guide for the eye to highlight the In-rich agglomerations. (c) Representative band structure that the SML system in (b) is likely to result in, with the In-rich agglomerations (QDs) offering a confining potential within the SML stack (QW).

used in SML devices. The *stack heights* (and therefore the height of the lateral InGaAs QW) for the three samples can be calculated using the lattice constants for InAs ( $a_{\text{InAs}} = 6.06 \text{ \AA}$ ) and GaAs ( $a_{\text{GaAs}} = 5.65 \text{ \AA}$ ) [62], with the growth sequence detailed in the previous paragraph, giving stack heights of approximately 11.5, 14.3 and 17.2 nm for samples A, B and C, respectively. Observing Figure 4.5(b), one can see this is a reasonable approximation to make.

As a reference, a 6.5-nm-thick  $\text{In}_{0.18}\text{Ga}_{0.82}\text{As}/\text{GaAs}$  QW was grown at  $600^\circ\text{C}$  with a V/III ratio of 10.7 and a growth rate of  $0.47 \mu\text{m h}^{-1}$ . This was also sandwiched between  $\text{Al}_x\text{Ga}_{1-x}\text{As}$  barriers. The choice of thickness and In composition was so that the QW had a similar overall In content to the SML samples.

**Table 4.1:** Summary of the three SML and one QW samples studied.

Sample name	GaAs spacer thickness (ML)	Stack/QW height (nm)
A	1.5	11.5
B	2.0	14.3
C	2.5	17.2
QW	-	6.5

## 4.2.2 Evidence for a Two-Dimensional System

### Zero-Field Photoluminescence

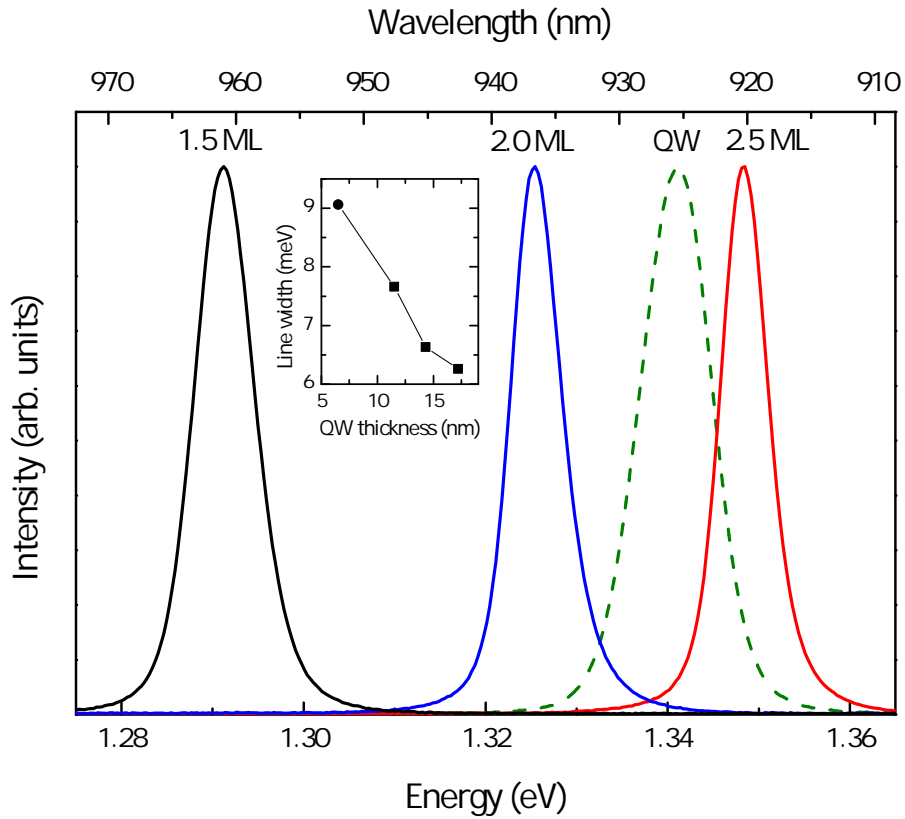


**Figure 4.6:** 2-K zero-field normalised PL from the three SML samples and the QW sample. The inset shows the linewidth dependence on the stack height of the three SML samples (or the QW thickness, indicated by the circle).

Figure 4.6 shows 2-K zero-field PL spectra from the three SML samples and the QW. Immediately striking are the narrow linewidths (defined as the full width at

half maximum) of  $7.66 \pm 0.01$ ,  $6.63 \pm 0.01$  and  $6.26 \pm 0.01$  meV for samples A, B and C, respectively. This is far narrower than is typically the case for InAs/GaAs SK QDs, and indeed is narrower than that of the QW ( $9.06 \pm 0.01$  meV). Reassuringly, this is in agreement with literature that SML systems offer superior luminescence to bulk InGaAs, InGaAs QWs and SK QDs [20, 143, 144, 151]. Though it is not represented in Figure 4.6, it is also of note that the PL from the SML samples was incredibly intense, dwarfing that from the QW and indeed most other samples measured in our laboratory. The PL intensity is, however, very sensitive to external factors (e.g., what part of the sample is being excited, or changes to the optical fibre bringing excitation light to the sample), and so we prefer to simply comment on it rather than rely on it as evidence, especially seeing as PL measurements were not undertaken simultaneously.

If PL were to be from the In-rich QDs, which are highly non-uniform in shape and size, then one would expect it to be inhomogeneously broadened to linewidths similar, if not wider, than those from InAs/GaAs self-assembled QDs; typically in the order of 25 to 40 nm at low temperatures [168, 169]. Even highly-uniform InAs/GaAs QDs have linewidths of more than double those seen here [170]. Therefore, the behaviour of SML samples studied in this work is clearly QW-like.

Furthermore, PL linewidth is seen to decrease with increasing GaAs spacer-layer thickness. Larger GaAs spacers means a larger stack height and this behaviour is as one would expect for a QW [171]: Broadening of QW linewidths is a result of monolayer fluctuations in the QW thickness and increasing the size of the QW reduces the relative size of these monolayer fluctuations, thus reducing linewidths. The QW sample has the smallest QW thickness and therefore it makes sense that it has the largest linewidth.

The PL peak energies (deduced from Gaussian fits to the PL spectra) blueshift with increasing spacer-layer thickness, which can be explained by a thicker GaAs spacer layer meaning a higher Ga content in the InGaAs QW, shifting the band gap toward that of GaAs (1.52 eV at room temperature), which is larger than that of InAs (0.42 eV at room temperature) [62].

Room-temperature (300 K) PL data, as shown in Figure 4.7, are for all samples homogeneous and inhomogeneously broadened, with the non-Lorentzian line shapes

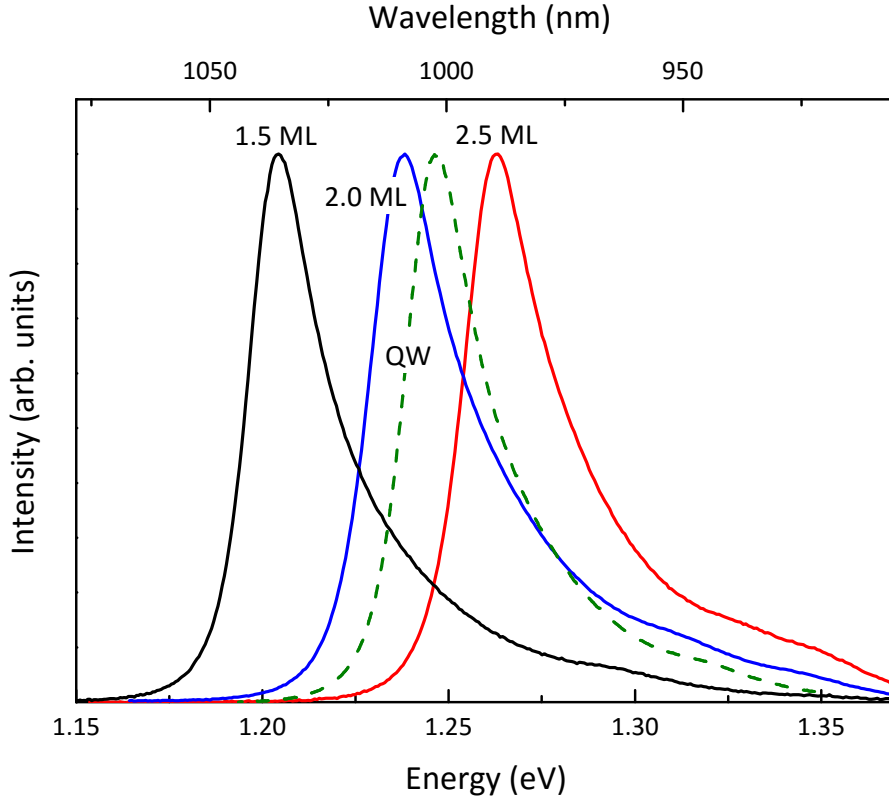


**Figure 4.7:** Room-temperature zero-field normalised PL from the three SML samples and the QW sample, showing both homogeneous and inhomogeneous broadening compared to the low-temperature PL.

suggesting the presence of excited states that are being populated by the extra thermal energy. The linewidths— $26.6 \pm 0.1$ ,  $31.4 \pm 0.1$ ,  $31.6 \pm 0.1$  and  $25.9 \pm 0.1$  meV, for samples A, B, C and the QW, respectively—follow less of a trend than the low-temperature results, most likely because thermal excitation is masking the underlying physics that is visible at 2 K. A blueshift in PL peak energies with increasing spacer-layer thickness is still clearly visible. Further temperature dependence data are included in [Appendix A](#).

### Magneto-Photoluminescence

Applying a magnetic field  $B$  in the growth direction  $z$ , known as Faraday geometry, confines excitons in the lateral direction (along SML depositions) and thus enables us to probe excitonic properties in this lateral direction. [Figure 4.8](#) shows the dependence of the PL peak energy on the magnetic field for all four samples at

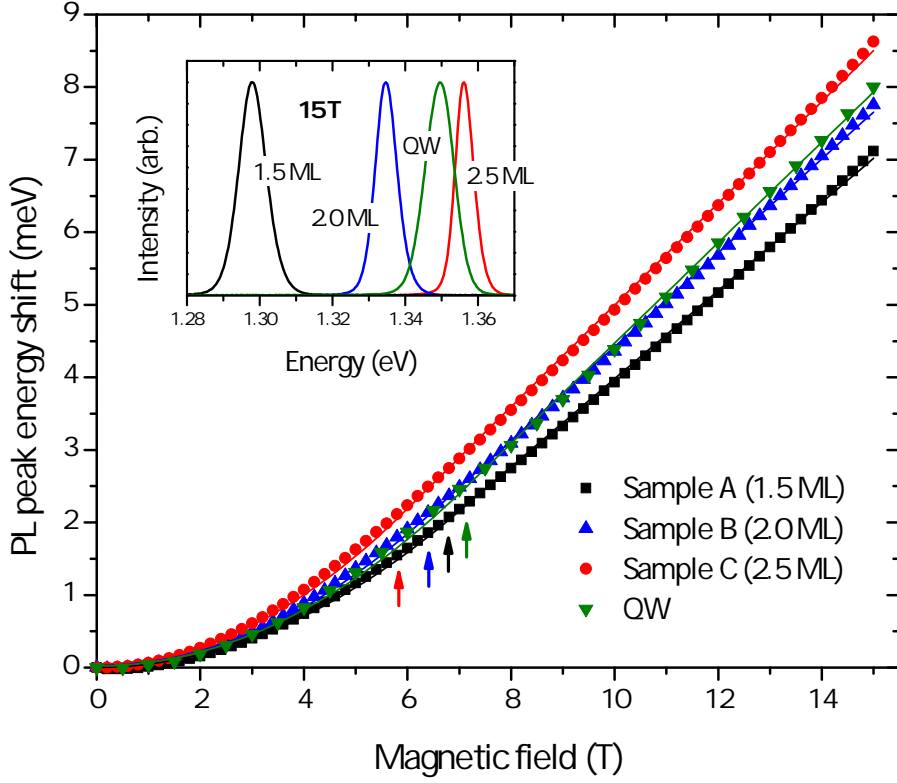


**Figure 4.8:** 2-K magneto-PL in Faraday geometry for the three SML samples and the QW, showing the PL peak energy shift dependence on magnetic field  $B$ . Shapes represent the data, whilst solid lines show the excitonic model fit. The crossover from low- to high-field regime is indicated by the arrow for each sample. The inset shows the individual PL spectra for the four samples at 15 T. Parameters interpreted from excitonic fitting are summarised in [Table 4.2](#).

2 K, whilst the inset shows the individual PL spectra at 15 T. The data clearly show two regimes: a low-field regime where the PL peak energies demonstrate a quadratic dependence on  $B$ , followed by a high-field regime where this dependence is instead linear. The crossover between these regimes, indicated by the arrows, is at the critical field  $B_c$ , a value for which is deduced from the excitonic model ([Section 2.8.5](#)). The fitting of the excitonic model to the data is shown by the solid lines in [Figure 4.8](#) and the parameters extracted are summarised in [Table 4.2](#).

The lateral exciton Bohr radii are  $13.8 \pm 0.1$ ,  $14.3 \pm 0.1$  and  $14.9 \pm 0.1$  nm and the reduced masses are  $(0.095 \pm 0.001)m_0$ ,  $(0.090 \pm 0.001)m_0$  and  $(0.083 \pm 0.001)m_0$  for samples A, B and C, respectively.  $m_0$  is the free electron mass. This demonstrates that excitons are approximately 30 nm wide in all three SML samples; considerably larger than the 5-nm In-rich agglomerations and extending across several of them.

The reduced mass decreases as the stack height increases, and thus as In content decreases. This could be as a result of a reduction in strain in the system when In content is lower, an effect which has been theoretically and experimentally observed in literature [172–174]. In Reference 174, a linear dependence of the reduced mass on strain is observed for InAs QDs in GaAs. This system may include a different strain profile to a SML system, and such a direct comparison cannot be made. Nonetheless, it seems reasonable to at least speculate that a lower In content means reduced strain and thus a lower reduced mass, though we do not have enough data to state this with any certainty.

The QW Bohr radius of  $13.6 \pm 0.1$  nm and reduced mass of  $(0.084 \pm 0.001)m_0$  is similar to that of the SML samples, thereby reinforcing our postulation that SML emission is from the lateral InGaAs QW, and not the In-rich QDs.

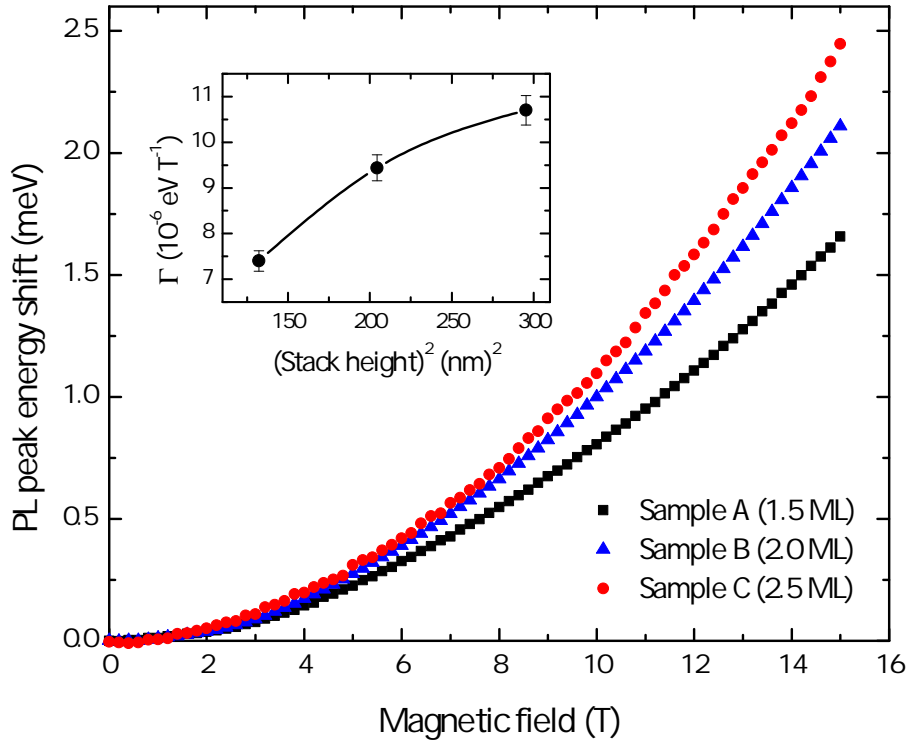


**Figure 4.9:** 2-K magneto-PL in Voigt geometry for the three SML samples. The inset shows the diamagnetic energy shift coefficient  $\Gamma$  dependence on the square of the stack height.

We now turn our attention to the low-temperature Voigt geometry ( $B \perp z$ ) magneto-PL data, shown in Figure 4.9. Immediately noticeable is that the data are only quadratic in  $B$  and the high-field regime is never reached. Furthermore, the

**Table 4.2:** Parameters extracted from the excitonic-model-fitting of Faraday- and Voigt-geometry magneto-PL data. No data was taken for the QW in Voigt geometry.

Sample	Faraday geometry ( $B \parallel z$ )			Voigt geometry ( $B \perp z$ )		
	$a_B$ (nm)	$\mu$ ( $m_0$ )	$\Gamma$ ( $10^{-6}$ eV T $^{-1}$ )	$a_B$ (nm) <sup>a</sup>	$\mu$ ( $m_0$ ) <sup>b</sup>	$\Gamma$ ( $10^{-6}$ eV T $^{-1}$ )
A	$13.8 \pm 0.1$	$0.095 \pm 0.001$	$43.9 \pm 0.3$	$< 9.4$	$< 0.26$	$7.40 \pm 0.22$
B	$14.3 \pm 0.1$	$0.090 \pm 0.001$	$50.4 \pm 0.5$	$< 9.4$	$< 0.20$	$9.44 \pm 0.28$
C	$14.9 \pm 0.1$	$0.083 \pm 0.001$	$59.5 \pm 0.6$	$< 8.9$	$< 0.16$	$10.7 \pm 0.3$
QW	$13.6 \pm 0.1$	$0.084 \pm 0.001$	$48.5 \pm 0.6$	-	-	-

<sup>a</sup> Calculated from Equation 2.40 with a maximum field of 15 T or 17 T for sample C.

<sup>b</sup> Calculated from Equation 2.44 with a maximum field of 15 T or 17 T for sample C and  $\Gamma$  from fits to the data.

total size of the shift is approximately three times smaller than for Faraday geometry. Vertical Bohr radii must be  $\lesssim 10$  nm (calculated using Equation 2.40 with a field of  $B = 12$  T, lower than the maximum laboratory field to account for the difficulty in seeing a transition near the extrema of the data), demonstrating strong vertical confinement that increases with decreasing stack height (spacer-layer thickness).

The diamagnetic shift coefficient  $\Gamma = e^2 a_B^2 / 8\mu$  shows a slightly sub-linear dependence on the square of the stack height, as shown in the inset of Figure 4.9. If the reduced mass remained constant and the Bohr radius in the growth direction was determined solely by the stack height, this dependence would be linear. Therefore, either the reduced mass must be increasing with increasing stack height, or the vertical extent of the exciton wave function saturates at its intrinsic (unconfined) size as the stack height increases past a certain point. We have already seen that the lateral reduced mass decreases with increasing stack height and it seems unlikely that the vertical reduced mass would instead be increasing, making the latter postulate more plausible.

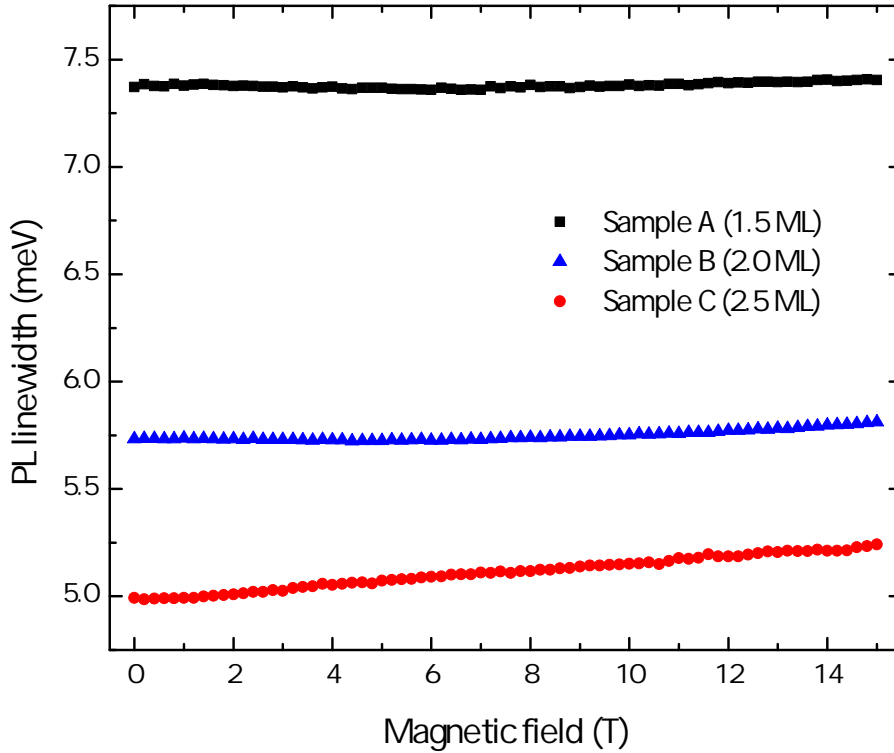


**Figure 4.10:** Voigt-geometry PL linewidth dependence on the magnetic field. Strong vertical confinement means the magnetic field has marginal effect in squeezing exciton wave functions.

Further evidence of this strong vertical confinement can be seen by observing the dependence of the PL linewidth on the magnetic field in Voigt geometry, as shown in [Figure 4.10](#). The conventional argument is that PL linewidths should monotonically increase with increasing field [175]: As the magnetic field strength is increased, the exciton wave function is squeezed and it sees less and less of the sample, leading to a reduced disorder averaging (i.e., averaging over the local fluctuations in QW width) and an inhomogeneous broadening of the linewidth. Only sample C, with the largest stack height, shows such a trend, whilst the linewidths for the other two samples are largely unaffected by the magnetic field. The strong vertical confinement seen in the Voigt-geometry magneto-PL means that it is this, rather than the magnetic field, that determines the vertical extent of the exciton wave function, at least for the two samples (A and B) with the smallest stack height. Increasing the field just has an effect in squeezing the exciton wave function for sample C, which has the largest stack height. This further proves that it is the stack height that is providing the strong vertical confinement, rather than localisation in the In-rich agglomerations.

Faraday-geometry PL linewidths show a much more interesting shape ([Figure 4.11](#)): For all SML samples, up to a field of around 6 T, a clear decrease in linewidth is seen, after which the previously explained monotonic increase returns. This can be explained by the introduction of a second disorder length scale  $\chi_2$  [171]. The first correlation length  $\chi_1$  relates to the monolayer fluctuations in the QW width, and is much smaller than  $a_B$ . The second correlation length  $\chi_2$  represents fluctuations in the size of the highly non-uniform In-rich agglomerations and thus is around the size of  $a_B$ . At low fields, the exciton wave function is much larger than the In-rich agglomerations and it is therefore these larger-scale fluctuations that dominate the linewidth broadening. Gradually, as the field is increased, the exciton is squeezed until it reaches a point when the inhomogeneity in In-rich agglomerations no longer dominate (i.e., when the size of the exciton wave function is similar to or smaller than the size of the In-rich agglomerations) and thus the local QW-width fluctuations govern the extent of linewidth broadening. This gives further weight to argument that excitons are confined only within the lateral InGaAs QW, with wave functions extending laterally across several In-rich agglomerations, as represented schematically in [Figure 4.12](#). If excitons were instead confined within the In-rich

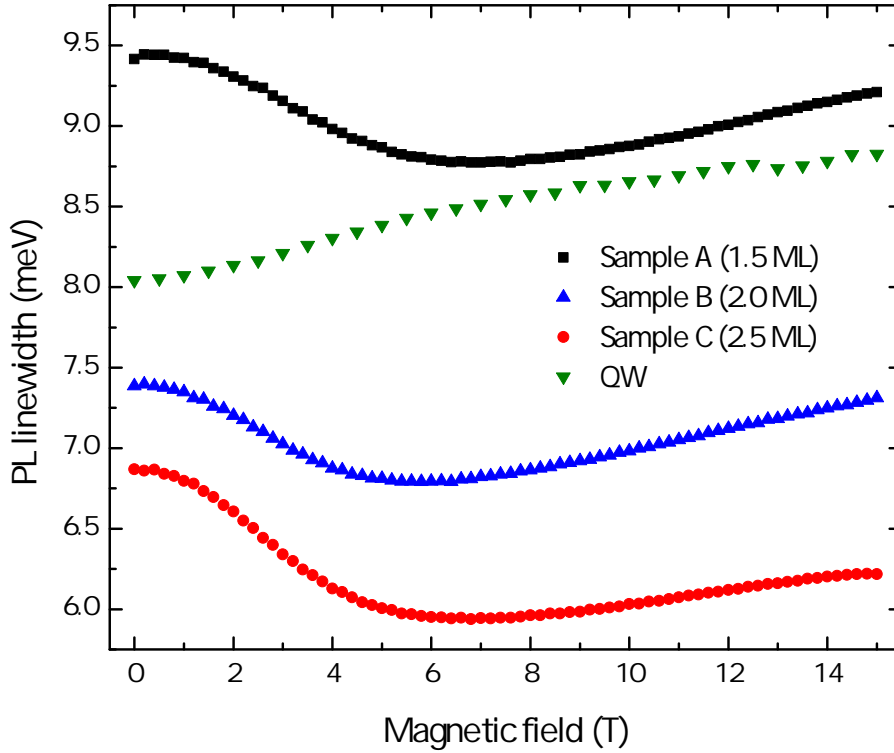


**Figure 4.11:** Faraday-geometry PL linewidth dependence on the magnetic field. Two disorder length scales result in the initial reduction in linewidth with field, followed by the subsequent monotonic increase.

agglomerations (were 0D), then their wave function would not see the larger scale fluctuations described by  $\chi_2$ . This is supported by the QW linewidth (green triangles in Figure 4.11), which shows only the monotonic increase due to there being no larger disorder length scale  $\chi_2$  and only the smaller well-width fluctuations.

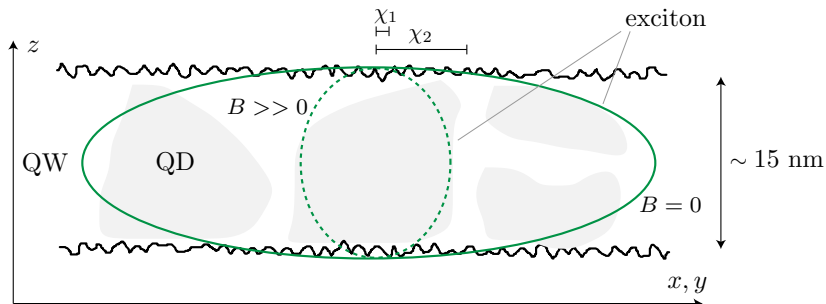


**Figure 4.12:** A schematic representation of the two disorder length scales,  $\chi_1$  and  $\chi_2$ , present in the SML samples. Ellipses illustrate exciton sizes at  $B = 0$  (solid line) and  $B \gg 0$  (dashed line). Applying a magnetic field squeezes the exciton so it only sees the smaller  $\chi_1$ , which is most likely due to monolayer fluctuations in the QW thickness.

The zero-field PL linewidths for the individual samples in Faraday and Voigt

geometry are different, whereas one would expect them to be the same. A likely explanation for this is systematic errors in the measurement setup: In Faraday geometry, the excitation light is shone straight from the optical fibre onto the sample, whilst in Voigt geometry, it is first reflected by  $90^\circ$  by a mirror. In this latter geometry, the light hits many different areas of the sample, systematically increasing the linewidth.

The conclusion from the data presented thus far is that excitons are unequivocally 2D: Zero-field linewidths are QW-like and depend on stack height, lateral Bohr radii extend over several In-rich agglomerations, vertical confinement is strong and governed by the stack height and linewidth dependencies on magnetic field show evidence for two disorder length scales, and, again, strong vertical confinement.

### 4.2.3 Evidence for a Zero-Dimensional System

In contrast to low-temperature measurements, a number of excited-state peaks can be resolved at high temperature, as demonstrated by the PL spectrum in [Figure 4.13\(b\)](#), taken at 17 T and 400 K for sample C in Faraday geometry. The field dependence of three of the most prominent of these peaks (the main PL peak and two excited-state peaks) is plotted in [Figure 4.13\(a\)](#), with the PL peak energies determined by a multiple-Lorentzian fit of the spectra. The fitted Lorentzian peaks are shown by red solid lines in [Figure 4.13\(b\)](#), their sum by the blue solid line, and the data are represented by the thicker black line. In apparent contradiction to our conclusion that the SML systems are 2D, the data can be fitted with a FD spectrum ([Equation 2.35](#)), indicative of a 0D system. This yields an exciton effective mass of  $(0.051 \pm 0.001)m_0$  and a confinement energy  $\hbar\omega_0$  of  $\sim 9$  meV.

All three SML samples show similar behaviour at high temperature. Data from sample C was chosen to be presented here as excited-state peaks were somewhat easier to resolve, compared to the other two samples. It is particularly interesting that excited-state peaks are present at high temperatures; of course, higher temperatures mean that carriers can be excited to higher energy states, but if these peaks are from the In-rich QDs, then clearly the extra thermal energy isn't enough to remove carriers from the dots. At 400 K,  $k_B T \approx 34$  meV, and thus the depth of the potential well confining carriers must be greater than this. We will return to

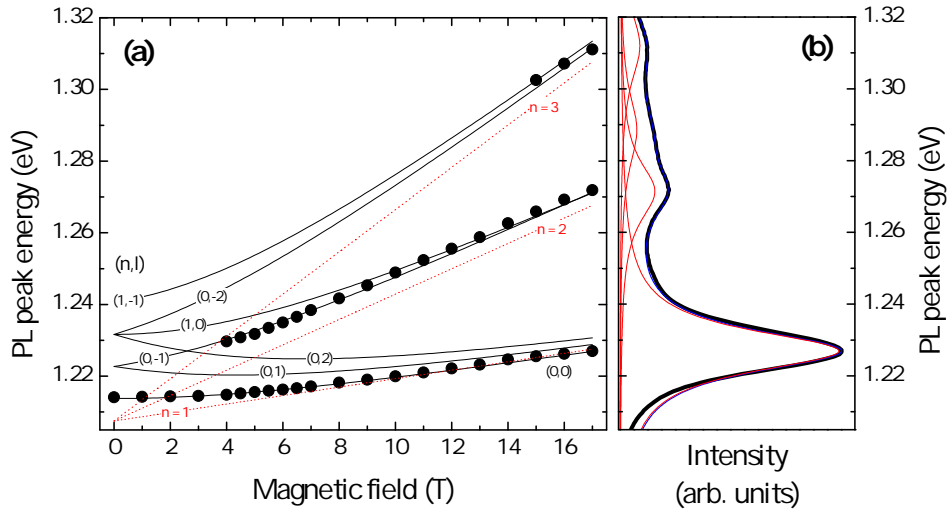


**Figure 4.13:** (a) 400-K magneto-PL for sample C in Faraday geometry. The solid lines are fits to a FD spectrum with Landau-level index  $n$  and orbital angular momentum  $l$ . The (red) dotted lines show the best attempt at a Landau-level fit. (b) 400-K 17-T spectrum corresponding to the 17-T data points in (a). The data are represented by the thick black line, the individual Lorentzian fitting peaks by the thin red lines, and the sum of the fitting peaks by the blue line.

this discussion later, armed with additional data.

#### 4.2.4 Comparison with the Quantum Well

The next logical step is to compare the magnetic-field dependence of excited states in the QW with that of the SML samples. However, whilst the SML samples show little dependence on laser power, the line shape and width of the QW PL spectra are greatly affected. Excited-state peaks become prominent as the power is increased, and at high temperatures this leads to a broad, unresolvable PL spectrum, as demonstrated by the 15-T 300-K spectra shown in [Figure 4.14](#) (Faraday geometry). It is clear that optical pumping is having a greater effect in the QW than in the SML samples, which is attributed to a shorter carrier lifetime in the SML samples.

To verify this, room-temperature TRPL measurements were performed on all four samples. [Figure 4.15](#) shows the decay data for the QW and sample A at their respective PL peak energies (986 nm and 1029 nm), highlighting an order-of-magnitude difference in the intensity-weighted average carrier lifetimes  $\tau$ . For sample A, the lifetime is  $\tau_{\text{SML}} = 4.5$  ns, whilst for the QW, it is  $\tau_{\text{QW}} = 43$  ns. Even shorter lifetimes of  $<1$  ns have been demonstrated at low temperature for SML samples in literature [[153](#)]. Similarly-fast decay times were seen for the other SML samples.

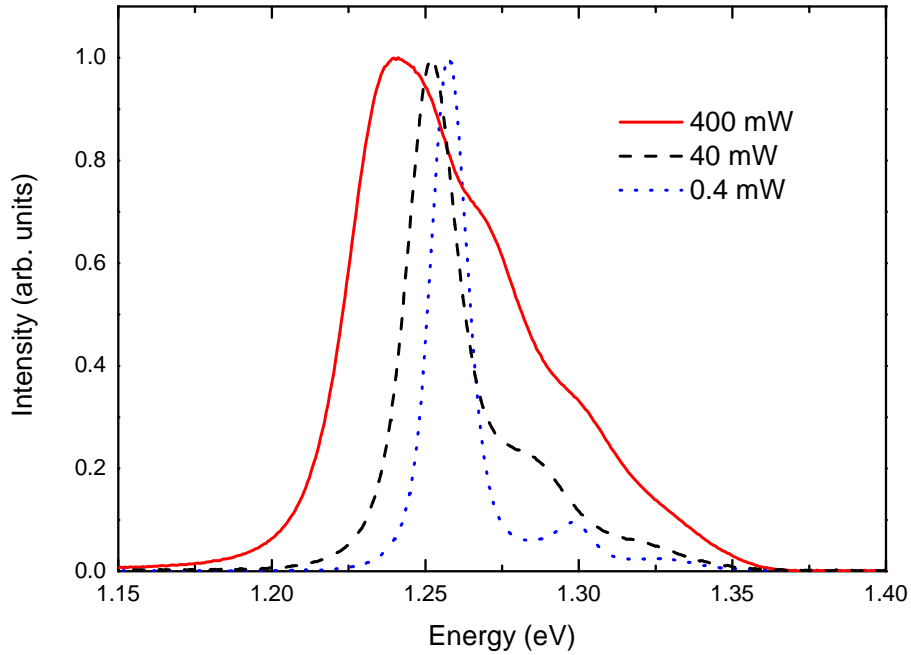


**Figure 4.14:** 15-T 300-K PL spectra of the QW sample in Faraday geometry with excitation laser powers of 400, 40 and 0.4 mW.

The SML time-resolved data show a slightly convex shape, as highlighted in the inset to [Figure 4.15](#) (which shows the same data as the main graph but focussing on this convexity). The rate of decay is therefore time dependent and this indicates that a second recombination process must be occurring. For SML systems, various plausible decay paths exist for excitons photogenerated in the GaAs barrier: Capture in the QW and direct recombination there; capture in the QW, relaxation to and recombination from QD states, or; direct capture in and recombination from QD states. Which of these dominates and which leads to the convexity cannot be determined from the SML data obtained, but nonetheless, we have highlighted the complex dynamics of carrier distribution after the initial optical pumping.

Because of this power-dependence of the QW sample, we compare the excited states in the SML samples at 300 K to the excited states of the QW sample at 2 K, or to put it another way; since we cannot observe optically populated excited states in the SML samples at low temperatures, we have to thermally populate them by using high temperatures. In contrast to the SML samples, the QW excited-state field dependence could not be fitted by a FD spectrum. Instead, PL peak energies follow a Landau-level fit ([Section 2.8.1](#)), yielding an exciton reduced mass

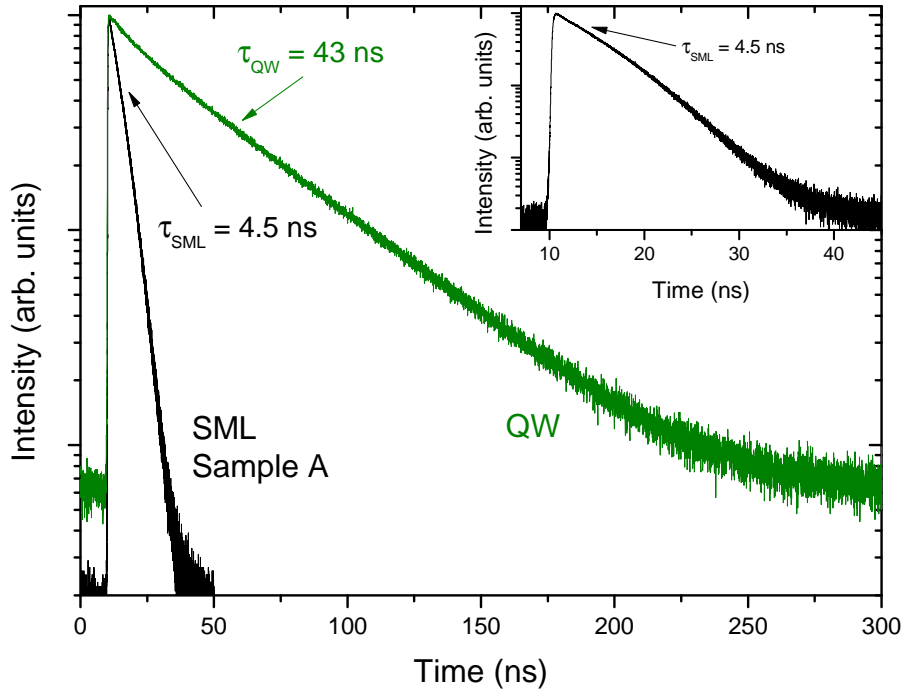


**Figure 4.15:** Room-temperature TRPL measured at the main PL peak wavelength of 1029 nm for sample A (black), and 986 nm for the QW (green). The intensity-weighted average carrier lifetimes  $\tau$  are indicated by the arrows. The inset shows the same data as the main graph for sample A, but enlarged so its convexity is clearer.

of  $(0.061 \pm 0.001)m_0$ . Figure 4.16 shows the 2-K excited-state field dependence of the QW sample with a Landau-level fit (solid black lines) and the best attempt at a FD fit (dashed red lines). This reinforces the notion that SML samples aren't simply an InGaAs QW, as initial measurements led us to believe, but at least at high temperatures, 0D states play a role in PL emission.

PL data were taken at a range of temperatures and this enables us to analyse the temperature dependence of the PL peak energies, comparing it to the empirical Varshni model introduced in Section 2.2.4. At high powers, all four samples show a good Varshni temperature dependence, so-much-so that the SML samples have been used to calibrate the thermometer in the laboratory. Figure 4.17 shows the high-power temperature dependence of the PL peak energy, with the expected range for  $\text{In}_x\text{Ga}_{1-x}\text{As}$  shown by the grey shaded area (the upper bound being for InAs, with  $\alpha = 0.276 \text{ meV K}^{-1}$  and  $\beta = 93 \text{ K}$ , and the lower bound being GaAs, with  $\alpha = 0.541 \text{ meV K}^{-1}$  and  $\beta = 204 \text{ K}$ ) [62]. The three SML samples and the QW fall within this, more toward the values expected for pure GaAs, as one would

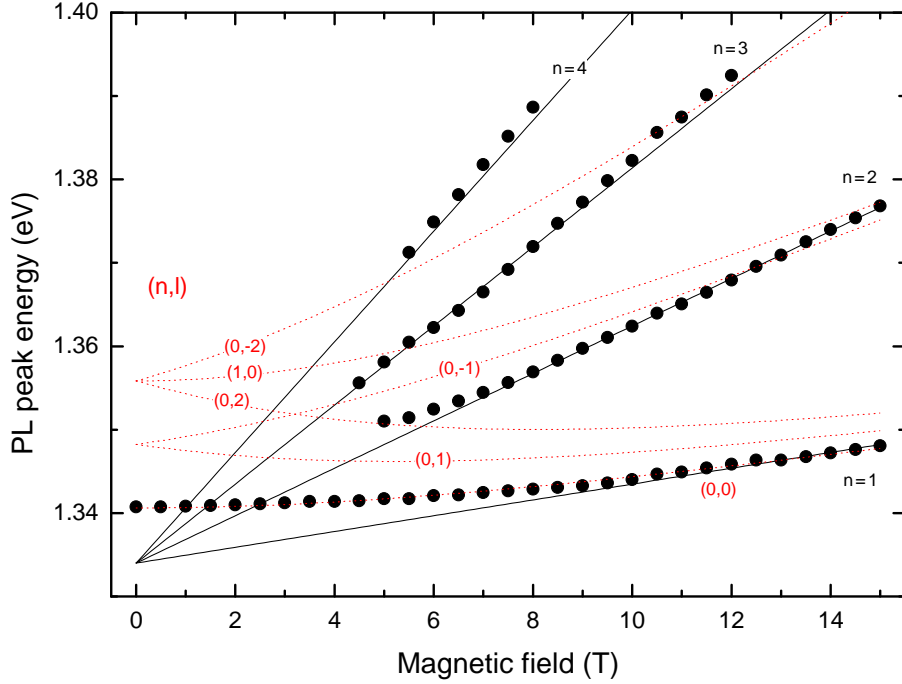


**Figure 4.16:** 2-K field-dependence of the main and excited-state PL peaks for the QW, in Faraday geometry. Solid (black) lines show a Landau-level fit, whilst the dotted (red) lines are the best attempt at a FD fit.

expect considering the smaller fraction of InAs deposited compared to GaAs. Values obtained from Varshni fits to the data, which for the SML samples all lie within the expected bounds when taking uncertainties into account, are presented in [Table 4.3](#). Values for the uncertainties are given by the fitting procedure and it is important to point out that the shape of the fitted line is relatively insensitive to the  $\beta$  parameter, providing large uncertainties. We see no trend in the Varshni parameters, though given the large uncertainties, it would be difficult to justify the validity of any trend that was seen. Interestingly, the QW Varshni parameters are larger than expected for GaAs.

At lower laser powers, an S-shaped dependence develops between 0 and 50 K, as highlighted by the enlarged plot of the temperature-dependence data for the QW and sample A, presented in [Figure 4.18](#). This is commonly attributed to potential fluctuations in the InGaAs QW [[176–178](#)], and owing to its appearance in the QW data, it is unlikely to be due to the In-rich agglomerations. The S-shaped curve is slightly more pronounced for the QW, though this effect is small compared

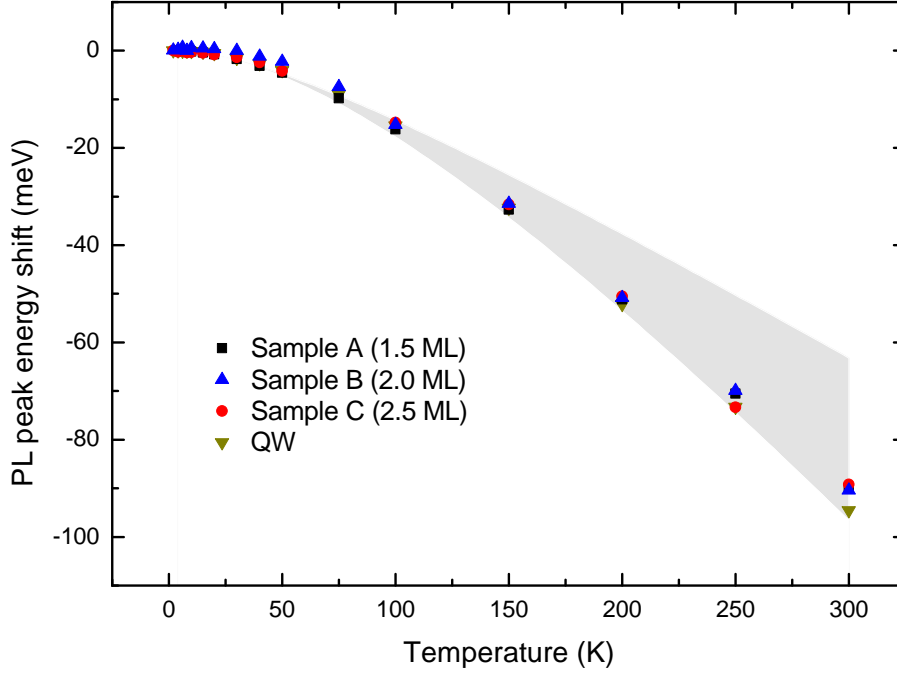


**Figure 4.17:** Temperature dependence of the PL peak energy for all four samples at high power (700 mW). Grey shaded area represents the expected range for  $\text{In}_x\text{Ga}_{1-x}\text{As}$ .

to SML samples with Sb incorporated, which show a strong localising effect than conventional SML systems [166]. This again demonstrates that the low-temperature excitonic properties of the SML samples are largely unaffected by the In-rich agglomerations. Indeed, the more pronounced S-shaped curve in the QW indicates that compositional fluctuations have a greater effect in the QW than the SML samples.

**Table 4.3:** Varshni parameters obtained from the fitting of data in Figure 4.17.

Sample	$\alpha$ (meV K <sup>-1</sup> )	$\beta$ (K)
A	$0.49 \pm 0.01$	$190 \pm 10$
B	$0.54 \pm 0.03$	$230 \pm 31$
C	$0.52 \pm 0.04$	$214 \pm 39$
QW	$0.59 \pm 0.04$	$261 \pm 19$

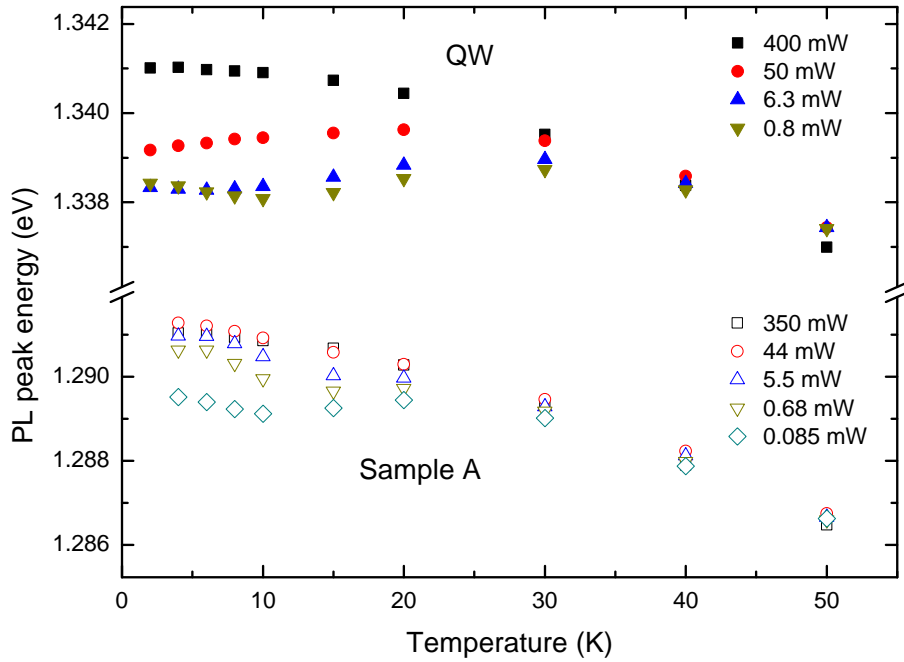


**Figure 4.18:** Temperature dependence of the PL peak energies for the QW and sample A, focussed on 0 to 50 K to show an S-shaped dependence at lower powers.

## 4.2.5 Heterodimensionality

To summarise our findings so far: Zero-field PL line shapes and widths demonstrated unequivocally QW-like emission, whilst magneto-PL supported this by showing large lateral Bohr radii extending over several In-rich agglomerations, and vertical Bohr radii governed by the stack height (QW thickness). Linewidth dependence on magnetic field in Faraday geometry demonstrated the presence of two disorder length scales, with excitons seeing both (QW-thickness fluctuations and In-rich agglomerations). In Voigt geometry, a lack of field dependence of linewidth supported strong vertical confinement. Temperature-dependence data demonstrated an S-shaped curve similar to the QW, again demonstrating their 2D nature. In contrast, at elevated temperatures, 0D states become visible.

We resolve this paradox by proposing that stacked layers of SML InAs in GaAs form a *heterodimensional* system: Heavy holes are confined in the In-rich agglomerations (QDs) and are thus 0D, whilst electrons are too light to be confined in these relatively shallow potentials, and instead extend over several of them, seeing only the lateral InGaAs QW (i.e., are 2D). The electrons, as the lighter and much more

extended charge carrier, define the low-temperature optical properties of the exciton and it is thus that we observe such strong 2D characteristics. It is only at high temperatures that excited hole states can become occupied, allowing observation of their 0D nature.

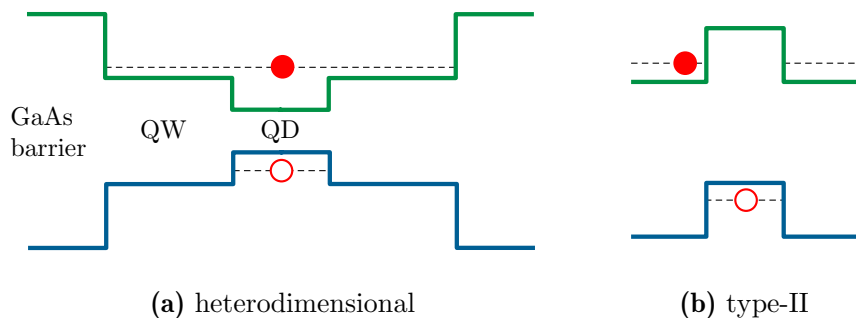


**Figure 4.19:** Example band structure of (a) a heterodimensional system, and (b) a type-II system.

This allows us to speculate more about the short nature of the TRPL carrier lifetimes. Localisation in compositional fluctuations in InGaN/GaN QWs is believed to inhibit the non-radiative recombination of carriers from defect states (believed to be the reason behind bright LEDs fabricated from this material system), and it makes sense that the In-rich agglomerations in the SML samples could similarly be preventing the capture of holes into defect states, thereby ensuring decay times are as fast as possible.

An example band structure of this system of 0D holes in 2D electrons is illustrated in [Figure 4.19\(a\)](#), and a schematic representation of the extent of electron and hole wave functions is shown in [Figure 4.20](#). It is important to point out the discrete difference between a heterodimensional system and a type-II system: In type-II systems ([Figure 4.19\(b\)](#)), either electrons or holes are prevented from occupying QD states due to a potential barrier, whilst in heterodimensional systems, a potential well exists for both carriers, but is only deep enough to confine the heavier holes.

### Modified Fock–Darwin

The FD fit presented in [Section 4.2.3](#) is a single-particle model, in which the exciton has assumed the role of the single particle, and thus the electron and hole effective masses are encompassed within the exciton reduced mass. We now have a value

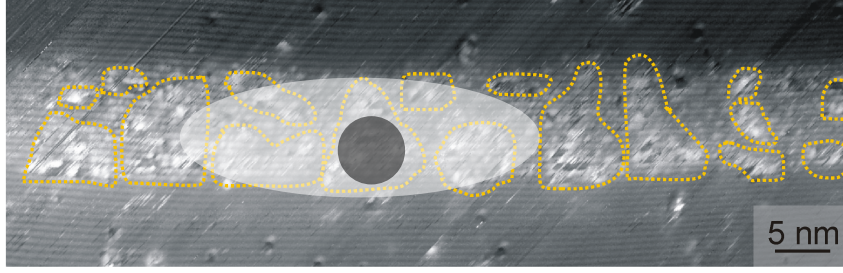


**Figure 4.20:** Schematic representation of the extent of electron (white) and hole (grey) wave functions in a heterodimensional system. Electrons see only the lateral InGaAs QW and extend over several In-rich QDs, whilst the heavier holes are confined within the QDs.

for the hole confinement energy,  $\hbar\omega_0^h \approx 9$  meV, and as the electron is unconfined, its confinement energy is zero ( $\hbar\omega_0^e = 0$ ). These can be used in the modified FD introduced in [Section 2.8.4](#) and demonstrated in [Reference 65](#), in which the exciton confinement energy is simply a sum of the electron and hole confinement energies,  $\hbar\omega_0 = \hbar(\omega_0^e + \omega_0^h)$ . In doing so, we are assuming that electron and hole wave functions are identical on the same atomic shell; this is of course not the case in a heterodimensional system, where the unconfined nature of electrons will mean their wave functions are different to those of the confined holes. However, we are only using this description to verify that our data can be fitted by a FD spectrum in which heterodimensionality exists, rather than in an attempt to obtain any meaningful parameters. Indeed, due to a large number of fitting parameters for this modified description, any parameters obtained have large errors—or conversely, a large range of fitting parameters will fit the same data. As such, this simplified technique is justified.

Using [Equation 2.36](#), the fit in [Figure 4.21](#) was obtained, yielding effective masses of  $m_e^* = 0.052m_0$  and  $m_h^* = 0.49m_0$ . These lie in between the InAs and GaAs effective masses of  $0.026m_0$  to  $0.067m_0$  for electrons, and  $0.41m_0$  to  $0.51m_0$  for holes [[62](#)]. Though the uncertainty on these values is large (and not stated as they are difficult to quantify), it is reassuring that InGaAs-like effective masses and heterodimensional confinement energies fit the data well.

## 4.2.6 Modelling

To give further weight to the argument that SML systems are heterodimensional, two sets of calculations were performed: One-band effective-mass and eight-band

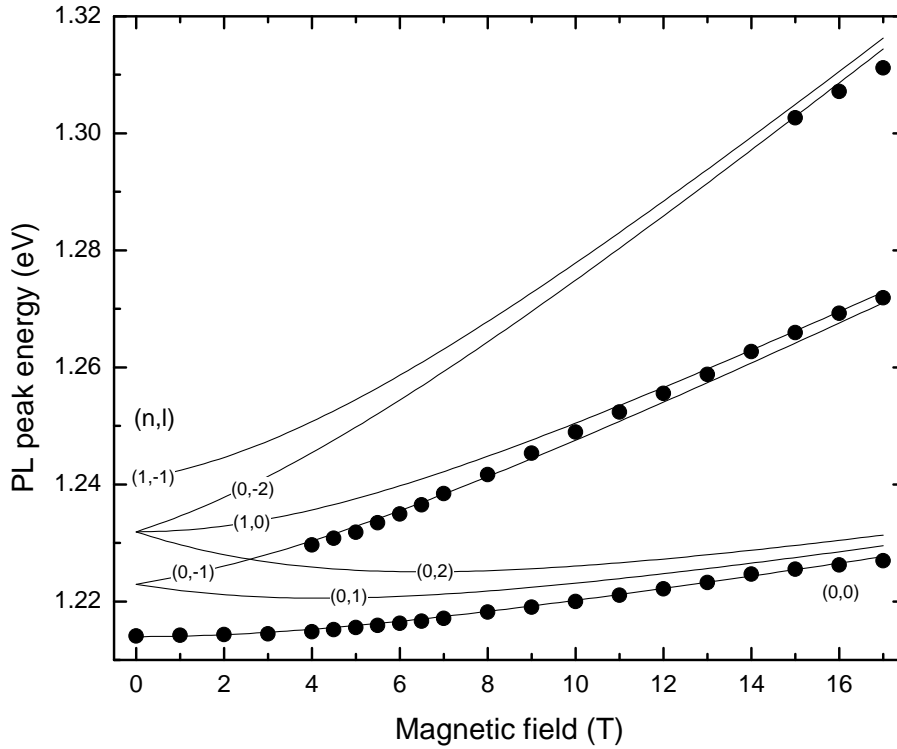


**Figure 4.21:** Same data as [Figure 4.13](#), but this time fitted with a modified FD (see [Section 2.8.4](#)), giving effective masses of  $m_e^* = 0.052m_0$  and  $m_h^* = 0.49m_0$ .

$\mathbf{k} \cdot \mathbf{p}$  calculations, the former undertaken at Lancaster University and the latter at Technische Universität Berlin.

### One-Band Schrödinger Calculations

COMSOL was used to calculate electron and hole energy levels in a model QW–QD heterostructure, using the method outlined in [Section 3.5.3](#). The Schrödinger equation was solved in 2D for each band separately and the results combined using a conduction-band:valence-band offset of 60:40. A schematic of the modelled system is shown in [Figure 4.22](#): A circular  $\text{In}_x\text{Ga}_{1-x}\text{As}$  QD with a diameter of 5 nm is embedded in a 13-nm-high  $\text{In}_y\text{Ga}_{1-y}\text{As}$  QW of infinite lateral width, all encased in a 300-nm-thick GaAs matrix. Parameters are from [Reference 62](#). Though this model is a very simplified representation of an actual SML system, it is justified due to the fact that the same physics is observed in all three samples, despite different spacer-layer thickness and thus differences in QD and QW In composition. Sample morphology is highly non-uniform in any case, making an accurately-representative

model covering an average SML system difficult to achieve. Strain is omitted because the strain profile is likely to be markedly different in a real SML system to a single dot in a well.

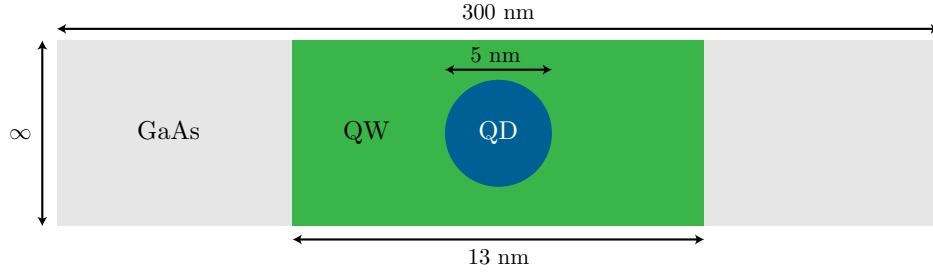


**Figure 4.22:** Schematic representation of the QW–QD heterostructure modelled, consisting of a 5-nm-diameter  $\text{In}_x\text{Ga}_{1-x}\text{As}$  QD in a 13-nm-high  $\text{In}_y\text{Ga}_{1-y}\text{As}$  QW.

As an initial step, a representative calculation was performed, based on  $x = 0.5$  and  $y = 0.15$ , the resulting band structure for which is shown in [Figure 4.23](#). As expected, the electron ground state is in the QW, whilst the hole’s is in the QD.

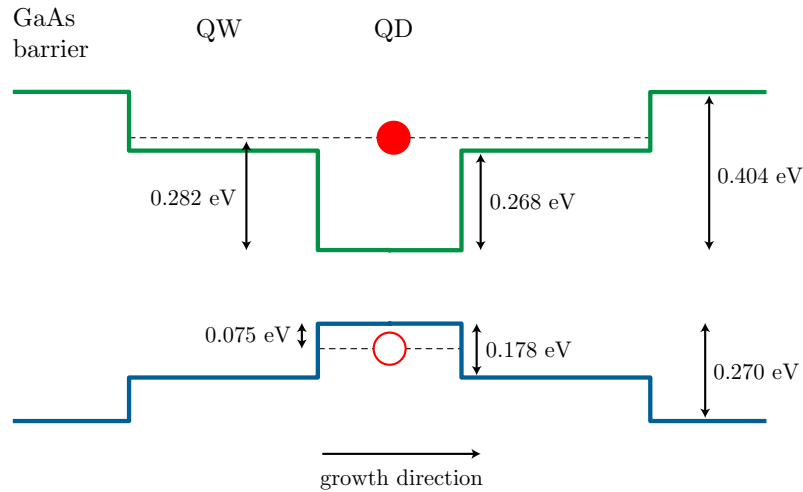


**Figure 4.23:** Calculated ground-state energy levels for an electron and hole in the system shown in [Figure 4.22](#), with an In content of  $x = 0.5$  for the QD and  $y = 0.15$  for the QW. The resulting confinement is heterodimensional.

To explore this further,  $x$  and  $y$  were then varied over a large parameter space of In composition, representative of the likely maximum and minimum in QD and QW In content. The minimum In content of the QD was taken to be  $x = 0.2$ , representing the maximal segregation of In through the SML stack for sample C (with biggest spacers and thus smallest average In content), with the maximum,  $x = 1$ , occurring if no In segregation occurs and all the In remains in the QD. The latter of these cases

corresponds to the minimum In content of the QW,  $y = 0$ , whilst the maximal In content in the QW occurs for the maximal segregation of In for sample A, and thus  $y = 1/3 \approx 0.33$ . These extrema cases are of course improbable, as demonstrated by XSTM [19, 20] and transmission electron microscopy [154] images.

Figure 4.24 shows a confinement “phase” diagram for differing In content. Three phases are present, one in which both electron and hole are confined in the QD (yellow), one in which the electron and hole see only the QW (blue), and the heterodimensional phase, where the hole is confined in the QD whilst the electron sees only the QW (green). Very strong clustering of In is required for both electrons and holes to be 2D, which for our modelled system implies  $x$  must be at least  $2.2y + 0.33$ . For both carriers to be 0D, the distribution of In must be very uniform, and  $x$  must be less than  $1.1y + 0.06$ .

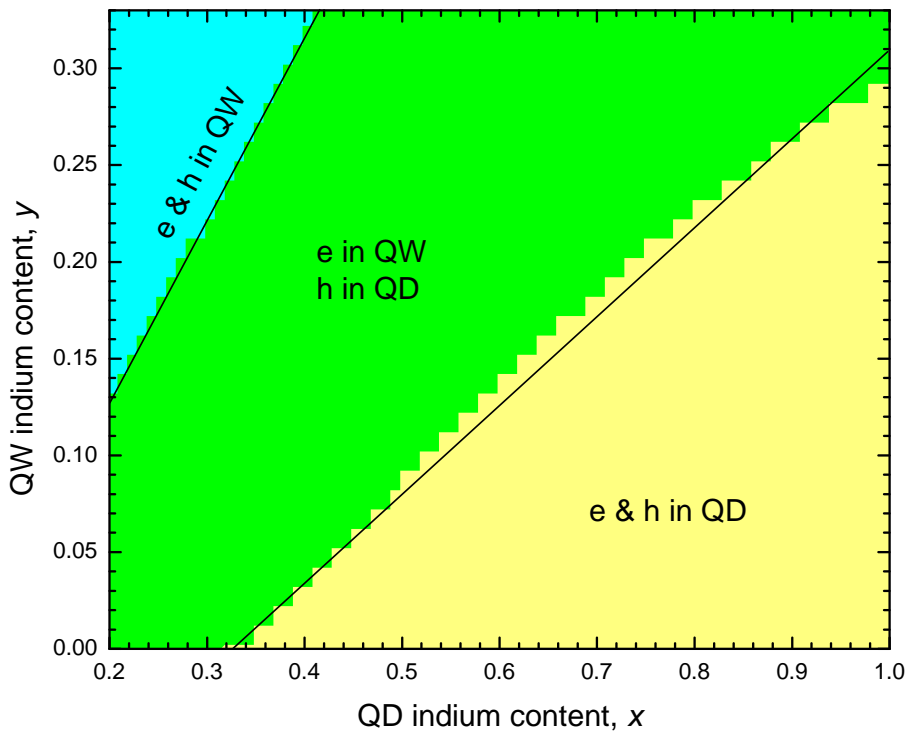


**Figure 4.24:** Phase diagram of electron  $e$  and hole  $h$  confinement for the system shown in Figure 4.22, with varying In content. The shaded regions are defined by the calculation, whilst the solid lines are guides to the eye indicating the approximate positions of the phase boundaries, corresponding to  $x = 2.2y + 0.33$  and  $x = 1.1y + 0.06$ .

The heterodimensional phase undoubtedly occupies the most probable parameter space and thus heterodimensionality is almost inevitable in this system, explaining

the similar behaviour of all three SML samples.

### Eight-band $\mathbf{k} \cdot \mathbf{p}$ Calculations

Eight-band  $\mathbf{k} \cdot \mathbf{p}$  calculations with a self-consistent Hartree approach were performed at Technische Universität Berlin, to model a periodic 2D array of 5-nm-diameter QDs in a 14-nm-high  $\text{In}_{0.25}\text{Ga}_{0.75}\text{As}$  QW. The Coulomb interaction between electrons and holes, as well as lateral coupling between dots, are taken into account, as is strain and piezoelectricity. The In content of each dot varies by a  $\cos^2$  function in the two orthogonal directions in the plane of the sample, superposed by a broad Gaussian distribution over all of the dots. This variation in In content is chosen to mimic the non-uniform morphology of the dots, whilst ensuring the exciton is centred on the middle dot. The peak In content in the centre of the middle dot is chosen to be 0.5 and 0.75, and a reference QW with no dots is also modelled.

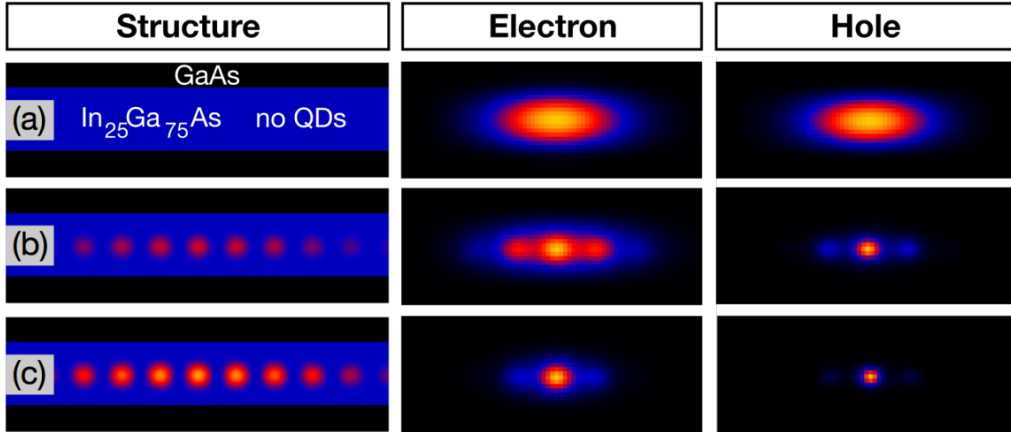


**Figure 4.25:** Colour contour plots of the electron and hole wave functions in a 14-nm  $\text{In}_{0.25}\text{Ga}_{0.75}\text{As}$  QW with (a) no QDs, (b) an array of QDs with In content  $x \leq 0.5$  and (c) an array of QDs with  $x \leq 0.75$ . The QD In content is defined by a  $\cos^2$  function for each dot, superposed by a Gaussian distribution spanning the entire array and centred on the middle dot. The left-hand panel shows this morphology, and the right two panels show the electron and hole wave functions.

Figure 4.25 shows the morphology of the model in the left panel, and the results from these calculations as colour contour plots of the electron and hole wave functions in the right two panels. For lower In content, the electron is delocalised over several dots, and increasing the In content increases the localisation. The hole is consistently more localised and less affected by lateral coupling. Coloumb attraction has an effect in localising electrons, but this isn't sufficient to eliminate the heterodimensional behaviour that these results demonstrate. The holes, which are

already localised, are affected less by the Coulomb interaction.

It is important to note that both sets of calculations only characterise the ground states of the charge carriers, and are thus strictly valid only at 0 K. Higher temperatures allow excited states to be occupied and carriers to be excited out of QD states and into QW states. This alters the heterodimensional phase of [Figure 4.24](#) slightly: The blue region, in which electrons and holes are both 2D, will be enlarged as holes are given extra thermal energy to escape the QDs. The yellow region, in which electrons and holes are both 0D, will shrink as electrons are pushed out of QDs and into the QW. The green region will shift according to the enlargement or shrinking of the other two regions. However, the size of this effect is small and the heterodimensional phase still occupies the most probable parameter space. At 400 K, the thermal energy  $k_{\text{B}}T \approx 34$  meV, which is relatively small compared to the confining potentials of  $>100$  meV illustrated in [Figure 4.23](#) (though any quantification from these simplified measurements is of course for the simplified dot-in-a-well model, not a real SML system, and as such should be treated with caution). Indeed, it is only heating to 400 K that enables the experimental observation of 0D excited states.

### 4.2.7 Discussion

The experimental and theoretical results presented in the preceding sections have demonstrated, unequivocally, that SML systems with spacer-layer thickness similar to those found in SML devices, are heterodimensional. Now, it is important to discuss the implications of this to our understanding of said devices.

We postulate that heterodimensionality is at least partly the reason why high-speed VCSELs have already been shown to operate at up to  $20 \text{ Gb s}^{-1}$  at  $85^\circ\text{C}$  [[160](#), [162](#)], using a device structure very similar to that studied here (10-fold 0.5 ML InAs / 2.3 ML GaAs). As discussed in [Section 4.1.3](#), the trapping of carriers in states not contributing to lasing, such as wetting layer states, is a key problem preventing the high-speed operation of conventional SK QD lasers. SML systems resolve this problem in two ways: Firstly, there are no wetting layer states for carriers to become trapped in, and secondly, the 2D electrons couple to several In-rich agglomerations

simultaneously, availing them to agglomerations that are lasing.

Holes are still confined in QD-like states and thus the advantages of a reduced density of states can still be exploited, such as a high material gain due to a reduction in the number of states that need to be filled to achieve a given gain. At the same time, the relatively shallow confining potential of the agglomerations means that excess holes cannot build up in agglomerations that are not lasing, where they can recombine via non-radiative mechanisms. High temperature stability is another key advantage of QD lasers and it is encouraging that these QD properties are robust up to 400 K; indeed, it was only these higher temperatures that enabled the occupation of excited hole states. This confinement of holes up to higher temperatures limits intrinsic losses, implying a decreased dependence of the threshold current on temperature.

Short carrier lifetimes, as demonstrated by TRPL measurements, validate this postulation of efficient carrier injection, with an approximately order-of-magnitude faster lifetime than the QW. The extended nature of photo-generated electrons means they are quickly available to recombine with holes. Efficient carrier injection is crucial for VCSELs with high modulation bandwidths, and thus fast data transfer for datacoms applications.

As discussed in [Section 4.1.3](#), various systems have been fabricated in an attempt to solve the carrier injection problem, such as the lateral coupling of QD states to enhance carrier distribution [134, 135], or the introduction of a QW injection layer close to SK QDs to allow the rapid tunnelling of electrons into lasing QD states [132]. Whilst these systems have been successful in, for example, increasing bit rates, they involve somewhat complicated growth procedures. On the other hand, SML systems are easy to fabricate, a key advantage when their production moves from research-based to commercial applications.

An inherently higher dot density is a fundamental advantage of SML systems, and whilst SK QDs can be fabricated with dot densities approaching that of the  $\sim 10^{12} \text{ cm}^{-2}$  seen for SML systems, this again requires somewhat more complex fabrication techniques. A high density of dots means that the 2D electrons are available to a large number of lasing states, increasing the material gain. The fact that these dots are not uniform seems to have little negative effect on optical properties and

device performance, since, at least at low temperatures, the extended electrons define the optical properties of the system. Even at high temperatures, PL emission is intense, relatively narrow and without magneto-PL measurements could well be believed to be entirely 2D.

It is not just lasers for which this uncovering of the underlying charge-carrier confinement in SML systems is of relevance. InGaN/GaN QWs demonstrate strong carrier localisation due to compositional fluctuations [179] and this phenomena is believed to be the reason behind the bright emission of GaN-based LEDs (which are ubiquitous in modern LED lighting), inhibiting the non-radiative recombination of carriers from defect states. Furthermore, the onset of “efficiency droop”—the reduction in efficiency of GaN-based LEDs at the high drive currents needed for typical lighting—coincides with the saturation of these localised states [180]. The concept of heterodimensionality and its consequences on carrier distribution could help explain, and possibly solve, this problem.

# Chapter 5

## Photoelectrolysis

This chapter focusses on the development of and results from a theoretical model of a semiconductor electrode for use in a photoelectrolytic system. The use of nanostructures at the SEI is proposed as a method of limiting the flattening of bands under illumination, thus increasing the maximum photovoltage that can be generated.

A review of current and historic research literature is presented in [Section 5.1](#), before a brief motivation behind our work in [Section 5.2](#) and an outline of the model scheme in [Section 5.3](#). Finally, results from this model are summarised in [Section 5.4](#).

### 5.1 Literature Review

This section documents some of the most relevant literature relating to the use of photoelectrolysis for the renewable production of hydrogen. In [Section 5.1.1](#), historical photoelectrolysis work is discussed, before more specific PEC designs and limitations are introduced in [Sections 5.1.2](#), [5.1.3](#) and [5.1.4](#).

#### 5.1.1 Historical Perspective

The first demonstration of oxygen evolution driven by sunlight was reported by Boddy [\[181\]](#) in 1968, using an n-TiO<sub>2</sub> single-crystal electrode, and early the following decade Fujishima and Honda [\[182\]](#) proposed such a system could be used in a PEC to split water. Their paper has to-date received a staggering 12,000+ citations, just missing out on a spot in the top-100 list of most-cited papers [\[11\]](#). A rush of

research activity ensued in the following decade, with various groups investigating different n- and p-type materials. n-TiO<sub>2</sub> was the most extensively studied, in various different forms, from oxide films to TiO<sub>2</sub> powder sprayed on a Ti sheet (e.g., [Reference 183](#), see [Reference 184](#) for more examples). In 1976, Dutoit et al. [[185](#)] reported on a detailed study of the frequency dispersion of n-TiO<sub>2</sub>, enabling them to construct Mott-Schottky plots ( $C^{-2}$  vs.  $V$ ) and as such obtain values for the flat-band potential, which at a pH of 7 lay around  $-0.3\text{ V}$  vs. SHE. These studies all required an external bias to shift bands to sufficient positions for water splitting to occur, and taking into account this extra energy from the power source, values for solar-to-hydrogen (STH) conversion efficiency (defined as  $\nu = (1.23\text{ V})(J_{\text{op}})/P_{\text{in}}$ , where  $J_{\text{op}}$  is the rate of hydrogen production converted to a current density, and  $P_{\text{in}}$  is the incident solar irradiance [[186](#)]) of around 0.6% were reported [[184](#), [187](#)].

The first semiconductor to electrolyse water without an external bias was n-SrTiO<sub>3</sub> [[188](#), [189](#)], with a flat-band potential of  $-1.2\text{ V}$  vs. SHE [[190](#)]. Various other n-type perovskites (e.g., KTaO<sub>3</sub> and K(TaNb)O<sub>3</sub>) and titanates (e.g., FeTiO<sub>3</sub>), as well as other oxides such as Fe<sub>2</sub>O<sub>3</sub>, were researched extensively with differing success [[184](#)]. The main limiting problems were instability, inadequate band gaps, or flat-band potentials much more positive than the hydrogen-production potential, thus requiring large biases.

P-type semiconductors were found to be much less successful, with p-GaP being reported as the only stable semiconductor that could photoelectrolyse with a reasonable external bias [[191](#)]. Other p-type materials such as GaAs, AlGaAs and InP were found either to be unstable or required too large a bias [[184](#)]. High STH efficiencies, of 11 to 13%, were achieved with p-InP, which absorbs into the near-infrared ( $\sim 920\text{ nm}$ ) [[192](#)]. However, In-based electrodes are unlikely to be viable in a commercial setting due to abundance and cost considerations [[193](#)].

These results of the preceding decade were summarised by a number of review papers at the end of the 1970s [[184](#), [194](#)]. The main conclusions were that, although significant progress had been made in demonstrating the feasibility of hydrogen production by photoelectrolysis, economic viability was still a long way off: Those semiconductors that had demonstrated a sufficiently negative flat-band potential to be able to split water without an external bias, had large band gaps and were

thus inefficient at absorbing sunlight. For example, whilst  $\text{TiO}_2$  has sufficient band positions, its valence band edge energy is so low compared to the oxygen-production potential that around 1.5 eV of the incident photon's energy is wasted [195]. The concept of a “hydrogen economy” was first mooted in literature around this time, with various authors postulating that the depletion of fossil fuels would lead to an increasing reliance on hydrogen [184].

The difficulty in surmounting the research challenges posed, along with a collapse in the price of crude oil at the end of the 1980s, led to a significant decrease of interest in photoelectrolysis in the proceeding decades [22]. It wasn't until the early 2000s that photoelectrolysis came into favour once more, in part motivated by substantial increases in funding for renewable technologies [195, 196]. The ensuing research saw a vast broadening in its scope, with the creation of a large array of extensions to standard PECs, of which a few of the most common and relevant will be discussed next. Numerous detailed reviews have been published, many of which are referenced here: For example, Ager et al. [186] present a comprehensive summary of experimental data from literature, with a particular focus on STH efficiencies and electrode stabilities.

### 5.1.2 Tandem (Multi-Junction) Cells

Few semiconductor materials have band edges that straddle both the oxygen- and hydrogen-production potentials, and those that do usually have band gaps so large that they absorb only a small fraction of the solar spectrum. One approach to address this problem is to use an n-type anode and a p-type cathode, illuminating both simultaneously. When the two electrodes are ohmically connected, their Fermi levels align and thus the conduction and valence band edges of the p-type material are higher than those of the n-type material, as illustrated in [Figure 5.1](#) for a simple p–n tandem PEC. In such a cell, the band alignments of the individual electrodes only have to align with their respective half-reaction potentials for water splitting to occur: The conduction band edge of the p-type material must be higher in energy (at a lower potential) than the hydrogen-production potential, and the valence band edge of the n-type material lower than the oxygen-production potential. Thus, our semiconductor material needn't have such a large band gap [184, 186, 197].

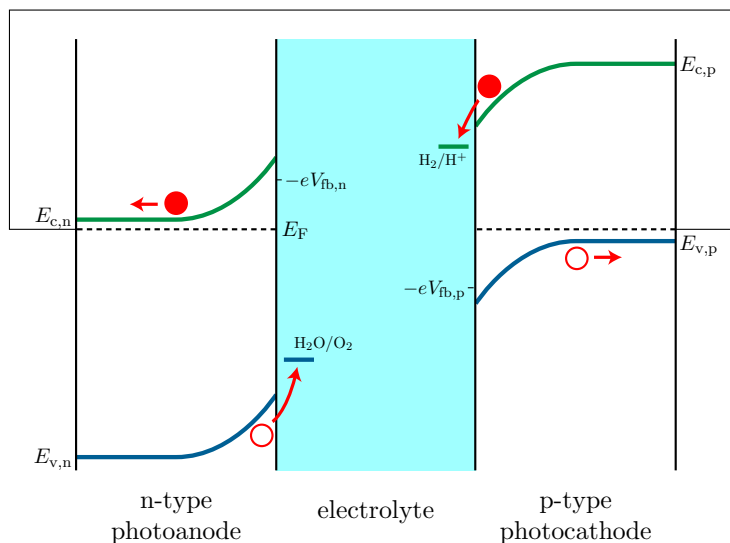


**Figure 5.1:** A simplified p–n tandem PEC, in which an n-type anode and p-type cathode are jointly responsible for providing the photovoltage to split water. The n-type valence band edge  $E_{v,n}$  and p-type conduction band edge  $E_{c,p}$  must straddle the oxygen- and hydrogen-production potentials, respectively.

This first demonstration of such a p–n PEC, using n-TiO<sub>2</sub> and p-GaP electrodes, was achieved by Yoneyama et al. [198]. The following year, Nozik [199] demonstrated the same material system could split water without needing an external bias, at the same time achieving a higher STH efficiency than a single electrode (though it was still low, <1%). Various other material systems were explored, such as n-GaP/p-GaP and p-CdTe/n-TiO<sub>2</sub>, with similarly low STH efficiencies and the ever-present plague of unstable electrodes [186].

Another approach to the tandem cell system is the use of a photovoltaic solar cell coupled to an electrolyser, the solar cell providing the photovoltage required to split water. In its simplest, most detached form, this could be a commercial solar cell coupled to a commercial electrolyser. More complex and integrated architectures, developed at the turn of the millennium, have demonstrated the highest STH efficiencies to-date: Over 16% was achieved at the U.S. National Renewable Energy Laboratory by Khaselev and Turner [200] and Khaselev et al. [201] using a multi-junction n/p-GaInP/GaAs structure, illustrated in Figure 5.2. The current record STH efficiency, of 18.3%, was achieved in 2000 by Licht et al. [202], using a complex AlGaAs/Si architecture. In the same paper, they theoretically calculate maximum STH efficiencies of 30% using InP/GaInAs as the photovoltaic material.

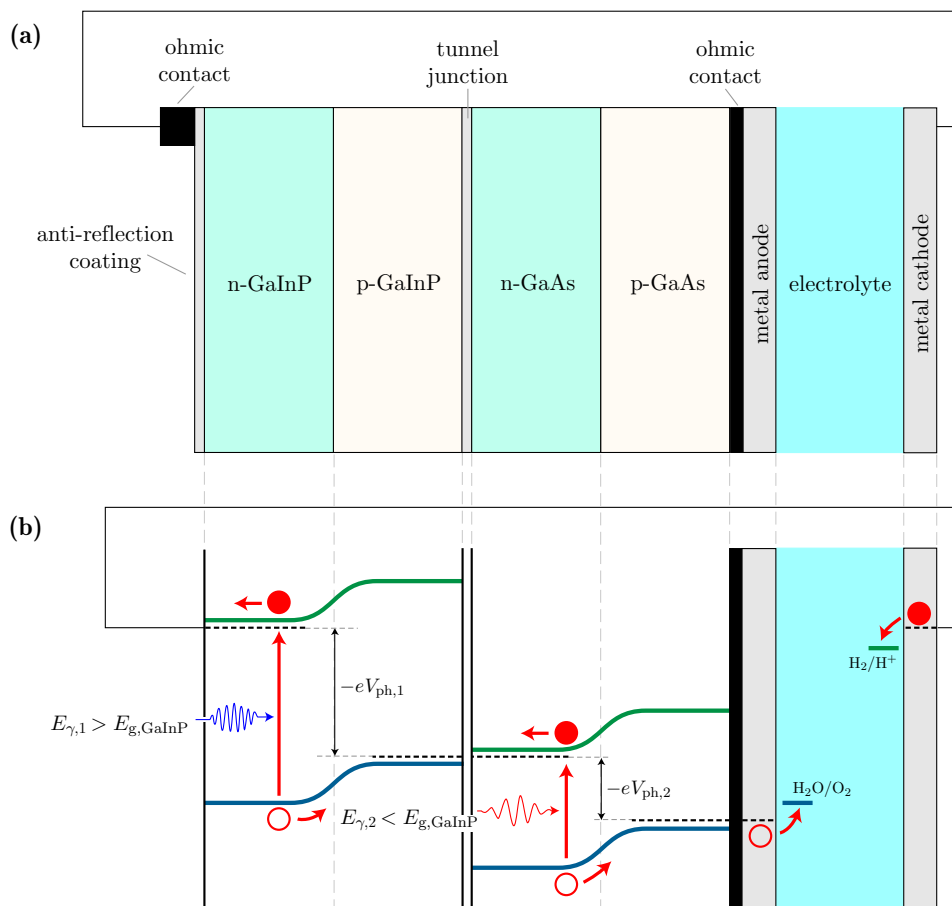


**Figure 5.2:** Simplified representation of a multi-junction n/p-GaInP/GaAs tandem PEC. **(a)** shows the layered structure, which can be thought of as a multi-junction photovoltaic solar cell ohmically connected to an anode and cathode such that the photovoltage drives the water-splitting reaction. **(b)** Band structure of the same cell architecture. Sunlight shines on the larger-band-gap GaInP; photons with an energy greater than the band gap of GaInP,  $E_{\gamma,1} > E_{g,\text{GaInP}}$ , are absorbed in the GaInP layers, whilst those with less energy than the band gap of GaInP pass through and (if their energy is greater than the band gap of GaAs) are absorbed in the GaAs layers. The p–n junctions in the two materials split up carriers and a photo-generated current ensues, leading to a separate photovoltage for each material,  $V_{\text{ph},1}$  and  $V_{\text{ph},2}$ .

In recent years, there have been significant efforts to create fully integrated devices (with complete contact between all components and therefore without any wiring), and in 2011, Reece et al. [203] reported an STH efficiency of 2.5% for such a device based on a three-junction amorphous-Si cell. As conceptually attractive as full integration may seem, it must be remembered that this brings the need for the immediate separation of the explosive mixtures of oxygen and hydrogen that are formed, consuming additional energy and therefore reducing the overall efficiency.

Whilst photovoltaic–electrolyser systems based on III-V and II-VI materials clearly rule the roost in terms of STH efficiencies, one should bear in mind other considerations: Such complex systems require complex, and often costly, semiconductor

deposition and processing. Furthermore, these systems utilise rare and expensive metals; they hardly meet the criteria of sustainability, which is a central aim of photoelectrolysis research. To this end, there has been much recent research focussing on Earth-abundant materials. In 2014, an STH efficiency of  $>12\%$  was achieved by the use of two perovskite solar cell in series, coupled to catalysts formed from Earth-abundant NiFe [204].

### 5.1.3 Nanostructured Electrodes and Nanoparticles

The research of thin-film electrodes has been prevalent since the 1980s, when a number of groups proposed their use to limit recombination losses [21]. The idea was to make an electrode thin enough so photo-generated carriers are readily available at the SEI, reducing the probability of recombination occurring. This developed into other forms of nanostructured electrode materials, such as mesoporous films [205] (made up of arrays of nanoscale crystals), nanorods and nanowires [195]. Such electrodes also enable the exploitation of quantum size effects (i.e., band-gap tuning), meaning more of the solar spectrum can be absorbed by the use of different sized nanostructures in the same device [75]. Success has been sporadic, but some notable improvements upon flat single-crystal electrodes have been reported. For example, mesoporous  $\text{TiO}_2$  has been shown to have an incident-photon-to-current conversion efficiency of 600 times that of a standard  $\text{TiO}_2$  electrode, attributed to better light harvesting and the improved photo-generation and collection of carriers [206]. Overall STH efficiencies remain modest, for example,  $10.4\%$  for nanocrystalline  $\text{TiO}_2$  films [207]. In 2011, Wang et al. [208] showed that water splitting is possible using GaN nanowires grown by molecular beam epitaxy, and more recently, in 2014, Wang et al. [209] demonstrated a tandem silicon/hematite core/shell nanowire array decorated with gold nanoparticles could split water without an external bias, achieving an STH efficiency of  $6\%$ . They postulate the nanowire array provides enhanced light absorption, rapid carrier collection and transport, along with the capturing of a large part of the solar spectrum, due to the presence of the narrower-band-gap silicon.

Of note when considering nanostructures is that, depending on their size, the creation of a complete space-charge region may not be possible [74]. Indeed, the

voltage drop across the nanostructure may be negligible and thus there is no significant electric field to separate carriers. Transport to the electrolyte interface—if the nanoparticle isn't small enough so that carrier wave functions already occupy the entire nanoparticle—will therefore be via diffusion (rather than drift) [195] and the photoresponse will be determined by the rate of electron and hole transfer to the electrolyte [75]: If electrons transfer faster than holes, the interface will act like a p-type SEI, and vice-versa if holes transfer faster than holes. The surprising consequence of this is that the same nanocrystalline film can exhibit n- or p-type behaviour, depending on the electrolyte used [210].

Suspended nanoparticles have also seen significant interest in literature, and water splitting by the use of a “powdered” semiconductor material was first demonstrated at the end of the 1980s, using  $\text{TiO}_2$  as the semiconductor [211, 212]. Nanoparticle PECs consist of a semiconductor powder (often an oxide) of nanoparticles, to which oxygen- and/or hydrogen-evolution catalysts can be fused (usually noble metals). The purpose of these catalysts is to lower the overpotentials required for oxygen and hydrogen evolution to occur, as well providing an interface to enhance charge carrier separation [205]. Each particle can be thought of as a separate PEC at which oxygen and hydrogen evolution occurs. A simplified schematic band diagram is shown in [Figure 5.3](#). Nanoparticle PECs are attractive due to their simplicity and lack of complex (and costly) electrode design. Furthermore, illumination does not have to be directional, as is the case for planar electrodes. However, as oxygen and hydrogen evolution occurs simultaneously, a method for the rapid separation of this explosive mixture must be included within any cell design, reducing the overall efficiency. This can be addressed in a number of ways, as discussed in [Reference 12](#) (such a discussion is beyond the scope of this thesis).

The size of the nanoparticles can have a large impact on their water-splitting ability [12]. Larger, micron-sized particles are often seen as desirable: The larger they are, the more likely that they are able to support a full space-charge region, resulting in more efficient charge-carrier separation. Furthermore, larger particles scatter incident photons more effectively, thus increasing the amount of light passing through the particles.

Today, STH efficiencies from nanoparticle PECs are still a long way off that of

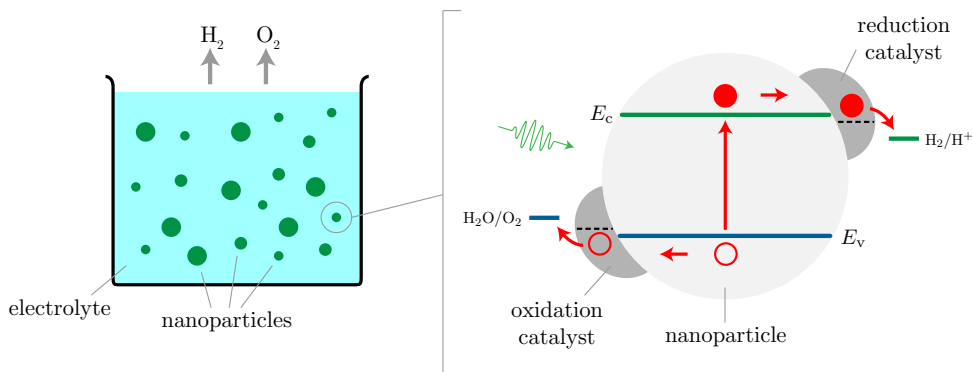


**Figure 5.3:** A simplified schematic band diagram of a small nanoparticle, from which photo-generated carriers transfer to the electrolyte via catalysts. Nanometre-sized particles, such as in this diagram, are too small to support a space-charge region, and transport is via diffusion (or simply because the carrier wave functions already occupy the entire particle). Micron-sized particles may encompass a space-charge region and charge transport is instead via drift. Adapted from [Reference 12](#).

their bulk counterparts [12]. To the author’s best knowledge, the current record stands at 5 %, achieved in 2014 by Liao et al. [213] using CoO in pure water, though the system was only stable for a few hours. In 2015, Liu et al. [214] achieved a high quantum yield—defined as the number of water molecules decomposed (split), divided by the number of photons absorbed—of 16 %, with a lower STH efficiency of  $\sim 2\%$ , by the use of carbon nanodots embedded in  $C_3N_4$ . Also of note is that these two examples split water without the use of catalysts, which are often fabricated from rare-Earth metals. Apart from these two examples, all other literature report STH efficiencies of  $<1\%$ , and quantum yields of  $<7\%$ . In other words, photoelectrochemical water-splitting by the use of suspended nanoparticles has not yet proven itself as efficient, stable, or cost-effective. A comprehensive review of literature relating to nanoparticle PECs can be found in [Reference 12](#).

### 5.1.4 Electrode Stability

Perhaps the second most fundamental problem facing photoelectrolysis research, after appropriate band alignment, is electrode lifetime. Typically, device lifetimes reported in literature are less than one day, and those devices with longer lifetimes are usually photovoltaic–electrolyser systems rather than integrated PECs [186]. Recently, the passivation of electrodes as a solution to instability has seen much attention. The standard approach is the deposition of ultra-thin, optically trans-

parent and conductive metal or metal-oxide films on the electrode surface [215], which if chosen correctly will provide a lower-energy route for charge transfer to the electrolyte, protecting the electrode. Furthermore, passivation may have the added bonus of removing surface states, which can trap carriers and worsen carrier transfer efficiency. Therefore, a carefully selected passivation layer may not only protect the electrode, but increase the overall efficiency of the device as well. A recent review of electrode surface passivation can be found in [Reference 216](#).

It is clear that, despite significant effort over the past four decades, fundamental problems still impede the progress of photoelectrolysis research toward commercial applications. Demonstrations of high efficiencies come from complex and costly PEC designs (e.g., multi-junction cells) or are based on expensive rare-Earth materials, whilst cost-effective devices rarely demonstrate efficient water-splitting capability (e.g., nanoparticles). All the while, electrode stability remains an ever-present problem. For research to progress, *innovation* in both materials development and device design is clearly needed.

## 5.2 Innovation Using Nanostructures

The limiting factor in a PEC's ability to generate hydrogen is the flat-band potential, which (for an n-type semiconductor electrode) must be higher in energy than the hydrogen-production potential. It represents the semiconductor Fermi level when illumination, and the subsequent flow of photo-generated carriers, has had the effect of completely flattening the bands. We propose the novel use of semiconductor nanostructures at the SEI to limit this band flattening and thus increase the maximum photovoltage that can be generated.

Type-II systems, such as GaSb/GaAs QDs, confine one carrier (e.g., holes), whilst the other is free to roam in the bulk material. Consider the placement of such nanostructures at the SEI: Upon illumination, excitons are generated near the surface of the semiconductor and soon split up by the built-in electric field. For an n-type semiconductor, electrons flow to the counter electrode, whilst holes travel towards the nanostructures at the SEI. If these nanostructures offer a suitable

confining potential, holes may become trapped. This excess of positive charges at the SEI counters the effect that the flow of carriers has in flattening the bands, thus increasing the maximum photovoltage that the PEC can generate and increasing the likelihood that the semiconductor (and therefore, counter-electrode) Fermi level will be pushed above the hydrogen-production potential. Of course, it is unlikely that this localisation of holes will completely stop their transfer to the electrolyte, but a certain transfer of holes is needed for oxygen production to occur at the SEI and thus for the two gas-evolution half reactions to proceed as a complete chemical reaction. An ideal schematic of the band structure of such a system is illustrated in Figure 5.4.

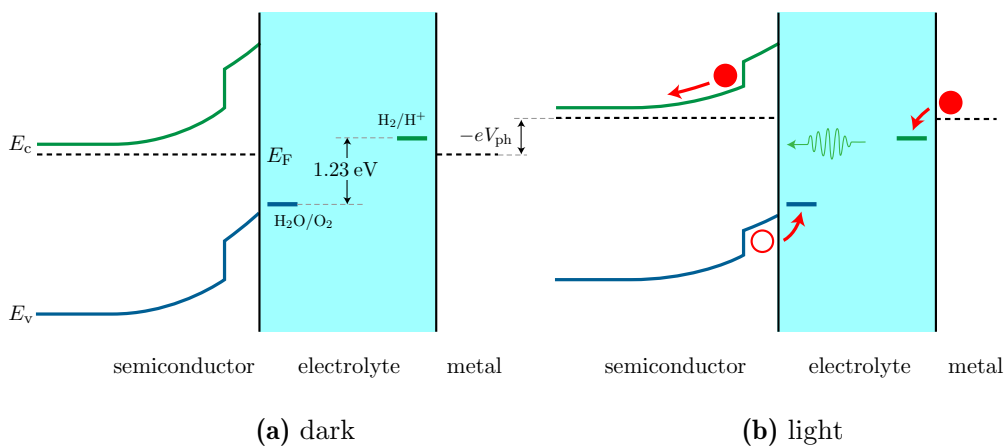


**Figure 5.4:** Ideal band structure of a PEC utilising nanostructures (e.g., QDs) at the SEI to limit the flattening of the bands due to photo-generated current.

The aim of the work presented here is to find a suitable material system, that meets the water-splitting requirements presented in Section 2.10.5, aided by the use of nanostructures at the SEI. To do so, a modelling scheme is developed, encompassing theoretical calculations from nextnano to calculate the band alignment, carrier distribution and energy levels in a semiconductor electrode.

### 5.3 Modelling Setup

Details behind the mathematical calculations, which were performed using nextnano, are outlined in Section 3.5.4. What remains here is to describe the structural setup and modelling methodology used to simulate a semiconductor electrode.

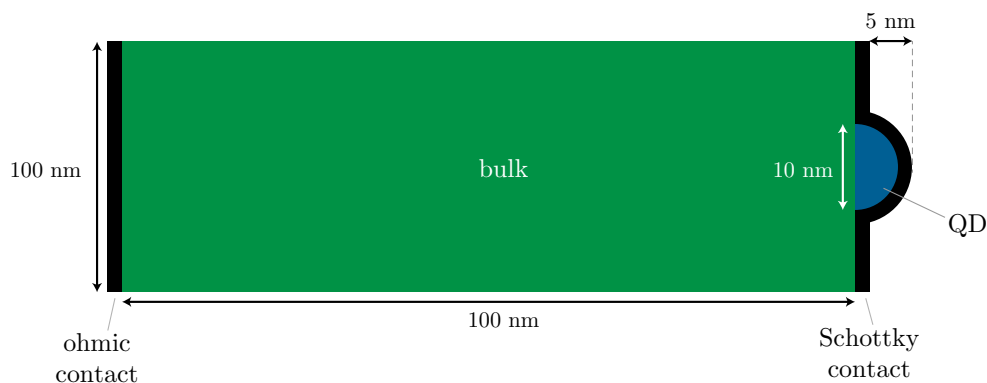


**Figure 5.5:** A simple two-dimensional (2D) semiconductor electrode model with a QD included at the SEI.

Figure 5.5 shows a simple 2D semiconductor electrode. The bulk substrate material is back-contacted with an ohmic contact (that in a real PEC would be connected to the counter electrode). On the surface of the bulk material is a 10-nm-diameter, 5-nm-high QD, and the SEI is in turn contacted by a Schottky junction. This Schottky junction mimics the band bending at the SEI. The self-consistent solving of the drift–diffusion, Schrödinger and Poisson equations gives us information about the energy levels and current distribution. The inclusion of strain in the calculation requires that the model must be 2D (or higher) rather than 1D. The dimensions of the bulk semiconductor electrode material are likely to be much larger in practice (i.e., in the order of mm), however the 100 nm chosen is sufficiently large that results are the same as if it were that large.

The Schottky junction requires, as an input, the Schottky barrier height, which is calculated using the method outlined in Section 2.10.4, using values from literature. The key question when modelling nanostructures at the SEI is whether the Schottky barrier height should be calculated for the substrate or the nanostructure(s). In the case of SK QDs on the surface, the majority of contact with the electrolyte will be with the bulk semiconductor (in the spaces between the dots) and this will lead to the formation of a space-charge region in the bulk material that would be expected for a standard bulk-SEI. The QDs are likely to be too small to support a full space-charge region, but this should not affect the ability of the bulk semiconductor’s space-charge region to split up photo-generated carriers (which are likely to be generated in the bulk semiconductor); that is, it is the bulk Schottky barrier height that determines the carrier-splitting capability of the electrode, and will thus be used in calculations.

This approach has been employed before in literature, for example, in the case of a thin film of colloidal QDs at a Schottky junction [217].

The calculations performed in this thesis are intended as a proof of concept rather than an all-encompassing first-principles physical calculation, which we believe is unnecessary at least until the desired material system has been tested experimentally and proven to produce desirable results. At that later stage, a more rigorous calculation to model the constructed system could provide invaluable feedback, or indeed vice versa, the experimental data could help refine a complete theoretical model. Extensions to the current model could include optical absorption (e.g., the Beer–Lambert Law), carrier transfer at the electrodes (e.g., the Butler–Volmer equation) and mass transport in the electrolyte [218].

## 5.4 Results

The aforementioned model was used with a wide variety of material systems to test their suitability for photoelectrolysis. An introductory model of band bending in bulk InGaN, chosen as the substrate, is implemented and discussed in Section 5.4.1, before various type-II systems are modelled in Section 5.4.2. In Section 5.4.3, the best of these type-II systems are explored further, before band bending at the SEI for a QD system is elucidated in Section 5.4.4. Finally, the findings from these results are discussed in Section 5.4.5.

### 5.4.1 Bulk Semiconductor Electrodes

A good start for the selection of a suitable semiconductor electrode material system utilising QDs at the SEI, is to ascertain what bulk material has suitably positioned band edges to be able to split water. Recently,  $\text{In}_x\text{Ga}_{1-x}\text{N}$  has shown great promise in literature, in part due to a tunable band gap (achieved by varying the In content  $x$ ), high carrier mobilities and a good chemical stability [15, 208, 219, 220]. As will be seen later, the band alignment of InGaN means fabricating a type-II system is easily achievable. Thus, it seems InGaN is a sensible material with which to start. In a similar vein, a type-II system is easier to achieve using an n-InGaN, and therefore that is what will be studied here.

InGaN typically forms a wurtzite lattice structure, however, under certain conditions and when grown on a zinc-blende substrate, it can take a zinc-blende form. The materials of the two differing lattice structures of InGaN are similar but discretely different (e.g., the electron effective mass is  $0.20m_0$  for wurtzite and  $0.15m_0$  for zinc-blende [13]). Unfortunately, this distinction isn't always made in literature, and fewer reliable material parameters exist for zinc-blende InGaN, due to its relative rarity. Therefore, it seems reasonable to assume that any parameters for which the crystal structure isn't explicitly stated are for wurtzite InGaN.

## GaN

It soon becomes apparent, upon researching input parameters for the model, that there is sparse agreement in literature on a number of these parameters. For example, experimentally- and theoretically-determined values for the electron affinity of GaN range from 2.6 to 4.1 eV [6, 221], flat-band potentials at a pH of 0 from  $-0.65$  to  $-0.38$  V vs. SHE, and the dependence of  $V_{fb}$  on pH from 45 to 71 mV per pH unit. This leads to a large variance in the height of the Schottky barrier, as shown in Figure 5.6 for a pH of 7, which also includes an error of  $\pm 0.2$  V for the electrode–vacuum potential conversions (Section 2.9.1). For smaller electron affinities, the Schottky barrier becomes negative, which seems unlikely given that water splitting has been experimentally demonstrated using GaN [222, 223]. Indeed, a value of  $\phi_B \approx 0.8$  eV has been reported for various alkaline solutions [224].

We can work back from this literature value for the Schottky barrier (using 0.77 eV in potassium chloride, pH  $\approx 11$ ) to obtain a value for the electron affinity. The flat-band potentials at this pH demonstrate less variance (due to their dependence on pH also varying), all falling at around  $-1.1 \pm 0.1$  V vs. SHE, where the error value is obtained from the standard deviation in literature values. The electron affinity is calculated to be  $\chi = 4.0 \pm 0.2$  eV. The dotted lines in Figure 5.6 illustrate this when  $\chi = 4.0 \pm 0.2$  eV is used to compute the band structure at a pH of 7, resulting in a Schottky barrier height of  $\phi_B = 0.5 \pm 0.3$  eV.

Of course, it is difficult to state any conclusion with certainty from these plots. Instead, they serve to highlight the challenges in accurately modelling band bending in photoelectrolytic systems. It is somewhat reassuring that calculated values almost

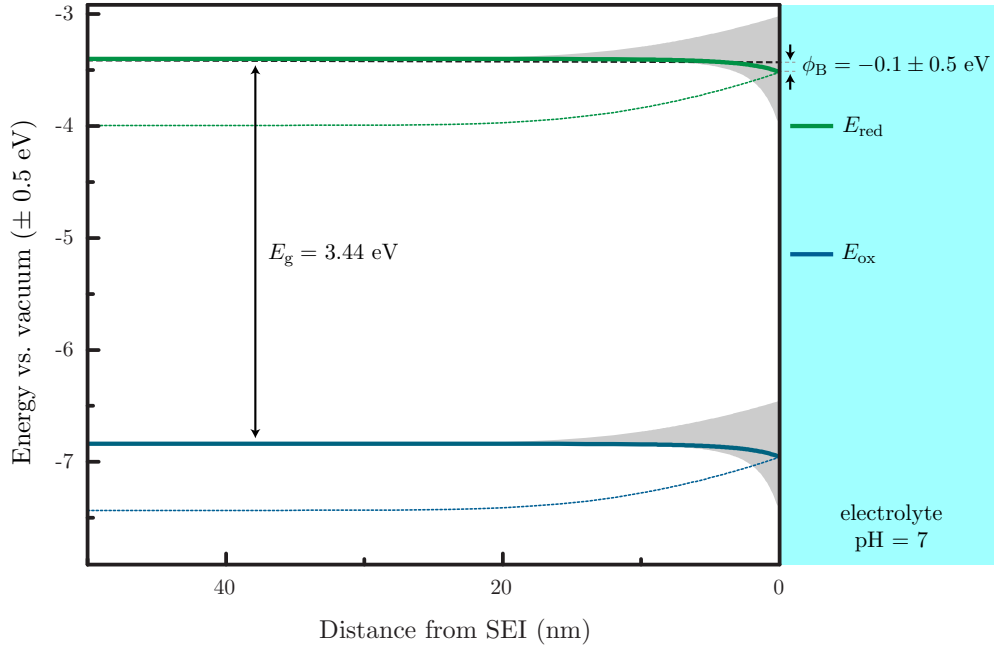


**Figure 5.6:** Simulated band structure of a wurtzite n-GaN semiconductor electrode in water (pH = 7) with a dopant (Si) concentration of  $1 \times 10^{18} \text{ cm}^{-2}$ . For  $\phi_B = -0.1 \pm 0.5 \text{ eV}$  (deduced from  $\chi = 3.4 \pm 0.5 \text{ eV}$  and  $V_{fb} = 3.5 \pm 0.2 \text{ V}$  vs. vacuum), the conduction band edge is shown as a green solid line, the (heavy hole) valence band edge as a blue solid line and the Fermi energy as a dashed black line. The uncertainties in the band edge values are shaded in grey. For  $\phi_B = 0.5 \pm 0.3 \text{ eV}$  (obtained from literature), an electron affinity of  $\chi = 4.0 \pm 0.2 \text{ eV}$  is obtained and the subsequent conduction and valence band edges are shown as dotted lines (uncertainties are omitted for clarity). Other parameters were taken from Reference 13 or the nextnano database [14]. Band edges are positioned relative to the vacuum by the electron affinity, and it is this that gives rise to the  $\pm 0.5 \text{ eV}$  uncertainty in the energy axis. The hydrogen- and oxygen-production potentials are positioned using Equations 2.50 and 2.52, such that  $E_{red} = 4.0 \pm 0.2 \text{ V}$  vs. vacuum and  $E_{ox} = -5.2 \pm 0.2 \text{ V}$  vs. vacuum. The error arises from their conversion to values relative to the vacuum from values relative to the standard hydrogen electrode (SHE).

compare when uncertainties are taken into account (e.g.,  $\phi_B = 0.5 \pm 0.3 \text{ eV}$  taken from the literature value of the Schottky barrier and flat-band potential, and  $\phi_B = -0.1 \pm 0.5 \text{ eV}$ ) as calculated from literature values for the electron affinity and flat-band potential). We speculate that, as water splitting has been demonstrated using GaN as an electrode [222, 223], the electron affinity lies more toward the higher of the literature values, but not large enough to push the conduction band edge to a lower energy than the hydrogen-production potential; a value of a little less than 4 eV seems reasonable.

## InGaN

Values for the electron affinity of InN suffer from similar uncertainties, ranging from 5.1 to 5.8 eV [221, 225]. We shall assume a value of  $5.5 \pm 0.3$  eV, based on the average and corresponding standard deviation in these values. The electron affinity for InGaN can thus be interpolated, using a bowing parameter of 1.4 eV [13] for the band gap of InGaN, in the knowledge that the band gap bowing has been shown to be purely due to the bowing of the conduction band edge [221]. There are fewer literature values of the flat-band potential of InGaN with varying In content, though it is well established that it increases in potential with increasing In incorporation [15, 226]. Beach [15] observed the flat-band potential at an In content of  $x = 0, 0.045, 0.085$  and  $0.140$ . At a pH of 7, the difference between  $V_{fb}$  when  $x = 0$  and when  $x = 0.140$  was 0.2 V, corresponding to a shift of  $\sim 0.14$  V per 10% In content increase.

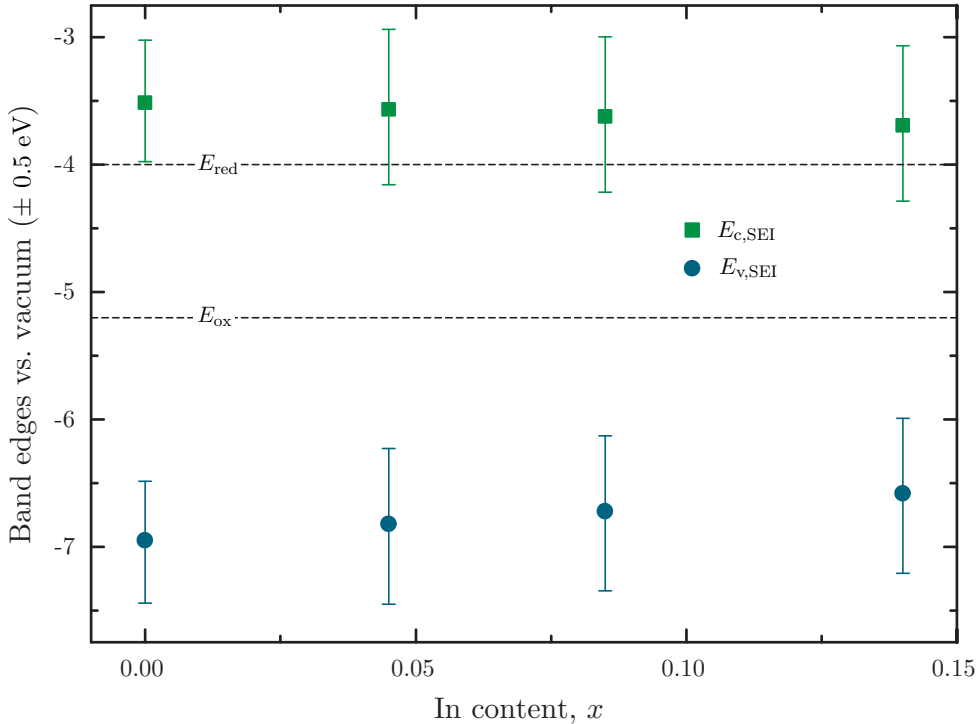


**Figure 5.7:** Conduction and (heavy hole) valence band edges at the SEI,  $E_{c,SEI}$  and  $E_{v,SEI}$ , for varying In content. Values for  $V_{fb}$  were taken from Reference 15 and  $\phi_B$  was calculated using these and a non-linear interpolation of  $\chi$  from  $3.4 \pm 0.5$  eV for GaN, to  $5.5 \pm 0.3$  eV for InN, with a bowing parameter of 1.4 eV [13].

For illustrative purposes, a plot of the calculated SEI conduction and valence band edges at these four In content values, alongside the hydrogen- and oxygen-

production potentials, is shown in [Figure 5.7](#). As expected, the valence band edge at the SEI is consistently lower in energy than the oxygen-production potential  $E_{\text{ox}}$ . The conduction band edge at the SEI is always higher than the hydrogen-production potential  $E_{\text{red}}$ , though not within the uncertainty limits. Beach [15] discovered that, at a pH of 7, only the samples with  $x = 0$  and  $x = 0.045$  had an SEI conduction band edge clearly above  $E_{\text{red}}$ , whilst for the sample with  $x = 0.085$ , it was almost at the same value, and for the sample with  $x = 0.140$ , it lay below  $E_{\text{red}}$ . As before, the uncertainties are too large to come to any definite conclusion, though it is clear that hydrogen evolution is only likely for  $\text{In}_x\text{Ga}_{1-x}\text{N}$  with a low In content. The following investigation will therefore focus on the use of  $\text{In}_x\text{Ga}_{1-x}\text{N}$  with  $x < 0.3$  as the bulk material for the semiconductor electrode.

#### 5.4.2 Type-II Quantum Dot Materials

The next step is to select a material for the QDs at the SEI that has band edges aligned such that a hole-confining type-II system is formed. Fortunately, the exceptionally low valence band edge and relatively low conduction band edge of GaN means that a type-II system is easily achievable. Twenty of the most common semiconductor materials were investigated as a material for the QD, grown on top of bulk n-GaN. The band structure was computed by eight-band  $\mathbf{k} \cdot \mathbf{p}$  calculations in `nextnano`, and the resulting values for  $E_{\text{F}} - \varepsilon_{\text{h},0}$  are shown for each system in [Figure 5.8\(a\)](#), where  $\varepsilon_{\text{h},0}$  is the lowest heavy hole energy state in the QD. Immediately noticeable was that, of these twenty material systems, only two exhibit type-I behaviour (AlN and CdTe, highlighted by hollow bars), whilst a further two have a type-II broken-gap band alignment, indicated by a negative  $E_{\text{F}} - \varepsilon_{\text{h},0}$ , and a further few (e.g., GaAs and InAs) are a borderline case between normal type-II and type-II broken-gap. A few material systems, such as CdSe, unexpectedly formed a type-II system, despite literature values for band edges implying a type-I system [227]. The explanation for this is that strain from the lattice mismatch between GaN and, for example, CdSe, has the effect of pushing up the QD conduction band edge so that it exceeds the bulk conduction band edge. In contrast to the previous section, no contacts were applied and hence the Schottky barrier at the SEI isn't taken into account.

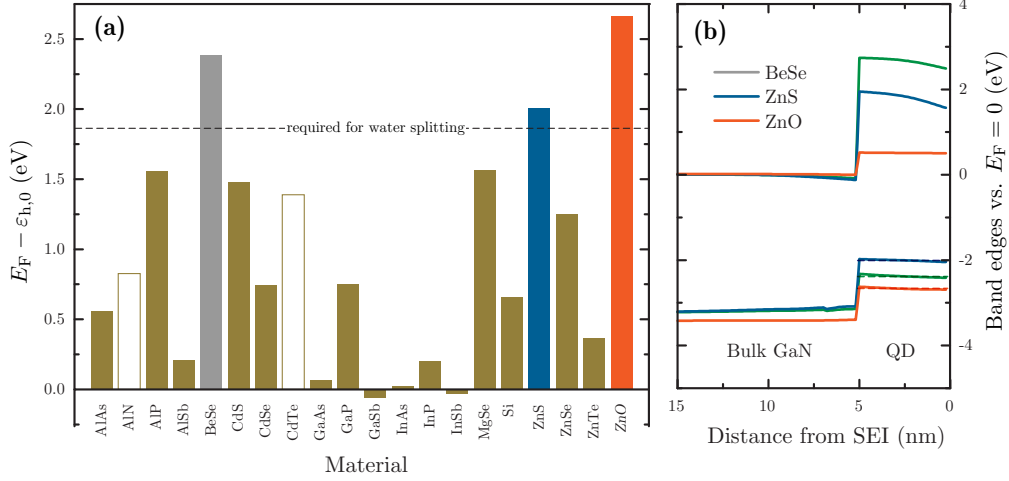


**Figure 5.8:** Eight-band  $\mathbf{k} \cdot \mathbf{p}$  calculations with strain, for a QD fabricated from different materials, grown on n-GaN. Italics indicate that the ZnO/n-GaN system is wurtzite (growth along the  $l$  axis), whilst the others are zinc-blende. The data are from a one-dimensional (1D) slice through the centre of the dot, along the growth direction. (a)  $E_F - \varepsilon_{h,0}$  for each of the different materials, of which three clearly meet the water-splitting requirement that  $E_F - \varepsilon_{h,0} > 1.8$  eV. Two of the materials (shown by hollow bars) result in a type-I system, whilst the rest are type-II (with broken-gap alignment highlighted by a negative  $E_F - \varepsilon_{h,0}$ ). (b) Band alignment of the three systems that meet the water-splitting requirement, showing the conduction band edge  $E_c$  and the (heavy hole) valence band edge  $E_v$  (solid lines), along with the first of the confined hole states  $\varepsilon_{h,0}$  (dashed lines).

Section 2.10.5 tells us that the band gap of the semiconductor electrode must be greater than 1.8 eV for water splitting to occur. This requirement is driven by the need for the electron-donating and electron-accepting states to straddle the hydrogen- and oxygen-production potentials, and in a hole-confining type-II system, it is the counter-electrode (and hence, upon equilibration, bulk-semiconductor) Fermi level  $E_F$  that is the electron-donating state, and the lowest of the confined hole states  $\varepsilon_{h,0}$  that is the electron-accepting state. Thus, the requirement should be modified such that it is  $E_F - \varepsilon_{h,0}$  that must be greater than 1.8 eV, not the band gap.<sup>1</sup> As such, it is this value that is presented in Figure 5.8(a), with the dashed line representing the threshold for this condition to be met. The band alignments of the three materials that satisfy it—BeSe, ZnS and ZnO—are shown in Figure 5.8(b), along with the first of the confined hole states (indicated by the dashed lines).

Of course, the requirement that  $E_F - \varepsilon_{h,0} > 1.8$  eV serves to exclude certain

<sup>1</sup>Depending on which text one reads, the original condition that  $E_g > 1.8$  eV may or may not take into account the energy loss of  $\alpha = E_c - E_F$  when electrons transfer from the conduction band edge in the semiconductor to the Fermi level in the counter electrode. The use of  $E_F$  in the new condition ( $E_F - \varepsilon_{h,0} > 1.8$  eV), as opposed to  $E_c$ , is inconsequential as  $\alpha$  is likely to be negligible for a heavily-doped n-type semiconductor. As such, one suspects that a system with  $E_F - \varepsilon_{h,0}$  of slightly less than 1.8 eV will still achieve water splitting.

materials, rather than state definitively that a system will split water; for that, the absolute positions of  $E_F$  and  $\varepsilon_{h,0}$  relative to the hydrogen- and oxygen-production potentials must be taken into account. In a similar vein, it is important to remember that [Figure 5.8](#) shows the results for an *isolated* system, without a Schottky barrier formed at the SEI, and not under illumination. This approach is taken initially to gather what systems are likely to be able to split water (based on a substrate that we know can split water) before we consider the effect of band bending at the SEI. Given the large uncertainties in calculating the Schottky barrier height ([Section 5.4.1](#)), this simplified approach is justified.

### 5.4.3 BeSe, ZnO and ZnS

The three most promising materials from the calculations this far have been BeSe, ZnS and ZnO, and so we will now look at their band alignment on  $\text{In}_x\text{Ga}_{1-x}\text{N}$  with varying  $x$ . [Figure 5.9](#) shows the conduction and valence band edges for  $x = 0$  (i.e., GaN) and  $x = 0.3$ , relative to the vacuum, along with the corresponding wave function probability amplitudes for the heavy hole ground state. The  $\pm 0.6$  eV uncertainty in the position of the band edges and energy levels, due to uncertainties in literature values for  $\chi$  (used to convert energies to be relative to the vacuum), are not shown to keep the figure easy to read. Likewise for the  $\pm 0.2$  V uncertainty in the position of  $E_{\text{red}}$  and  $E_{\text{ox}}$ , due to electrode–vacuum conversions.

The wave function probability amplitudes verify that the hole is strongly localised within the QD. In the case of ZnS, strain near the perimeter of the dot result in a slightly deeper confining potential than directly in the centre, and thus the hole is not central in the dot. In 3D, this corresponds to ring-shaped confinement of holes.

Increasing the In content shrinks the band gap of the bulk material, making the energy difference  $E_F - \varepsilon_{h,0}$  smaller. The optimum system is the one with the smallest band gap possible (to maximise solar absorption), whilst ensuring  $E_F$  and  $\varepsilon_{h,0}$  still straddle the hydrogen- and oxygen-production potentials. These potentials are highlighted on the diagram, though it must be remembered that we are still simulating an isolated system, un-immersed in an electrolyte and without a Schottky barrier. Therefore, the positions of  $E_F$  and  $\varepsilon_{h,0}$  are likely to be lower than when in a PEC, presuming upwards band bending. Critically, this could push  $\varepsilon_{h,0}$  above  $E_{\text{ox}}$ ,

depending on the height of the Schottky barrier, which we saw in [Section 5.4.1](#) to have a great deal of uncertainty attached to it.

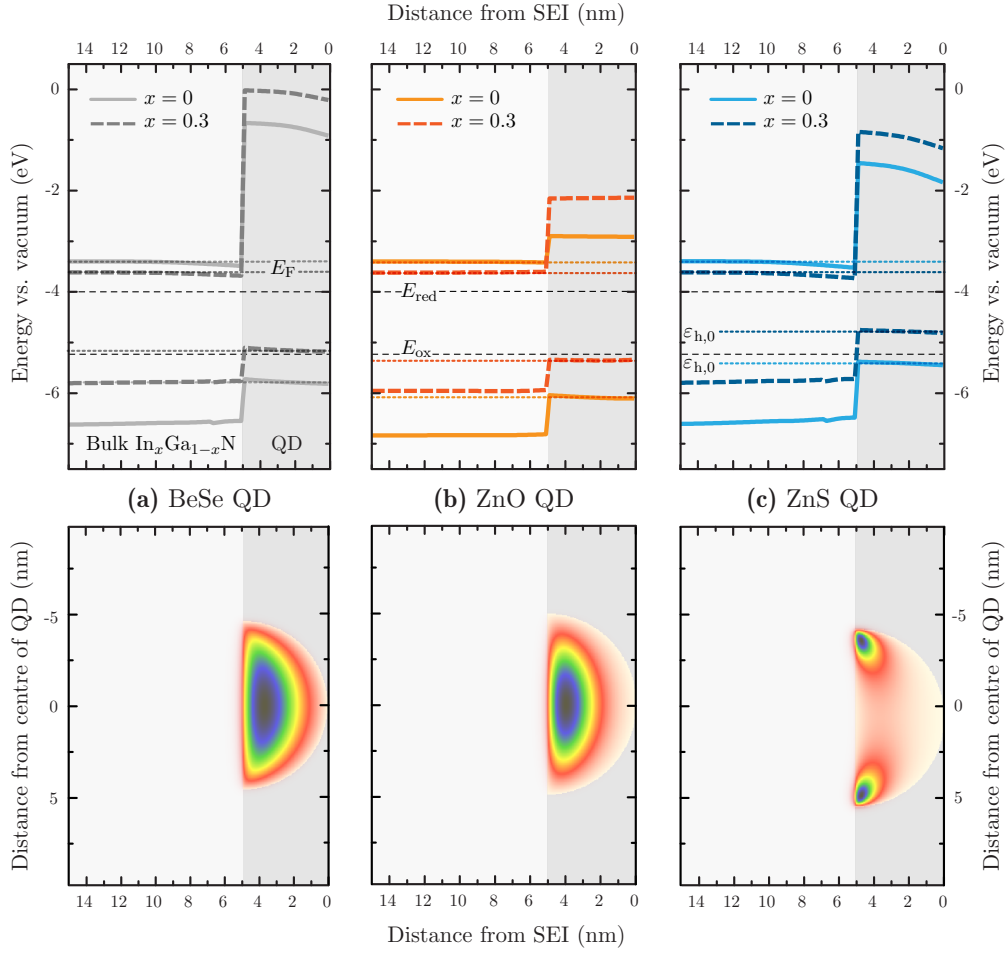


**Figure 5.9:** Top: Conduction and (heavy hole) valence band alignment for **(a)** BeSe, **(b)** ZnO and **(c)** ZnS QDs on  $\text{In}_x\text{Ga}_{1-x}\text{N}$ , for  $x = 0$  (thick solid lines, lighter colour) and  $x = 0.3$  (thick dashed lines, darker colour). The band edge data represent a 1D slice through the centre of the dot.  $E_F$  and  $\epsilon_{h,0}$  are also shown (thin dotted lines), with  $E_F$  lying close to the bulk conduction band edge, and  $\epsilon_{h,0}$  being completely confined in the QD. The thin (black) dashed lines represent the hydrogen- and oxygen-production potentials,  $E_{\text{red}}$  and  $E_{\text{ox}}$ . Uncertainties are omitted for clarity. Bottom: Contour plot of the corresponding wave function probability amplitudes for the heavy hole ground state  $|\psi_{h,0}|^2$ , overlaid on the model structure. Black represents the highest probability, through blue, green, yellow, then red, to white (transparent), which represents the lowest probability. Thus, the hole is shown to be localised in the QD for all three material systems.

In a similar vein to [Figure 5.8](#), we can compare  $E_F - \epsilon_{h,0}$ , this time for differing In content in the InGa<sub>N</sub> substrate, to ascertain whether it exceeds the required 1.8 eV. Band bending shifts both conduction and valence bands by an equal amount, and thus this comparison is unaffected by the presence (or absence) of a Schottky barrier. As can be seen in [Figure 5.10](#), ZnO QDs meet this criterion for the largest In content ( $x = 0.26$ ), closely followed by BeSe ( $x = 0.2$ ). Only for the smallest fraction of

In the bulk substrate ( $x < 0.06$ ) does the system with ZnS QDs show promise to be able to split water, and at these larger band gaps, absorption of the solar spectrum is likely to be poor. Thus far, ZnO QDs have proven themselves as the most desirable candidate.

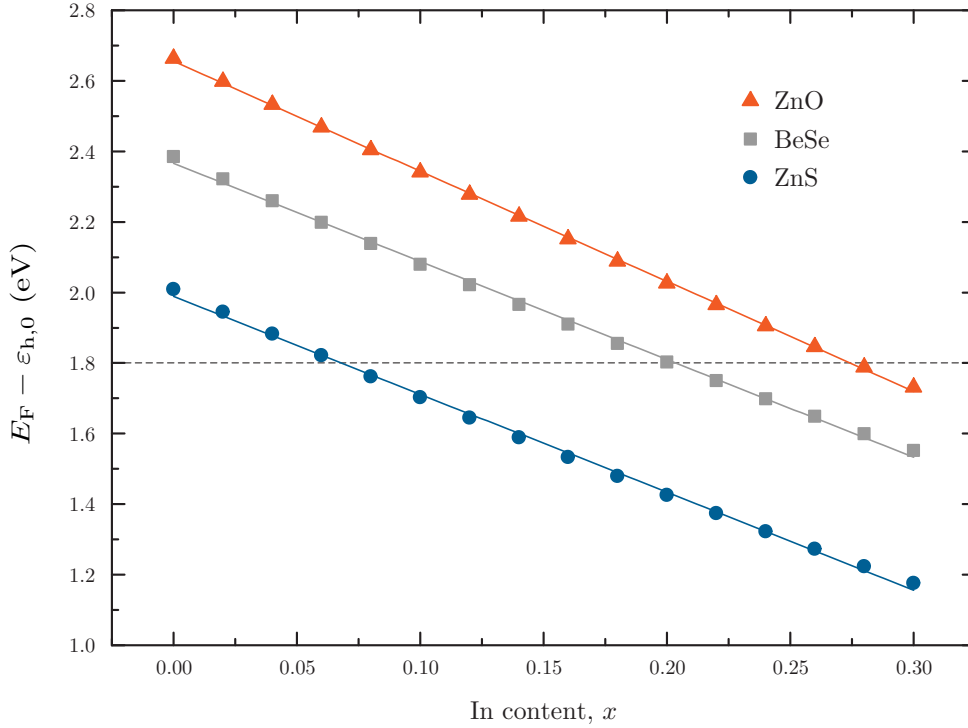


**Figure 5.10:** Dependence of  $E_F - \varepsilon_{h,0}$  on  $x$  for ZnO, BeSe and ZnS QDs on  $\text{In}_x\text{Ga}_{1-x}\text{N}$ . The solid lines represent linear fits to the data, corresponding to  $E_F - \varepsilon_{h,0} = -3.1x + 2.7$  for ZnO,  $E_F - \varepsilon_{h,0} = -2.8x + 2.4$  for BeSe and  $E_F - \varepsilon_{h,0} = -2.8x + 2.0$  for ZnS. The dashed line is the water-splitting criterion that  $E_F - \varepsilon_{h,0} > 1.8$  eV.

The absolute positions of  $E_F$  and  $\varepsilon_{h,0}$ , relative to the vacuum, are shown in Figures 5.11, 5.12 and 5.13, alongside the hydrogen- and oxygen-production potentials  $E_{\text{red}}$  and  $E_{\text{ox}}$ . Uncertainties, stemming from literature values for  $\chi$  and the electrode–vacuum conversion potential, are shown as error bars or the grey band for  $E_{\text{red}}$  and  $E_{\text{ox}}$ . As with Figure 5.9, the absence of band bending in the model means that the energy levels are likely to be pushed slightly higher in a real PEC.

As has been seen previously, the use of ZnO QDs proves the most promising: The confined hole state is consistently lower than for BeSe and ZnS, and ignoring uncertainties, it stays below the oxygen-production potential until over  $x = 0.3$ . Even with the oxygen-production requirement for an overpotential of 0.275 V (Section 2.10.5), the confined hole state stays lower than the oxygen-production potential

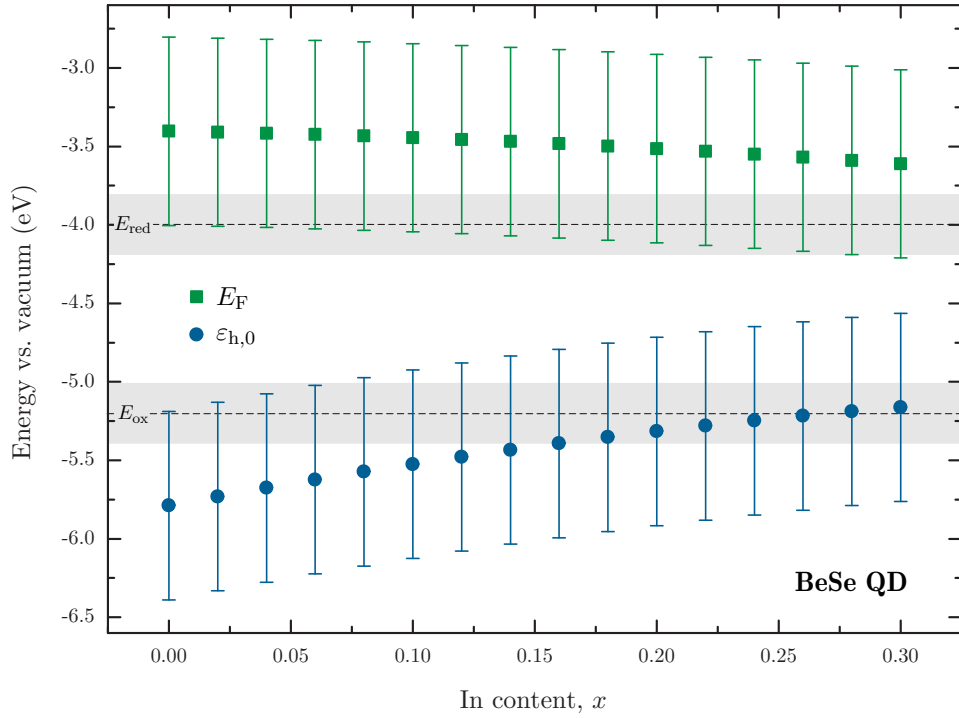


**Figure 5.11:** Fermi level  $E_F$  and first confined hole state  $\varepsilon_{h,0}$  for a BeSe QD on  $\text{In}_x\text{Ga}_{1-x}\text{N}$  with varying  $x$ . Hydrogen- and oxygen-production potentials,  $E_{\text{red}}$  and  $E_{\text{ox}}$ , are shown as dashed lines, with their associated uncertainty represented by the shaded grey areas.

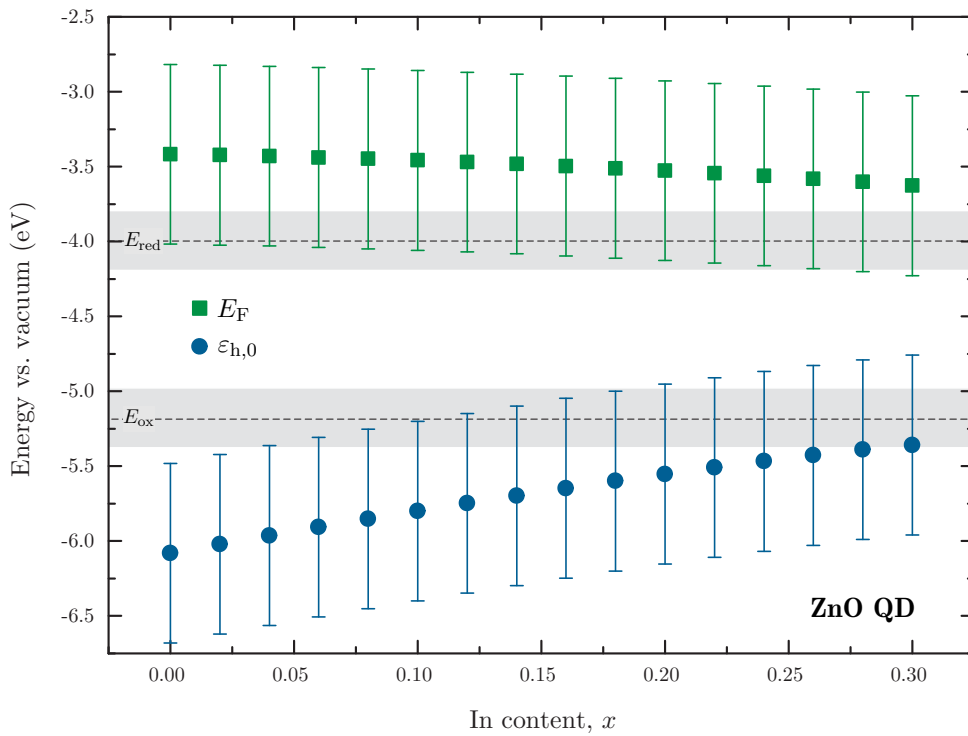


**Figure 5.12:** As Figure 5.11, but for a ZnO QD.

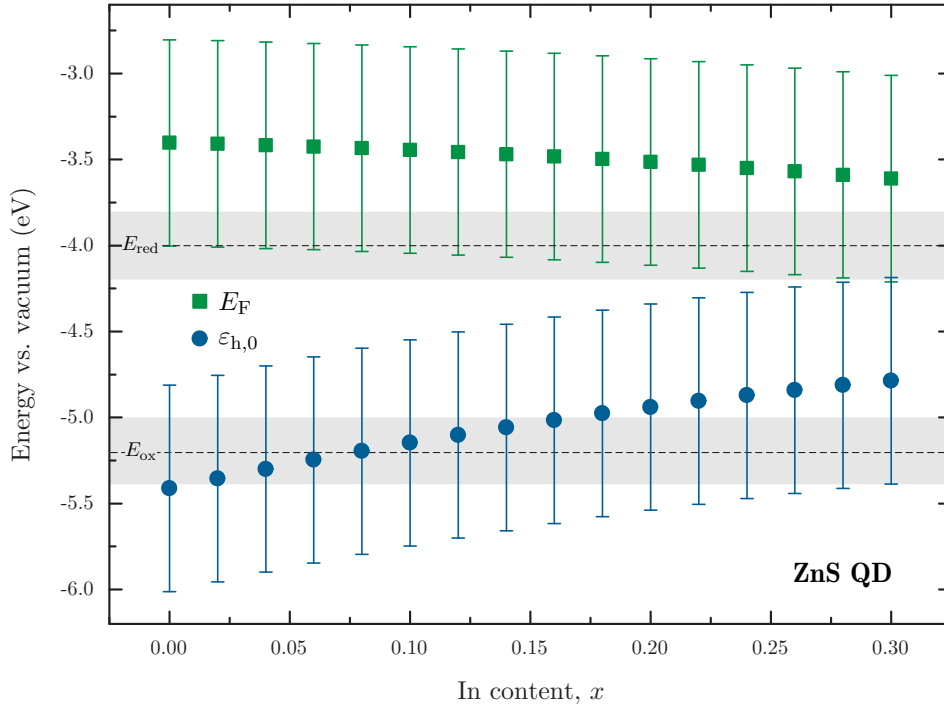


**Figure 5.13:** As Figure 5.11, but for a ZnS QD.

until  $x = 0.18$ . For all three materials,  $E_F$  is higher than  $E_{\text{red}}$ , though not within the uncertainties.

Previously, we speculated that the electron affinity of bulk GaN was higher than the average from literature values ( $\sim 4$  eV, rather than the average of 3.4 eV). If this higher value was used instead of the average in Figures 5.11, 5.12 and 5.13,  $E_F$  would be lie extremely close to  $E_{\text{red}}$ . However, given only a small overpotential of 0.050 V is required for hydrogen production, the system could still plausibly split water. Furthermore, that bulk n-GaN has been shown to successfully split water in a PEC [209, 222, 223] highlights the likeliness that, at least for  $x = 0$ ,  $E_F$  is sufficiently higher in energy than  $E_{\text{red}}$ . Of course, a higher electron affinity would be beneficial for oxygen production, meaning the confined hole states were at lower energies.

ZnO has thus far proven itself to be the best choice as our QD material, by merit of the position of its confined hole states with respect to the bulk InGaN Fermi level. It is also potentially advantageous that ZnO and InGaN both prefer to form the crystal structure of wurtzite (whilst ZnS prefers zinc-blende), and that they are both well established in terms of studies of their properties and growth (as

opposed to BeSe, for which there is barely any literature).

#### 5.4.4 Band Bending

The next logical step is to include band bending due to the SEI in our model (i.e., to insert our electrode into a electrolyte, so to speak). However, it was established early on that uncertainties in the Schottky barrier height are large, and so any results we obtain from its inclusion are borderline meaningless; we can create a variety of different systems that both can and cannot split water within the given uncertainties. Furthermore, the formation of band bending at a SEI with surface QDs is undocumented in literature, and the exact form that the Schottky barrier will take is not clear. Instead, we shall limit ourselves to a discussion of band bending at the SEI and present a few illustrative results for an “ideal” material system.

In regions of the semiconductor surface where there are no QDs, it seems reasonable to presume that the Schottky barrier formed will be equivalent to if the electrode was a bulk semiconductor electrode. We saw in [Section 5.1.3](#) that small nanostructures are not large enough to form a space-charge region, and as such, band bending is negligible. Surface QDs are likely to be small enough such that this is the case, and therefore the Schottky barrier height will certainly not be that of the QD material. The process of band bending is induced by the flow of carriers from the electrode to the electrolyte, and in the case of an n-type electrode, it is a flow of electrons that cause the bending ([Section 2.10.2](#)). The presence of QDs creates a potential barrier for electrons, making it energetically favourable for them to transfer to the electrolyte via the surface of the bulk semiconductor, rather than by tunnelling through the barrier. Effectively, the QDs have no impact on the band bending and the interface between a QD and the electrolyte is *not* a typical SEI; that is, a Schottky barrier does not form as there is no flow of electrons from the dot to the electrolyte.

Modelling this interface at the surface of the QD could take two conceivable forms; either no contact at all is specified and a large potential barrier is placed in the way (i.e., by the use of the dummy material “air” in `nextnano`), or a Schottky contact could be used whose height is simply the combination of the bulk Schottky barrier height and the QD potential barrier height as given from calculations

without any contacts. The latter treats the QD as a perturbation to the bulk band bending and can be used to illustrate an “ideal” band structure. The key word here is *illustrate*, and in the following, parameter values are cherry-picked (within the previously discussed uncertainties) to produce the most optimal band structure.

Starting with the desire for the Fermi level to be as close as possible to the hydrogen-production potential, whilst ensuring an overpotential of 0.050 V, gives us a value for the electron affinity of 3.9 eV. Choosing a higher  $x$  means a higher flat-band potential and thus a smaller Schottky barrier, whilst choosing a smaller  $x$  means less efficient absorption of the solar spectrum. For the case of  $x = 0$ , assuming the flat-band potential given by literature of  $-0.9$  V, we obtain a Schottky barrier height of  $\phi_B = 0.41$  eV. On the other hand, if  $x = 0.15$  (using a shift of  $\sim 0.14$  V per 10% In content increase [15] to give  $V_{fb} = -0.7$  V), the Schottky barrier height is only  $\phi_B = 0.2$  eV. ZnO has proven itself to be the most desirable QD material and as such is chosen here. Figure 5.14 shows the resulting band structure, along with the electron density, for both of these cases. The band bending has resulted in the separation of carriers such that the electron density is negligible near the SEI, whilst the hole is confined in the QD. The large Schottky barrier ( $x = 0$ ) means a more effective splitting up of carriers, but potentially to the detriment of pushing the hole ground state too high, such that the requirement for a 0.275 V overpotential isn’t met.

### 5.4.5 Discussion

The review into photoelectrolysis research presented in Section 5.1 concluded with the remark that “for research to progress, *innovation* in both materials development and device design is clearly needed”, and we believe that the use of nanostructures at the SEI, in an attempt to increase the maximum photovoltage that can be achieved, is an example of the kind of new research direction needed. The major conclusion that can be drawn from this section is that ZnO QDs grown on n-InGaN appear as a promising material system for use in a PEC, with suitably-positioned energy levels that straddle the oxygen- and hydrogen-production potentials, at least for low In content  $x$ . To the author’s best knowledge, this system has never been investigated experimentally, and there is therefore a huge scope for experimental work to expand

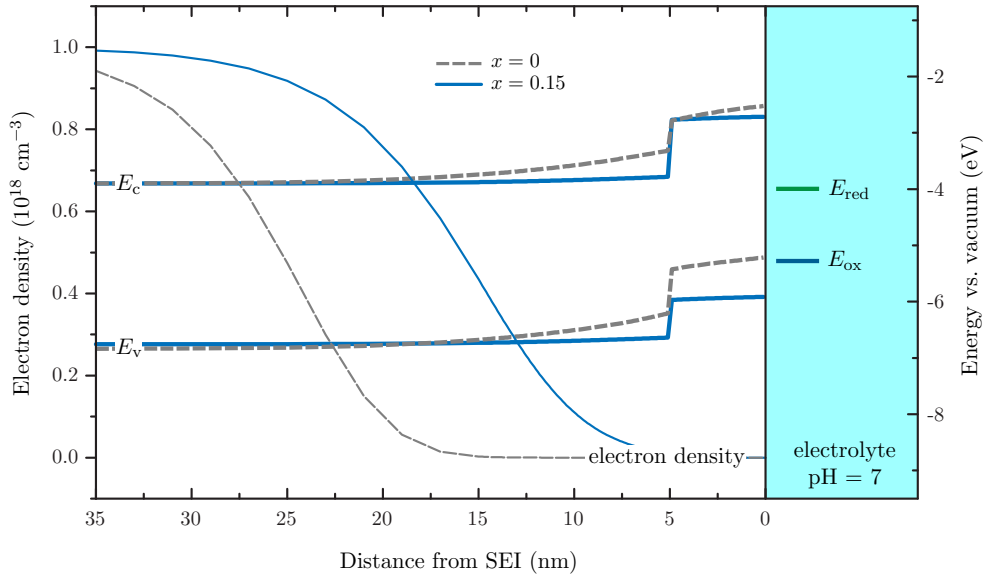


**Figure 5.14:** An illustration of the desired band structure and electron density, calculated by choosing the optimal parameter values within the uncertainties previously discussed.

upon the results presented here.

The effectiveness of a ZnO/InGaN system in part depends on how much In can be incorporated before  $E_F$  is pushed to a lower energy than  $E_{\text{red}}$ , or  $\epsilon_{h,0}$  raises above  $E_{\text{ox}}$ . The band gap of wurtzite GaN is 3.51 eV [13], corresponding to 352 nm, a wavelength too small to absorb the majority of solar radiation (see Figure 2.17). For  $\text{In}_{0.15}\text{Ga}_{0.85}\text{N}$ , this decreases to 2.92 eV (425 nm), for  $\text{In}_{0.3}\text{Ga}_{0.70}\text{N}$  it is 2.40 eV (517 nm) and for  $\text{In}_{0.5}\text{Ga}_{0.50}\text{N}$  it is as low as 1.80 eV (689 nm). The peak in solar radiation is at a little over 500 nm, and thus it is highly desirable that an In content of approaching (or better, exceeding)  $x = 0.3$  achieves water splitting. Our results demonstrate this may be possible, within uncertainties, for a ZnO/InGaN system, but experimental verification is needed to provide a definitive answer.

Stability is, of course, another key factor in whether ZnO/InGaN will be successful as a photoelectrode. III-nitrides, including InGaN, have a good reputation for their photo-stability [15, 219, 220]. In general, p-type semiconductors are seen to be more stable than n-type, due to a lower Fermi level and thus higher redox potential when immersed in an electrolyte [228]. However, the type-II system required for a p-type electrode would be an electron-confining one, which is much more difficult to achieve using InGaN as the bulk semiconductor. Furthermore, it should be noted that “good stability” in literature usually refers to the measuring of the

photocurrent density over a period of hours, or at most, days [186, 228], and thus doesn't necessarily mean the semiconductor in question is capable of uninterrupted PEC operation for months or years, which is of course what is desirable (especially if the electrode is to be fabricated from rare materials). Therefore, the use of other techniques to improve stability, as discussed in [Section 5.1.4](#), will be imperative in any economically- and environmentally-viable PEC.

Following on from this, the abundance of the materials used to fabricate electrodes must be taken into consideration. Both Ga and In are scarce elements and thus the ideal photoelectrolysis system should avoid their use [193]. However, this should not deter us from their use in research towards a proof-of-concept; if the system we propose proves photoelectrolytically viable, then further research innovation (e.g., the development of new materials and novel structures) will expand on our work to make it economically viable. An example of this in action is the development of *copper zinc tin sulphide* as an Earth-abundant and thus cheaper alternative to CdTe and copper indium gallium sulphide [193]. Though used in smaller quantities, Zn, nitrogen and oxygen are much more prevalent in the Earth's crust and atmosphere.

The final caveat to the potential of ZnO/InGaN is whether or not such a system can be easily fabricated. InGaN itself is regarded as a challenging material to grow, especially with a large In content [219, 229], but nonetheless, commercially-grown InGaN substrates have been available for a number of years [230]. The fabrication of ZnO QDs has been demonstrated numerous times in literature, using various different methods, from simple thermal vapour transport [231] to much more complex chemical techniques (e.g., [Reference 232](#)). Furthermore, the growth of 5-nm-diameter ZnO QDs on GaN has been demonstrated by sintering, details of which can be found in [Reference 233](#).

Of course, surface QDs are but one example of a nanostructure that could achieve the goal of confining holes near the surface of a semiconductor electrode. Thin films have already been used in an attempt to limit recombination losses [21] and their use to trap holes seems an attractive proposition. However, questions are then raised about the process by which holes transfer to the electrolyte to partake in the oxygen-production reactions; is the confining potential such that it would slow down the

rate of transfer, to the detriment of the water-splitting process? It would also raise questions about the formation of band bending; if electrons were not permitted to be within the film, then equilibration of the semiconductor and redox Fermi levels would necessitate the tunnelling of electrons through the thin film. How would this effect the subsequent magnitude of the band bending?

Another potentially less problematic geometry would be the use QDs with a thin capping layer, such that they are still near the surface of the semiconductor and holes trapped within them can still help limit the photo-induced flattening of the bands. However, holes being confined away from the surface may mean that they are never able to reach the surface, thus limiting the ability of the electrode to drive oxygen-production reactions.

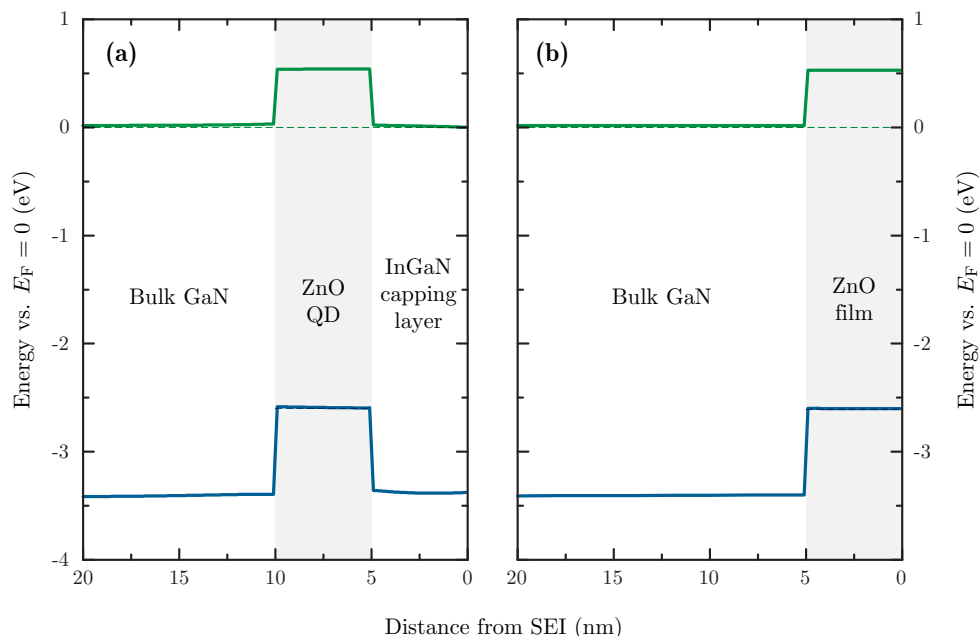


**Figure 5.15:** Conduction and valence band edges (solid lines) for (a) a buried ZnO QD with a 5-nm-thick capping layer between it and the SEI, and (b) a 5-nm ZnO film at the SEI. The thin dashed lines represent the Fermi level (near the conduction band) and the heavy hole ground state (in the nanostructure).

Both of these systems are type-II, with the hole being strongly localised in the nanostructure, as demonstrated by the calculated band structure and energy levels in [Figure 5.15](#).

In summary, we believe that our work has provided a step forwards in photoelectrolysis research, demonstrating the desirability of testing a ZnO/InGaN QD material

system in an experimental PEC setup. Furthermore, data from any experimental investigation could prove invaluable in the further development of the model created herein.

# Chapter 6

## Conclusions

The experimental and theoretical study of semiconductor nanostructures for two diverse applications has been detailed in this thesis: Firstly, charge-carrier confinement in SML QD–QW heterostructures and the implication of this for the creation of high-speed VCSELs for datacoms applications. Secondly, the novel use of nanostructures at the SEI in a PEC to increase the maximum photovoltage that can be generated by illumination.

### 6.1 Sub-Monolayer InAs in GaAs

The SML deposition of InAs with GaAs spacer layers of a few MLs results in the formation of a lateral InGaAs QW with low In content, in which are embedded QD–like In-rich agglomerations with a wide distribution of shapes and sizes. Charge-carrier confinement in this QD–QW heterostructure was investigated by the use of magneto-PL, TRPL and Schrödinger equation modelling.

Low-temperature zero-field PL measurements revealed narrow linewidths akin to that of a QW, whilst in-field measurements demonstrated large lateral Bohr radii that extend over several of the In-rich agglomerations, and vertical Bohr radii governed by the height of the SML stack. The linewidth dependence on the magnetic field in Faraday geometry ( $B$  parallel to the growth direction) indicated the presence of two disorder length scales, one corresponding to the monolayer fluctuations in QW width, and the other to the larger-scaler fluctuations in In composition due to the In-rich agglomerations. If excitons were confined only to the In-rich agglom-

erations, then the presence of the larger length scale would not be visible in PL field dependences. Accordingly, the QW sample only showed an indication of the smaller length scale. In Voigt geometry ( $B$  perpendicular to the growth direction), linewidths were only weakly dependent, if at all, on the magnetic field, consistent with vertical confinement in a QW. This far, the SML samples had demonstrated themselves as being unequivocally 2D.

Conversely, high-temperature high-field PL allowed excited states to become resolved and such states could be fitted by a FD spectrum, demonstrating their 0D nature. To explain this paradox, we postulated that SML systems were *heterodimensional* and that the lighter electrons see only the lateral InGaAs QW, whilst the heavier holes are confined within the In-rich agglomerations.

To verify this prediction, theoretical calculations of the confined electron and hole states were performed. One-band effective-mass modelling allowed a phase diagram of varying In composition in the QW and QD to be drawn, demonstrating a large heterodimensional phase encompassing the most probable parameter space. Eight-band  $\mathbf{k} \cdot \mathbf{p}$  measurements took into account strain, piezoelectricity and the Coulomb interaction between electron and holes, showing that the electron was consistently more extended than the hole.

This offers an explanation for the high-speed operation of SML VCSELs that have already been demonstrated. Efficient carrier injection is explained by the absence of a wetting layer for carriers to become trapped in, as well as the 2D coupling of electrons to several In-rich agglomerations, availing them quickly to states that are lasing. At the same time, the relatively shallow confining potential of the In-rich agglomerations means that excess holes cannot build up in states that aren't lasing. Short carrier lifetimes demonstrate the efficient injection of carriers, which is essential for high-modulation-bandwidth lasers for datacoms use. SML systems have the advantage of being relatively simple to fabricate, compared to other specially-designed systems that achieve fast carrier injection (e.g., QW injection layer close to SK QDs).

### 6.1.1 Further Work

There is a broad scope for the expansion of research into SML systems, in part due to the lack of attention that has been given to them compared to, for example, SK QDs, and in part because the heterodimensionality we have uncovered here could offer new insight into previously-unexplained results.

Starting with an immediate extension to our own work, the reader may have noticed that Voigt-geometry measurements on the QW sample were not included; the simple explanation for this is that none were carried out. Though we have validated our theory of heterodimensionality without these results, it would still be worthwhile to ensure that they meet our expectations. Studying our samples in higher fields (e.g., pulsed fields, which can easily achieve 50 T) would be useful to determine a value for the vertical Bohr radius and, as excited states tend to be better resolved at higher fields, to add more data points to the FD plots.

Micro-PL, which is analogous to standard PL but with a smaller laser spot size, is commonly used to observe the PL from individual QDs, and one might think it would form a suitable extension. [Reference 151](#) claim to have seen individual SML-QD spectra for a 10-fold 0.5-ML-InAs/2.5-ML-GaAs stack using micro-PL at low excitation power densities, with a laser spot size of 2  $\mu\text{m}$ . However (assuming this number is a diameter), a 2- $\mu\text{m}$ -diameter circle would excite an approximately 3- $\mu\text{m}^2$  area of the sample, which, given a lateral density for In-rich agglomerations of  $\sim 10^{12} \text{ cm}^{-2}$ , corresponds to  $\sim 10^4$  QDs. Unless the density of In-rich agglomerations in their SML system is distinctly different to those studied here, it is hard to believe how individual QDs would be visible. Indeed, some brief micro-PL studies on the samples studied here revealed no individual QD peaks.

As the size of the GaAs spacer layer increases, the SML depositions become better defined and more like the nominal picture illustrated in [Figure 4.5\(a\)](#). Zero-field PL measurements performed by Lenz et al. [\[20\]](#) revealed QW-like emission up to 32 ML (the largest spacer-layer thickness studied). It would be interesting to observe these samples in a magnetic field, to ascertain whether the few-ML-high In-rich islands are sufficiently distinct to confine holes, and if not, when the onset of heterodimensional behaviour occurs.

Whilst XSTM and transmission electron microscopy images have given a good

indication of the nature of In composition in SML stacks, it would be invaluable to compliment these with a full 3D atom-by-atom image. This could be achieved by the use of *atom probe tomography*, which in recent years has demonstrated its use in producing atomic-resolution 3D images of semiconductor nanostructures [234, 235]. The 3D atom probe is effectively a field ion microscope combined with a time-of-flight mass spectrometer, in which a needle-shaped specimen is placed under a large pulsed voltage, causing single ions to be released from the specimen’s apex and to be accelerated towards a detector screen. Whilst the technique was traditionally pioneered for high-conductivity materials (i.e., metals), the use of a pulsed laser to provide additional thermal excitation has meant that, nowadays, semiconductor nanostructure imaging is achievable. A drawback of atom probe tomography, compared to XSTM, is that imaging length scales are typically tens of nm laterally and hundreds of nm vertically, compared to the  $\mu\text{m}$ -size image sizes achievable by XSTM; hence, it should be used to complement XSTM results, rather than to replace.

The simple dot-in-a-well models presented here are justified because we don’t have detailed compositional information about SML systems, and integrating a more complex structure into the models would mean enough assumptions and approximations as to make the results from them questionable. However, the use of atom probe tomography could provide enough detail to render more sophisticated structural modelling viable; that is, using the same modelling methods as previous, but with a modified sample structure. Another approach would be to use an atomistic approach to model the strain and subsequent distribution of In, coupled to a continuum model (e.g., eight-band  $\mathbf{k} \cdot \mathbf{p}$ ) to compute the resulting electronic structure [236]. Atomistic calculations are frequently employed to model semiconductor nanostructures, though usually only for single QDs (up to a few million atoms) [237, 238], begging the question as to whether the modelling of a full SML stack would be computationally achievable.

Thinking more broadly, SML systems could be modified or implemented alongside other nanostructures to fulfil different purposes, as discussed in the context of recent literature in Section 4.1.4. One particularly interesting modification is the addition of an Sb flush during the growth process, with the aim of improving wavelength and confinement tunability [166]. The emission wavelength of pure

InAs/GaAs SML systems is limited to above 1100 nm and alloying with Sb enables this to be further redshifted. Quandt et al. [166] concluded that the addition of Sb leads to an increase in carrier localisation, which viewed in the light of the heterodimensionality uncovered herein, may not be a good thing for device applications; for example, we contend that the 2D nature of electrons is essential for efficient carrier injection in SML VCSELs. Clearly, magneto-PL measurements on such samples would help determine the exact nature of electronic confinement, and whether or not SML systems with an Sb flush are still heterodimensional.

SML InAs/GaAs might not be the only system to exhibit heterodimensionality and the insight gained into carrier localisation here could also be applied to the study of GaN-based LEDs. These LEDs, which are commonplace in modern solid state lighting, offer bright emission despite high defect densities. It is thought that carrier localisation due to compositional fluctuations prevents non-radiative recombination from defect states, but the nature of the localisation is not well understood [180]. Interestingly, the theoretical modelling of InGaN/GaN QWs with random alloy disorder has predicted that holes are predominantly localised by alloy concentration fluctuations, whereas electron localisation is weaker and arises from a combination of the QW width and alloy concentration fluctuations [179]. This mixture of 0D and 2D states could be experimentally investigated using similar techniques to those employed in this thesis. In particular, magneto-electroluminescence could be used to study the dependence of localisation on excitation current.

## 6.2 Photoelectrolysis

In this section, mathematical modelling has been employed to give an insight into carrier confinement and band structure in nanostructured systems, for the potential use in a PEC to generate renewable hydrogen. It was proposed that the presence of a hole-confining nanostructure at the SEI, for an n-type electrode, would limit the amount by which illumination flattens the bands, increasing the maximum photovoltage that can be generated.

A model has been developed that requires only the input of the flat-band potential and a few other common material properties to simulate the band struc-

ture, confined carrier energy levels, carrier densities and currents, by use of the Schrödinger, Poisson and drift–diffusion equations. However, discrepancies between a number of literature values—most notably that of the flat-band potential and electron affinity—means that uncertainties in the output from the model are large. The results most affected by these uncertainties are those for systems with band bending at the SEI, due to the need for both the flat-band potential and electron affinity as inputs. As such, we were unable to state results modelling the SEI with any degree of confidence.

However, the water-splitting capability of GaN was demonstrated by use of the Schottky barrier height from literature. At a pH of 7, a barrier height of  $\phi_B = 0.5 \pm 0.3$  eV gives an electron affinity of  $\chi = 4.0 \pm 0.2$  eV, resulting in a semiconductor Fermi level that is higher in energy than the hydrogen-production potential, and a valence band edge that is lower in energy than the oxygen-production potential.

Calculations not including band bending were much more successful and conclusive, requiring only the electron affinity as an input (and this was only to compare computed energies to the oxygen- and hydrogen-production potentials). The band edges of  $\text{In}_x\text{Ga}_{1-x}\text{N}$  were computed for varying  $x$ , and were found to straddle to the oxygen- and hydrogen-production potentials at low In content.

To explore the use of nanostructures at the SEI, surface QDs fabricated from twenty different materials were modelled on n-GaN. For BeSe, ZnO and ZnS, the critical quantity of  $E_F - \varepsilon_{h,0}$  (the Fermi level minus the confined hole ground state) was found to be above the 1.8 eV required for water splitting to occur. By modelling these three materials on  $\text{In}_x\text{Ga}_{1-x}\text{N}$ , with varying  $x$ , we were able to determine that ZnO was the most desirable, having  $E_F - \varepsilon_{h,0}$  greater than 1.8 eV for the highest In content ( $x = 0.26$ ). Furthermore,  $E_F$  was found to be higher in energy than  $E_{\text{red}}$  and  $\varepsilon_{h,0}$  lower than  $E_{\text{ox}}$  (excluding uncertainties) for up to  $x = 0.3$ , without band bending.

Large uncertainties again plagued any attempt at the inclusion of a Schottky barrier at the SEI; within uncertainties, ZnO/InGaN QDs can be shown to be able and to not be able to split water. Nonetheless, it is reassuring that a system capable of splitting water more than lies within said uncertainties. Ultimately, experimental

work will prove whether this is the case or not, and could provide invaluable feedback for the further development of our model.

### 6.2.1 Further Work

Our work on photoelectrolysis is only in its infancy, and there is much potential for further research. The ultimate goal is the fabrication of a PEC utilising ZnO/InGaN QDs, so that the flat-band potential and water-splitting capability can be observed.

The work in this thesis involved the construction of a semiconductor sample holder for use in a PEC, but unfortunately, as of yet, no PEC measurements have been carried out. The sample holder had to fulfil the requirements of holding a small ( $\sim$ cm) semiconductor sample in electrical contact with an external circuit (and thus the counter electrode), in a water-tight design. To this end, the design illustrated in [Figure 6.1](#) was fabricated. A cylindrical polytetrafluoroethylene (PTFE) shell has a hole through its core and a shallow square indent at one end, in which the sample sits. A metallic spring is passed through the core of the PTFE shell, which pushes a metal (e.g., brass) contact into the sample's ohmic back contact. The other end of the spring is contacted by a metal screw, which is screwed in place to compress the spring. A PTFE cap is screwed onto the top of the cylinder, and this cap has a circular aperture in it and a small lip underneath for a silicone o-ring to sit. Screwing the cap in place pushes the o-ring onto the sample and thus makes the setup water-tight. Light is shone onto the semiconductor through the circular aperture in the cap.

There are a number of techniques one can use to measure the flat-band potential of a semiconductor electrode. One such technique is that of *electrochemical impedance spectroscopy* (EIS), whereby the impedance of a system is measured over a range of alternating-current frequencies. This can be achieved for a PEC by modelling it as an equivalent circuit, consisting of a number of electrical components that behave in a similar manner to the PEC in question. A so-called Randles Cell ([Figure 6.2](#)), or a variation thereof, is commonly used for PEC measurements, which typically takes the form of a resistor, representing charge transfer resistance, in parallel with a capacitor, that represents the double-layer capacitance at the SEI, all in series with another resistor, representing the resistance of the solution. The Poisson

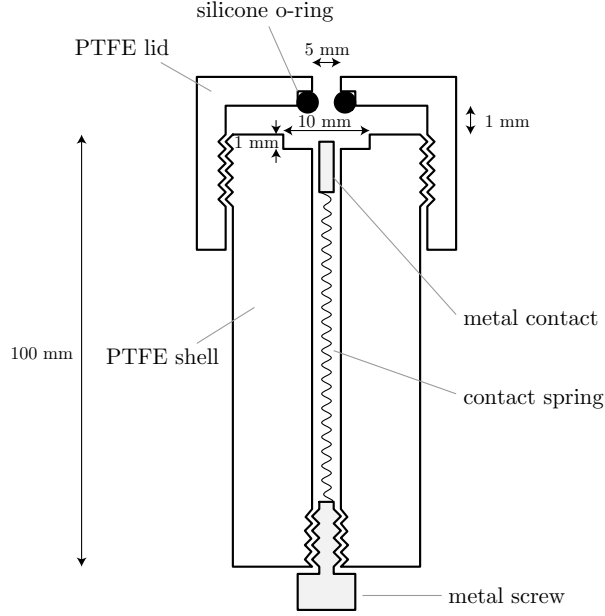


**Figure 6.1:** A water-tight polytetrafluoroethylene (PTFE) sample holder design to be use in a PEC, enabling light to be shone on a semiconductor electrode, which is electrically connected to an external circuit.

equation (Equation 3.25) can be solved at the SEI to give the so-called *Mott–Schottky Equation*:

$$\frac{1}{C^2} = \frac{2}{\epsilon\epsilon_0 A^2 e N_d} \left( V - V_{fb} - \frac{k_B T}{e} \right), \quad (6.1)$$

where  $C$  is the SEI capacitance,  $A$  is the SEI area exposed to the electrolyte and  $V$  is the potential of the cell.  $C$  can be determined from the equivalent circuit used, and a Mott–Schottky plot of  $1/C^2$  vs. potential  $V$  can be constructed. As such,  $V_{fb}$  can be determined from the intercept on the  $V$  axis (which is at  $V_{fb} - \frac{k_B T}{e}$ ), and the donor density  $N_d$  can be obtained from the slope (which is  $\frac{2}{\epsilon\epsilon_0 A^2 e N_d}$ ). More detailed information on EIS can be found in References 239 and 240.

It is also desirable to quantify the stability of the semiconductor electrode, and this is usually achieved by measuring the photocurrent density as a function of time, when under constant illumination. A significant drop in photocurrent indicates that the electrode has undergone unwanted oxidation or reduction reactions. Measuring the amount of hydrogen and oxygen produced would be another good indicator of electrode stability.

The PEC we have proposed here is, of course, simply a basis for further exper-

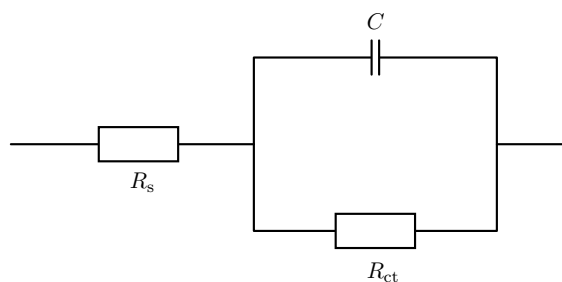


**Figure 6.2:** A simplified Randles Cell, with a resistor  $R_s$  representing the solution's resistance, another resistor  $R_{ct}$  representing the charge transfer resistance and a capacitor  $C$  representing the double-layer capacitance at the SEI.

imental and theoretical work that will optimise and ultimately commercialise an economically- and environmentally-viable photoelectrolytic system. Indeed, some of the extensions to conventional PECs that have been discussed in [Section 5.1](#), such as the use of novel multi-junction and nanostructured electrodes, will no doubt be utilised in the process.

Thinking ahead, the successful fabrication of a functioning and efficient PEC that splits water without an external bias would open the door to a whole host of technological opportunities. Further optimisation and fabrication into practical real-world devices could yield a variety of different implementations, from off-grid hydrogen-generation stations to provide power to remote communities, to solar-powered hydrogen vehicles. It is reassuring that the interest in using hydrogen as an energy carrier is on the rise [\[241\]](#), and the development of photoelectrolysis into a economically-viable technology will ensure that this hydrogen is as renewable as can be.



# Appendix A

## Temperature Dependence

Extra temperature dependence data for Sample C. [Figure A.1](#) shows the evolution of the PL spectra with varying temperature and [Figure A.2](#) shows the linewidth for varying temperature. All samples showed similar dependences.

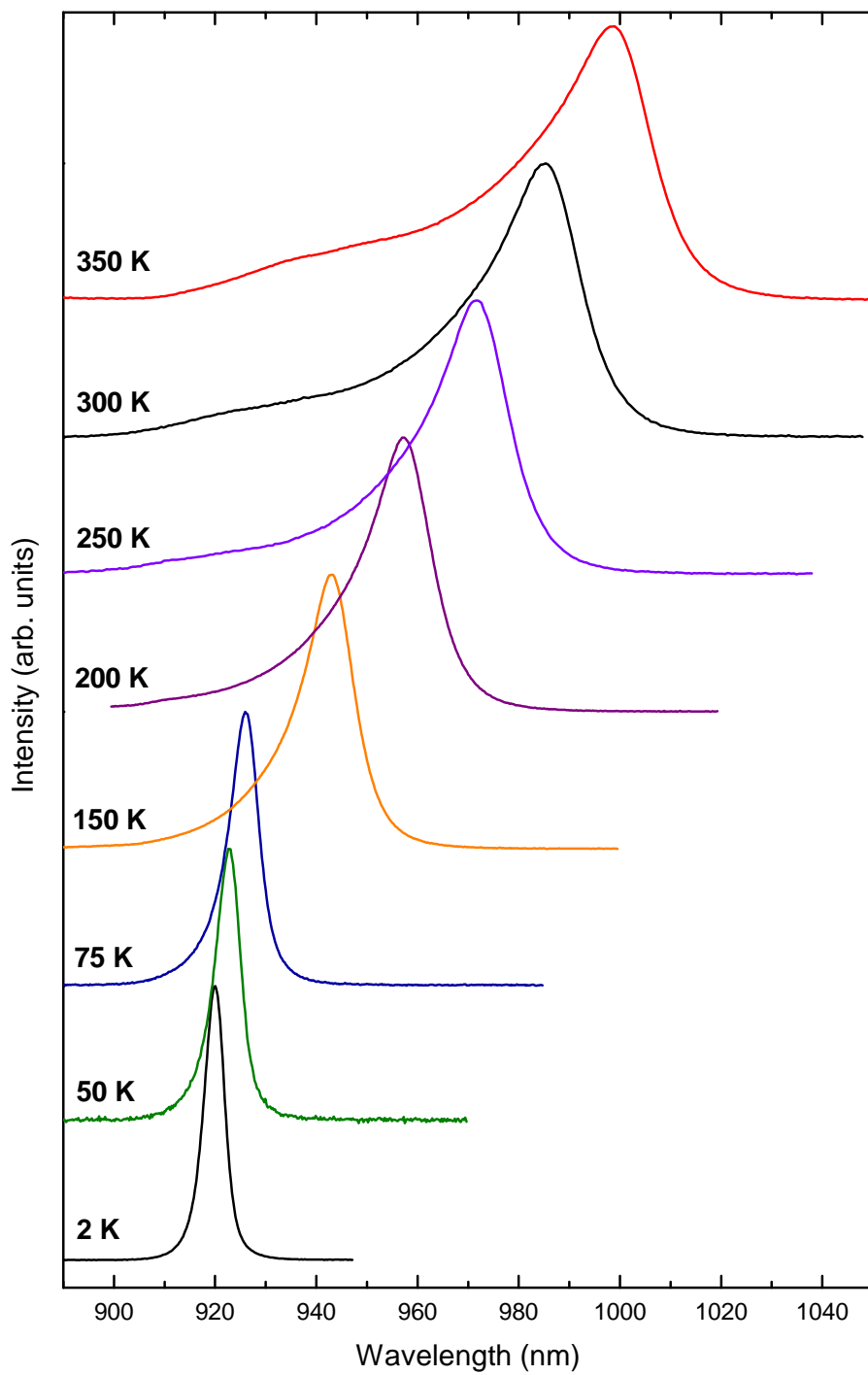


**Figure A.1:** Evolution of the PL spectra for Sample C with varying temperature.

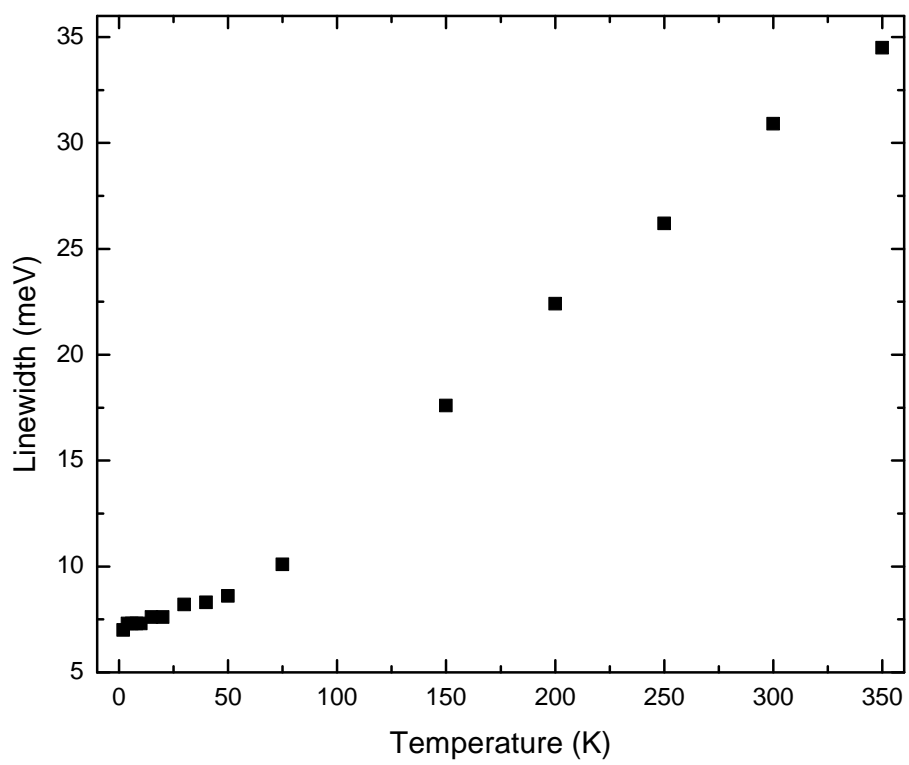


**Figure A.2:** PL linewidth of Sample C for varying temperature.



# References

- [1] The Shift Project Data Portal. Available at <http://www.tsp-data-portal.org/>. Accessed 21 April 2016.
- [2] Wikipedia. Energy density graph, 2008. Available at [https://commons.wikimedia.org/wiki/File:Energy\\_density.svg](https://commons.wikimedia.org/wiki/File:Energy_density.svg) under the public domain. Accessed 21 April 2016.
- [3] Czochralski process image. Available at [https://commons.wikimedia.org/wiki/File:Czochralski\\_Process.svg](https://commons.wikimedia.org/wiki/File:Czochralski_Process.svg) under the public domain. Accessed 20 February 2016.
- [4] B. van Zeghbroeck. *Principles of Semiconductor Devices*. University of Colorado, 2011. Available at <http://eee.colorado.edu/~bart/book>.
- [5] J. I. Pankove. *Optical Processes in Semiconductors*. Dover Books on Physics. Dover Publications, New York, 1971.
- [6] Ioffe Physical Technical Institute, 2014. Available at <http://www.ioffe.ru/SVA/NSM/Semicond/>. Accessed 24 February 2016.
- [7] A. Beck. Solar spectrum. Available at [https://commons.wikimedia.org/wiki/File:Solar\\_spectrum\\_en.svg](https://commons.wikimedia.org/wiki/File:Solar_spectrum_en.svg) under the Creative Commons Attribution-Share Alike 3.0 Unported License. Accessed 24 February 2016.
- [8] Wikipedia. Laser diodes, 2015. Available at [https://en.wikipedia.org/wiki/Laser\\_diode](https://en.wikipedia.org/wiki/Laser_diode) under the GNU Free Documentation License. Accessed 29 March 2016.

- [9] R. van de Krol. Principles of photoelectrochemical cells. In *Photoelectrochemical Hydrogen Production*, Electronic Materials: Science & Technology, chapter 2. Springer, 2011.
- [10] Wikipedia. Bloch function. Available at [https://commons.wikimedia.org/wiki/File:Bloch\\_function.svg](https://commons.wikimedia.org/wiki/File:Bloch_function.svg) under the [Creative Commons Attribution 4.0 International License](#). Accessed 24 February 2016.
- [11] Thomson Reuters. Web of Science website. Available at <https://www.webofknowledge.com/>.
- [12] D. M. Fabian, S. Hu, N. Singh, F. A. Houle, T. Hisatomi, K. Domen, F. E. Osterloh, and S. Ardo. Particle suspension reactors and materials for solar-driven water splitting. *Energy and Environmental Science*, 8:2825, 2015. DOI: [10.1039/C5EE01434D](https://doi.org/10.1039/C5EE01434D).
- [13] I. Vurgaftman and J. R. Meyer. Band parameters for nitrogen-containing semiconductors. *Journal of Applied Physics*, 94:3675, 2003. DOI: [10.1063/1.1600519](https://doi.org/10.1063/1.1600519).
- [14] S. Birner. next**nano** software package. Available at <http://www.nextnano.com>.
- [15] J. D. Beach. *In(x)Ga(1-x)N for photoelectrochemical water splitting*. PhD thesis, Colorado School of Mines, 2001. Available at [https://www.researchgate.net/publication/35736595\\_InxGa1-xN\\_for\\_photoelectrochemical\\_water\\_splitting](https://www.researchgate.net/publication/35736595_InxGa1-xN_for_photoelectrochemical_water_splitting).
- [16] D. T. Sawyer, A. Sobkowiak, and J. L. Roberts. *Electrochemistry for Chemists*. Wiley, 1995.
- [17] K. Rajeshwar. Fundamentals of semiconductor electrochemistry and photoelectrochemistry. In S. Licht, A. J. Bard, and M. Stratmann, editors, *Encyclopedia of Electrochemistry, Volume 6, Semiconductor Electrodes and Photoelectrochemistry*, chapter 1. Wiley-VCH, 2002.
- [18] A. Mutig. *High Speed VCSELs for Optical Interconnects*. Springer Theses. Springer Berlin Heidelberg, 2011.

- [19] A. Lenz, H. Eisele, J. Becker, L. Ivanova, E. Lenz, F. Luckert, K. Pötschke, A. Strittmatter, U. W. Pohl, D. Bimberg, and M. Dähne. Atomic structure of buried InAs sub-monolayer depositions in GaAs. *Applied Physics Express*, 3: 105602, 2010. DOI: [10.1143/APEX.3.105602](https://doi.org/10.1143/APEX.3.105602).
- [20] A. Lenz, H. Eisele, J. Becker, J.-H. Schulze, T. D. Germann, F. Luckert, K. Pötschke, E. Lenz, L. Ivanova, A. Strittmatter, D. Bimberg, U. W. Pohl, and M. Dähne. Atomic structure and optical properties of InAs submonolayer depositions in GaAs. *Journal of Vacuum Science & Technology B*, 29:04D104, 2011. DOI: [10.1116/1.3602470](https://doi.org/10.1116/1.3602470).
- [21] C. Grimes, O. Varghese, and S. Ranjan. *Light, Water, Hydrogen: The Solar Generation of Hydrogen by Water Photoelectrolysis*. Fuel Cells and Hydrogen Energy. Springer US, 2007.
- [22] L. M. Peter. Photoelectrochemical water splitting: A status assessment. *Electroanalysis*, 27:864, 2015. DOI: [10.1002/elan.201400587](https://doi.org/10.1002/elan.201400587).
- [23] NASA. Liquid hydrogen—the fuel of choice for space exploration. Available at [http://www.nasa.gov/topics/technology/hydrogen/hydrogen\\_fuel\\_of\\_choice.html](http://www.nasa.gov/topics/technology/hydrogen/hydrogen_fuel_of_choice.html). Accessed 21 April 2016.
- [24] U.S. Department of Energy, Energy Efficiency and Renewable Energy. Comparison of fuel cell technologies chart, 2011. Available at [http://www1.eere.energy.gov/hydrogenandfuelcells/fuelcells/pdfs/fc\\_comparison\\_chart.pdf](http://www1.eere.energy.gov/hydrogenandfuelcells/fuelcells/pdfs/fc_comparison_chart.pdf). Accessed on 21 April 2016.
- [25] U.S. Department of Energy, Energy Efficiency and Renewable Energy. Where the Energy Goes: Gasoline Vehicles. Available at <https://www.fueleconomy.gov/feg/atv.shtml>. Accessed on 21 April 2016.
- [26] W. Lin and K. E. Benson. Silicon crystal growth. In *Microelectronic Materials and Processes*, Nato Science Series E, chapter 1. Springer Netherlands, 1986.
- [27] C. Kittel. *Introduction to Solid State Physics*. John Wiley & Sons, New York, USA, 6th edition, 2004.

- [28] H. P. Meyers. *Introductory Solid State Physics*. Taylor & Francis, 2nd edition, 1997.
- [29] J. S. Blakemore. *Solid State Physics*. Cambridge University Press, 1985.
- [30] D. Jacobsson, F. Panciera, J. Tersoff, M. C. Reuter, S. Lehmann, S. Hofmann, K. A. Dick, and F. M. Ross. Interface dynamics and crystal phase switching in GaAs nanowires. *Nature*, 531:317, 2016. DOI: [10.1038/nature17148](https://doi.org/10.1038/nature17148).
- [31] R. Turton. *The Physics of Solids*. Oxford University Press, New York, 2000.
- [32] R. Pässler. Parameter sets due to fittings of the temperature dependencies of fundamental bandgaps in semiconductors. *Physica Status Solidi (B)*, 216:975, 1999. DOI: [10.1002/\(SICI\)1521-3951\(199912\)216:2;975::AID-PSSB975;3.0.CO;2-N](https://doi.org/10.1002/(SICI)1521-3951(199912)216:2;975::AID-PSSB975;3.0.CO;2-N).
- [33] Y. P. Varshni. Temperature dependence of the energy gap in semiconductors. *Physica*, 34:149, 1967. DOI: [10.1016/0031-8914\(67\)90062-6](https://doi.org/10.1016/0031-8914(67)90062-6).
- [34] H. Haug and S. W. Koch. *Quantum Theory of the Optical and Electronic Properties of Semiconductors*. World Scientific, Singapore, 1990.
- [35] nanotechweb.org, IOP Publishing. Silicon carbide nanoflowers bloom, 2004. Available at <http://nanotechweb.org/cws/article/tech/19739>. Accessed on 3 March 2016.
- [36] NC State News. Researchers create ‘nanoflowers’ for energy storage, solar cells, 2012. Available at <https://news.ncsu.edu/2012/10/wms-cao-flower/>. Accessed on 3 March 2016.
- [37] B. C. Tappan, M. H. Huynh, M. A. Hiskey, D. E. Chavez, E. P. Luther, J. T. Mang, and S. F. Son. Ultralow-density nanostructured metal foams: Combustion synthesis, morphology, and composition. *Journal of the American Chemical Society*, 128:6589, 2006. DOI: [10.1021/ja056550k](https://doi.org/10.1021/ja056550k).
- [38] M. A. Reed, J. N. Randall, R. J. Aggarwal, R. J. Matyi, T. M. Moore, and A. E. Wetsel. Observation of discrete electronic states in a zero-dimensional

- semiconductor nanostructure. *Physical Review Letters*, 60:535, 1998. DOI: [10.1103/PhysRevLett.60.535](https://doi.org/10.1103/PhysRevLett.60.535).
- [39] J. He, H. J. Krenner, C. Pryor, J. P. Zhang, Y. Wu, D. G. Allen, C. M. Morris, M. S. Sherwin, and P. M. Petroff. Growth, structural, and optical properties of self-assembled (In,Ga)As quantum posts on GaAs. *Nano Letters*, 7:802, 2007. DOI: [10.1021/nl070132r](https://doi.org/10.1021/nl070132r).
- [40] D. Bimberg, M. Grundmann, and N. N. Ledentsov. *Quantum Dot Heterostructures*. Wiley, 1999.
- [41] C. R. Nave. HyperPhysics website. Available at <http://hyperphysics.phy-astr.gsu.edu/hbase/hframe.html>. Accessed on 1 March 2016.
- [42] P. Würfel. *Physics of Solar Cells: From Basic Principles to Advanced Concepts*. Wiley, Weinheim, 2009.
- [43] J. Frenkel. On the transformation of light into heat in solids. *Physical Review*, 37:17, 1931. DOI: [10.1103/PhysRev.37.17](https://doi.org/10.1103/PhysRev.37.17).
- [44] C. F. Klingshirn. *Semiconductor Optics*. Graduate Texts in Physics. Springer-Verlag Berlin Heidelberg, 2012.
- [45] S. W. Koch and M. Kira. Excitons in semiconductors. In *Optics of Semiconductors and Their Nanostructures*, Springer Series in Solid-State Sciences, chapter 1. Springer, 2004.
- [46] W. Edelstein, H. N. Spector, and R. Marasas. Two-dimensional excitons in magnetic fields. *Physical Review B*, 39:7697, 1989. DOI: [10.1103/PhysRevB.39.7697](https://doi.org/10.1103/PhysRevB.39.7697).
- [47] D. Chemla, D. Miller, P. Smith, A. Gossard, and W. Wiegmann. Room temperature excitonic nonlinear absorption and refraction in GaAs/AlGaAs multiple quantum well structures. *IEEE Journal of Quantum Electronics*, 20:265, 1984. DOI: [10.1109/JQE.1984.1072393](https://doi.org/10.1109/JQE.1984.1072393).
- [48] E. F. Schubert. *Light-Emitting Diodes*. Cambridge University Press, Cambridge, 2006.

- [49] P. N. Butcher, N. H. March, and M. P. Tosi. *Physics of Low-Dimensional Semiconductor Structures*. Physics of Solids and Liquids. Springer US, 2013.
- [50] R. Bhattacharya, B. Pal, and B. Bansal. On conversion of luminescence into absorption and the van Roosbroeck-Shockley relation. *Applied Physics Letters*, 100:222103, 2012. DOI: [10.1063/1.4721495](https://doi.org/10.1063/1.4721495).
- [51] J. Christen and D. Bimberg. Line shapes of intersubband and excitonic recombination in quantum wells: Influence of final-state interaction, statistical broadening, and momentum conservation. *Physical Review B*, 42:7213, 1990. DOI: [10.1103/PhysRevB.42.7213](https://doi.org/10.1103/PhysRevB.42.7213).
- [52] E. Kapon. *Semiconductor Lasers I: Fundamentals*. Optics and Photonics. Elsevier Science, 1999.
- [53] S. L. Chuang. *Physics of Photonic Devices*. Wiley Series in Pure and Applied Optics. John Wiley & Sons, 2009.
- [54] P. Zeeman. *Researches in Magneto-optics*. Macmillan, 1913.
- [55] F. A. Jenkins and H. E. White. Magneto-optics and electro-optics. In *Fundamentals of Optics*, chapter 32. McGraw-Hill, 1976.
- [56] R. Rinaldi, P. V. Giugno, R. Cingolani, H. Lipsanen, M. Sopanen, J. Tulkki, and J. Ahopelto. Zeeman effect in parabolic quantum dots. *Physical Review Letters*, 77:342, 1996. DOI: [10.1103/PhysRevLett.77.342](https://doi.org/10.1103/PhysRevLett.77.342).
- [57] X. Zhou, M. Royo, W. Liu, J. H. Lee, G. J. Salamo, J. I. Climente, and M. F. Doty. Diamagnetic and paramagnetic shifts in self-assembled InAs lateral quantum dot molecules. *Physical Review B*, 91:205427, 2015. DOI: [10.1103/PhysRevB.91.205427](https://doi.org/10.1103/PhysRevB.91.205427).
- [58] R. Hanson, B. Witkamp, L. M. K. Vandersypen, L. H. Willems van Beveren, J. M. Elzerman, and L. P. Kouwenhoven. Zeeman energy and spin relaxation in a one-electron quantum dot. *Physical Review Letters*, 91:196802, 2003. DOI: [10.1103/PhysRevLett.91.196802](https://doi.org/10.1103/PhysRevLett.91.196802).

- [59] L. D. Landau and E. M. Lifshitz. *Quantum Mechanics*. Pergamon Press, Oxford, 2nd edition.
- [60] K. J. Nash, M. S. Skolnick, P. A. Claxton, and J. S. Roberts. Diamagnetism as a probe of exciton localization in quantum wells. *Physical Review B*, 39: 10943, 1989. DOI: [10.1103/PhysRevB.39.10943](https://doi.org/10.1103/PhysRevB.39.10943).
- [61] M. Hayne and B. Bansal. High-field magneto-photoluminescence of semiconductor nanostructures. *Luminescence*, 27:179, 2012. DOI: [10.1002/bio.2342](https://doi.org/10.1002/bio.2342).
- [62] I. Vurgaftman, J. R. Meyer, and L. R. Ram-Mohan. Band parameters for III-V compound semiconductors and their alloys. *Journal of Applied Physics*, 89: 5815, 2001. DOI: [10.1063/1.1368156](https://doi.org/10.1063/1.1368156).
- [63] V. Fock. Bemerkung zur quantelung des harmonischen oszillators im magnetfeld. *Zeitschrift für Physik*, 47:446, 1928. DOI: [10.1007/BF01390750](https://doi.org/10.1007/BF01390750).
- [64] C. G. Darwin. The diamagnetism of the free electron. *Mathematical Proceedings of the Cambridge Philosophical Society*, 27:86, 1931. DOI: [10.1017/S0305004100009373](https://doi.org/10.1017/S0305004100009373).
- [65] A. Babinski, M. Poteski, S. Raymond, J. Lapointe, and Z. R. Wasilewski. Fock-Darwin spectrum of a single InAs/GaAs quantum dot. *Physica Status Solidi (C)*, 3:3748, 2006. DOI: [10.1002/pssc.200671548](https://doi.org/10.1002/pssc.200671548).
- [66] L. P. Kouwenhoven, D. G. Austing, and S. Tarucha. Few-electron quantum dots. *Reports on Progress in Physics*, 64:701, 2001. DOI: [10.1088/0034-4885/64/6/201](https://doi.org/10.1088/0034-4885/64/6/201).
- [67] A. J. Bard and L. R. Faulkner. *Electrochemical Methods: Fundamentals and Applications*. John Wiley & Sons, 2nd edition, 2000.
- [68] W. A. Donald, R. D. Leib, J. T. O'Brien, M. F. Bush, and E. R. Williams. Absolute standard hydrogen electrode potential measured by reduction of aqueous nanodrops in the gas phase. *Journal of the American Chemical Society*, 130:3371, 2008. DOI: [10.1021/ja073946i](https://doi.org/10.1021/ja073946i).

- [69] F. N. Crespilho, V. Z. José R. Siqueira Jr, A. J. F. Carvalho, F. C. Nart, and O. N. Oliveira Jr. Using electrochemical data to obtain energy diagrams for layer-by-layer films from metallic phthalocyanines. *International Journal of Electrochemical Science*, 1:151, 2006. Available at <http://www.electrochemsci.org/papers/1040151.pdf>.
- [70] H. Reiss. The Fermi level and the redox potential. *Journal of Physical Chemistry*, 89:3783, 1985. DOI: [10.1021/j100264a005](https://doi.org/10.1021/j100264a005).
- [71] P.H. Rieger. *Electrochemistry*. Prentice-Hall, 1987. ISBN 9780132489072.
- [72] C. T. Sah. *Fundamentals of Solid-state Electronics*. World Scientific, 1991.
- [73] P. Salvador and C. Gutiérrez. Mechanisms of charge transfer at the semiconductor-electrolyte interface. *Journal of the Electrochemical Society*, 131:326, 1984. DOI: [10.1149/1.2115569](https://doi.org/10.1149/1.2115569).
- [74] Z. Zhang and J. T. Yates. Band bending in semiconductors: Chemical and physical consequences at surfaces and interfaces. *Chemical Reviews*, 112:5520, 2012. DOI: [10.1021/cr3000626](https://doi.org/10.1021/cr3000626).
- [75] M. Grätzel. Photoelectrochemical cells. *Nature*, 414:338, 2001. DOI: [10.1038/35104607](https://doi.org/10.1038/35104607).
- [76] J. Schefold. Flatband potentials, barrier heights, and charge transfer at the n-InP/electrolyte contact. *Journal of the Electrochemical Society*, 139:2862, 1992. DOI: [10.1149/1.2068993](https://doi.org/10.1149/1.2068993).
- [77] M. F. Weber and M. J. Dignam. Efficiency of splitting water with semiconducting photoelectrodes. *Journal of the Electrochemical Society*, 131:1258, 1984. DOI: [10.1149/1.2115797](https://doi.org/10.1149/1.2115797).
- [78] Shyam S. Kocha and John A. Turner. Displacement of the bandedges of GaInP<sub>2</sub> in aqueous electrolytes induced by surface modification. *Journal of the Electrochemical Society*, 142:2625, 1995. DOI: [10.1149/1.2050065](https://doi.org/10.1149/1.2050065).
- [79] J. Singh. *Electronic and Optoelectronic Properties of Semiconductor Structures*. Cambridge University Press, 2007.

- [80] A. C. Jones and M. L Hitchman. Overview of chemical vapour deposition. In *Chemical Vapour Deposition*, chapter 1. The Royal Society of Chemistry, 2009. DOI: [10.1039/9781847558794](https://doi.org/10.1039/9781847558794).
- [81] C. J. Chen. *Introduction to Scanning Tunneling Microscopy*. Oxford University Press, Columbia University, New York, 2nd edition, 2008.
- [82] E. T. Yu. Cross-sectional scanning tunneling microscopy. *Chemical Reviews*, 97:1017, 1997. DOI: [10.1021/cr960084n](https://doi.org/10.1021/cr960084n).
- [83] M. Wahl. *Time-Correlated Single Photon Counting (Technical Note)*. PicoQuant GmbH, Berlin, Germany. Available at [https://www.picoquant.com/images/uploads/page/files/7253/technote\\_tcspec.pdf](https://www.picoquant.com/images/uploads/page/files/7253/technote_tcspec.pdf). Accessed on 29 January 2016.
- [84] COMSOL. Multiphysics software product suite, . Available at <https://www.comsol.com>.
- [85] M. Ehrhardt and T. Koprucki. *Multi-Band Effective Mass Approximations: Advanced Mathematical Models and Numerical Techniques*. Lecture Notes in Computational Science and Engineering. Springer International Publishing, 2014.
- [86] X. Marie and N. Balkan. *Semiconductor Modeling Techniques*. Springer Series in Materials Science. Springer Berlin Heidelberg, 2012.
- [87] R. L. Liboff. *Introductory Quantum Mechanics*. Addison-Wesley, 2003.
- [88] J. Peiró and S. Sherwin. Finite difference, finite element and finite volume methods for partial differential equations. In *Handbook of Materials Modeling*. Springer, 2005.
- [89] COMSOL. Multiphysics user’s guide, . Available as part of software package.
- [90] COMSOL. Multiphysics model library, conical quantum dot, . Available at [https://www.comsol.com/model/download/194983/models.mph.conical\\_quantum\\_dot.pdf](https://www.comsol.com/model/download/194983/models.mph.conical_quantum_dot.pdf).

- [91] S. Birner. *Modeling of semiconductor nanostructures and semiconductor-electrolyte interfaces*. PhD thesis, Technische Universität München, 2011. Available at <https://mediatum.ub.tum.de/doc/1084806/1084806.pdf>.
- [92] T. B. Bahder. Eight-band  $\mathbf{k}\cdot\mathbf{p}$  model of strained zinc-blende crystals. *Physical Review B*, 41:11992, 1990. DOI: [10.1103/PhysRevB.41.11992](https://doi.org/10.1103/PhysRevB.41.11992).
- [93] D. Jena.  $\mathbf{k}\cdot\mathbf{p}$  theory of semiconductors. 2004. Lecture course notes from University of Notre Dame. Available at <http://www3.nd.edu/~djena/kdotp.pdf>.
- [94] D. Munteanu and J.-L. Autran. A 2-D/3-D Schrödinger-Poisson drift-diffusion numerical simulation of radially-symmetric nanowire MOSFETs. In X. Peng, editor, *Nanowires - Recent Advances*, chapter 15. 2012. DOI: [10.5772/52587](https://doi.org/10.5772/52587).
- [95] Science Node. Transatlantic network extends 100-gigabit connectivity between US and Europe, 2014. Available at <https://sciencenode.org/feature/transatlantic-network-extends-100-gigabit-connectivity-between-us-and-europe.php>. Accessed 27 March 2016.
- [96] Submarine cable networks website. Available at <http://www.submarinenetworks.com/>. Accessed 27 March 2016.
- [97] R. G. H. van Uden, R. Amezcua Correa, E. Antonio Lopez, F. M. Huijskens, C. Xia, G. Li, A. Schülzgen, H. de Waardt, A. M. J. Koonen, and C. M. Okonkwo. Ultra-high-density spatial division multiplexing with a few-mode multicore fibre. *Nature Photonics*, 8:865, 2014. DOI: [10.1038/nphoton.2014.243](https://doi.org/10.1038/nphoton.2014.243).
- [98] ISPreview. UK Scientists Squeeze 1.125Tbps Through a Single Fibre Optic Receiver, 2016. Available at <http://www.ispreview.co.uk/index.php/2016/02/uk-scientists-squeeze-1-125tbps-through-a-single-fibre-optic-receiver.html>. Accessed 27 March 2016.
- [99] B. J. Puttnam, R. S. Luís, W. Klaus, J. Sakaguchi, J. M. Delgado Mendinueta, Y. Awaji, N. Wada, Y. Tamura, T. Hayashi, M. Hirano, and J. Marciante. 2.15 Pb/s transmission using a 22 core homogeneous single-mode multi-core

- fiber and wideband optical comb. In *2015 European Conference on Optical Communication (ECOC)*, page 1, 2015. DOI: [10.1109/ECOC.2015.7341685](https://doi.org/10.1109/ECOC.2015.7341685).
- [100] National Institute of Information and Japan Communications Technology. Going beyond the limits of optical fibers, 4 2015. Available at <http://www.nict.go.jp/en/press/2015/04/24-1.html>. Accessed 28 March 2016.
- [101] Infonetics Research. In Data Center Optics Market, 40G Transceivers Ubiquitous, 100G Accelerating, 10 2015. Available at <http://www.infonetics.com/pr/2015/1H15-Data-Center-Optics-Highlights.asp>. Accessed on 28 March 2016.
- [102] Y. C. Chang and L. A. Coldren. High-efficiency, high-speed VCSELs for optical interconnects. *Applied Physics A*, 95:1033, 2009. DOI: [10.1007/s00339-009-5112-7](https://doi.org/10.1007/s00339-009-5112-7).
- [103] Black Box Technology Blog. 8 Advantages of Choosing Fiber Over Copper Cable, 2015. Available at <http://blog.blackbox.com/technology/2015/04/8-advantages-to-choosing-fiber-over-copper-cable/>. Accessed on 28 March 2016.
- [104] The Fibre Optic Association. Copper or Fiber? What’s the real story? Available at <http://www.thefoa.org/tech/fo-or-cu.htm>. Accessed on 28 March 2016.
- [105] D. A. B. Miller. Physical reason for optical interconnection. *International Journal of Optoelectronics*, 11:155, 1997. Available at <http://www-ee.stanford.edu/~dabm/189.pdf>.
- [106] D. A. B. Miller. Optics for digital image processing. In *Semiconductor Quantum Optoelectronics: From Quantum Physics to Smart Devices*, page 433. Taylor & Francis, 1999.
- [107] N. N. Ledentsov, D. Bimberg, F. Hopfer, A. Mutig, V. A. Shchukin, A. V. Savel’ev, G. Fiol, E. Stock, H. Eisele, M. Dähne, D. Gerthsen, U. Fischer, D. Litvinov, A. Rosenauer, S. S. Mikhrin, A. R. Kovsh, N. D. Zakharov, and P. Werner. Submonolayer quantum dots for high speed surface emitting lasers. *Nanoscale Research Letters*, 2:417, 2007. DOI: [10.1007/s11671-007-9078-0](https://doi.org/10.1007/s11671-007-9078-0).
- [108] D. Bimberg. Ultrafast VCSELs for datacom. *IEEE Photonics Journal*, 2:273, 2010. DOI: [10.1109/JPHOT.2010.2047386](https://doi.org/10.1109/JPHOT.2010.2047386).

- [109] D. G. Kam, M. B. Ritter, T. J. Beukema, J. F. Bulzacchelli, P. K. Pepeljugoski, Y. H. Kwark, L. Shan, X. Gu, C. W. Baks, R. A. John, G. Hougham, C. Schuster, R. Rimolo-Donadio, and B. Wu. Is 25 Gb/s on-board signaling viable? *IEEE Transactions on Advanced Packaging*, 32:328, 2009. DOI: [10.1109/TADV.2008.2011138](https://doi.org/10.1109/TADV.2008.2011138).
- [110] A. F. Benner, M. Ignatowski, J. A. Kash, D. M. Kuchta, and M. B. Ritter. Exploitation of optical interconnects in future server architectures. *IBM Journal of Research and Development*, 49, 2005. DOI: [10.1147/rd.494.0755](https://doi.org/10.1147/rd.494.0755).
- [111] T. Wipiejewski, H.-D. Wolf, L. Korte, W. Huber, G. Kristen, C. Hoyler, H. Hedrich, O. Kleinbub, T. Albrecht, J. Mueller, A. Orth, Z. Spika, S. Lutgen, H. Pflaeging, J. Harrasser, K. Droegemueller, V. Plickert, D. Kuhl, J. Blank, D. Pietsch, H. Stange, and H. Karstensen. VCSELs for datacom applications. 1999. DOI: [10.1117/12.347093](https://doi.org/10.1117/12.347093).
- [112] E. Haglund. *VCSELs for High-Speed, Long-Reach, and Wavelength-Multiplexed Optical Interconnects*. PhD thesis, Chalmers University of Technology, Göteborg, Sweden, 2015. Available at <http://publications.lib.chalmers.se/records/fulltext/221221/221221.pdf>.
- [113] R. Paschotta. *Encyclopedia of Laser Physics and Technology*. Wiley, 2008. Online version available at <https://www.rp-photonics.com/encyclopedia.html>. Accessed 29 March 2016.
- [114] Princeton Optronics. High Power CW and QCW VCSEL Diode Laser Arrays. Available at <http://www.princetonoptronics.com/technology/our-technology/#IV>. Accessed 10 August 2016.
- [115] A. Larsson. Advances in VCSELs for communication and sensing. *IEEE Journal of Selected Topics in Quantum Electronics*, 17:1552, 2011. DOI: [10.1109/JSTQE.2011.2119469](https://doi.org/10.1109/JSTQE.2011.2119469).
- [116] P. Wolf, P. Moser, G. Larisch, W. Hofmann, and D. Bimberg. High-speed and temperature-stable, oxide-confined 980-nm vcsels for optical interconnects. *IEEE Journal of Selected Topics in Quantum Electronics*, 19:1701207, 2013. DOI: [10.1109/JSTQE.2013.2246773](https://doi.org/10.1109/JSTQE.2013.2246773).

- [117] H. Li. *Temperature-stable, energy-efficient, and high bit-rate 980 nm VCSELs*. PhD thesis, Technische Universität Berlin, 2015.
- [118] P. Westbergh, R. Safaisini, E. Haglund, J. S. Gustavsson, A. Larsson, M. Geen, R. Lawrence, and A. Joel. High-speed oxide confined 850-nm VCSELs operating error-free at 40 Gb/s up to 85°C. *IEEE Photonics Technology Letters*, 25:768, 2013. DOI: [10.1109/LPT.2013.2250946](https://doi.org/10.1109/LPT.2013.2250946).
- [119] P. Moser, J. A. Lott, P. Wolf, G. Larisch, H. Li, and D. Bimberg. Error-free 46 Gbit/s operation of oxide-confined 980 nm VCSELs at 85°C. *Electronics Letters*, 50:1369, 2014. DOI: [10.1049/el.2014.1703](https://doi.org/10.1049/el.2014.1703).
- [120] R. Chin, N. Holonyak Jr., B. A. Vojak, K. Hess, R. D. Dupuis, and P. D. Dapkus. Temperature dependence of threshold current for quantum-well  $\text{Al}_x\text{Ga}_{1-x}\text{AsGaAs}$  heterostructure laser diodes. *Applied Physics Letters*, 36:19, 1980. DOI: [10.1063/1.91290](https://doi.org/10.1063/1.91290).
- [121] N. Holonyak, R. Kolbas, R. Dupuis, and P. Dapkus. Quantum-well heterostructure lasers. *IEEE Journal of Quantum Electronics*, 16:170, 1980.
- [122] Y. Arakawa and H. Sakaki. Multidimensional quantum well laser and temperature dependence of its threshold current. *Applied Physics Letters*, 40:939, 1982. DOI: [10.1063/1.92959](https://doi.org/10.1063/1.92959).
- [123] M. Asada, Y. Miyamoto, and Y. Suematsu. Gain and the threshold of three-dimensional quantum-box lasers. *IEEE Journal of Quantum Electronics*, 22:1915, 1986. DOI: [10.1109/JQE.1986.1073149](https://doi.org/10.1109/JQE.1986.1073149).
- [124] N. Kirstaedter, N. N. Ledentsov, M. Grundmann, D. Bimberg, V. M. Ustinov, S. S. Ruvimov, M. V. Maximov, P. S. Kop'ev, Z. I. Alferov, U. Richter, P. Werner, U. Gosele, and J. Heydenreich. Low threshold, large to injection laser emission from (InGa)As quantum dots. *Electronics Letters*, 30:1416, 1994. DOI: [10.1049/el:19940939](https://doi.org/10.1049/el:19940939).
- [125] N. Kirstaedter, O. G. Schmidt, N. N. Ledentsov, D. Bimberg, V. M. Ustinov, A. Yu. Egorov, A. E. Zhukov, M. V. Maximov, P. S. Kopev, and Zh. I. Alferov.

Gain and differential gain of single layer InAs/GaAs quantum dot injection lasers. *Applied Physics Letters*, 69:1226, 1996.

- [126] D. Bimberg, N. Kirstaedter, N. N. Ledentsov, Z. I. Alferov, P. S. Kop'ev, and V. M. Ustinov. InGaAs-GaAs quantum-dot lasers. *IEEE Journal of Selected Topics in Quantum Electronics*, 3:196, 1997. DOI: [10.1109/2944.605656](https://doi.org/10.1109/2944.605656).
- [127] M. Grundmann, N. N. Ledentsov, N. Kirstaedter, F. Heinrichsdorff, A. Krost, D. Bimberg, A. O. Kosogov, S.S. Ruvimov, P. Werner, V.M. Ustinov, P.S. Kop'ev, and Zh.I. Alferov. Semiconductor quantum dots for application in diode lasers. *Thin Solid Films*, 318:83, 1998. DOI: [10.1016/S0040-6090\(97\)01144-9](https://doi.org/10.1016/S0040-6090(97)01144-9).
- [128] N. N. Ledentsov, V. M. Ustinov, V. A. Shchukin, P. S. Kop'ev, Zh. I. Alferov, and D. Bimberg. Quantum dot heterostructures: Fabrication, properties, lasers (review). *Semiconductors*, 32:343, 1998. DOI: [10.1134/1.1187396](https://doi.org/10.1134/1.1187396).
- [129] N.N. Ledentsov, J. Böhrer, D. Bimberg, S. V. Zaitsev, V. M. Ustinov, A. Yu. Egorov, A. E. Zhukov, M. V. Maximov, P. S. Kop'ev, Zh. I. Alferov, A. O. Kosogov, U. Gösele, and S. S. Ruvimov. 3D arrays of quantum dots for laser applications. In *Symposium D Compound Semiconductor Electronics and Photonics*, volume 421 of *MRS Proceedings*, page 133, 1996. DOI: [10.1557/PROC-421-133](https://doi.org/10.1557/PROC-421-133).
- [130] Y. M. Shernyakov, A. Y. Egorov, A. E. Zhukov, S. V. Zaitsev, A. R. Kovsh, I. L. Krestnikov, A. V. Lunev, N. N. Ledentsov, M. V. Maksimov, A. V. Sakharov, V. M. Ustinov, C. Chen, P. S. Kop'ev, Zh. I. Alferov, and D. Bimberg. Quantum-dot cw heterojunction injection laser operating at room temperature with an output power of 1 W. *Technical Physics Letters*, 23:149, 1997. DOI: [10.1134/1.1261567](https://doi.org/10.1134/1.1261567).
- [131] P. G. Eliseev, H. Li, G. T. Liu, A. Stintz, T. C. Newell, L. F. Lester, and K. J. Malloy. Ground-state emission and gain in ultralow-threshold InAsInGaAs quantum-dot lasers. *IEEE Journal on Selected Topics in Quantum Electronics*, 7:135, 2001. DOI: [10.1109/2944.954121](https://doi.org/10.1109/2944.954121).

- [132] S. Fathpour, Z. Mi, and P. Bhattacharya. High-speed quantum dot lasers. *Journal of Physics D: Applied Physics*, 38:2103, 2005. DOI: [10.1088/0022-3727/38/13/005](https://doi.org/10.1088/0022-3727/38/13/005).
- [133] J. Urayama, T. B. Norris, H. Jiang, J. Singh, and P. Bhattacharya. Temperature-dependent carrier dynamics in self-assembled InGaAs quantum dots. *Applied Physics Letters*, 80:2162, 2002. DOI: [10.1063/1.1462860](https://doi.org/10.1063/1.1462860).
- [134] C. Cornet, C. Platz, P. Caroff, J. Even, C. Labbé, H. Folliot, A. Le Corre, and S. Loualiche. Approach to wetting-layer-assisted lateral coupling of InAs/InP quantum dots. *Physical Review B*, 72:035342, 2005. DOI: [10.1103/PhysRevB.72.035342](https://doi.org/10.1103/PhysRevB.72.035342).
- [135] C. Cornet, M. Hayne, P. Caroff, C. Levallois, L. Joulaud, E. Homeyer, C. Paranthoen, J. Even, C. Labbé, H. Folliot, V. V. Moshchalkov, and S. Loualiche. Increase of charge-carrier redistribution efficiency in a laterally organized superlattice of coupled quantum dots. *Physical Review B*, 74:245315, 2006. DOI: [10.1103/PhysRevB.74.245315](https://doi.org/10.1103/PhysRevB.74.245315).
- [136] Y. Tanaka, K. Takada, M. Ishida, Y. Nakata, T. Yamamoto, M. Yamaguchi, K. Nishi, M. Sugawara, and Y. Arakawa. High-speed modulation in 1.3- $\mu\text{m}$  InAs/GaAs high-density quantum dot lasers. In *Communications and Photonics Conference and Exhibition (ACP), 2010 Asia*, page 577, 2010. DOI: [10.1109/ACP.2010.5682637](https://doi.org/10.1109/ACP.2010.5682637).
- [137] W. W. Chow, M. Lorke, and F. Jahnke. Will quantum dots replace quantum wells as the active medium of choice in future semiconductor lasers? *IEEE Journal on Selected Topics in Quantum Electronics*, 17:1349, 2011. DOI: [10.1109/JSTQE.2011.2157085](https://doi.org/10.1109/JSTQE.2011.2157085).
- [138] A. E. Zhukov, M. V. Maksimov, and A. R. Kovsh. Device characteristics of long-wavelength lasers based on self-organized quantum dots. *Semiconductors*, 46:1225, 2012. DOI: [10.1134/S1063782612100223](https://doi.org/10.1134/S1063782612100223).
- [139] J. Wu, S. Chen, A. Seeds, and H. Liu. Quantum dot optoelectronic devices: lasers, photodetectors and solar cells. *Journal of Physics D: Applied Physics*, 48:363001, 2015. DOI: [10.1088/0022-3727/48/36/363001](https://doi.org/10.1088/0022-3727/48/36/363001).

- [140] O. Brandt, L. Tapfer, K. Ploog, R. Bierwolf, M. Hohenstein, F. Phillipp, H. Lage, and A. Heberle. InAs quantum dots in a single-crystal GaAs matrix. *Physical Review B*, 44:8043, 1991. DOI: [10.1103/PhysRevB.44.8043](https://doi.org/10.1103/PhysRevB.44.8043).
- [141] O. Brandt, H. Lage, G. C. La Rocca, A. Heberle, and K. Ploog. Role of broken translational invariance for the optical response of excitons in low-dimensional semiconductors. *Surface Science*, 267:319, 1992. DOI: [10.1016/0039-6028\(92\)91146-3](https://doi.org/10.1016/0039-6028(92)91146-3).
- [142] V. Bressler-Hill, A. Lorke, S. Varma, P. M. Petroff, K. Pond, and W. H. Weinberg. Initial stages of InAs epitaxy on vicinal GaAs(001)-(2×4). *Physical Review B*, 50:8479, 1994. DOI: [10.1103/PhysRevB.50.8479](https://doi.org/10.1103/PhysRevB.50.8479).
- [143] P. D. Wang, N. N. Ledentsov, C. M. Sotomayor Torres, P. S. Kopev, and V. M. Ustinov. Optical characterization of submonolayer and monolayer InAs structures grown in a GaAs matrix on (100) and highindex surfaces. *Applied Physics Letters*, 64:1526, 1994. DOI: [10.1063/1.111880](https://doi.org/10.1063/1.111880).
- [144] A. Y. Egorov, A. E. Zhukov, P. S. Kop'ev, N. N. Ledentsov, M. V. Maksimov, and V. M. Ustinov. Growth of (In,Ga)As GaAs quantum-well heterostructures through the deposition of submonolayer strained InAs layers. *Semiconductors*, 28:363, 1994.
- [145] G. M. Guryanov, G. E. Cirlin, A. O. Golubok, S. Ya. Tapishev, N. N. Ledentsov, V. A. Shchukin, M. Grundmann, D. Bimberg, and Zh. I. Alferov. An intermediate (1.0-1.5 monolayers) stage of heteroepitaxial growth of InAs on GaAs(100) during submonolayer molecular beam epitaxy. *Surface Science*, 352354:646, 1996. DOI: [10.1016/0039-6028\(95\)01220-6](https://doi.org/10.1016/0039-6028(95)01220-6). Proceedings of the 15th European Conference on Surface Science.
- [146] V. A. Shchukin, D. Bimberg, V. G. Malyshev, and N. N. Ledentsov. Vertical correlations and anticorrelations in multisheet arrays of two-dimensional islands. *Physical Review B*, 57:12262, 1998. DOI: [10.1103/PhysRevB.57.12262](https://doi.org/10.1103/PhysRevB.57.12262).
- [147] Q. Xie, P. Chen, and A. Madhukar. InAs island-induced-strain driven adatom migration during GaAs overlayer growth. *Applied Physics Letters*, 65:2051, 1994. DOI: [10.1063/1.112790](https://doi.org/10.1063/1.112790).

- [148] Q. Xie, A. Madhukar, P. Chen, and N. P. Kobayashi. Vertically self-organized InAs quantum box islands on GaAs(100). *Physical Review Letters*, 75:2542, 1995. DOI: [10.1103/PhysRevLett.75.2542](https://doi.org/10.1103/PhysRevLett.75.2542).
- [149] J. Tersoff, C. Teichert, and M. G. Lagally. Self-organization in growth of quantum dot superlattices. *Physical Review Letters*, 76:1675, 1996. DOI: [10.1103/PhysRevLett.76.1675](https://doi.org/10.1103/PhysRevLett.76.1675).
- [150] V. A. Shchukin and D. Bimberg. Spontaneous ordering of nanostructures on crystal surfaces. *Review of Modern Physics*, 71:1125, 1999. DOI: [10.1103/RevModPhys.71.1125](https://doi.org/10.1103/RevModPhys.71.1125).
- [151] Z. Xu, K. Leosson, D. Birkedal, V. Lyssenko, J. M. Hvam, and J. Sadowski. InGaAs/GaAs quantum-dot-quantum-well heterostructure formed by submonolayer deposition. *Nanotechnology*, 14:1259, 2003. DOI: [10.1088/0957-4484/14/12/005](https://doi.org/10.1088/0957-4484/14/12/005).
- [152] Z. Xu, D. Birkedal, M. Juhl, and J. M. Hvam. Submonolayer InGaAs/GaAs quantum-dot lasers with high modal gain and zerolinerwidth enhancement factor. *Applied Physics Letters*, 85:3259, 2004. DOI: [10.1063/1.1806564](https://doi.org/10.1063/1.1806564).
- [153] Z. Xu, Y. Zhang, J. M. Hvam, J. Xu, X. Chen, and W. Lu. Carrier dynamics in submonolayer InGaAs/GaAs quantum dots. *Applied Physics Letters*, 89:013113, 2006. DOI: [10.1063/1.2219394](https://doi.org/10.1063/1.2219394).
- [154] T. Niermann, F. Kießling, M. Lehmann, J.-H. Schulze, T. D. Germann, K. Ptschke, A. Strittmatter, and U. W. Pohl. Atomic structure of closely stacked InAs submonolayer depositions in GaAs. *Journal of Applied Physics*, 112:083505, 2012. DOI: [10.1063/1.4758301](https://doi.org/10.1063/1.4758301).
- [155] A. E. Zhukov, A. R. Kovsh, S. S. Mikhrin, N. A. Maleev, V. M. Ustinov, D. A. Livshits, I. S. Tarasov, D. A. Bedarev, M. V. Maximov, A. F. Tsatsul'nikov, I. P. Soshnikov, P. S. Kop'ev, Z. I. Alferov, N. N. Ledentsov, and D. Bimberg. 3.9 W CW power from sub-monolayer quantum dot diode laser. *Electronics Letters*, 35:1845, 1999. DOI: [10.1049/el:19991264](https://doi.org/10.1049/el:19991264).

- [156] S. S. Mikhlin, A. E. Zhukov, A. R. Kovsh, N. A. Maleev, V. M. Ustinov, Y. M. Shernyakov, I. P. Soshnikov, D. A. Livshits, I. S. Tarasov, D. A. Bedarev, B. V. Volovik, M. V. Maximov, A. F. Tsatsul'nikov, N. N. Ledentsov, P. S. Kop'ev, D. Bimberg, and Zh. I. Alferov. 0.94  $\mu\text{m}$  diode lasers based on Stranski-Krastanow and sub-monolayer quantum dots. *Semiconductor Science and Technology*, 15:1061, 2000. DOI: [10.1088/0268-1242/15/11/309](https://doi.org/10.1088/0268-1242/15/11/309).
- [157] A. R. Kovsh, A. E. Zhukov, N. A. Maleev, S. S. Mikhlin, D. A. Livshits, Y. M. Shernyakov, M. V. Maximov, N. A. Pihtin, I. S. Tarasov, V. M. Ustinov, Zh. I. Alferov, J. S. Wang, L. Wei, G. Lin, J. Y. Chi, N. N. Ledentsov, and D. Bimberg. High power lasers based on submonolayer InAs-GaAs quantum dots and InGaAs quantum wells. *Microelectronics Journal*, 34:491, 2003. DOI: [10.1016/S0026-2692\(03\)00082-X](https://doi.org/10.1016/S0026-2692(03)00082-X).
- [158] S. A. Blokhin, N. A. Maleev, A. G. Kuzmenkov, A. V. Sakharov, M. M. Kulagina, Y. M. Shernyakov, I. I. Novikov, M. V. Maximov, V. M. Ustinov, A. R. Kovsh, S. S. Mikhlin, N. N. Ledentsov, G. Lin, and J. Y. Chi. Vertical-cavity surface-emitting lasers based on submonolayer InGaAs quantum dots. *IEEE Journal of Quantum Electronics*, 42:851, 2006. DOI: [10.1109/JQE.2006.880125](https://doi.org/10.1109/JQE.2006.880125).
- [159] F. Hopfer, A. Mutig, M. Kuntz, G. Fiol, D. Bimberg, N. N. Ledentsov, V. A. Shchukin, S. S. Mikhlin, D. L. Livshits, I. L. Krestnikov, A. R. Kovsh, N. D. Zakharov, and P. Werner. Single-mode submonolayer quantum-dot vertical-cavity surface-emitting lasers with high modulation bandwidth. *Applied Physics Letters*, 89:141106, 2006. DOI: [10.1063/1.2358114](https://doi.org/10.1063/1.2358114).
- [160] F. Hopfer, A. Mutig, G. Fiol, M. Kuntz, V. A. Shchukin, V. A. Haisler, T. Warming, E. Stock, S. S. Mikhlin, I. L. Krestnikov, D. A. Livshits, A. R. Kovsh, C. Bornholdt, A. Lenz, H. Eisele, M. Dahne, N. N. Ledentsov, and D. Bimberg. 20 Gb/s 85°C error-free operation of VCSELs based on submonolayer deposition of quantum dots. *IEEE Journal of Selected Topics in Quantum Electronics*, 13:1302, 2007. DOI: [10.1109/JSTQE.2007.905133](https://doi.org/10.1109/JSTQE.2007.905133).
- [161] A. N. Al-Omari, G. P. Carey, S. Hallstein, J. P. Watson, G. Dang, and K. L.

- Lear. Low thermal resistance high-speed top-emitting 980-nm VCSELs. *IEEE Photonics Technology Letters*, 18:1225, 2006. DOI: [10.1109/LPT.2006.875059](https://doi.org/10.1109/LPT.2006.875059).
- [162] J. A. Lott, V. A. Shchukin, N. N. Ledentsov, A. Stinz, F. Hopfer, A. Mutig, G. Fiol, D. Bimberg, S. A. Blokhin, L. Y. Karachinsky, I. I. Novikov, M. V. Maximov, N. D. Zakharov, and P. Werner. 20 Gbit/s error free transmission with 850 nm GaAs-based vertical cavity surface emitting lasers (VCSELs) containing InAs-GaAs submonolayer quantum dot insertions. In *Physics and Simulation of Optoelectronic Devices XVII*, volume 7211, page 721114, 2009. DOI: [10.1117/12.816947](https://doi.org/10.1117/12.816947).
- [163] D. Z.-Y. Ting, S. V. Bandara, S. D. Gunapala, J. M. Mumolo, S. A. Keo, C. J. Hill, J. K. Liu, E. R. Blazejewski, S. B. Rafol, and Y.-C. Chang. Submonolayer quantum dot infrared photodetector. *Applied Physics Letters*, 94:111107, 2009. DOI: [10.1063/1.3095812](https://doi.org/10.1063/1.3095812).
- [164] P. Lam, J. Wu, M. Tang, Q. Jiang, S. Hatch, R. Beanland, J. Wilson, R. Allison, and H. Liu. Submonolayer InGaAs/GaAs quantum dot solar cells. *Solar Energy Materials and Solar Cells*, 126:83, 2014. DOI: [10.1016/j.solmat.2014.03.046](https://doi.org/10.1016/j.solmat.2014.03.046).
- [165] T. Switaiski, U. Woggon, D. E. Alden Angeles, A. Hoffmann, J.-H. Schulze, T. D. Germann, A. Strittmatter, and U. W. Pohl. Carrier dynamics in InAs/GaAs submonolayer stacks coupled to Stranski-Krastanov quantum dots. *Physical Review B*, 88:035314, 2013. DOI: [10.1103/PhysRevB.88.035314](https://doi.org/10.1103/PhysRevB.88.035314).
- [166] D. Quandt, J.-H. Schulze, A. Schliwa, Z. Diemer, C. Prohl, A. Lenz, H. Eisele, A. Strittmatter, U. W. Pohl, M. Gschrey, S. Rodt, S. Reitzenstein, D. Bimberg, M. Lehmann, and M. Weyland. Strong charge-carrier localization in InAs/GaAs submonolayer stacks prepared by Sb-assisted metalorganic vapor-phase epitaxy. *Physical Review B*, 91:235418, 2015. DOI: [10.1103/PhysRevB.91.235418](https://doi.org/10.1103/PhysRevB.91.235418).
- [167] B. Herzog, N. Owschimikow, J.-H. Schulze, R. Rosales, Y. Kaptan, M. Kolarczik, T. Switaiski, A. Strittmatter, D. Bimberg, U. W. Pohl, and U. Woggon. Fast gain and phase recovery of semiconductor optical amplifiers based on

- submonolayer quantum dots. *Applied Physics Letters*, 107:201102, 2015. DOI: [10.1063/1.4935792](https://doi.org/10.1063/1.4935792).
- [168] Photoluminescence characterization of InAs/GaAs quantum dot bilayers. *Materials Science and Engineering: B*, 88.
- [169] H. Lee, W. Yang, and P. C. Sercel. Temperature and excitation dependence of photoluminescence line shape in InAs/GaAs quantum-dot structures. *Physical Review B*, 55:9757, 1997. DOI: [10.1103/PhysRevB.55.9757](https://doi.org/10.1103/PhysRevB.55.9757).
- [170] T. Yang, J. Tatebayashi, S. Tsukamoto, M. Nishioka, and Y. Arakawa. Narrow photoluminescence linewidth ( $< 17\text{meV}$ ) from highly uniform self-assembled InAs/GaAs quantum dots grown by low-pressure metalorganic chemical vapor deposition. *Applied Physics Letters*, 84:2817, 2004. DOI: [10.1063/1.1711163](https://doi.org/10.1063/1.1711163).
- [171] B. Bansal, M. Hayne, B. M. Arora, and V. V. Moshchalkov. Magnetic field-dependent photoluminescence linewidths as a probe of disorder length scales in quantum wells. *Applied Physics Letters*, 91:251108, 2007. DOI: [10.1063/1.2825417](https://doi.org/10.1063/1.2825417).
- [172] M. Yahyaoui, K. Sellami, S. Ben Radhia, K. Boujdaria, M. Chamarro, B. Eble, C. Testelin, and A. Lemaître. Effects of strain on the optoelectronic properties of annealed InGaAs/GaAs self-assembled quantum dots. *Semiconductor Science and Technology*, 29:075013, 2014. DOI: [10.1088/0268-1242/29/7/075013](https://doi.org/10.1088/0268-1242/29/7/075013).
- [173] C. Pryor. Eight-band calculations of strained InAs/GaAs quantum dots compared with one-, four-, and six-band approximations. *Physical Review B*, 57:7190, 1998. DOI: [10.1103/PhysRevB.57.7190](https://doi.org/10.1103/PhysRevB.57.7190).
- [174] S. A. Khattak. *Exciton confinement in strain-engineered InAs quantum dots in metamorphic  $\text{In}_x\text{Ga}_{1-x}\text{As}$* . PhD thesis, Lancaster University, 2015. Available at [http://www.research.lancs.ac.uk/portal/en/publications/exciton-confinement-in-strainengineered-inas-quantum-dots-in-metamorphic-inxga1xas\(4d168973-92fd-4e6e-b17b-437393e6ee14\).html](http://www.research.lancs.ac.uk/portal/en/publications/exciton-confinement-in-strainengineered-inas-quantum-dots-in-metamorphic-inxga1xas(4d168973-92fd-4e6e-b17b-437393e6ee14).html).
- [175] J. B. B. de Oliveira, E. A. Meneses, and E. C. F. da Silva. Magneto-optical studies of the correlation between interface microroughness parameters and the

- photoluminescence line shape in GaAs/Ga<sub>0.7</sub>Al<sub>0.3</sub>As quantum wells. *Physical Review B*, 60:1519, 1999. DOI: [10.1103/PhysRevB.60.1519](https://doi.org/10.1103/PhysRevB.60.1519).
- [176] R. Heitz, I. Mukhametzhanov, A. Mudhukar, A. Hoffmann, and D. Bimberg. Temperature dependent optical properties of self-organized InAs/GaAs quantum dots. *Journal of Electronic Materials*, 28:520, 1999. DOI: [10.1007/s11664-999-0105-z](https://doi.org/10.1007/s11664-999-0105-z).
- [177] Q. Li, S. J. Xu, M. H. Xie, and S. Y. Tong. Origin of the ‘S-shaped’ temperature dependence of luminescent peaks from semiconductors. *Journal of Physics: Condensed Matter*, 17:4853, 2005. DOI: [10.1088/0953-8984/17/30/011](https://doi.org/10.1088/0953-8984/17/30/011).
- [178] V. K. Dixit, S. Porwal, S. D. Singh, T. K. Sharma, S. Ghosh, and S. M. Oak. A versatile phenomenological model for the S-shaped temperature dependence of photoluminescence energy for an accurate determination of the exciton localization energy in bulk and quantum well structures. *Journal of Physics D*, 47:65103, 2014. DOI: [10.1088/0022-3727/47/6/065103](https://doi.org/10.1088/0022-3727/47/6/065103).
- [179] D. Watson-Parris, M. J. Godfrey, P. Dawson, R. A. Oliver, M. J. Galtrey, M. J. Kappers, and C. J. Humphreys. Carrier localization mechanisms in In<sub>x</sub>Ga<sub>1-x</sub>N/GaN quantum wells. *Physical Review B*, 83:115321, 2011. DOI: [10.1103/PhysRevB.83.115321](https://doi.org/10.1103/PhysRevB.83.115321).
- [180] T. J. Badcock, S. Hammersley, D. Watson-Parris, P. Dawson, M. J. Godfrey, M. J. Kappers, C. McAleese, R. A. Oliver, and C. J. Humphreys. Carrier density dependent localization and consequences for efficiency droop in In-GaN/GaN quantum well structures. *Japanese Journal of Applied Physics*, 52:08JK10, 2013. DOI: [10.7567/JJAP.52.08JK10](https://doi.org/10.7567/JJAP.52.08JK10).
- [181] P. J. Boddy. Oxygen evolution on semiconducting TiO<sub>2</sub>. *Journal of the Electrochemical Society*, 115:199, 1968. DOI: [10.1149/1.2411080](https://doi.org/10.1149/1.2411080).
- [182] A. Fujishima and K. Honda. Electrochemical photolysis of water at a semiconductor electrode. *Nature*, 238:37, 1972. DOI: [10.1038/238037a0](https://doi.org/10.1038/238037a0).

- [183] A. Fujishima, K. Kohayakawa, and K. Honda. Hydrogen production under sunlight with an electrochemical photocell. *Journal of the Electrochemical Society*, 122:1487, 1975. DOI: [10.1149/1.2134048](https://doi.org/10.1149/1.2134048).
- [184] M. Tomkiewicz and H. Fay. Photoelectrolysis of water with semiconductors. *Applied Physics*, 18:1, 1979. DOI: [10.1007/BF00935899](https://doi.org/10.1007/BF00935899).
- [185] E. C. Dutoit, F. Cardon, and W. P. Gomes. Electrochemical reactions involving holes at the illuminated TiO<sub>2</sub> (rutile) single crystal electrode. *Berichte der Bunsengesellschaft für physikalische Chemie*, 80:475, 1976. DOI: [10.1002/bbpc.19760801208](https://doi.org/10.1002/bbpc.19760801208).
- [186] J. W. Ager, M. R. Shaner, K. A. Walczak, I. D. Sharp, and S. Ardo. Experimental demonstrations of spontaneous, solar-driven photoelectrochemical water splitting. *Energy and Environmental Science*, 8:2811, 2015. DOI: [10.1039/C5EE00457H](https://doi.org/10.1039/C5EE00457H).
- [187] J. G. Mavroides, D. I. Tchernev, J. A. Kafalas, and D. F. Kolesar. Photoelectrolysis of water in cells with TiO<sub>2</sub> anodes. *Materials Research Bulletin*, 10:1023, 1975. DOI: [10.1016/0025-5408\(75\)90210-X](https://doi.org/10.1016/0025-5408(75)90210-X).
- [188] M. S. Wrighton, A. B. Ellis, P. T. Wolczanski, D. L. Morse, H. B. Abrahamson, and D. S. Ginley. Strontium titanate photoelectrodes. efficient photoassisted electrolysis of water at zero applied potential. *Journal of the American Chemical Society*, 98:2774, 1976. DOI: [10.1021/ja00426a017](https://doi.org/10.1021/ja00426a017).
- [189] J. G. Mavroides, J. A. Kafalas, and D. F. Kolesar. Photoelectrolysis of water in cells with SrTiO<sub>3</sub> anodes. *Applied Physics Letters*, 28:241, 1976. DOI: [10.1063/1.88723](https://doi.org/10.1063/1.88723).
- [190] J. M. Bolts and M. S. Wrighton. Correlation of photocurrent-voltage curves with flat-band potential for stable photoelectrodes for the photoelectrolysis of water. *The Journal of Physical Chemistry*, 80:2641, 1976. DOI: [10.1021/j100565a004](https://doi.org/10.1021/j100565a004).
- [191] M. Tomkiewicz and J. M. Woodall. Photoassisted electrolysis of water by

- visible irradiation of a p-type gallium phosphide electrode. *Science*, 196:990, 1977. DOI: [10.1126/science.196.4293.990](https://doi.org/10.1126/science.196.4293.990).
- [192] E. Aharon-Shalom and A. Heller. Efficient p-InP(Rh-H alloy) and p-InP(Re-H alloy) hydrogen evolving photocathodes. *Journal of the Electrochemical Society*, 129:2865, 1982. DOI: [10.1149/1.2123695](https://doi.org/10.1149/1.2123695).
- [193] L. M. Peter. Towards sustainable photovoltaics: the search for new materials. *Philosophical Transactions of the Royal Society of London A: Mathematical, Physical and Engineering Sciences*, 369:1840, 2011. DOI: [10.1098/rsta.2010.0348](https://doi.org/10.1098/rsta.2010.0348).
- [194] L. A. Harris and R. H. Wilson. Semiconductors for photoelectrolysis. *Annual Review of Materials Science*, 8:99, 1978. DOI: [10.1146/annurev.ms.08.080178.000531](https://doi.org/10.1146/annurev.ms.08.080178.000531).
- [195] L. M. Peter and K. G. Upul Wijayantha. Photoelectrochemical water splitting at semiconductor electrodes: Fundamental problems and new perspectives. *ChemPhysChem*, 15:1983, 2014. DOI: [10.1002/cphc.201402024](https://doi.org/10.1002/cphc.201402024).
- [196] CNN. Who's funding the green energy revolution? Available at <http://edition.cnn.com/2012/06/12/world/renewables-finance-unep/>. Accessed 28 April 2016.
- [197] W. A. Smith, I. D. Sharp, N. C. Strandwitz, and J. Bisquert. Interfacial band-edge energetics for solar fuels production. *Energy and Environmental Science*, 8:2851, 2015. DOI: [10.1039/C5EE01822F](https://doi.org/10.1039/C5EE01822F).
- [198] H. Yoneyama, H. Sakamoto, and H. Tamura. A photo-electrochemical cell with production of hydrogen and oxygen by a cell reaction. *Electrochimica Acta*, 20:341, 1975. DOI: [10.1016/0013-4686\(75\)90016-X](https://doi.org/10.1016/0013-4686(75)90016-X).
- [199] A. J. Nozik. p-n photoelectrolysis cells. *Applied Physics Letters*, 29:150, 1976. DOI: [10.1063/1.89004](https://doi.org/10.1063/1.89004).
- [200] O. Khaselev and J. A. Turner. A monolithic photovoltaic-photoelectrochemical device for hydrogen production via water splitting. *Science*, 280:425, 1998. DOI: [10.1126/science.280.5362.425](https://doi.org/10.1126/science.280.5362.425).

- [201] O. Khaselev, A. Bansal, and J. A. Turner. High-efficiency integrated multijunction photovoltaic/electrolysis systems for hydrogen production. *International Journal of Hydrogen Energy*, 26:127, 2001. DOI: [10.1016/S0360-3199\(00\)00039-2](https://doi.org/10.1016/S0360-3199(00)00039-2).
- [202] S. Licht, B. Wang, S. Mukerji, T. Soga, M. Umeno, and H. Tributsch. Efficient solar water splitting, exemplified by RuO<sub>2</sub>-catalyzed AlGaAs/Si photoelectrolysis. *The Journal of Physical Chemistry B*, 104:8920, 2000. DOI: [10.1021/jp002083b](https://doi.org/10.1021/jp002083b).
- [203] S. Y. Reece, J. A. Hamel, K. Sung, T. D. Jarvi, A. J. Esswein, J. J. H. Pijpers, and D. G. Nocera. Wireless solar water splitting using silicon-based semiconductors and earth-abundant catalysts. *Science*, 334:645, 2011. DOI: [10.1126/science.1209816](https://doi.org/10.1126/science.1209816).
- [204] J. Luo, J.-H. Im, M. T. Mayer, M. Schreier, M. K. Nazeeruddin, N.-G. Park, S. D. Tilley, H. J. Fan, and M. Grätzel. Water photolysis at 12.3% efficiency via perovskite photovoltaics and earth-abundant catalysts. *Science*, 345:1593, 2014. DOI: [10.1126/science.1258307](https://doi.org/10.1126/science.1258307).
- [205] F. E. Osterloh and B. A. Parkinson. Recent developments in solar water-splitting photocatalysis. *MRS Bulletin*, 36:17, 2011. DOI: [10.1557/mrs.2010.5](https://doi.org/10.1557/mrs.2010.5).
- [206] M. K. Nazeeruddin, A. Kay, I. Rodicio, R. Humphry-Baker, E. Mueller, P. Liska, N. Vlachopoulos, and M. Graetzel. Conversion of light to electricity by cis-X<sub>2</sub>bis(2,2'-bipyridyl-4,4'-dicarboxylate)ruthenium(II) charge-transfer sensitizers (X = Cl-, Br-, I-, CN-, and SCN-) on nanocrystalline titanium dioxide electrodes. *Journal of the American Chemical Society*, page 6382, 1993. DOI: [10.1021/ja00067a063](https://doi.org/10.1021/ja00067a063).
- [207] M. K. Nazeeruddin, P. Péchy, T. Renouard, S. M. Zakeeruddin, R. Humphry-Baker, P. Comte, P. Liska, L. Cevey, E. Costa, V. Shklover, L. Spiccia, G. B. Deacon, C. A. Bignozzi, and M. Grätzel. Engineering of efficient panchromatic sensitizers for nanocrystalline TiO<sub>2</sub>-based solar cells. *Journal of the American Chemical Society*, 123:1613, 2001. DOI: [10.1021/ja003299u](https://doi.org/10.1021/ja003299u).

- [208] D. Wang, A. Pierre, M. G. Kibria, K. Cui, X. Han, K. H. Bevan, H. Guo, S. Paradis, A.-R. Hakima, and Z. Mi. Wafer-level photocatalytic water splitting on gan nanowire arrays grown by molecular beam epitaxy. *Nano Letters*, 11:2353, 2011. DOI: [10.1021/nl2006802](https://doi.org/10.1021/nl2006802).
- [209] X. Wang, K.-Q. Peng, Y. Hu, F.-Q. Zhang, B. Hu, L. Li, M. Wang, X.-M. Meng, and S.-T. Lee. Silicon/hematite core/shell nanowire array decorated with gold nanoparticles for unbiased solar water oxidation. *Nano Letters*, 14:18, 2014. DOI: [10.1021/nl402205f](https://doi.org/10.1021/nl402205f).
- [210] G. Hodes, I. D. J. Howell, and L. M. Peter. Nanocrystalline photoelectrochemical cells: A new concept in photovoltaic cells. *Journal of the Electrochemical Society*, 139:3136, 1992. DOI: [10.1149/1.2069045](https://doi.org/10.1149/1.2069045).
- [211] G. N. Schrauzer and T. D. Guth. Photocatalytic reactions. 1. photolysis of water and photoreduction of nitrogen on titanium dioxide. *Journal of the American Chemical Society*, 99:7189–7193, 1977. DOI: [10.1021/ja00464a015](https://doi.org/10.1021/ja00464a015).
- [212] Tomoji Kawai and Tadayoshi Sakata. Photocatalytic decomposition of gaseous water over TiO<sub>2</sub> and TiO<sub>2</sub>-RuO<sub>2</sub> surfaces. *Chemical Physics Letters*, 72:87, 1980. DOI: [10.1016/0009-2614\(80\)80247-8](https://doi.org/10.1016/0009-2614(80)80247-8).
- [213] L. Liao, Q. Zhang, Z. Su, Z. Zhao, Y. Wang, Y. Li, X. Lu, D. Wei, G. Feng, Q. Yu, X. Cai, J. Zhao, Z. Ren, H. Fang, F. Robles-Hernandez, S. Baldelli, and J. Bao. Efficient solar water-splitting using a nanocrystalline CoO photocatalyst. *Nature Nanotechnology*, 9:69, 2014. DOI: [10.1038/nnano.2013.272](https://doi.org/10.1038/nnano.2013.272).
- [214] J. Liu, Y. Liu, N. Liu, Y. Han, X. Zhang, H. Huang, Y. Lifshitz, S.-T. Lee, J. Zhong, and Z. Kang. Metal-free efficient photocatalyst for stable visible water splitting via a two-electron pathway. *Science*, 347:970, 2015. DOI: [10.1126/science.aaa3145](https://doi.org/10.1126/science.aaa3145).
- [215] J. R. McKone, N. S. Lewis, and H. B. Gray. Will solar-driven water-splitting devices see the light of day? *Chemistry of Materials*, 26:407, 2014. DOI: [10.1021/cm4021518](https://doi.org/10.1021/cm4021518).

- [216] R. Liu, Z. Zheng, J. Spurgeon, and X. Yang. Enhanced photoelectrochemical water-splitting performance of semiconductors by surface passivation layers. *Energy and Environmental Science*, 7:2504, 2014. DOI: [10.1039/C4EE00450G](https://doi.org/10.1039/C4EE00450G).
- [217] J. P. Clifford, K. W. Johnston, L. Levina, and E. H. Sargent. Schottky barriers to colloidal quantum dot films. *Applied Physics Letters*, 91:253117, 2007. DOI: [10.1063/1.2823582](https://doi.org/10.1063/1.2823582).
- [218] E. Kemppainen, J. Halme, and P. Lund. Physical modeling of photoelectrochemical hydrogen production devices. *Journal of Physical Chemistry C*, 119:21747, 2015. DOI: [10.1021/acs.jpcc.5b04764](https://doi.org/10.1021/acs.jpcc.5b04764).
- [219] C. Mauder, Ö. Tuna, B. Gutrath, V. Balmes, H. Behmenburg, M. V. Rzheutskii, E. V. Lutsenko, G. P. Yablonskii, M. Noyong, U. Simon, M. Heuken, H. Kalisch, and A. Vescan. Highly n-type doped InGaN films for efficient direct solar hydrogen generation. *Physica Status Solidi (C)*, 9:964, 2012. DOI: [10.1002/pssc.201100400](https://doi.org/10.1002/pssc.201100400).
- [220] T. Tao, T. Zhi, B. Liu, M. Li, Z. Zhuang, J. Dai, Y. Li, F. Jiang, W. Luo, Z. Xie, D. Chen, P. Chen, Z. Li, Z. Zou, R. Zhang, and Y. Zheng. Significant improvements in InGaN/GaN nano-photoelectrodes for hydrogen generation by structure and polarization optimization. *Scientific Reports*, 6:20218, 2016. DOI: [doi:10.1038/srep20218](https://doi.org/10.1038/srep20218).
- [221] P. G. Moses, M. Miao, Q. Yan, and C. G. Van de Walle. Hybrid functional investigations of band gaps and band alignments for AlN, GaN, InN, and InGaN. *The Journal of Chemical Physics*, 134:084703, 2011. DOI: [10.1063/1.3548872](https://doi.org/10.1063/1.3548872).
- [222] W. Ohara, D. Uchida, T. Hayashi, M. Deura, and K. Ohkawa. Hydrogen generation for 500 hours by photoelectrolysis of water using GaN. In *Symposium U Materials for Catalysis in Energy*, volume 1446 of *MRS Proceedings*, 2012. DOI: [10.1557/opl.2012.1249](https://doi.org/10.1557/opl.2012.1249).
- [223] S.-Y. Liu, J. K. Sheu, Y.-C. Lin, S. J. Tu, F. W. Huang, M. L. Lee, and W. C. Lai. Mn-doped GaN as photoelectrodes for the photoelectrolysis of water under visible light. *Optical Express*, 20:A678, 2012. DOI: [10.1364/OE.20.00A678](https://doi.org/10.1364/OE.20.00A678).

- [224] K. Al-Heuseen, M. R. Hashim, and N. K. Ali. Electrical properties of electrolyte-GaN junction during photoelectrical etching processing. *AIP Conference Proceedings*, 1341:301, 2011. DOI: [10.1063/1.3587006](https://doi.org/10.1063/1.3587006).
- [225] J. W. Ager and N. R. Miller. Taming transport in InN. *Physica Status Solidi (A)*, 209:83, 2012. DOI: [10.1002/pssa.201100069](https://doi.org/10.1002/pssa.201100069).
- [226] W. Luo, B. Liu, Z. Li, Z. Xie, D. Chen, Z. Zou, and R. Zhang. Stable response to visible light of InGaN photoelectrodes. *Applied Physics Letters*, 92:262110, 2008. DOI: [10.1063/1.2955828](https://doi.org/10.1063/1.2955828).
- [227] Y. Hinuma, A. Grüneis, G. Kresse, and F. Oba. Band alignment of semiconductors from density-functional theory and many-body perturbation theory. *Physical Review B*, 90:155405, 2014. DOI: [10.1103/PhysRevB.90.155405](https://doi.org/10.1103/PhysRevB.90.155405).
- [228] K. Aryal, B. N. Pantha, J. Li, J. Y. Lin, and H. X. Jiang. Hydrogen generation by solar water splitting using p-InGaN photoelectrochemical cells. *Applied Physics Letters*, 96:052110, 2010. DOI: [10.1063/1.3304786](https://doi.org/10.1063/1.3304786).
- [229] F.K. Yam and Z. Hassan. InGaN: An overview of the growth kinetics, physical properties and emission mechanisms. *Superlattices and Microstructures*, 43:1, 2008. ISSN 0749-6036. DOI: [10.1016/j.spmi.2007.05.001](https://doi.org/10.1016/j.spmi.2007.05.001).
- [230] Semiconductor Today website. TDI introduces InGaN substrates. Available at [http://www.semiconductor-today.com/news\\_items/NEWS\\_2007/AUG\\_07/TDI\\_170807.htm](http://www.semiconductor-today.com/news_items/NEWS_2007/AUG_07/TDI_170807.htm).
- [231] N. Wang, Y. Yang, and G. Yang. Great blue-shift of luminescence of ZnO nanoparticle array constructed from ZnO quantum dots. *Nanoscale Research Letters*, 6:1, 2011. DOI: [10.1186/1556-276X-6-338](https://doi.org/10.1186/1556-276X-6-338).
- [232] H. Chen, Z. Wei, K. Yan, Y. Bai, Z. Zhu, T. Zhang, and S. Yang. Epitaxial growth of ZnO nanodisks with large exposed polar facets on nanowire arrays for promoting photoelectrochemical water splitting. *Small*, 10:4760, 2014. DOI: [10.1002/smll.201401298](https://doi.org/10.1002/smll.201401298).

- [233] D. Wang, F. Wang, Y. Wang, Y. Fan, B. Zhao, and D. Zhao. Interfacial emission adjustment in ZnO quantum dots/p-GaN heterojunction light-emitting diodes. *The Journal of Physical Chemistry C*, 119:2798, 2015. DOI: [10.1021/jp509655j](https://doi.org/10.1021/jp509655j).
- [234] M. Müller, A. Cerezo, G. D. W. Smith, L. Chang, and S. S. A. Gerstl. Atomic scale characterization of buried  $\text{In}_x\text{Ga}_{1-x}\text{As}$  quantum dots using pulsed laser atom probe tomography. *Applied Physics Letters*, 92:233115, 2008. DOI: [10.1063/1.2918846](https://doi.org/10.1063/1.2918846).
- [235] A. D. Giddings, J. G. Keizer, M. Hara, G. J. Hamhuis, H. Yuasa, H. Fukuzawa, and P. M. Koenraad. Composition profiling of InAs quantum dots and wetting layers by atom probe tomography and cross-sectional scanning tunneling microscopy. *Physical Review B*, 83:205308, 2011. DOI: [10.1103/PhysRevB.83.205308](https://doi.org/10.1103/PhysRevB.83.205308).
- [236] P. Sengupta, S. Lee, S. Steiger, H. Ryu, and G. Klimeck. Atomistic and continuum modeling of a zincblende quantum dot heterostructure. 2014. arXiv:1407.5420 [cond-mat.mes-hall]. Available at <http://arxiv.org/abs/1407.5420>.
- [237] M. A. Migliorato, V. Haxha, R. Garg, I. W. Drouzas, José María Ulloa Herrero, P. M. Koenraad, M. J. Steer, H. Y. Liu, M. Hopkinson, and D. J. Mowbray. Atomistic modelling of III-V semiconductors: from a single tetrahedron to millions of atoms. In *Proceedings of the 17th European Workshop on Heterostructure Technology*, Padova, Italia, 2008. Universidad de Padova. Available at <http://oa.upm.es/3901/>.
- [238] M. A. Migliorato, A. G. Cullis, M. Fearn, and J. H. Jefferson. Atomistic simulation of strain relaxation in  $\text{In}_x\text{Ga}_{1-x}\text{As}/\text{GaAs}$  quantum dots with nonuniform composition. *Physical Review B*, 65:115316, 2002. DOI: [10.1103/PhysRevB.65.115316](https://doi.org/10.1103/PhysRevB.65.115316).
- [239] Gamry Instruments. Basics of electrochemical impedance spectroscopy: Application note. Available at <http://www.gamry.com/application-notes/EIS/basics-of-electrochemical-impedance-spectroscopy/>. Accessed on 17 May 2016.

- [240] K. Gelderman, L. Lee, and S. W. Donne. Flat-band potential of a semiconductor: Using the Mott–Schottky equation. *Journal of Chemical Education*, 84:685, 2007. DOI: [10.1021/ed084p685](https://doi.org/10.1021/ed084p685).
- [241] Hydrogen on the rise. *Nature Energy*, 1:16127, 2016. DOI: [10.1038/nenergy.2016.127](https://doi.org/10.1038/nenergy.2016.127).